

**PROGRADATION AND EROSION OF A FINE-GRAINED,
TIDALLY DOMINATED DELTA**

A CASE STUDY OF THE JIANGSU COAST

PROGRADATION AND EROSION OF A FINE-GRAINED, TIDALLY DOMINATED DELTA

A CASE STUDY OF THE JIANGSU COAST

Proefschrift

ter verkrijging van de graad van doctor
aan de Technische Universiteit Delft,
op gezag van de Rector Magnificus prof. ir. K.C.A.M. Luyben,
voorzitter van het College voor Promoties,
in het openbaar te verdedigen op Maandag 4 April 2016 om 12:30 uur

door

Min Su

Master of Science in Harbor, Coastal and Nearshore Engineering

Hohai University, China

geboren te Heze, China

Dit proefschrift is goedgekeurd door de

promotors: Prof. dr. ir. M.J.F. Stive
Prof. dr. ir. Z.B. Wang

Samenstelling promotiecommissie:

Rector Magnificus

voorzitter

Prof. dr. ir. M.J.F. Stive

Technische Universiteit Delft, promotor

Prof. dr. ir. Z.B. Wang

Technische Universiteit Delft, promotor

Onafhankelijke leden:

Prof. dr. ir. W.S.J. Uijtewaal

Technische Universiteit Delft

Prof. dr. ir. H.J. de Vriend

Technische Universiteit Delft

Prof. dr. J.A. Roelvink

UNESCO-IHE, Technische Universiteit Delft

Prof. dr. Leo C. van Rijn

Deltares

Overige leden:

Prof. dr. C.K. Zhang

Hohai University, China



ISBN: 978-90-6464-995-0

Copyright © 2016 by Min Su

Author email: m.su@tudelft.nl; smin-1@163.com

An electronic version of this dissertation is available at : <http://repository.tudelft.nl/>.

Front cover: figure from “ideldesign/Shutterstock”.

Back cover: Nanking, sive Kiangnan, Imperii Sinarvm provincia nona. It was drawn by Martino Martini and published by Joan Blaeu (a Dutch cartographer). Available at: <http://www.geheugenvannederland.nl/>. Source: Nederlands Scheepvaartmuseum.

All rights reserved. No part of the material protected by this copyright notice may be reproduced or utilized in any form or by any means, electronic or mechanical, including photocopying, recording or by any information storage and retrieval system, without the prior permission of the author.

To my family

SUMMARY

A large proportion of the world population lives in the coastal zone, which is facing a variety of natural and anthropogenic impacts on its evolution. A better understanding of coastal evolution can be obtained when it is based on an accurate knowledge of coastal dynamics. This thesis aims to study the long-term (hundreds of years) coastal evolution of the Jiangsu coast, China, under both natural and anthropogenic impacts.

The recent (hundreds of years) evolution of the Jiangsu coast is closely related to the shifting course of the Yellow River. The coastline of Jiangsu experienced a rapid progradation stage (1128~1855), when the Yellow River discharged into the Yellow Sea, and a following modification stage (after 1855), when the Yellow River abandoned its prior course. Simultaneously, the sedimentary environment of the Jiangsu coast changed from sandy to silty. In contrast, the tide, which is a dominant driving force for the sediment transport and morphological changes along the Jiangsu coast, has been stable for at least thousands of years.

As one of the fundamental factors controlling the coastal evolution, local hydrodynamics has at the outset drawn our attention. A large tidal wave model containing the Bohai Sea, the Yellow Sea and the East China Sea is established to investigate the near-field hydrodynamic conditions of the Jiangsu coast. For instance, existing knowledge always suggested that the geographical position of the Shandong Peninsula is crucial for the local tidal wave system off the Jiangsu coast. However, this is a hypothesis without any verification. Moreover, the role of the local bathymetry on the formation of the radial tidal current off the Jiangsu coast is debatable. These two factors of influence are assessed based on the tidal wave system (Chapter 2). The results demonstrate that the Shandong Peninsula plays a secondary role, rather than a crucial role on the Jiangsu local tidal wave system. The radial tidal current is independent of the geographic position of Shandong Peninsula and local ridge-channel morphologies.

Besides the existence of the special tidal wave system, another characteristic of the Jiangsu coast is the existence of the silt-dominated sedimentary environment. To gain insight into the characteristics of silt-dominant sediment, flume experiments with various wave and current conditions have been conducted with two sediment samples from the field (Chapter 3). A high concentration layer is observed near the bottom together with ripples under wave-only conditions. Moreover, a significant vertical sediment sorting phenomenon has been found near-bottom for both sediment samples. As a widely used instrument for measuring suspended sediment concentration in both field and laboratory conditions, the Optical Backscatter Sensor (OBS), has been introduced, requiring additional caution due to its sensitivity to sediment grain size. As observed in the flume experiments, vertical sorting leads to vertical grain size differences in a water column. Thus, traditional approaches converting OBS signals based on one fixed calibra-

tion curve (i.e. against the bottom sediment) may lead to large deviations over silt-sand mixed suspensions. To extend the application of OBS for fine mixed sediment, we take the grain size effect into account and propose a new approach (Chapter 4). The new approach introduces an accompanying sediment sample besides the original bed samples for calibrating the OBS instrument. Besides, a multi-fraction sediment model is developed to predict the vertical distribution of sediment grain sizes. The reliability of this approach has been validated by the flume experiments.

Regarding the aforementioned coastal evolution of the Jiangsu coast since 1128, previous studies using a geological approach failed to reach a satisfactory agreement. To investigate the long-term evolution of the Jiangsu coast, a large-scale morphodynamic model is established (Chapter 5, 6). Due to the scarcity of historical data, we have simplified several data, such as the bathymetric data and the hydrodynamic conditions (e.g. river discharge). Historical maps, records and geological measurements have been utilized for determining model settings and validating the model results. We first focus on the formation and the development of the deltaic system (Chapter 5). In spite of the simplifications on model setting, the model shows a good capability to reproduce the development of the AYD. Sensitivity analyses of uncertainties (e.g. sediment discharge, accommodation space) on the performance of long-term morphodynamic model are further conducted. Subsequently, we focus on the modification stage of the AYD, when the Yellow River shifted its course after 1855. In this stage, the fluvial impact on the coastal evolution disappeared, while the impact of wave and human activity rose. Therefore, we take tides, waves and artificial revetments (sea dikes) into account in the model to understand the ongoing coastal behavior (Chapter 6). Based on modelling results, the Yellow River has been proven as one of the sediment sources for the RSRs, and the relevant contribution is neither restricted to the northern RSRs nor to a certain period (even at present). Moreover, the results show that the sea dikes play a significant role on the evolution of the nearshore regions, and that wind waves play a remarkable role on the erosion of offshore shoals. In the perspective of time and hydrodynamic forces, tide is the most dominant force governing the overall evolution of the Jiangsu coast.

This thesis addresses the long-term morphological evolution of the Jiangsu coast through a process-based morphodynamic modelling approach. The corresponding insights and findings improve our understanding on the long-term evolution of the Jiangsu coast.

SAMENVATTING

DE kusten, waar het merendeel van de wereldbevolking woont, worden in toenemende mate aan een verscheidenheid van natuurlijke en antropogene invloeden op haar evolutie blootgesteld. Een beter begrip van de evolutie van de kust kan worden verkregen op basis van een grondige kennis van de kustdynamiek. Dit proefschrift is gericht op het bestuderen van de lange termijn (honderden jaren) kustevolutie van de Jiangsu kust, China, onder invloed van zowel natuurlijke als antropogene effecten.

De recente evolutie (honderden jaren) van de Jiangsu kust is nauw verweven met de veranderingen van het verloop van de Gele Rivier. Overeenkomstig met de veranderingen in het verloop van de rivier, heeft ook de kustlijn van Jiangsu een snelle progradatie fase ondergaan toen de Gele Rivier uitmondde in de Gele Zee (1128 ~ 1855), en in een volgend stadium (na 1855), toen het verloop van de Gele Rivier wijzigde. Tegelijkertijd, veranderde de afzetting van het sediment aan de kust van de Jiangsu van zand in slib. Integenstelling is het getijde, ondanks dat het een dominante drijvende kracht voor sedimenttransport en morfologische veranderingen langs de kust van Jiangsu is, voor ten minste duizend jaar stabiel gebleven.

Een van de fundamentele factoren die de evolutie van de kust domineert, is in de eerste plaats de lokale hydrodynamica. Een aanzienlijk vloedgolf model met de Bohai Zee, de Gele Zee en de Oost-Chinese Zee is gecreëerd om de aantrekkingskracht van de hydrodynamische omstandigheden van de Jiangsu kust te onderzoeken. Bijvoorbeeld, in de huidige kennis is altijd gesuggereerd dat de geografische positie van het schiereiland Shandong van een cruciaal belang is voor het lokale golfsysteem van de kust van Jiangsu. Echter, deze hypothese is nooit bewezen. Bovendien, is de rol van de lokale bathymetrie over de vorming van de radiale getijde huidige voor de kust van Jiangsu discutabel. Deze twee invloedrijke factoren worden op basis van het golfsysteem (hoofdstuk 2). De resultaten tonen echter aan dat het schiereiland van Shandong, in plaats van een cruciale rol, slechts een secundaire rol speelt op het lokale golfsysteem van Jiangsu. De radiaal getijden stroming is onafhankelijk van de geografische positie van schiereiland van Shandong en van de morfologie van de lokale kanaalrichels.

De Jiangsu kust wordt naast het bestaan van het speciale golfsysteem, gekenmerkt door het met slib gedomineerde sedimentaire milieu. Om inzicht te krijgen in de eigenschappen van het slib-dominante sediment, zijn gootexperimenten met verschillende golf- en stroomcondities uitgevoerd met twee sedimentmonsters uit het veld (hoofdstuk 3). Een laag met een hoge concentratie wordt waargenomen in bij de bodem, samen met rimpelingen onder omstandigheden van alleen golven. Bovendien blijkt dat een belangwekkende sortering van verticaal sediment in de buurt van de bodem plaats vindt voor beide sedimentmonsters. Als een veelgebruikt instrument voor meting van de concentratie van zwevend sediment in de veld- en laboratoriumomstandigheden wordt de Opti-

sche Backscatter Sensor (OBS) geïntroduceerd met extra voorzichtigheid vereist door de OBS gevoeligheid voor de grootte van de sedimentkorrel. Zoals opgemerkt in de experimenten in de meetgoot, leidt verticale sorteren tot verschillende verticale korrel groottes in de waterkolom. De omzetting van OSB signalen volgens traditionele benaderingen op basis van een vaste ijkcurve (d.w.z. versus bodemsediment), kunnen tot grote afwijkingen van slib-zand gemengde suspensie leiden. Om de toepassing van OBS voor fijne gemengd sediment uit te breiden, houden we rekening met het effect van de grootte van de korrel en stellen een nieuwe aanpak voor (hoofdstuk 4). De nieuwe benadering introduceert een begeleidende sedimentmonster, naast de originele bodemmonsters, om het OBS instrument te kalibreren. Daarnaast, is een multi-fractie sediment model ontwikkeld om de verticale verdeling van de korrelgroottes van sediment te voorspellen. De betrouwbaarheid van deze aanpak is gevalideerd door goot experimenten.

Met betrekking tot de bovengenoemde evolutie van de kust van de Jiangsu (sinds 1128), hebben eerdere studies met een geologische benadering tot geen bevredigende overeenkomst geleid. Om de lange termijn evolutie van de kust van Jiangsu te onderzoeken, is een grootschalige morfo-dynamisch model opgezet (hoofdstuk 5, 6). Als gevolg van gebrek aan historische gegevens, zijn verschillende vereenvoudigingen van o.a. bathymetrische gegevens en hydrodynamische voorwaarden (bijv. rivier afvoer) gemaakt. Historische kaarten, documenten en geologische metingen zijn goed gebruikt voor de bepaling van de modelinstellingen en het valideren van de modelresultaten. De eerste focus is op de vorming en ontwikkeling van het deltaïsche systeem (hoofdstuk 5). Ondanks de vereenvoudigingen van de instelling van het model, toont het model een goede vooruitzicht om de ontwikkeling van de AYD te reproduceren. Gevoeligheidsanalyses van onzekerheden (i.e. sediment afvoer, ruimtelijke aanpassing) worden verder uitgevoerd om het resultaat van het morfo-dynamische lange termijn model te testen. Vervolgens richten we ons op de veranderingen van de AYD in het stadium waarin de Gele Rivier zich verplaatst. In dit stadium is het fluviale impact op de kust evolutie verdwenen, terwijl de impact van het golfklimaat en van menselijke activiteiten toeneemt. Daarom nemen we het getij, het golfklimaat en de kunstmatige zeedijken op in het model, om de verdere ontwikkeling van de kust te begrijpen (hoofdstuk 6). Op basis van de modelleringsresultaten, is aangetoond dat de Gele Rivier als één van de bronnen voor het sediment voor de RSRs, en dat de relevante bijdrage evenmin beperkt is tot de noordelijke RSRs noch tot een bepaalde periode (zelfs tot op heden). Bovendien is uit de resultaten gebleken dat de zeedijken een belangrijke rol spelen bij de evolutie van de near-shore regio's en dat windgolven een opmerkelijke rol spelen bij de erosie van de ondieptes offshore. Het getij is de meest dominante en sturende kracht op de gehele evolutie van de Jiangsu kust.

Dit proefschrift adresseert de langdurige, morfologische evolutie van de Jiangsu kust via een procesgeoriënteerde morfo-dynamische modelleringsaanpak. De bijbehorende inzichten en bevindingen leiden tot een beter inzicht op de lange termijn evolutie van de Jiangsu kust.

This samenvatting was translated by Mariette van Tilburg and Marcel Stive.

CONTENTS

Summary	vii
Samenvatting	ix
1 Introduction	1
1.1 Context	2
1.1.1 Coastline evolution	2
1.1.2 River delta	3
1.1.3 Tidal sand ridges	4
1.2 Study area: the Jiangsu coast	4
1.3 Problem definition and Research objectives	7
1.3.1 Investigation of the tidal wave system in the Yellow Sea	7
1.3.2 Conversion of OBS signal to sediment concentration with high accuracy in a silt-sand suspension	9
1.3.3 Evolution of the Jiangsu coast throughout a relatively long time scale (since 1578)	9
1.4 Outline	10
2 Tidal wave propagation in the Yellow Sea	11
2.1 Introduction	13
2.2 Model Set Up and Performance	16
2.2.1 Model set up	16
2.2.2 Model performance	18
2.3 Results and influence factor analyses	24
2.3.1 Co-tidal charts and tidal current field	24
2.3.2 Analyses of influencing factors for tidal motions	25
2.4 Discussion on the factors of influence on the tidal wave and tidal current pattern	28
2.4.1 Regional bathymetry	28
2.4.2 The role of the geometric position of Shandong Peninsula	30
2.5 Conclusion	35
3 Laboratory study on the fine sediment transport	37
3.1 Introduction	39
3.2 Flume experiment	40
3.3 Experiment Results and Discussions	46
3.3.1 Bed forms	46
3.3.2 High concentration layer under waves	49
3.3.3 Vertical profile of suspended sediment concentration	50
3.3.4 Vertical profile of sediment grain size	53

3.4	Conclusions.	54
4	Conversion of electro-optical signals to sediment concentration in a silt-sand suspension	55
4.1	Introduction	57
4.2	Approaches for converting OBS measurements	58
4.2.1	Existing methods.	58
4.2.2	Improved approach	60
4.3	Laboratory experiment	63
4.3.1	Experiment description	63
4.3.2	OBS Calibration	63
4.4	Examination of the improved approach.	64
4.4.1	Verification of the modelled grain size distribution	64
4.4.2	OBS output conversion	65
4.4.3	Comparison between the optical and suction concentrations	68
4.5	Discussion	71
4.5.1	Advantage of the improved approach in a silt-sand suspension environment	71
4.5.2	The accuracy of the improved approach	72
4.5.3	Suggestions on the selection of the accompanying sediment sample (AS)	73
4.6	Conclusion	74
5	Exploratory morphodynamic hindcast of the evolution of the Abandoned Yellow River delta, 1578-1855 AD	75
5.1	Introduction	77
5.2	Study area, data and methods.	78
5.2.1	General information	78
5.2.2	Spatial distribution of the AYD	82
5.2.3	Morphodynamic modeling	83
5.3	Model results	91
5.3.1	Model results for the AYD	91
5.3.2	Contribution of uncertainty to delta evolution	97
5.4	Discussion	102
5.4.1	Reliability of the reference run	102
5.4.2	Suggestion on the spatial distribution of the AYD	105
5.4.3	Limitation of this study	107
5.5	Conclusion	108
6	Exploratory morphodynamic modelling on the evolution of the Jiangsu coast since 1855	113
6.1	Introduction	115
6.2	Data and methods	118
6.2.1	Data on morphological changes of the Jiangsu coast.	118
6.2.2	Data on the fine sediment distribution in the RSRs	121
6.2.3	Morphodynamic modelling	122

6.3	Model Results	126
6.3.1	Morphological evolution along the Jiangsu coast	126
6.3.2	Distribution of sedimentation (the OYR-derived sediment)	128
6.3.3	Preliminary results on the contribution of tide, wave and human activities on the morphological evolution of the Jiangsu coast	132
6.3.4	Transport of the OYR-derived sediment after 1855	135
6.4	Discussion	138
6.4.1	The contribution of the OYR-derived sediment to the RSRs	138
6.4.2	Fate or fortune: with a consideration of coarsened sediment bed	139
6.4.3	Limitations and suggestions for the further research	140
6.5	Conclusion	141
7	Conclusions and future work	143
7.1	Synthesis and conclusions	144
7.1.1	Hydrodynamic aspect (tidal wave systems)	144
7.1.2	Improve the OBS utilization in a silt-sand environment	144
7.1.3	Long-term simulation of the morphodynamic evolution of the Jiangsu coast, with an emphasis on reproducing the evolution of the AYD	145
7.2	Future work and recommendations	147
	References	149
	Acknowledgements	165
	Curriculum Vitae	167
	List of Publications	169

1

INTRODUCTION

Love is ever the beginning of knowledge, as fire is of light.

Thomas Carlyle (1795 ~ 1881)

1.1. CONTEXT

1.1.1. COASTLINE EVOLUTION

THE coastline is the interface between the land and the sea. The alternation of a coastline over a long time (i.e. geological time scale) can be explored by approaches of geology and geomorphology. In these approaches, understanding the manner in which the coastline responds to secular variations of the influencing factors becomes crucial. To this end, researchers have been concerned about the coastal evolution with alternative approaches, for example the process-based morphodynamic modelling, which considers the co-adjustments of process and form on the morphological time scale (de Vriend et al., 1993; Wang et al., 1995; Dronkers, 2005). Knowledge on coastal evolution can then be enhanced through understanding the morphodynamic processes in response to changes of external conditions (Wright and Thom, 1977; Elias and van der Spek, 2006; Dastgheib et al., 2008; van der Wegen and Roelvink, 2008).

Analyzing shoreline change raises the issue of large-scale system evolution in space (Carter and Woodroffe, 1997). Meanwhile, the sediment along the coast may have developed over a long-term time scale (mostly in Holocene or Pleistocene: 10^3 to 10^6 years before), except at coasts adjacent to rivers which frequently shift their courses, e.g. the Yellow River (Figure 1.1). It is reported that the Yellow River has experienced at least five major avulsions in the past (Kidder and Zhuang, 2015).

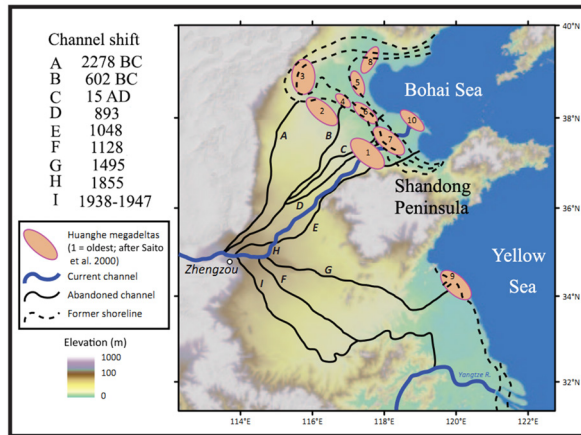


Figure 1.1: Map indicating the approximate course shifts of the Yellow River and corresponding locations of deduced deltas in the past thousands of years (modified after Kidder and Tregear, 1965; Wang and Aubrey, 1987; Zhuang, 2015).

1.1.2. RIVER DELTA

A river delta can be formed when a river flows into a relatively larger water body (e.g. ocean, lake or gulf). The deltaic morphology is controlled by both sediment supply from the river and the reworking role of local hydrodynamic conditions, e.g. tides and waves (Seybold et al., 2009). The deltaic system can change dramatically by a modest modification of the influence factors, e.g. fluvial discharge, marine energy, accommodation regime (Giosan, 2007). If a river goes through changes upstream, e.g. a course shift, a previously formed delta lobe may be abandoned. The Abandoned Yellow River Delta (AYD) is a remarkable example of an abandoned delta (Figure 1.1). It is formed when the Yellow River shifted its course to the Southern Yellow Sea through the Jiangsu coast during 1128~1855 (Xue, 1993; Kidder and Zhuang, 2015).

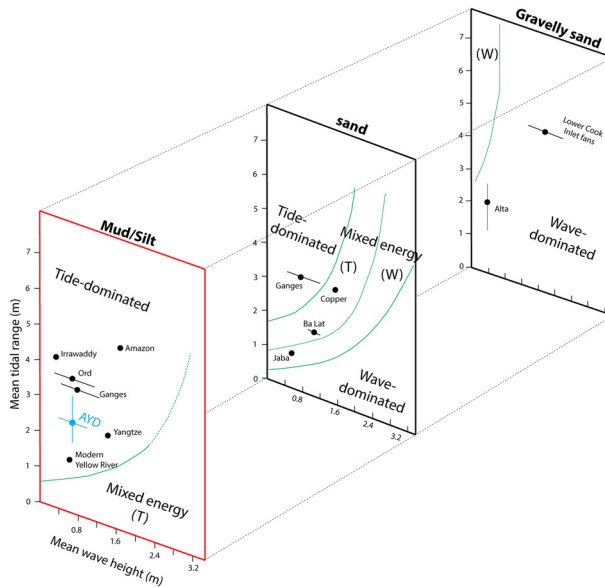


Figure 1.2: Classification of coastline based on the relative ratio between tidal range and wave height, taking the grain size effect into account (adopted from Orton and Reading, 1993).

Besides a classical tripartite system to classify a delta (Galloway, 1975), which discriminates through the shape of deltaic system, a modified classification system was proposed by Orton and Reading (1993). The updated classification criterion has accounted for the grain size influence (Figure 1.2). It is illustrated that the effectiveness of tide gradually increases with the decrease of the sediment size (van Maren, 2004). Fine grain size dominated coastlines are mainly dominated by tide forcing.

1.1.3. TIDAL SAND RIDGES

TIDAL sand ridges are common features on modern shelves, including shallow seas and continental shelves (Berne et al., 2002; Wang et al., 2012). They are composed of a group of large and elongate sand bodies, which are parallel to the direction of tidal currents (Wang et al., 2012). The essential requirements for the formation are abundant sediment (i.e. sand) and strong tidal currents (Dyer and Huntley, 1999). Due to a different shape of tidal currents, the pattern of tidal sand ridges also varies, e.g. the radial sand ridges in the Southern Yellow Sea (Zhang et al., 2013), linear sand ridges in the North Sea (Van de Meene and Van Rijn, 2000), and finger-shape sand ridges in the Bohai Strait (Liu et al., 1998). Although the tidal current is thought as the principle reason of the formation, storm-effects, pre-existing morphology and sea level rise are also factors of influence (Van de Meene and Van Rijn, 2000; Li and King, 2007).

1.2. STUDY AREA: THE JIANGSU COAST

THE Jiangsu coast is located in eastern China, surrounded by the Shandong Peninsula and the Yangtze River Delta (Figure 1.3). The length of the Jiangsu coast is about 954 km (Rao et al., 2015). Approximately 90% belongs to the class of a silty coast, while a rocky coast is only located in the northernmost Jiangsu coast (i.e. the Haizhou Bay). The Jiangsu coast contains two large-scale geomorphological units (Figure 1.3): the Abandoned Yellow River Delta (AYD) and the Radial Sand Ridges (RSRs).

The AYD is formed by the silty sediment carried by the Yellow River during 1128~1855 (Ren and Shi, 1986). A relative high progradation rate of the deltaic system is reported after 1578 when humans successfully trained the river course (Berne et al., 2002). Since 1855, the Yellow River shifted northward to the Bohai Sea (Figure 1.1) and the AYD is abandoned and experiences erosion (Zhou et al., 2014).

The RSRs off the central Jiangsu coast is the most distinguishable sand ridge system on the Chinese continental shelf (Figure 1.4). These sand ridges cover an area of 22,470 km², sketching 200 km in the N-S direction and 90 km in the E-W direction (Wang et al., 2012). The water depth generally ranges from 0 to 25 m and nearly 86% of ridges are submerged (Fu and Zhu, 1986; Wang et al., 1998). Recently, the Chinese government has planned a large-scale reclamation (>1800 km² between 2010 and 2020) near the Jiangsu Coast (Zhang and Chen, 2012). Both the nearshore tidal flats and the largest ridges of the radial sand ridge system are included in the reclamation plan.

The morphological evolution of the Jiangsu coast has a great link with the evolution of the AYD. A sketch diagram of historical evolution of the Jiangsu shoreline is shown in Figure 1.5. It shows that a relatively stable condition is broken by the shift of Yellow

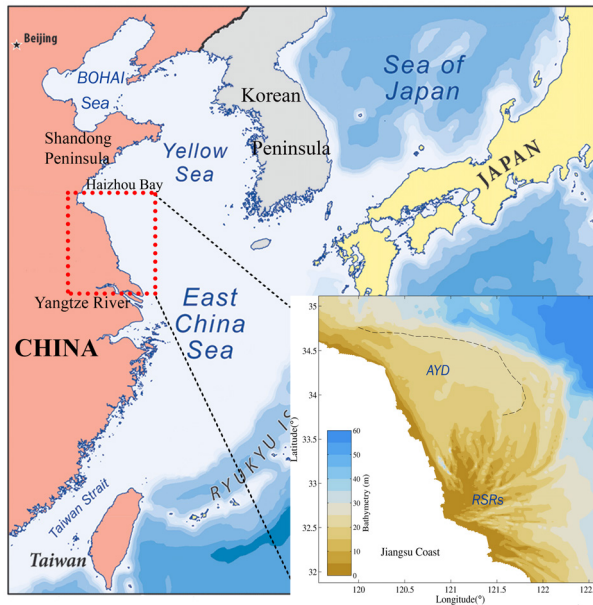


Figure 1.3: Map showing the geographical location of the Jiangsu coast. The enlarged Jiangsu coast indicates the detailed morphology near the Jiangsu coast. The abandoned Yellow River Delta (AYD) is bounded by the black dashed line (according to Xia et al., 2015). Series of ridges off the central Jiangsu coast is the Radial Sand Ridges (RSRs).

River. During 1128~1855 AD, the progradation rate of most of the Jiangsu coast was extraordinarily obvious (Figure 1.5). The general progradation trend of the Jiangsu coast changed completely after 1855, when the Yellow River shifted it away. The whole Jiangsu coast is then featured by a trend of “erosion in the north, sedimentation in the south”. Specifically, the previous vicinity region of the river mouth suffers significant erosion, while huge tidal flats are formed along the central and southern Jiangsu coast (Zhou et al., 2014).

Before the Yellow River discharged into the Southern Yellow Sea, the Jiangsu coast was a sandy coast featured by a series of barrier-lagoon systems (Ye, 1986). Owing to the huge sediment supply of the Yellow River, the Jiangsu coast changed from a sandy coast to a silty coast (Liu et al., 2010; Xue et al., 2011). At present, the sediment along the Jiangsu coast is a mixture of clay, silt and sand. The spatial distribution of sediment composition is quite complicated (Shi et al., 2012), and depends on different morphological feature (Figure 1.6). Silty sediment is abundant in the AYD region, although the bottom sediment of the nearshore zone has showing a coarsening trend (Chen et al., 2014). With respect to the central and southern of the Jiangsu coast, clay/silt is abundant in the tidal flats and channels of the RSRs, whereas ridges are mainly made of fine sand.

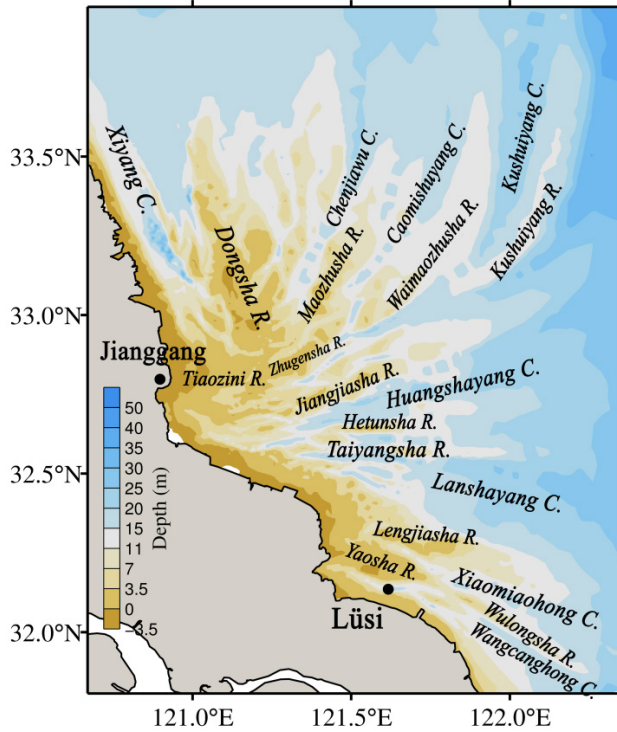


Figure 1.4: Detailed morphological map around the Radial Sand Ridges off the Jiangsu coast, including the names of series of ridges and channels.

Note that, simultaneously with the changes of fluvial influence before and after 1855, the dominant hydrodynamic process of the deltaic system changes as well. With respect to the progradation stage (i.e. before 1855), both fluvial and tidal forcing are relative important for the deltaic system due to the large water discharge of the Yellow River and energetic tidal forcing (Uehara et al., 2002). For the erosion stage (i.e. after 1855), the wave effect has been stated as notable for the morphological evolution of the AYD (Liu et al., 2011; Zhang et al., 2015) in the absence of fluvial influence. Nevertheless, the AYD is still under a tide-dominated condition (Figure 1.2) according to the classification criterion by Orton and Reading (1993). Thus, the tide force is the main important driving force for the long-term morphological processes of the Jiangsu coast. Semi-diurnal tides in particular are the dominant tidal constituents in this region (Cheng, 2009). Previous studies illustrate that the Jiangsu coastal zone is characterized by an amphidromic system in the north and a progressive tidal wave system in the south. A commonly accepted viewpoint is that the geographic position of the Shandong Peninsula plays a key role on

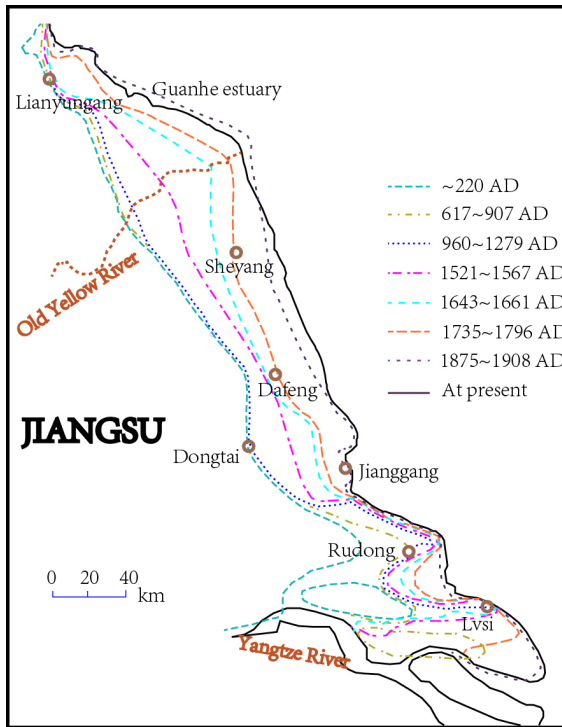


Figure 1.5: Historical evolution of the Jiangsu coast, based on Zhang (1984).

the local tidal wave system (Zhang et al., 1999; Xu et al., 2016). Furthermore, the interaction between the preceding two tidal wave systems is hypothesized to be the main reason producing the radial-shaped tidal current pattern, which eventually shaped the RSRs off the central Jiangsu coast.

1.3. PROBLEM DEFINITION AND RESEARCH OBJECTIVES

1.3.1. INVESTIGATION OF THE TIDAL WAVE SYSTEM IN THE YELLOW SEA

IN the relationship between hydrodynamics, sediment transport and morphological changes, the hydrodynamic condition is the basis for the other two units. The mechanism of the tidal wave propagation in the Yellow Sea has been a research focus for many years. Although great efforts have been achieved based on existing studies (e.g. Fang, 1986), it is still necessary to advance the knowledge on the underlying mechanism of tidal wave propagation around the Jiangsu coast. With respect to tidal wave simulations, the consideration of influencing factors, such as the tide generating forces and river discharges, varies in different models (e.g. Bao et al., 2001; Song et al., 2013). It is unknown

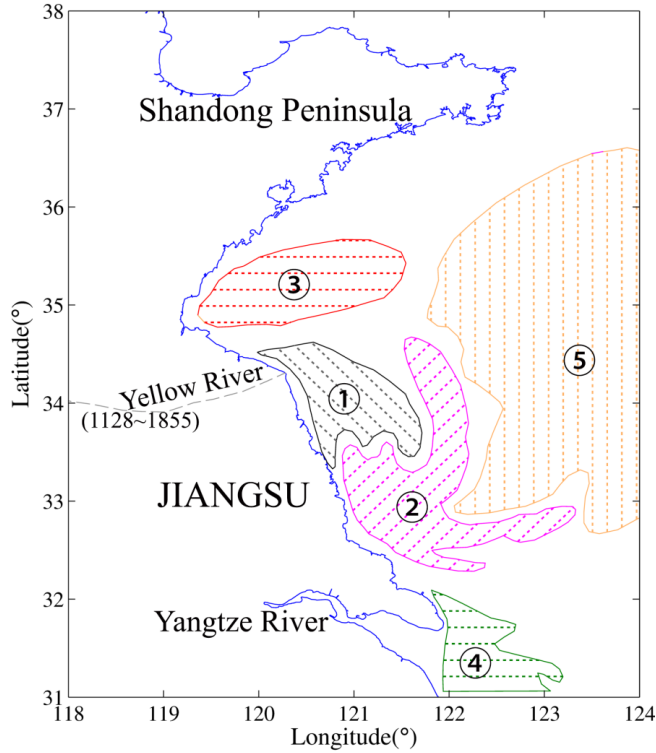


Figure 1.6: General sediment distributions in the Yellow Sea (only shown the regions near the Jiangsu coast, modified after Shi et al., 2012). Silt-clay and clayey-silt in ① (AYD) and ⑤ (central Yellow Sea mud patches); sand in ② (RSRs) and ③ (Haizhou Bay); sand-silt-clay mixture in ④ (Yangtze River Delta).

to what extent these two factors can influence a large-scale tidal wave system, especially the tidal regimes near the Jiangsu coast. In regard to the near-field hydrodynamics of the Jiangsu Coast, the geographic position of the Shandong Peninsula is always hypothesized as crucial for the local rotating tidal wave system and radial tidal current system (e.g. Zhang et al., 1999), while no validation has been conducted yet. Additionally, many studies have focused on the radial tidal current system around the RSRs, especially its relationship with local bathymetry (Zhu and Chang, 2001; Ye, 2012). However, these researches fail to reach an agreement.

In this context, the related objectives of this thesis are:

- 1) Examining the effects of two influencing factors, i.e. tide generating forces and river discharges on the performance of a large-scale tidal wave model;
- 2) Investigating the role of the geographic position of the Shandong Peninsula on the formation of the rotating tidal wave system, and examining the relationship between the radial tidal current off the Jiangsu coast and local bathymetry.

1.3.2. CONVERSION OF OBS SIGNAL TO SEDIMENT CONCENTRATION WITH HIGH ACCURACY IN A SILT-SAND SUSPENSION

THE Optical Backscatter Sensor (OBS) has been widely used to measure suspended sediment concentration (SSC) in both field and laboratory conditions (Greenwood and Jagger, 1995; Downing, 2006). Compared with the traditional suction method, it can obtain a high temporal and spatial resolution of SSC (Downing et al., 1981; Wren et al., 2000). However, OBS is very sensitive to many factors (e.g. sediment concentration magnitude, bubbles and particle size), and the most significant factor suggested is the grain size (Downing, 2006). Small particle sizes (especially less than 100 μm ; Conner and De Visser, 1992) in particular have a more significant influence on the OBS response (Greenwood and Jagger, 1995; Van Rijn et al., 2000). For instance, output can change with 70% when particle size ranges from 20 μm to 50 μm (Wren et al., 2000). Thus, converting OBS output to sediment concentration should be done with caution, especially for non-homogeneous sediment environments with a silt-sand mixture.

In this context, the related objectives of this thesis are:

3) Carrying out a series of flume experiments based on the field-collected silt-sand mixtures, under various hydrodynamic conditions; and measuring the SSC by both the OBS approach and the suction method;

4) Proposing an approach to convert OBS signal to SSC with relatively high reliability for silt-sand suspension, taking the grain size effect into account.

1.3.3. EVOLUTION OF THE JIANGSU COAST THROUGHOUT A RELATIVELY LONG TIME SCALE (SINCE 1578)

ACCORDING to the shift of river course, the significant evolution of the Jiangsu coast can be divided into two stages. At the first stage (1128~1855), the whole Jiangsu coast experienced seaward progradation. This stage has drawn little attention (Liu et al., 2013; Xia et al., 2015), even though several existing studies have applied a geological approach to predict the spatial distribution of the deltaic system (e.g. Gao et al., 1989; Liu et al., 2013). Furthermore, these studies failed to reach an agreement on the spatial extension of both the subaerial delta and subaqueous delta. As a foundation for the subsequent evolution of the Jiangsu coast, the existing knowledge on the evolution of the deltaic system and the Jiangsu coast at this stage is insufficient. To avoid the restriction of geological approach and to investigate the evolution process of the AYD, an alternative way (viz. the process-based morphodynamic approach) should be applied.

For the following stage after 1855, the deltaic system suffered significant erosion due to the course shift of the Yellow River when no more sediment was supplied to the Jiangsu

coast. Although the modification of Jiangsu shoreline can be summarized through the analysis of historical maps (e.g. Zhou et al., 2014), there is a lack of process-based dynamic understanding, especially under the influence of various hydrodynamic factors (e.g. tides, waves) and human interventions (e.g. construction of sea dikes). Furthermore, there is little study on evaluating the effect of these hydrodynamic processes and human interventions on the large-scale and long-term morphological evolutions. It is hard for the geological approach to meet such objectives. Besides, existing studies also have various different points of view on whether and to what extent the erosion of the AYD feed the RSRs (e.g. Fu and Zhu, 1986; Wang et al., 2012). Herein, it is important to enrich our understanding of the evolution of AYD and the relevant impact on the Jiangsu coast.

In this context, the related objectives of this thesis are:

5) Reproducing the evolution of the AYD through a process-based morphodynamic model, including both the progradation and the erosion stages;

6) Investigating the influence of the Yellow River derived sediment on the RSRs, e.g. whether it is a sediment source for the RSRs; the influence of the Yellow River derived sediment on the RSRs.

1.4. OUTLINE

THIS thesis focuses on the morphological evolution mechanism of the Jiangsu coast on a long-term scale (i.e. hundreds of years). In chapter 2, the tidal wave system of the Yellow Sea is investigated, with emphasis on the formation of the rotating tidal wave system around the Jiangsu coast. In chapter 3, the sediment transport characteristics of silty sediment are revealed through flume experiments under wave-only and wave-current combination conditions. Since OBS is a commonly applied instrument for measuring the suspended sediment concentration, chapter 4 mainly focuses on how to effectively convert the OBS signals to sediment concentrations in a silt-sand dominated environment. Based on the understanding of the silty sediment and local hydrodynamic conditions, in chapter 5, attention is paid to the progradation of the AYD during 1578~1855 AD, including evolution mechanism and reasonable estimation on the spatial distribution of delta. Subsequently, the erosion process of the AYD and the simultaneous evolution of the Jiangsu coast are investigated in chapter 6. Finally, in chapter 7, a synthesis summarizes the relevant findings of the preceding chapters and proposes several recommendations for the future studies.

2

TIDAL WAVE PROPAGATION IN THE YELLOW SEA



This Chapter is based on a journal paper published in *Coastal Engineering Journal*:

Su, M., Yao, P., Wang Z.B., Zhang C.K., Stive M.J.F. (2015), Tidal wave propagation in the Yellow Sea, *Coastal Engineering Journal*, 57 (3), 1550008, doi: 10.1142/S0578563415500084.

Abstract: To investigate the near-field and far-field hydrodynamic conditions along the Jiangsu Coast in large scale, a two-dimensional tidal wave model which covers the Bohai Sea, the Yellow Sea and the East China Sea is developed and validated. After a brief review of previous models, some influencing factors, such as tide generating force, river discharges as well as shoreline changes due to land reclamation, are examined in this study. We suggest that whether these factors should be considered in the model depends on the different purposes and geographical regions of interest. Then, a series of experiments are designed to further investigate the previously proposed important factors of influence (i.e. local bathymetry and the role of Shandong Peninsula (SDP)) on the tidal motions in the Yellow Sea. The numerical experimental results show that the interaction between the tidal wave system in the northern Yellow Sea and the incoming tidal wave plays a main role on the formation of the rotating tidal wave system in the southern Yellow Sea, whereas the role of geographic position of the SDP is secondary. With respect to the tidal current, it is found that the radial shape of it is independent of the local bathymetry, but may be generated by the convergent tidal wave formed by the meeting of the rotating tidal wave in the southern Yellow Sea and the incoming tidal wave from the East China Sea. Furthermore, a certain water depth is crucial for the intensity of current velocity to generate the special topography of radial sand ridges.

Highlights:

- The interaction between the tidal wave system in the northern Yellow Sea and the incoming tidal wave is the key to the formation of the rotating tidal wave system in the Southern Yellow Sea.
- The role of geographic position of the Shandong Peninsula is secondary on the formation of rotating tidal wave system in the southern Yellow Sea.
- The radial shape of tidal current near the Jiangsu Coast is independent of the local bathymetry, while may be controlled by the special local tidal wave systems.

2.1. INTRODUCTION

THE east part of the Chinese marginal seas (BYECS) includes the Bohai Sea, the Yellow Sea and the East China Sea, bounded by the Chinese main land, Taiwan Island, the Korean Peninsula, Kyushu Island and Ryukyu Island (Figure 2.1). In the BYECS, the tide force is the main important driving force for the morphological processes, while waves and storms are secondary effects (Lin et al., 2000; Lie, 1999; Lee et al., 2011; Wang et al., 2012). Semi-diurnal tides in particular, are the dominant tidal constituents in this region (Cheng, 2009). The southwest of the Yellow Sea, where the Jiangsu Coast is located, is famous for abundant tidal flats which account for 25% of the tidal flat resources in China (Tao et al., 2011a). Near the Jiangsu Coast, the hydrodynamic condition is very special because of its radial tidal current (RTC) pattern (Zhang et al., 2013). In order to gain a better understanding of this hydrodynamic feature, it is necessary to advance the knowledge about the underlying mechanism of tidal wave propagation in the whole BYECS first.

The mechanism of the tidal wave propagation in the BYECS has been a research focus for many years. The first study can be traced back to 1933, which was conducted by Ogura (1933). Several studies have been performed to establish a first impression of the tidal wave system in this region by using observed data (e.g. Fang, 1986). Since the late 1970's, numerical modeling has become the most commonly used method (see Table 2.1), besides analytical modeling (Kang, 1984; Shen et al., 1993). Many meaningful results have been generated based on these models with different focuses and model settings (e.g. mesh resolution, area of domain). Analytical models are always used to explore internal tidal dynamics (e.g. tidal amphidromic points formation, tidal wave propagation pattern) based on idealized domains. 2D and 3D models mainly focus on practical issues, such as tidal wave propagation and tidal current in the BYECS.

The consideration of influencing factors, such as the tide generating force (TGF) and river discharges, varies in different models (Table 2.1). Although the influence of TGF on the tidal amplitude in the Yellow Sea and in the East China Sea is commented to be several percent (An, 1977; Kang et al., 1991; Kang et al., 1998), some research still suggests that the contribution of TGF should not be neglected in the BYECS in order to generate an accurate tidal motion (e.g. Song et al., 2013; Yu et al., 2006). As many studies have ignored TGF, it is necessary to analyze and discuss where the most affected region is and to what extent the accuracy can be affected by ignoring TGF in this large-scale model. Similarly, as BYECS is surrounded by many rivers (Figure 2.1) which are always ignored by previous studies, it is also unclear to what extent the river discharge can influence the tidal wave pattern. In addition to the influences of these natural physical processes, the

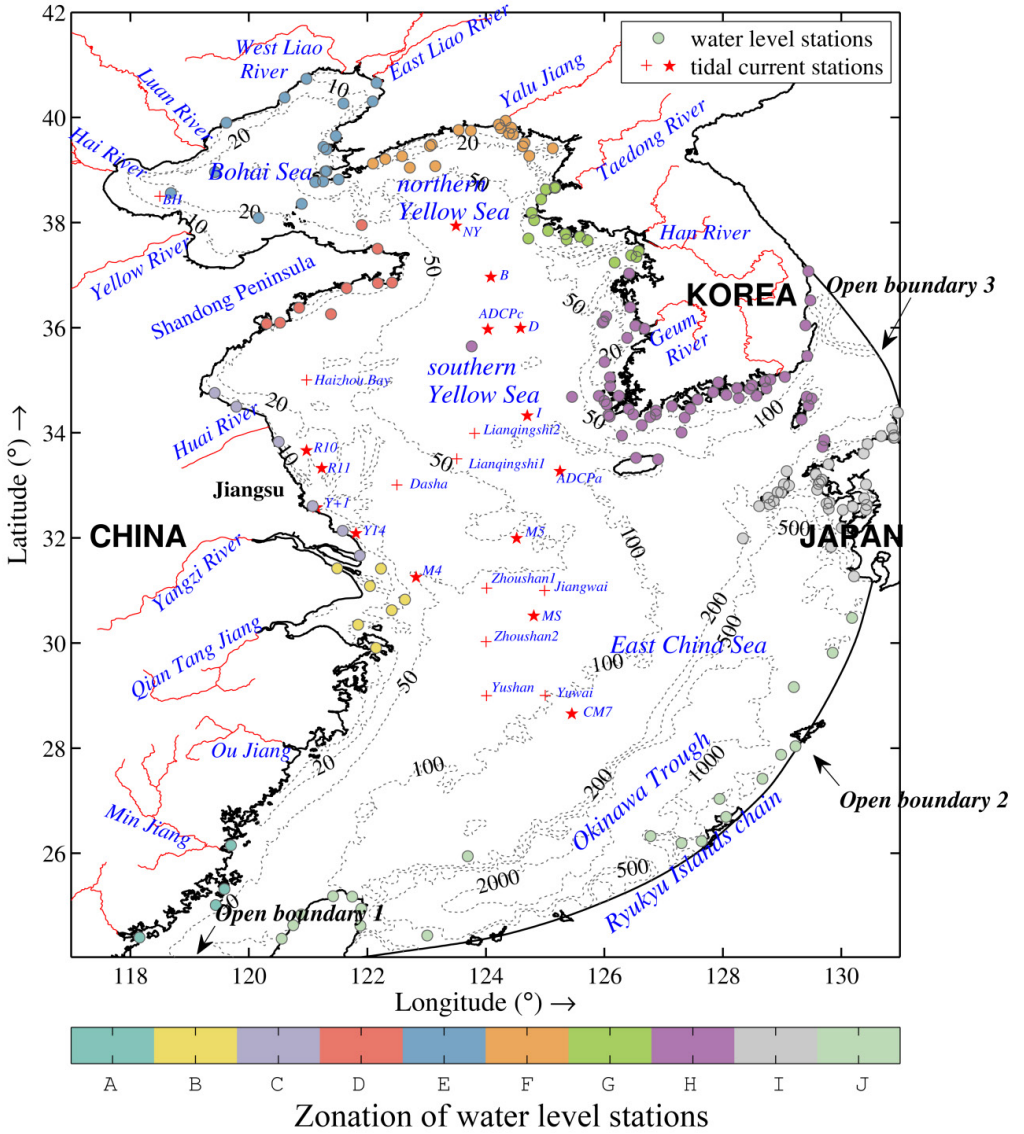


Figure 2.1: Map of the the Bohai Sea, the Yellow Sea and the East China Sea, and distribution of the main rivers. Bathymetry contours are given in m. Circle dots show the location of the water level observation stations, which are divided into 10 zones (A-J) represented by different colours. Red crosses and stars show the location of tidal current observation stations.

Table 2.1: Summary of the some tidal models about BYECS.

Authors	Domain	Resolution	TGF
Choi (1980)	BYE	12'×15'	No
Kang (1991)	BYE	7.5'×10'	Yes
Zhao (1994)	BYE	15'×15'	Yes
Kang (1998)	BYE	3.75'×5'	Yes
Lin (2000)	BYE	6'×6'	Yes
Zhu (2000)	BYE	10'×10'	Yes
Chen (2008)	BYE	4'×4'	Yes
Wan (1998)	BYE	5'×5'×5 layers	No
Guo (1998)	BYE	12.5 km×20 layers	No
Wang (1999)	BYE	10'×10'×6 layers	Yes
Bao (2001)	BYE	5'×5'×15 layers	No
Li (2003)	BYE	8~32 km×20 layers	No
Zhu (2012a)	BYE	1.5~50 km×10 layers	-
Zhu (2012b)	BYE	2'×2'×22 layers	-

human intervention on the coastal line is also important in the BYECS. For example, a large-scale reclamation (> 1800 km² between 2010 and 2020) is implemented by the Chinese government near the Jiangsu Coast. It is necessary to identify to what extent such abrupt shoreline changes can influence the tidal wave motion on both near- and far-field. Therefore, further studies are required to focus on these questions and to provide suggestions on the setup of large-scale models.

In regard to the near-field hydrodynamics of the Jiangsu Coast, many studies have focused on the RTC and its formation mechanism. There are three main different understandings to interpret its formation. The first is the bathymetry control assumption, which considers that RTC is generated by the local radial sand ridges (Ren, 1986; Zhang, 1991). The second theory suggests that RTC is independent of the local bathymetry but controlled by the special local tidal wave systems (Zhu and Chang, 2001a). The local tidal wave pattern is convergent-like, which is hypothesized to be formed by the meeting of the progressive wave from the East China Sea and the rotating tidal wave system in the southern Yellow Sea. And the geographic position of the Shandong Peninsula (SDP) is thought to play a significant role on the formation of such tidal wave and tidal current pattern (Huang and Wang, 1987; Zhang et al., 1996; Wang et al., 1998; Zhang et al., 1998). The third opinion, considering the effects of both bathymetry and tidal wave system, suggests that the formation of RTC is due to the interaction between tidal waves and topography/local shorelines (e.g. Wang et al., 2012; Lin et al., 2000; Ye, 2012). Comparing these theories, there are two points, local bathymetry and the role of SDP on the local tidal wave system and the tidal current pattern, requiring further study to determine

their effects.

Therefore, in this study, a large-scale model covering the domain of BYECS is set up, with special interests in the southern Yellow Sea, to investigate the overall tidal motion in the near-field of the Jiangsu Coast. After the verification of the model, the effects of influencing factors, such as TGE, river discharge as well as shoreline changes due to land reclamation, on the performance of the model are examined using numerical experiments. Then, a series of experiments are carried out to explore the effect of the local bathymetry and the role of SDP on the tidal wave and tidal current pattern.

2.2. MODEL SET UP AND PERFORMANCE

2.2.1. MODEL SET UP

THIS study focuses on the tidal wave propagation and the tidal current pattern in the Yellow Sea, where the tidal current changes are predominantly horizontal (Xing et al., 2012). A 2DH modeling method is considered to be adequate for this study, since it requires less computation time compared with the 3D method especially for large-scale domain. Therefore, a 2DH tidal wave model is setup based on the Delft3D modeling system (Deltares, 2012), focusing on the tidal dynamics in the BYECS with a special interest in the southern Yellow Sea. The Delft3D-FLOW module is developed by resolving the Navier-Stokes equations for incompressible fluids under shallow water conditions and under the Boussinesq assumptions. More details of the numerical schemes can be found in the Delft 3D-FLOW user's manual (Deltares, 2012).

The model domain covers an area which is bounded by latitudes of 24° and 41°N and by longitudes of 117° and 131°E (Figure 2.1). To fit the coastal lines, orthogonal curvilinear grids are applied with a resolution from approximately 0.7'×0.7' to 2.8'×2.8', under spherical coordinates. A relatively higher grid resolution is used in the area of interest, e.g. the Jiangsu Coast, the Yellow Sea, while the grid is coarser in the area near open boundaries. The enlarged grids near the Jiangsu Coast are shown in Figure 2.2(a). Previous numerical studies were able to satisfy the basic requirement of the hydrodynamic analysis in the BYECS; however, finer grids are necessary for a more accurate simulation because the small scale changes of the topography and shoreline can only be considered by high resolution.

The bathymetry data (Figure 2.1) are obtained, first, from the General Bathymetric Chart of the Oceans (GEBCO) bathymetry database (IOC, IHO, and BODC, 2003) with 30 arc-second grid resolution. Other bathymetry data near the China coast, e.g. Jiangsu

area, are obtained by digitalizing the official marine charts published by the Maritime Safety Administration of the P. R. of China, to improve the simulation accuracy near the coastal region.

The open boundaries of this large-scale model are set at the deep-sea areas, sufficiently far away from the Jiangsu Coast. In total, there are three open boundaries included in this model (Figure 2.1). At these boundaries, the water level is prescribed by 13 astronomical tidal components (M2, S2, N2, K2, K1, O1, P1, Q1, Mf, MM, M4, MS4 and MN4), obtained from a global scale ocean model – TPXO7.2 model (<http://volkov.oce.orst.edu/tides/global.html>). Harmonic components of the tidal gauges near open boundaries (e.g. Ryukyu Islands), collected from the International Hydrographic Organization (IHO) tidal dataset, are used to correct the data obtained from the TPXO7.2 model. Then, the water levels at open boundaries are computed by:

$$\zeta(t) = A_0 + \sum_{i=1}^k A_i F_i \cos(\omega_i t + (V_0 + u)_i - g_i) \quad (2.1)$$

where, $\zeta(t)$ is the water level at time t ; A_0 is the mean water level over a certain period; k is the number of relevant constituents; i is the index of a constituent; A_i is the local tidal amplitude of a constituent; F_i is the nodal amplitude factor; ω_i is the frequency; $(V_0 + u)_i$ is the astronomical argument; g_i is the local phase lag.

As the model domain covers a large area and the water depth of several sections is relatively deep, TGF is included in this model and calculated based on the tidal potential of the equilibrium tide and the earth tide (Schwiderski, 1980; Deltares, 2012). For the equilibrium tide, the tidal potential is decomposed into the series:

$$\varphi = \sum_{\nu=0,1,2} \varphi_{\nu}(\lambda, \phi, t) \quad (2.2)$$

where, $\nu = 0, 1, 2$ refers to long-period species, diurnal species and semi-diurnal species, respectively:

$$\varphi_0 = K_i (1.5 \cos^2 \phi - 1) \cos(\omega_i t + 2\lambda + \chi_i) \quad (2.3)$$

$$\varphi_1 = K_i \sin(2\phi) \cos(\omega_i t + \lambda + \chi_i) \quad (2.4)$$

$$\varphi_2 = K_i \cos^2 \phi \cos(\omega_i t + 2\lambda + \chi_i) \quad (2.5)$$

where, λ, ϕ are geographical co-ordinates, K_i is the amplitude of the equilibrium tide;

ω_i is the frequency of the equilibrium tide; χ_i is the astronomical argument of the equilibrium tide (relative to GMT); t is the universal standard time. Then, the equilibrium tidal potential is corrected by the theory of the earth tide to obtain the net tidal potential. In the model, the TGF of 10 tidal constituents (M2, S2, N2, K2, K1, O1, P1, Q1, Mf, and MM) is considered, because all other constituents fall below 4% of the dominating semi-diurnal (M2) tide (Schwiderski, 1980; Dietrich, 1963).

Since there are many rivers flowing into the domain of the BYECS (Figure 2.1), the 14 rivers along the coastline of China and Korea are considered in this model. Multi-year averaged monthly discharges of these rivers are collected from database of Global River Discharge (Vorosmarty et al., 1998). These monthly discharges of different rivers are prescribed in the model as the river boundaries.

For the shallow water areas (e.g. tidal flats) inside the domain of the BYECS, the drying and flooding processes are considered in this model. The main scheme considering the drying and flooding processes is to conduct a series of checks on both water level points and velocity points (due to the use of staggered grids) before computation in each time step. For water level points, we used the maximum value (d_{max}) of four surrounding depth points as the water depth. At a velocity point, the bed level is the arithmetic average of the value specified in the vertices of the cell (d_{mean}). For the water levels at a velocity point, a so-called upwind method is applied (see the Delft 3D-FLOW Manual, Deltares, 2012, for more details). Then, whether computational grids are wet or dry is determined by comparing the total water depth at the water level point and the velocity point with the threshold depth δ (in this study $\delta=0.01\text{m}$).

The model was started at zero initial conditions (cold start), running three months (from 1 July to 1 October 2006), which cover the field investigation periods near the Jiangsu Coast. The first 7 days are considered as a spin-up period and omitted in the analysis. The simulation time frame is referred to as the Universal Time Coordinated (UTC) with the time step of 1 minute.

2.2.2. MODEL PERFORMANCE

VERIFICATION OF THE WATER LEVEL

IN the BYECS model, we setup 190 water level observation stations along the land boundaries (colored circles in Figure 2.1). The computed water levels at these stations are verified by the measured values in the form of harmonic constants. The harmonic constants of water level stations are collected from the International Hydrographic Organization (IHO) tidal dataset, the Admiralty Tidal Tables (Hydrographer of the Navy, 1979) and published papers by Zhang (2005) and Tao et al. (2011b). These points are

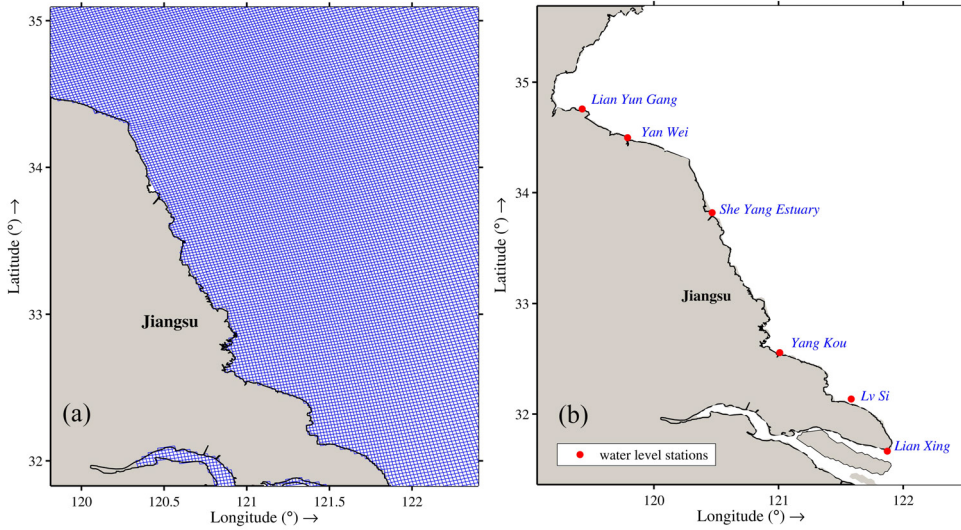


Figure 2.2: Grid (a) and distribution of water level observation stations (b) near the Jiangsu Coast.

numbered (from 1 to 190) and divided into 10 groups (A-J) in a clockwise direction for a clear illustration. Note that the phase lag in this study refers to UTC.

To graphically illustrate the results, we present the amplitude ratio (the simulated amplitude divided by the measurement) and the phase difference (the simulated phase subtracted by the measurement) into a circular bar chart. The amplitude ratio, which is dimensionless, can show how much the amplitude is overestimated or underestimated in the model. It is worth to emphasize that the amplitude ratio is more accurate to evaluate the model performance than the absolute amplitude error, because the same absolute differences may represent different agreements with the observations. Due to the limited space, only the simulated results of the M2 tide are shown in this paper (Figure 2.3). The outer, middle and inner circles present the number of the observation points, amplitude ratio and phase difference, respectively. The letters 'A-J' indicate the 10 regions of the observation points. Different colors indicate the different level of agreement between the measurements and the simulations. The color green, orange, and red indicate an error less than 0.1, 0.2 and over 0.2 for amplitude ratio, respectively, and less than 10° , 20° , and over 20° for phase difference, respectively.

In order to estimate the deviation between observations and simulations, the Root Mean Square (RMS) values for the four major tidal components (M2, S2, K1, and O1), in terms of amplitude ratio differences and phase differences, are obtained by Eq.(2.6), respectively.

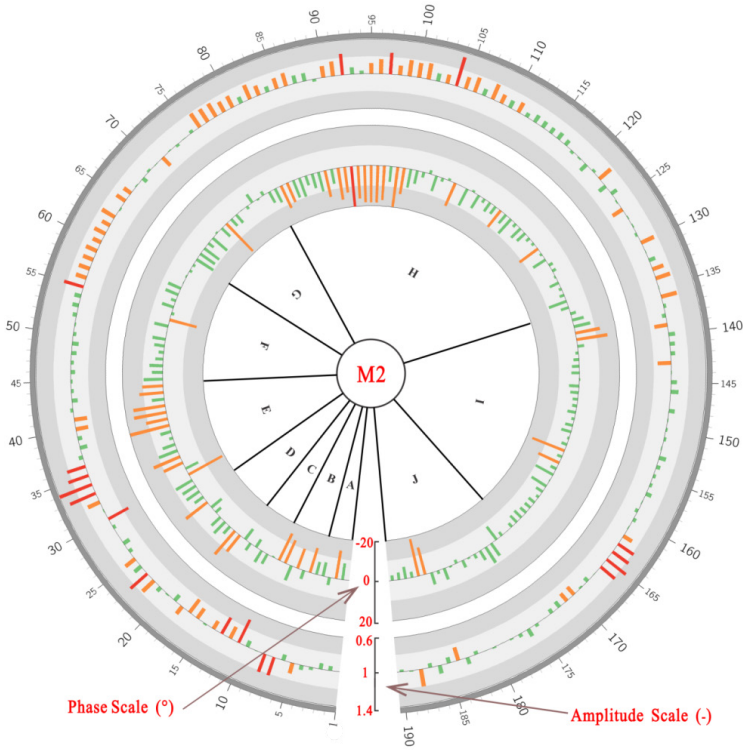


Figure 2.3: Harmonic constants comparison of the M2 tidal constituent.

$$RMS = \sqrt{\frac{\sum_1^N (x_i - \bar{x})^2}{N}} \quad (2.6)$$

where, x_i is the amplitude ratio a_c/a_o (or calculated phase g_c) of a tidal constituent; a_o and a_c are the observed and calculated amplitude, respectively; \bar{x} is 1 when calculating the RMS of the amplitude ratio; \bar{x} is the observed phase g_o when calculating the RMS of phase; N is the number of data. In general, the RMS values in terms of the amplitude ratio difference and the absolute phase difference are 0.12 and 8.35°, 0.14 and 9.98°, 0.20 and 12.94°, 0.22 and 8.99° for the M2, K1, S2, O1, respectively. Given that the number of tidal gauges is almost 200, the differences can be considered relatively small. Especially, the accuracy of the M2 constituent is satisfactory. In conclusion, this model can satisfactorily reproduce the tidal wave system in the Bohai Sea, the Yellow Sea, and the East China Sea.

A detailed comparison of the harmonic constants of the M2 tidal constituent near the Jiangsu Coast (Figure 2.2b) is given in Table 2.2. Generally, the results are in reason-

Table 2.2: Comparison of the harmonic constant of the M2 tidal constituent near the Jiangsu Coast.

Station	Observed		Calculated		$g_c - g_o$ (°)	a_c/a_o (-)
	a_o (m)	g_o (°)	a_c (m)	g_c (°)		
Lianyungang	1.70	310.16	1.45	309.56	-0.60	0.85
Yanwei	1.53	320.16	1.32	324.36	4.20	0.86
Sheyang estuary	0.90	58.16	0.92	53.67	-4.51	1.02
Yangkou	2.54	137.16	2.28	142.73	6.57	0.90
Lvsi	1.75	124.00	1.38	129.50	5.50	0.79
Lianxing	1.31	108.16	1.06	101.78	-6.38	0.81

Note: a_o and g_o represent the observed amplitude and phase, respectively; a_c and g_c represent the calculated amplitude and phase, respectively; $g_c - g_o$ is the phase-lag difference and a_c/a_o is the amplitude ratio.

able agreement with the observations. However, the relatively large deviation in several points (i.e. Lvsi port) illustrates that the grid may still be too coarse to accurately simulate the hydrodynamic conditions when the regional bathymetry is complex on smaller scales. To simulate the tide near the Jiangsu Coast with more accuracy, local model with re-fined grid is necessary.

VERIFICATION OF THE TIDAL CURRENT

IN this study, tidal currents have been verified at 22 observation stations, including 18 stations in the middle of the sea and 4 stations near the Jiangsu Coast (Figure 2.1). As to the area near the Jiangsu Coast, due to the shallow water depth and complicated bathymetry, long-term measurements are rare. Hence, short-term field measurements (Zhang, 2012) are used to validate the model. The field survey was conducted on 24 August 2006 and 31 August 2006, with an interval of one hour. With respect to the off-shore regions, three methods are applied to evaluate the agreement of long-term simulation. First, as Chen (2008) suggested, we validate computed tidal current at several tidal current observation stations in the middle of the sea (red crosses in Figure 2.1) by the prescribed time-series values in the Tidal Tables (National marine data and information service, 2005). Second, we validate some other observation stations (M5, MS, CM7, B, D, I, M4, ADCPa, and ADCPc, see Figure 2.1) with tidal current harmonic constants. The data are based on quasi-long-term tidal current measurements (Larsen et al., 1985; Guo and Yanagi, 1998; Teague et al., 1998). In addition, field measurements carried out by the Ocean University of China at station NY (see Figure 2.1) are selected to validate the continuous time-series results of our model (for more details on the measurements refer to Song et al., 2013 and Zhu, 2009).

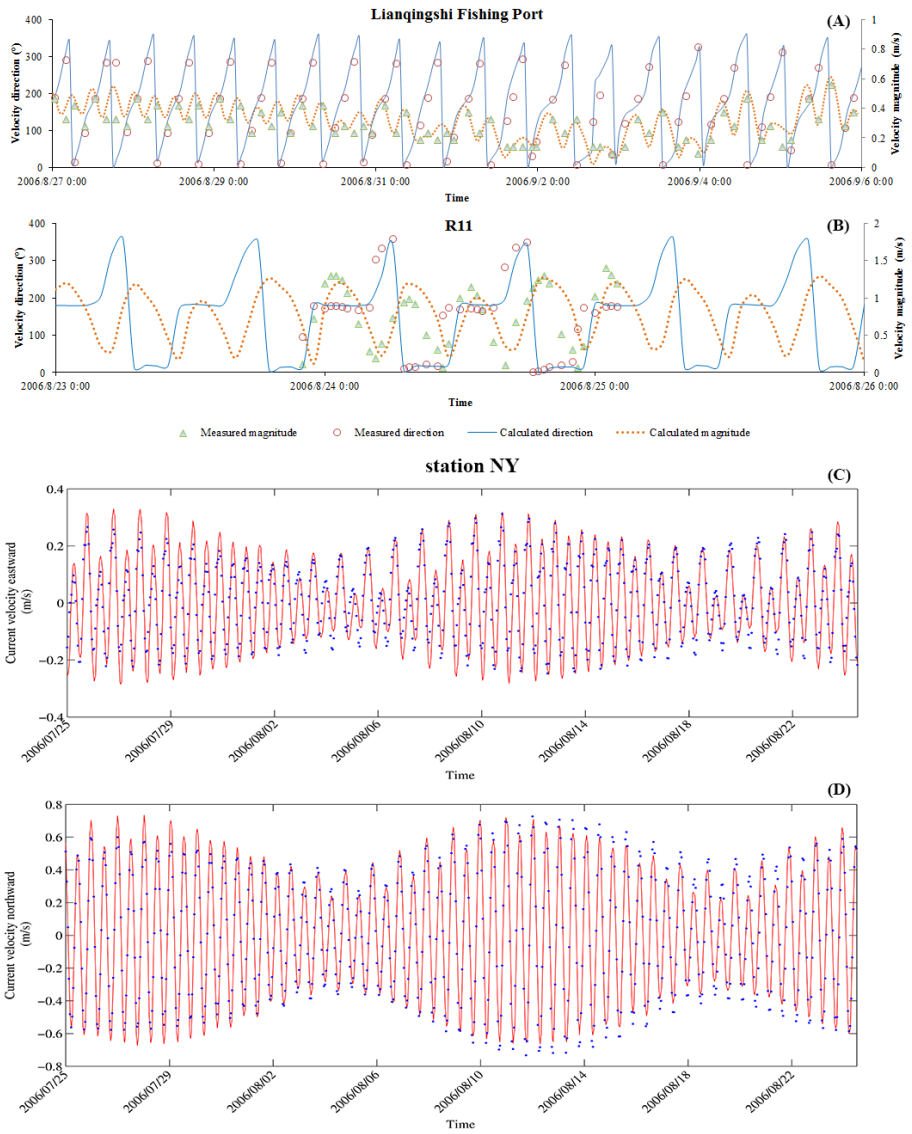


Figure 2.4: Validation of the tidal currents velocity.

Table 2.3: Comparisons between the simulated and observed M2 and S2 constituents of the tidal currents.

Station	Longi tude (°)	Latit ude (°)	M2				S2			
			U		V		U		V	
			H_c/H_o (-)	ΔG (°)						
M5	124.50	32.00	1.23	5.16	1.09	8.84	1.50	13.13	1.24	10.96
MS	124.80	30.52	1.10	14.26	0.96	18.53	1.67	8.36	1.65	0.23
CM7	125.45	28.65	1.09	1.96	0.98	3.77	0.88	2.73	1.00	5.55
B	124.08	36.95	1.07	0.85	0.93	0.99	1.00	2.14	0.88	3.94
D	124.58	36.00	1.21	16.13	1.03	20.79	0.99	17.97	1.02	18.72
I	124.69	34.30	0.89	2.07	1.01	10.39	0.85	4.24	1.07	9.72
M4	122.82	31.25	0.72	6.98	0.99	0.62	0.86	8.32	0.97	13.40
ADCPa	125.25	33.27	1.00	2.13	0.93	-2.07	1.10	13.53	1.00	8.96
ADCPc	124.03	35.97	1.23	10.23	0.99	-13.3	1.20	2.51	1.14	-1.59

Note: H_o and G_o represent the observed magnitude and phase of tidal current, respectively; H_c and G_c represent the calculated magnitude and phase of the tidal current, respectively; $\Delta G = G_c - G_o$ is the phase-lag difference and H_c/H_o is the magnitude ratio.

Model validation against time series data is shown in Figure 2.4. Figure 2.4a shows good agreement between the simulations and the predicted values from the Tidal Tables in the Lianqingshi Fishing Port (33.50° N, 123.51° E). For stations near the Jiangsu Coast (short-term validation), the simulated result (Figure 2.4b) at R11 station (33.69° N, 120.99° E) is a little different from the measured values, which is difficult to simulate in detail because the local complex bathymetry cannot be well represented by a large-scale model. Figure 2.4c and 2.4d show the comparisons between the time-series observation data at station NY (38.00° N, 123.50° E) with the model simulations in two directions. The results reveal that our model can capture the main feature of the tidal current reasonably in both directions. As to the harmonic constants of tidal current, comparisons are listed in Table 2.3 (taken the M2 and S2 constituents as examples). At most stations, the ratio of the velocity magnitude is almost 1, indicating a high degree of satisfaction. The relatively large deviation of phase at some stations (e.g. station D, MS and ADCPc) may be due to the large water depth, where tide induced current is only a part of the local current. In general, our model results are still reasonable. The present model can be used to simulate the tidal wave and tidal current in this large area.

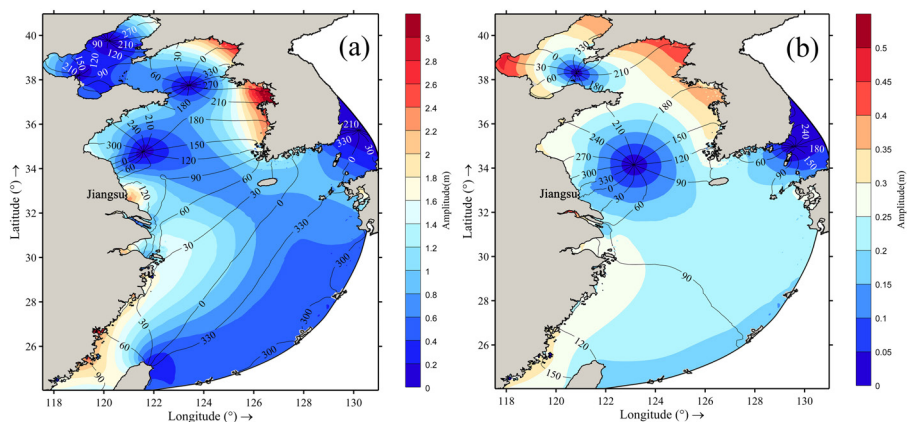


Figure 2.5: Simulated co-tidal chart of the M2 (a) and K1 (b) tidal constituents. Black lines denote co-phase lines referring to the UTC. The same notations are used in the following figures.

2.3. RESULTS AND INFLUENCE FACTOR ANALYSES

2.3.1. CO-TIDAL CHARTS AND TIDAL CURRENT FIELD

TIDAL wave motions are usually presented in the form of co-tidal charts. The simulated co-tidal charts of eight primary tidal constituents by the model are in good agreement with the co-tidal charts in the Marine Atlas of the Bohai Sea, Yellow Sea and East China Sea (Atlas of the Oceans Editorial Board, 1993) and those in the references (e.g. Fang, 1986; Kang et al., 1998). Figure 2.5 shows the co-tidal charts of the M2 and K1 tidal constituents simulated by the model. Additionally, the simulated position of the amphidromic point of the M2 tide in the southern Yellow Sea (34.80° N, 121.55° E) is very close to the location (34.60° N, 121.68° E) suggested by previous numerical results (Chen et al., 2013; Xing et al., 2012).

Figure 2.6a shows the simulated tidal ellipses of the M2 tidal constituent with a rotational direction. It is clear that a RTC field exists at the central Jiangsu Coast, and Jiang-gang is the focal point of the converging and diverging currents. Note that a clockwise flow pattern occurs in the radial sand ridge field, whereas a counterclockwise flow pattern appears in the north of the Jiangsu Coast. As tide-induced residual currents always play an important role in the marine processes, especially in the shallow coastal regions (Lie, 1999; Lee et al., 2011; Sanay et al., 2007), the Eulerian tidal-induced residual current of the M2 tide is also computed and shown in Figure 2.6b. It can be found that the direction of the residual current forms a clockwise circulation pattern over the sand ridges. The direction of the residual currents is mainly toward the ridges (landward) in several tidal channels, which indicates the accretion of the radial sand ridges.

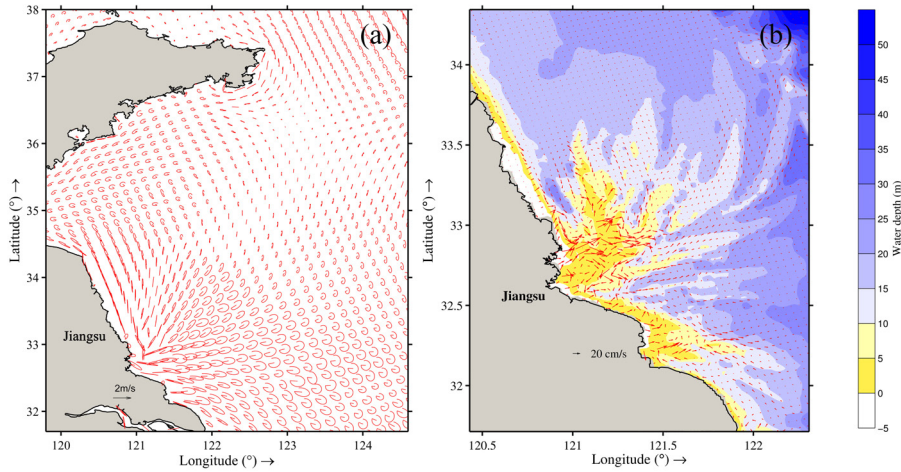


Figure 2.6: Simulated tidal ellipses (a) and Eulerian residual current (b) of the M2 tide constituent near the Jiangsu Coast.

2.3.2. ANALYSES OF INFLUENCING FACTORS FOR TIDAL MOTIONS

THE original model (case OM) considering TGF and river discharges is run as a reference model. Then, two experiments (case TGF and case RIV), in which these two factors are removed from the reference run respectively, are carried out to analyze the effect on tidal motions. Additionally, to address the near-field effect of the large-scale tidal flat reclamation, another case (case REC) considering the reclamation of the Jiangsu Coast is also simulated. The results of the M2 tidal constituent of each experiment are compared with the reference run to elaborate the influence of the various factors.

TIDE GENERATING FORCES AND RIVER DISCHARGES

THE effect of TGF on the tidal amplitude in the Yellow Sea and the East China Sea has been discussed and estimated to be several percent (An, 1977; Kang et al., 1991). Therefore, TGF was ignored in previous studies (e.g. Bao et al., 2001; Lee et al., 1999). Whereas, the importance of considering TGF for an accurate simulation in the BYECS, where the bottom topography changes from 2000 m (the Ryukyu Islands) to 18 m (the Bohai Sea), is addressed by several other studies, such as Yu et al. (2006) and Song et al. (2013).

Details on how TGF is considered in the model have been described in the previous section and more information can be found in Schwiderski (1980) and Deltares (2012). In case TGF, TGF is ignored and the results are compared with case OM to examine the

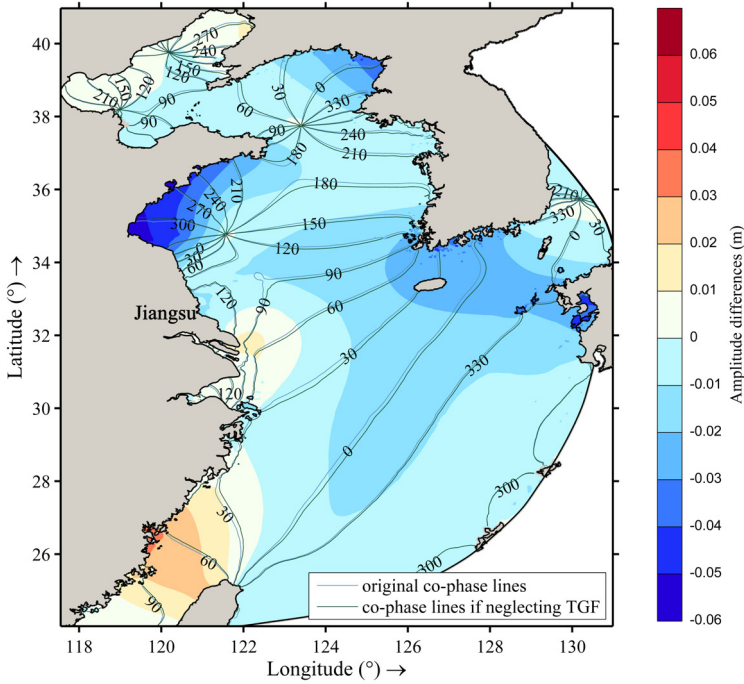


Figure 2.7: Computed phase and amplitude difference of the M2 constituent if ignoring TGF: blue lines and green lines represent the co-phase lines of case OM and case TGF, respectively; amplitude difference is obtained by subtracting the results of case TGF with the results of case OM. The same notations are used in the following figures.

effect of TGF on tidal motions. Figure 2.7 shows the calculated differences of phase and amplitude of the M2 tide. The difference of the co-phase lines is limited, while the position of the amphidromic points, especially the one in the Korea Strait near the East Sea (Japan Sea), shows an obvious change. The change of amplitude is also limited, but a relatively significant difference can be found in several of the areas, such as the Haizhou Bay. Thus, the influence of TGF varies from region to region. Whether TGF is required for accurate model simulation depends on the geographical region of interest and study purpose, and our results can provide suggestions for this decision.

There is little research considering the influence of river discharge on the large-scale tidal motions. By comparing case OM and case RIV (river discharges are ignored in case RIV), the regions most affected by river discharges and their consequences are investigated. The influence is restricted around the river estuaries. The enlarged computed differences of the M2 tide near the Yangtze Estuary are shown in Figure 2.8. The most noticeable phase and amplitude difference can be found in the channel, the estuary,

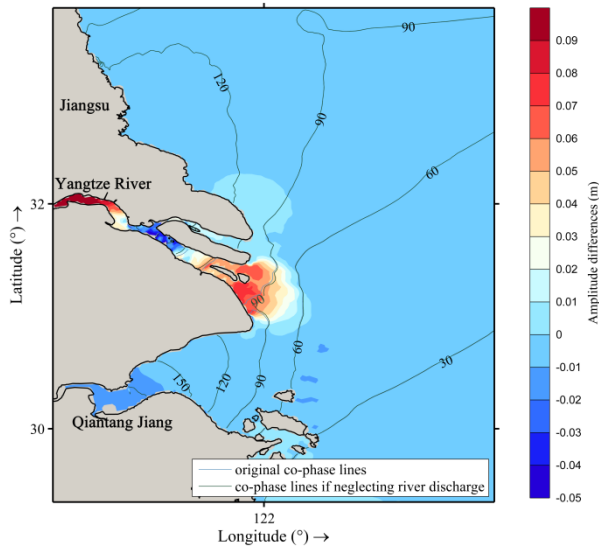


Figure 2.8: Computed phase and amplitude difference of the M2 constituent if ignore river discharges.

and the nearby coasts. The results demonstrate that the interaction between the tide and river discharge in these regions is significant. Thus, it is reasonable to omit the river discharges in the tidal wave model, except if the areas of interest are river estuaries and nearby coasts, where the effect of river can be significant.

LARGE-SCALE RECLAMATION

THE Jiangsu Coast has a high potential for land reclamation (Zhang et al., 2011) and the large reclamation projects are in progress at present (Wang et al., 2012). Another case, case REC, in which a new coastline is adopted to represent the condition after the reclamation of the radial sand ridges (Figure 2.9), is compared with case OM to investigate the near-field effect of reclamation on the tidal regime. The open boundaries are located sufficiently far away from the reclamation region, to inhibit the disturbance of open boundaries as Kang et al. (2013) suggested.

The comparison of the M2 tidal constituent between case REC and case OM is shown in Figure 2.9, focused on the Jiangsu Coast. The difference of the co-phase lines shows that both the incident tidal wave from the East China Sea (i.e. 60° co-phase line) and the rotating tidal wave in the northern part propagate faster around the reclamation region. In addition, the amphidromic point in the southern Yellow Sea moves slightly toward the northwest after reclamation. With respect to the amplitude difference, significant increases, approximately 10 - 20 cm, can be found in the south part of the Jiangsu Coast.

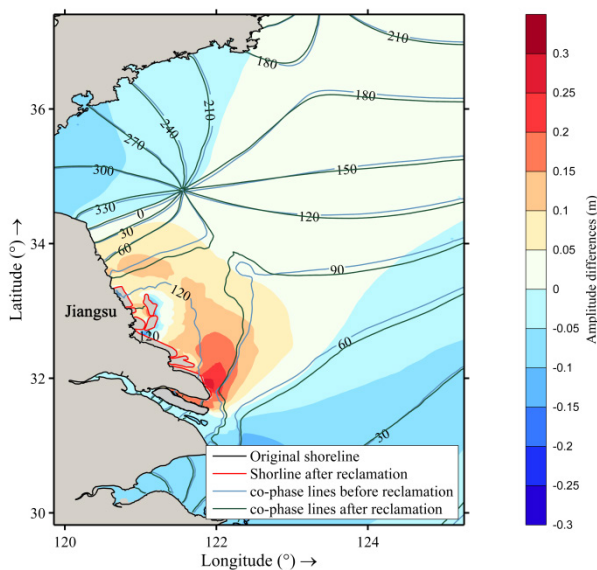


Figure 2.9: Computed phase and amplitude difference of the M2 constituent after reclamation near the Jiangsu Coast. Black and red lines indicate the present coastline and the coastline after reclamation, respectively.

Such changes may be due to the reduced tidal prism after reclamation. Moreover, the reflection from the new shoreline, which significantly and abruptly moves seaward after reclamation, is one of the possible reasons.

2.4. DISCUSSION ON THE FACTORS OF INFLUENCE ON THE TIDAL WAVE AND TIDAL CURRENT PATTERN

2.4.1. REGIONAL BATHYMETRY

THE bathymetry of the radial sand ridges is complex, with about 10 major ridges and 4 main tidal channels. Most of the sand ridges are periodically submerged and exposed during the tidal cycles. Zhu and Chang (2001a) studied the relationship between the local bathymetry (radial sand ridges) and the RTC based on a numerical model with relatively coarse grids. The local bathymetry was replaced by a shelving slope and a flat bottom (16 m). The results suggested that RTC is independent of the submarine topography. Opposite results are obtained by Ye (2012) based on a schematized model, also with a shelving slope and a flat bottom. The RTC disappeared if the topography was set to be a horizontal flat bed with a uniform depth of 30 m. Note that both the coarse grid and schematization may alter the accuracy of the tidal current and the tidal ellipse. Hence, it

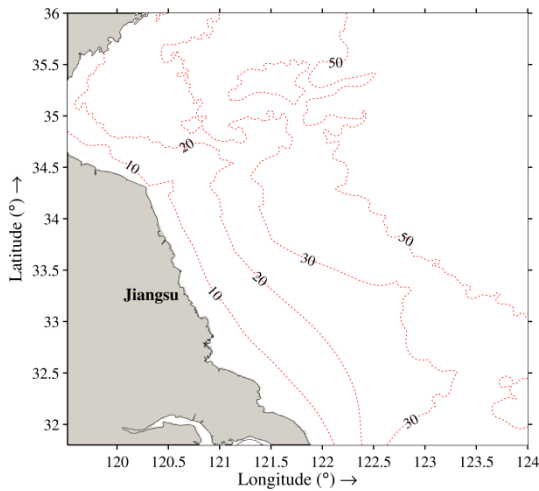


Figure 2.10: Scope and details of the new linearizing regional bathymetry.

is necessary to conduct a comprehensive analysis based on the present fine-grid model, using a series of alternative local bathymetries.

The new bathymetries, including a linear bathymetry and two uniform depths, cover the Jiangsu Coast and the eastern part of the Yellow Sea, leaving the bathymetry of the outside region unchanged. Linearizing regional bathymetry (case LI) means that the bathymetry near the Jiangsu Coast is replaced by a linearly interpolated one, according to the nearby depth (Figure 2.10). The scope of uniform depth is the same as the linearizing regional bathymetry. The water depth in the radial sand ridges generally ranges from 0 to 25 m. And, in certain parts of the tidal channels maximum depths can reach up to 50 m. (Wang et al., 2012). In order to ensure similar tidal prism and to ignore the influence of sudden changed bathymetry on the water current pattern, two uniform water depths are used in the experiments: 15 m and 30 m (case U15 and case U30).

The tidal ellipses of the M2 tidal constituent of these experiments are shown in Figure 2.11. It can be observed that RTC exists in all experiments. The results are in agreement with the research of Zhu and Chang (2001b). The unique topography of the radial sand ridges does not directly influence the special local flow pattern. However, a remarkable difference should be noted is the magnitude of the current velocity of these experiments. RTC becomes weaker with the increase of the water depth (Figure 2.11). One of the requirements for the formation of sand ridges is that the tidal current velocity should be between 0.5 – 2.5 m/s (Off, 1963). Therefore, if the previous bathymetry (before the existence of the radial sand ridges) is not suitable to generate the favorable current velocity, it is still unclear whether the radial sand ridges can be formed by currents only

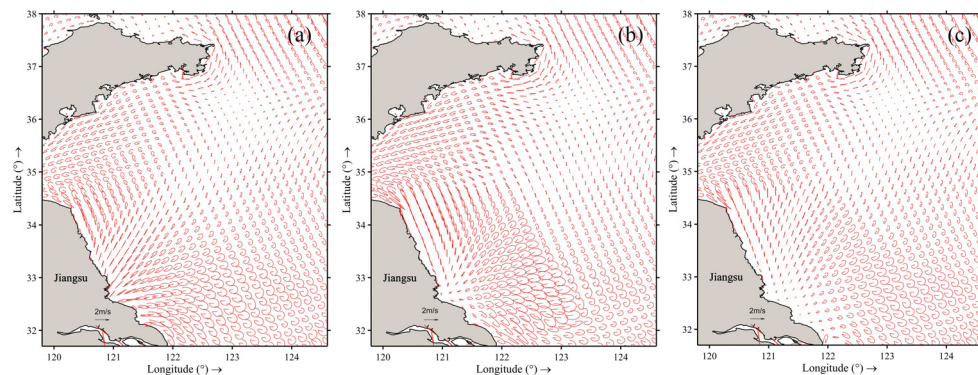


Figure 2.11: Tidal ellipses of the M2 tidal constituent for case LI (a), case U15(b) and case U30(c).

as suggested by Zhu and Chang (2001b). In this point of view, although the special local pattern is independent from the bathymetry, a certain critical water depth is still crucial for RTC to generate the special topography of the radial sand ridges. It is debatable when and how the radial sand ridges are generated. Further studies are necessary to focus on the interactions between the morphology changes and the hydrodynamics near the Jiangsu Coast.

With respect to the effect of the regional bathymetry on the tidal wave system, we take the experiment with the linear bathymetry (case LI) as an example (Figure 2.12). We notice that the amphidromic point in the southern Yellow Sea has an obvious movement toward the west. This movement may be due to the decrease of the bottom friction after linearization. Linear bathymetry causes less tidal energy dissipation than in case OM, which may lead to a faster incident tidal wave propagation speed, and finally the movement of the amphidromic point. In addition, it shows that the amplitude in the radial sand ridges reduces as much as 0.4 m, whereas the amplitude has a maximum growth of 0.6 m in the south of the Jiangsu Coast. It is because the meeting position of the rotating tidal wave and the incoming tidal wave (90° co-phase lines) has moved southward in case LI. And, this change causes the decrease of the amplitude in Jianggang (focal point in case OM) and an increase in the southern area. It also demonstrates that the special bathymetry in the radial sand ridges is the main reason for the large tidal range around Jianggang, where the mean tidal range is approximately 4 - 6 m (Wang et al., 2012).

2.4.2. THE ROLE OF THE GEOMETRIC POSITION OF SHANDONG PENINSULA

PREVIOUS studies suggest that the SDP is important for the formation of the rotating tidal wave system and then the radial tidal current field in the southern Yellow Sea

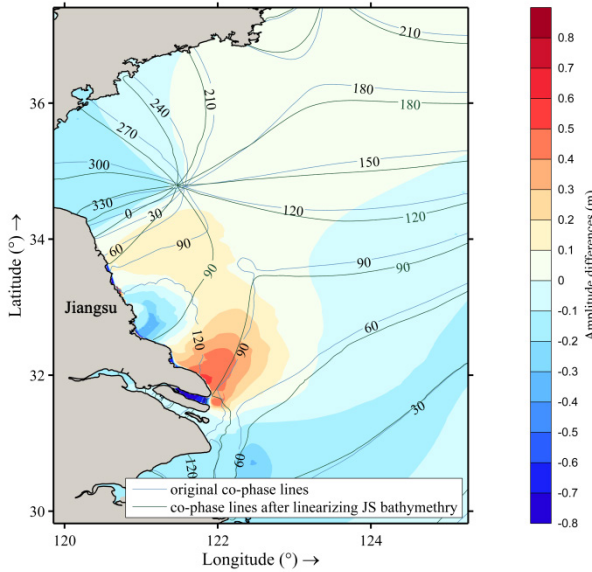


Figure 2.12: Computed phase and amplitude difference of the M2 constituent if linearized regional bathymetry.

(e.g. Choi, 1980; Zhang et al., 1996; Wang et al., 1998; Zhang et al., 1998; Wang et al., 2012; Kang et al., 1998; Kang et al., 2013). However, there has not yet a discussion or verification been made on this point of view. To further explore the influence of SDP on the tidal wave and tidal current system in the southern Yellow Sea, an experiment by removing SDP (case SDP) from the reference run is designed. The topography in the absence of SDP is generated by a linearized interpolation according to the depth of the nearby regions (Figure 2.13). The difference of the co-phase lines between case SDP and case OM is shown in Figure 2.14. The small difference concerning the 330° and 30° co-phase lines, located in the East China Sea and near the Taiwan Strait, respectively, demonstrates that the effect of removing SDP on the open boundary condition is minor. The disturbance (removing SDP) is located far away from the open boundaries.

INFLUENCE ON THE ROTATING TIDAL WAVE SYSTEM

COMPARISON between the simulation results of case SDP and case OM (Figure 2.14) shows that the amphidromic points in the Yellow sea of both M2 and K1 tide constituents have all moved southwest. The relative distances between the amphidromic points and the northwest boundary are basically not changed (d_1 and d_2 in Figure 2.14).

The domain of the whole Yellow Sea in case SDP can be roughly considered as a semi-enclosed rectangular basin (see blue dashed line in Figure 2.14). The relative position of

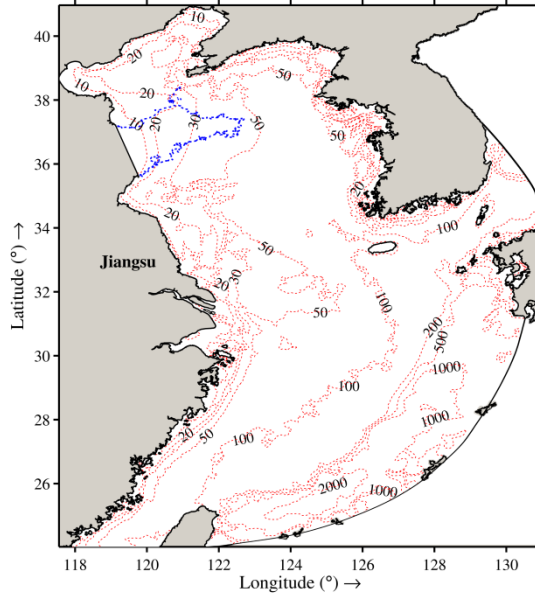


Figure 2.13: The domain and bathymetry of case SDP.

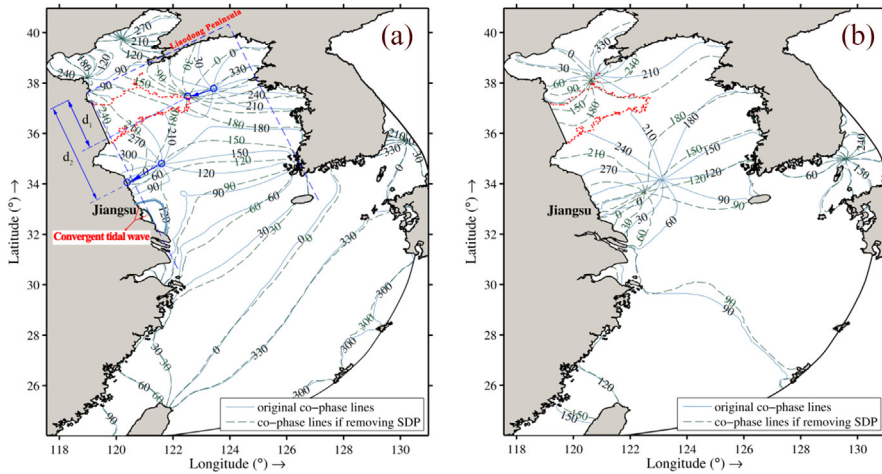


Figure 2.14: The comparison of co-phase lines between case OM and case SDP: the M2 tide (a) and K1 tide (b).

the two amphidromic points in Yellow Sea (case SDP) of the M2 tide simulated in our model is consistent with the result of an analytical model (e.g. Rizal, 2002). According to the relevant analytical model, the generation of the south amphidromic point was mainly due to the interaction between the northern rotating tidal wave system and the progressive tidal wave. Inspired by the results of analytical model, we hypothesize that the tidal wave system in the whole Yellow Sea is equivalent to the tidal wave propagation in a semi-enclosed basin. Therefore, the formation of the south amphidromic point (in the southern Yellow Sea) is mainly due to the interaction of the north amphidromic point and the incoming tidal wave. The SDP only plays a role to enhance the southern rotating tidal wave system by generating locally reflected tidal waves, which leads the amphidromic point to shift eastward (Figure 2.14).

Since the aforementioned hypothesis is proposed according to the present experimental study, and it has not been pointed out in previous studies, when discussing the rotating tidal wave in the southern Yellow Sea, additional experiment is necessary to validate it. Therefore, another experiment (case DAM) is carried out by adding a dam, starting from the head of the SDP towards the southeast (Figure 2.15). By comparing the co-phase lines of case DAM and case OM, the effect of adding a dam on the open boundaries is negligible (Figure 2.15). In the northern Yellow Sea, the tidal wave system is little changed, whereas the differences in the left side of the dam are remarkable (Figure 2.15). The tidal wave propagates slower compared with case OM, an almost 30° delay, which may be due to the delayed propagation of the tidal wave from the northern Yellow Sea, caused by the dam. Furthermore, the existence of the tidal wave from the northern Yellow Sea and its effect can also be observed from the northward movement of the amphidromic point in the southern Yellow Sea in case DAM. This northward movement is because of the imbalance between the reflected tidal wave by SDP and the incoming tidal wave from the northern Yellow Sea. Therefore, with respect to the rotating tidal wave system in the southern Yellow Sea, unlike the previous studies which suggested that it is only caused by the geographic position of SDP (i.e. reflected wave), we demonstrate that the interaction between the tidal wave systems in the southern Yellow Sea and the northern Yellow Sea indeed play a significant role.

INFLUENCE ON THE TIDAL CURRENT PATTERN

WITH respect to the special tidal current pattern (i.e. RTC), many previous studies suggested that SDP was essential for the formation of RTC and the evolution of the radial sand ridges. According to this point of view, if SDP had disappeared, the particular converge and diverge currents would neither exist nor generate the radial sand ridges (Zhu, 1998; Zhu and Chang, 2001a; Huang and Wang, 1987). However, our study shows

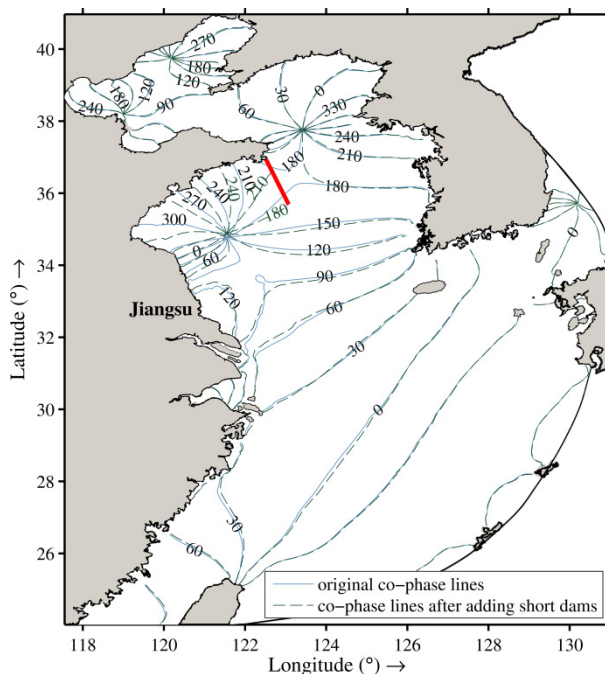


Figure 2.15: The comparison of co-phase lines between case OM and case DAM.

that the local tidal current field still has a radial shape (Figure 2.16). The focal point of the current field is Jianggang without any significant differences. It implies that RTC is not only independent from local bathymetry and the coastal line shape, which have been demonstrated by Zhu and Chang (2001a, 2001b), but also has little relation with the SDP.

By re-analyzing the results of case SDP and case OM, it is found that a convergent tidal wave exists identified by the 120° co-phase lines (see thick lines in Figure 2.14) in the area of the RTC. The 120° co-phase line in case SDP covers relatively smaller area than that in case OM. The rotation tidal wave system in the southern Yellow Sea exists in both case OM and case SDP. Hence, the convergent tidal wave is hypothesized to be formed by the meeting of the rotating tidal wave in the southern Yellow Sea and the incoming tidal wave from the East China Sea, in line with the second opinion mentioned in the introduction part. Since the tidal current is one of the components of the tidal wave system, we hypothesize that the convergent tidal wave may be the key factor for generating the radial shape of the current field. And the intensity of the current velocity is controlled by the local bathymetry, according to the previous experimental results (i.e. caseU15, caseU30 and case LI). Thus, many relevant processes and mechanisms, e.g. how the two tidal wave systems meet to generate a convergent tidal wave, how the

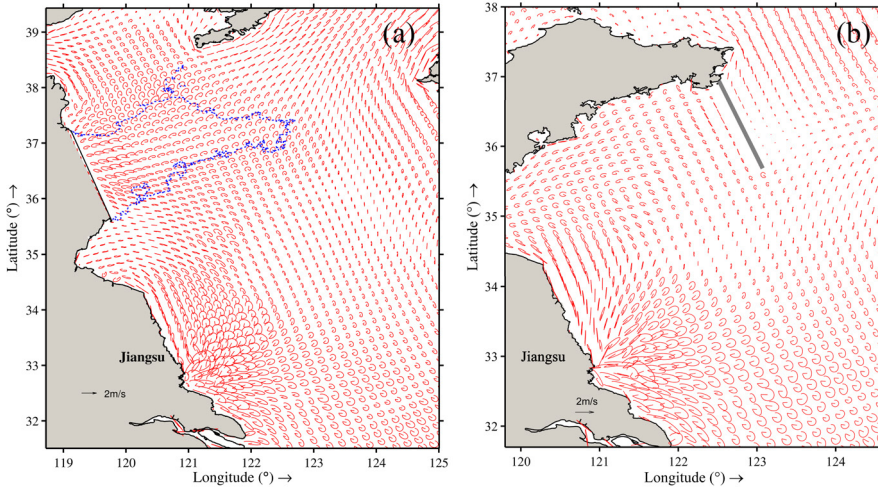


Figure 2.16: The tidal ellipses of the M2 tidal constituent of case SDP (a) and case DAM (b).

convergent tidal wave and the shape of the current field response if these two tidal waves change, etc., should gain more insights into to comprehensively interpret the formation mechanism of the RTC.

2.5. CONCLUSION

IN this study, a two-dimensional tidal model is developed with a relatively high resolution to study the tidal wave propagation in the BYECS. According to the verification of the simulated water levels and the tidal currents, this model shows a good capability to reproduce the tidal wave system in the BYECS.

The co-tidal charts computed by the present model are in good agreement with the published Marine Atlas and the previous models. Radial tidal current (RTC) pattern near the Jiangsu Coast is also well simulated by the present model. This study provides several suggestions on whether tide generating force (TGF) and river discharges are necessary for accurate simulation, because the requirement changes according to different regions of interest and study purposes. As the model is two-dimensional, the influence of the river on vertical flow structures cannot be considered. Besides, the large-scale reclamation at the central Jiangsu Coast is also investigated, and it shows that the tidal amplitudes at the southern Jiangsu Coast increase significantly after the large reclamation.

To further explore the previously proposed important factors of influence (i.e. local bathymetry and the role of SDP) on the formation mechanism of the tidal wave propaga-

tion and RTC in the Yellow Sea, a series of experiments are designed and conducted. The changes considered in these experiments can also affect the open boundaries. However, as the distance between the disturbance generation and the open boundaries is sufficiently far, the influence of these changes at the open boundaries is shown to be limited and it is ignored in our study. According to the experimental results, the formation of the rotating tidal wave system in the southern Yellow Sea is found to be formed mainly by the interaction between the north rotating tidal wave system in the northern Yellow Sea and the incoming tidal wave. The SDP only plays a role on enhancing the southern rotating tidal wave system, thus changing the position of the amphidromic point eastward. As to the tidal current in the central Jiangsu Coast, we hypothesize that the convergent tidal wave, formed by the meeting of the rotating tidal wave in the southern Yellow Sea and the incident tidal wave from the East China Sea, is crucial for its radial shape, and the local bathymetry influences the intensity of the current velocity. More detailed studies are necessary to verify these views.

Future works should be done to gain insight into the relationship between the morphological changes of the radial sand ridges and the surrounding hydrodynamics based on a local model. In addition, the present model is two-dimensional and mainly focuses on tidal current, so the effect of the river is only checked with depth-averaged discharge. Other effects, such as buoyancy, are beyond the scope of the present study, but it is worth to further pursue in the future through 3D models.

3

LABORATORY STUDY ON THE FINE SEDIMENT TRANSPORT



This Chapter is based on part of a journal paper published in *Coastal Engineering*:

Yao, P., Su, M., Wang Z.B., van Rijn, L., Zhang, C.K., Chen, Y.P., Stive, M.J.F. (2015) Experiment inspired numerical modelling of sediment concentration over sand-silt mixtures, *Coastal Engineering*, 105, 75-89, doi: 10.1016/j.coastaleng.2015.07.008.

Abstract: A series of flume experiments has been conducted to investigate sediment transport of sand-silt mixtures in both wave-only and wave-with-current conditions. Two types of sediments collected from a typical silty tidal flat were used: a silt-sized mixture with median grain size of 46 μm , and a very fine sand-sized mixture with median grain size of 88 μm . A High Concentration Layer (HCL) was observed near the bottom together with ripples under wave-only conditions. The different phenomena of wave ripples between these two bed materials are mainly due to high silt content of the silt-sized mixture (~60%), which would probably results in the hard (high-strength) sublayer. For the concentration profiles, we find that the vertical profile of the silt concentration appears different from the profile of the sand concentration, since the silt concentration decreases logarithmically within HCL, while homogeneously distributes outside the HCL. Besides, the near bed vertical sorting of sediment is significant, especially for a graded sediment (e.g. silt-sand mixed bed).

Highlights:

- We carried out a series of flume experiments on two types of silt-sand mixtures.
- Quasi-stationary high concentration layer was observed near bed under waves.
- The content of silt fraction of silt-sand mixtures can affect the shape of bed forms.
- The vertical suspended sediment concentration profile of silt fraction is different from that of sand fraction.
- The near bed vertical sorting of sediment is significant, especially for a graded sediment.

3.1. INTRODUCTION

DEPOSITES on tidal flats are generally a mixture of clay, silt and sand. As the bed composition affects the bed forms, sediment transport, morphological changes etc., it is necessary to understand the dynamic behavior of such mixtures in tidal flats. Historically, many studies have been conducted to describe the processes of sediment transport for pure non-cohesive sediments (e.g. Nielsen, 1992, van Rijn, 1993, Soulsby, 1997), and cohesive sediments (see Winterwerp and van Kesteren, 2004 for an overview). However, these existing theories are difficult to be applied to describe the behavior of the mixed sediment in the tidal flat area directly. Several experiments have demonstrated that the critical bed shear stress can increase dramatically with the increase of the clay component in the mixture (Mitchener and Torfs, 1996 and Jacobs et al., 2011). In addition to the clay content, van Ledden et al. (2004) and Bartzke et al. (2013) have suggested that the network structure (i.e., packing density) also plays a role on erosion behavior of mixed sediment. Therefore, in order to simultaneously predict the non-cohesive and the cohesive sediments transport in the mixture, the interaction between sand and mud should be considered.

Although van Ledden et al. (2004) argued that silt-dominated mud is rarely found in natural systems, yet such mixtures are found to be abundant in the tidal flats of China (Wang et al., 2002). For example, along the central Jiangsu coast (eastern China), a large area of silt dominated tidal flats exists sheltered behind the radial sand ridge field (Wang and Ke, 1997, Shi et al., 2012 and Zhang, 2012). The development of the silt-dominated tidal flats along the Jiangsu coast is attributed to the abundant sediment supply from two silt-enriched rivers: the Yangtze River which discharges in the south of this region, and the (Old-) Yellow river, which discharged into the north of this region in the period from 1128 to 1855 (Gao, 2009; for locations of the two rivers, see Chapter 1 and Chapter 5).

The mineral compositions of silt consist mainly of quartz and feldspar, which are basically non-cohesive (Lambe and Whitman, 1979). However, the erosion tests suggest that the silt-enriched mixtures exhibit cohesive-like behavior (Robert et al., 1998), but flocculation has not been observed based on the settling experiments on silt (Slaa et al., 2013, 2015). Thus, the silt (grain size larger than 8 μm and less than 64 μm) may hold the dual-features of both non-cohesive and cohesive sediments. We refer to these features of silt as pseudo-cohesive to differentiate from the non-cohesive and cohesive materials in this study.

The dynamics of the silt-dominated sediment have not yet been well understood. A few studies suggested that the sediment transport processes of the silt-dominated mix-

tures are different from both sand and cohesive mud (Cao et al., 2003, Cao et al., 2005 and Slaa et al., 2013). The sediment in the silt-enriched area is very sensitive to the hydrodynamic conditions. For example, during stormy weather, sediment concentrations near the bottom increase dramatically, forming a High silt-enriched Concentration Layer (HCL), which has been reproduced by several flume experiments (Zhao, 2003, Lamb and Parsons, 2005). When the weather becomes more moderate, the high density suspensions deposit rapidly, leading to massive sedimentation in tidal flats or tidal creeks. A typical example is the severe siltation happened in the Huanghua Harbor, China, after a gale (with a maximum wind speed of 31.9 m/s) on October 10 - 12, 2003 (Yang and Hou, 2004, Kuang et al., 2015). Van Maren (2007), Van Maren et al. (2009) and Slaa et al. (2013) identified that the sedimentation processes play a role in the morphodynamics of the Yellow River because of high silt contents. When the high density suspension deposits, the pore pressure dissipates faster for a silty bed than that for a clayey bed causing the bed in a rapid packing or in a consolidation-like behavior. Li and Cao (2009) compared the deposits of two tidal flats, and found that the wet bulk density of the deposit of a silty tidal flat (Rudong in the Jiangsu coast) is around 1.8 g/l after 24 h, while the wet bulk density of the deposit of a muddy tidal flat (near Tianjin) is only around 1.6 g/l even after a half year. Therefore, sediment of the silt-dominated mixtures yields different transport mechanisms compared with sand and cohesive mud.

In order to extend the knowledge of sediment transport in the silt range, a series of flume experiments was carried out. Two types of sediments, with different sand–silt–clay ratios, were collected from the silty tidal flats of the Jiangsu Coast, China. The present experimental study focuses mainly on the suspended sediment transport under various hydrodynamic (i.e. wave and current) conditions. Through the experimental study, we attempt to gain deeper insights into the sediment transport processes (i.e. the bed forms; the vertical distribution of the suspended sediment concentration) of the silt–sand mixtures on tidal flats.

3.2. FLUME EXPERIMENT

THE experiment was conducted in the wind–wave–current flume in Hohai University, Nanjing, China. The dimension of the flume is 80 m length, 1 m width and 1.5 m depth (Figure 3.1). A wave generator is set at one end of the flume for generating regular waves. Three wave height probes are installed on the wave paddle for the detection of the secondary reflected wave, which can automatically be absorbed by adjusting the placement of the paddle. A gravel beach slope is positioned at the other end of the

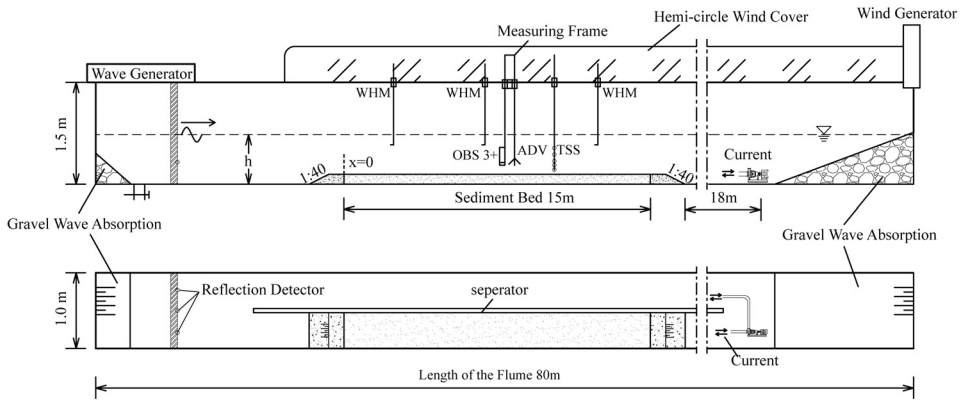


Figure 3.1: Front view (upper panel) and plan view (lower panel) of the flume with the different measurement devices. WHM=Wave Height Meter; OBS=optical backscatter sensor; ADV= Acoustic Doppler Velocimeter; TSS=transverse suction system. The arrow shown in the upper panel indicates the direction of wave propagation.

flume to minimize the reflection of the wave. These functionalities can guarantee the long time wave generation to be stationary during the experiments. In the case of regular wave conditions, preliminary tests showed that the shape of the wave had the same form as the Stokes second-order waves. A glass separator is installed along the central axis of the flume and current generators are positioned at the end of the separator (see plan view in Figure 3.1). By means of the current generators and the separator, stable, bidirectional and adjustable current can be generated inside the flume. The sediment consumption can be reduced by adding the separator as the sediments are cycled inside the flume and can be easily collected after the end of the experiment.

A flat sediment bed, with a length of 15 m and a thickness of 0.15 m, was placed at one side of the glass separator (Figure 3.1). The bed sediments for the experiment were collected from the silty tidal flats near Jianggang, located in the center of the Jiangsu coast (Figure 3.2a). The distribution and characteristics of the silt tidal flats/silt-enriched systems will not be introduced in this study, as they are reported in several previous studies (more details in Liu et al., 2011, Slaa et al., 2013, Wang and Ke, 1997, Wang et al., 2002, Wang et al., 2012, etc.). Fieldwork for sediment sampling was carried out in the period of September and November, 2013. The sediment samples were collected from the upper zone (referred to as Sediment S1) and the middle zone (referred to as Sediment S2) of the tidal flat, respectively. The sediments deposited at the surface layer of the tidal flats with a thickness of approximate 10 cm were sampled. These sediment samples were processed and used as the bed materials for the experiment. Before each group of experiments, the sediment bed was re-prepared to make sure that the bed composition

was the same. The grain size distributions of the two bed samples (i.e. sediments S1 and S2) were measured by a Malvern Mastersize 3000 laser particle size analyzer at the beginning and at the end of the experiments. Figure 3.2b shows the averaged sediment composition at the beginning of the experiments. The sediment S1 is a silt-enriched mixture with a median grain size of 46 μm , while the sediment S2 is a very fine sand-enriched mixture with a median size of 88 μm . At the front and at the end of the sediment bed, two concrete ramps were placed to support the sediment bed. Each ramp consisted of a 50 cm long horizontal section with the same elevation as the sediment bed, and a 1:40 side slope as the transition from the flume bottom to the horizontal section and the sediment bed. Next, the flume was slowly filled with water until the desired water depth was reached.

Water level elevation was measured by Wave Height Meters at 3 locations in the sediment section. The current velocity was measured by an Acoustic Doppler Velocimeter (ADV), which was fixed on a mobile beam of a measuring frame (Figure 3.3). During the steady state, the instantaneous current velocity was recorded at 7 elevations. Another beam of the measuring frame was attached with three Optical Backscatter Sensors (OBS 3+), with an interval of 3.5 cm, to vertically monitor the suspended sediment concentration (SSC) (Figure 3.3). There were 33 measuring points in total, and three points (i.e. 1 cm, 4.5 cm and 8 cm) were measured twice to check the repeatability (Table 3.1). The lowest vertical position of OBS was set at approximately 1 cm above the flat bed. Preliminary tests have shown that OBS sensors have no disturbing effect on the local bed forms.

The sediment concentration was self-generated from the sediment section when waves/currents were imposed. Sediment concentration measurements were conducted when the (quasi-) steady state of the sediment concentration (the sediment concentration is basically unchanged) was achieved, which can be easily figured out through the stability of OBS signals (Maa et al., 1992). Figure 3.4 shows an example of the OBS outputs in a preliminary test of sediment S1 at three different elevations under wave-only conditions. Time-series OBS outputs suggest that the sensors at lower elevations need more time (e.g., ~80 min for the lowest measuring point) to achieve the stable signals. The extended time may due to the complicated sediment exchange processes near the water-bed interface. Therefore, the steady state herein is defined based on the lowest measuring point.

A transverse suction system was fixed at a horizontal distance of 0.8 m from the OBS frame (Figure 3.3). The interval between the OBS and the suction system was determined by preliminary tests. As the sediment concentration was measured during the

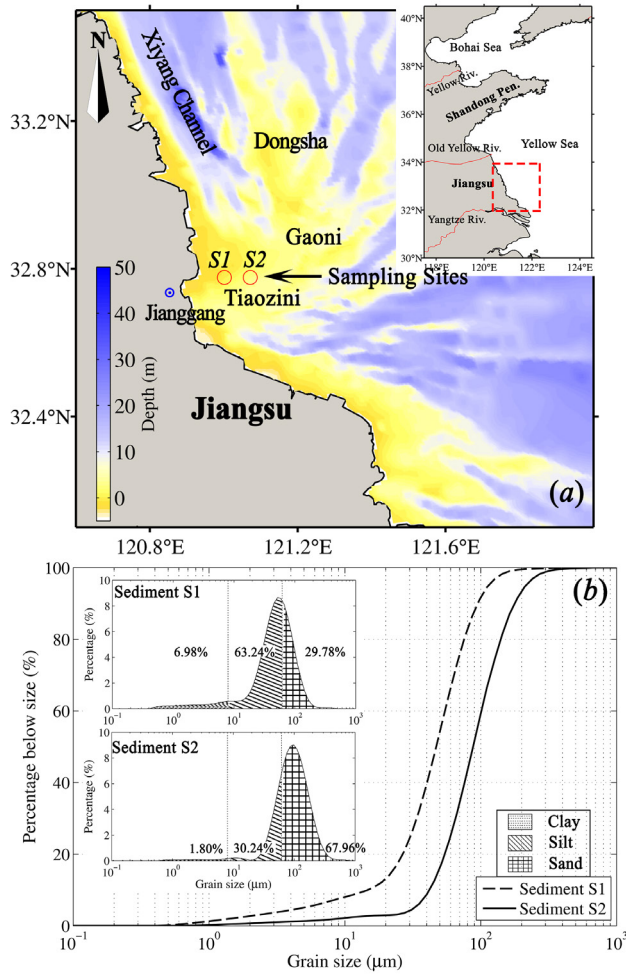


Figure 3.2: (a) Locations of the sampling sites; (b) Grain size distribution of two bed materials measured at the beginning of each experiment, averaged over all experimental groups. The upper left figure inside (b) represents the sediment composition by means of clay, silt and sand fractions. Herein, the clay fraction is defined as the particles with a diameter smaller than 8 μm; the silt fraction is defined as the particles with a diameter between 8 μm and 62 μm; the sand fraction is defined as the particles with a diameter larger than 62 μm. Different fractions are filled with different hatches.

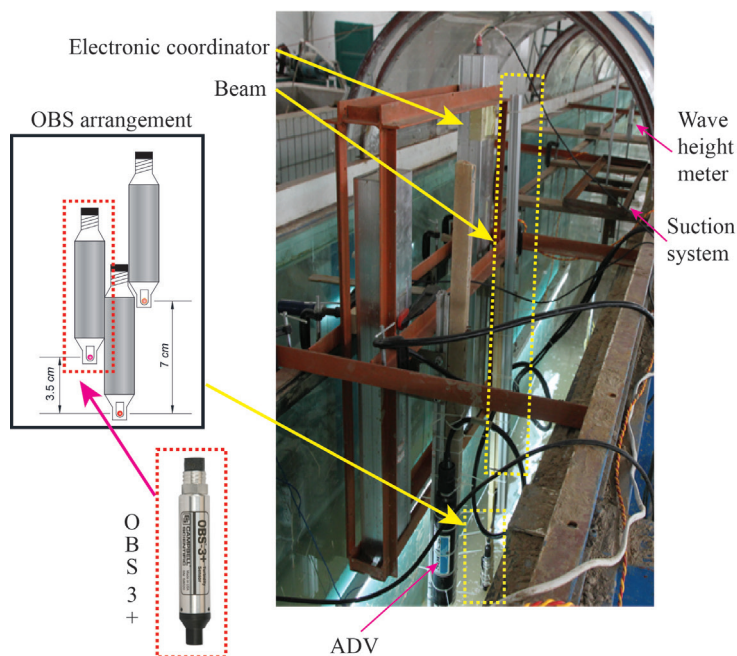


Figure 3.3: Schematic and photograph of the experiment design.

Table 3.1: Heights of three OBS sensors above the bed in the flume experiments.

Sensor	Measuring heights above the sediment bed (cm)									
1#	1.0	1.4	1.8	2.2	2.6	3	3.5	4	11	21
2#	4.5	4.9	5.3	5.7	6.1	6.5	7.0	7.5	14.5	24.5
3#	8.0	8.4	8.8	9.2	9.6	10	10.5	11	18	28

steady state, the concentration at the same elevation along the sediment bed should be on the same level. For wave-only conditions, the concentration profiles and sediment compositions were similar along the sediment bed, due to the slight advection effect. With respect to the wave-current conditions, preliminary test showed that the deviations of sediment concentration and sediment composition within 80 cm (between the positions of the OBS and suction system) were limited. For instance, in the case of experiment with the largest current velocity, i.e. s2-o3611 (details of the corresponding hydrodynamic conditions see Table 3.2), the discrepancies at the highest measured height of the suction system for sediment concentration and median grain size were less than 8% and 0.7%, respectively. Thus, the measurements of these methods are comparable and the setting of 80 cm is reasonable.

Through the suction system, the water-sediment samples were taken at six eleva-

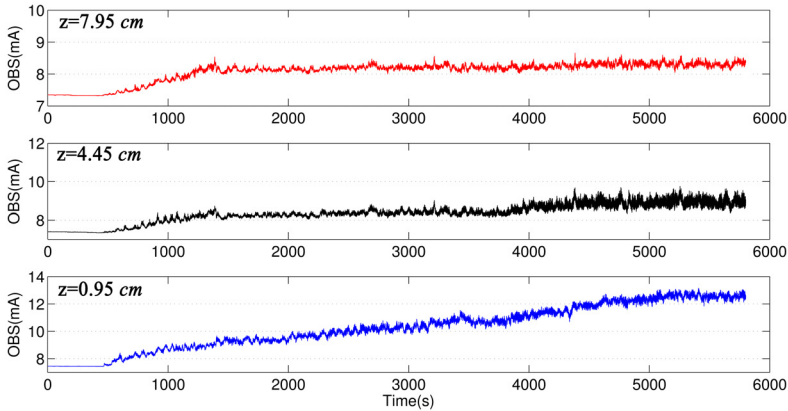


Figure 3.4: Time-series OBS outputs of a preliminary test for sediment S1 under wave-only conditions at three elevations. The wave height is 0.12 m with a constant period of 1.5 s. The water depth is 0.3 m. Note that Y-Axis scales are different at different elevations.

tions (from 1 cm to 11 cm above the bed, approximately). The duration of sampling was about 220 s, yielding the time-averaged sediment concentrations. The suction system consisted of an array of 6 horizontal intake nozzles with an inner diameter of 3 mm. The lowest intake tube was located at 1 cm above the original bed, and a scale bar measured its vertical position. During the experiments, the relative height of the suction system was corrected according to the local bed form. The vertical position is defined with respect to the mean bed level (after averaging over the ripples). The intake velocity for the water–sediment samples was about 50 cm/s, which exceeds the ambient current velocity to make sure the sampling efficiency. The sucked concentration is, therefore, considered as the ‘true’ concentration during the steady state (van Rijn et al. 2000). Samples were taken twice for each experiment with a time interval of 10 min and were put into 6 glass cylinders and 6 pycnometers, respectively (Figure 3.5). Time-averaged sediment concentration can be calculated quickly through the pre-calibrated pycnometers, while samples in the glass cylinders had to be filtered, dried and weighted to get the concentration. Furthermore, the filtered and dried sediment samples were dispersed and analyzed by a Malvern Mastersizer 3000 laser particle size analyzer, to obtain grain size distribution at the corresponding elevations. In the period between these two independent measurements, the wave ripple migrations at the measuring location were also measured. Thus, the average value of the two measurements is, approximately, taken as the ripple-averaged and time-averaged concentration. Furthermore, each experiment was repeated three times to ensure reproducible results.

The experiment started with fresh water and no initial concentration. Under wave-

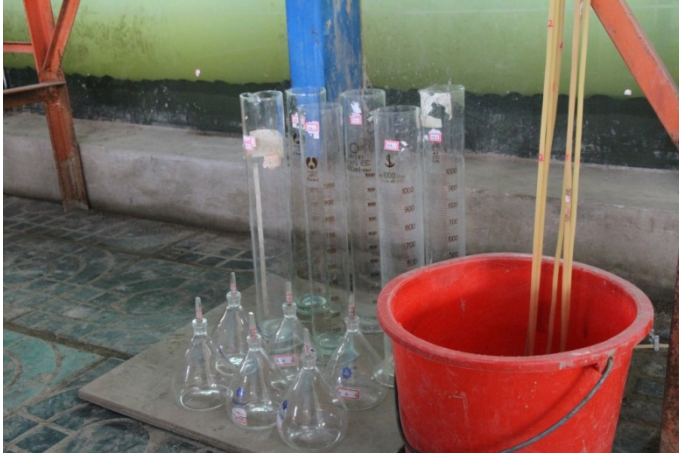


Figure 3.5: Containers of the collected water–sediment samples: six glass cylinders and six pycnometers.

only conditions, the horizontal sediment fluxes are rather small, so the sediment concentration profile measured during the steady state is considered as the fully developed equilibrium profile. However, when the current is introduced in the experiment, the equilibrium concentration needs a sufficient sediment source and a certain distance to be established. The length of sediment section in the present experiment (i.e. 15 m) is too short to develop the equilibrium concentration.

Experimental conditions for sediments S1 and S2 are listed in Table 3.2 and Table 3.3, respectively. The water depth (h) is approximately 0.3 m in all experiments. Only regular waves are implemented with wave heights (H) of 8–13 cm and wave periods (T) of 1.5 s. For wave-with-current conditions, various currents are combined with selected wave conditions. The depth-averaged current velocity (u_m) ranges from 25 to 40 cm/s in two directions. Experiment numbers in Table 3.2 and Table 3.3 are based on the measured hydrodynamic conditions. For example, s1-f3212 represents the experiment with sediment S1 under a wave height of 12 cm and a following current velocity of about 32 cm/s (letter ‘f’ represents following the wave direction; letter ‘o’ represents opposing the wave direction).

3.3. EXPERIMENT RESULTS AND DISCUSSIONS

3.3.1. BED FORMS

UNDER wave-only conditions, wave ripples can be observed in each experiment of sediments S1 and S2. When the current is superposed with waves, the shape of

Table 3.2: Basic measurements and derived data for sediment S1.

Experiment No.	h (m)	H (m)	T (s)	u_m (m/s)	η (cm)	λ (cm)	C_{ave} (g/l)
s1-0009	0.30	0.088	1.5	0.00	0.88	5.09	11.66
s1-0011	0.30	0.106	1.5	0.00	0.77	4.95	20.47
s1-0012	0.30	0.121	1.5	0.00	0.59	4.77	39.43
s1-0013	0.30	0.133	1.5	0.00	0.66	4.82	49.03
s1-f3212	0.30	0.115	1.5	0.30	-	-	-
s1-f3812	0.30	0.113	1.5	0.38	-	-	-
s1-o3112	0.30	0.116	1.5	-0.31	-	-	-
s1-o3812	0.30	0.120	1.5	-0.38	-	-	-

Note: All the parameters inside Table 3.2 and Table 3.3 are defined in the text, except C_{ave} is the HCL-averaged concentration by mass

Table 3.3: Basic measurements and derived data for sediment S2.

Experiment No.	h (m)	H (m)	T (s)	u_m (m/s)	η (cm)	λ (cm)	C_{ave} (g/l)
s2-0009	0.30	0.091	1.5	0.00	0.83	5.48	8.14
s2-0011	0.30	0.106	1.5	0.00	0.82	5.62	10.44
s2-0013	0.30	0.128	1.5	0.00	0.80	5.43	21.19
s2-f2911	0.30	0.106	1.5	0.29	1.13	6.30	-
s2-f3811	0.30	0.093	1.5	0.38	1.63	11.30	-
s2-o3011	0.30	0.123	1.5	-0.30	0.87	6.15	-
s2-o3611	0.30	0.121	1.5	-0.36	1.10	6.62	-
s2-o3911	0.30	0.110	1.5	-0.39	1.34	8.66	-

ripples varies with different sediment beds. After each group of the experiments, the recognizable ripple dimension (i.e. ripple height and length) was measured at various locations along the sediment bed and the measurements at the different locations were averaged to obtain the mean ripple height (η) and length (λ) (see Table 3.2 and Table 3.3). Figure 3.6 illustrates the bed forms under different hydrodynamic conditions during the steady state. Figure 3.6a and 3.6c show regular wave ripples corresponding to wave-only conditions. In contrast, the ripples are irregular and hard to recognize (difficult to measure) in wave-with-current conditions for sediment S1 (see Figure 3.6b). For some groups of the experiment, even a nearly flat bed was observed. Figure 3.6d presents a typical wave ripple of sediment S2 in wave-with-current conditions. The wave-current ripples are not only present but are also longer and higher compared to the wave-only conditions (Table 3.3).

After each experiment, bed materials were sampled along the sediment bed and were analyzed to obtain the sediment compositions. Table 3.4 lists the bed compositions (by means of clay, silt and sand fractions) measured at the end of the experiments. Compared with the original bed (see Figure 3.2b), the sediment composition and the median

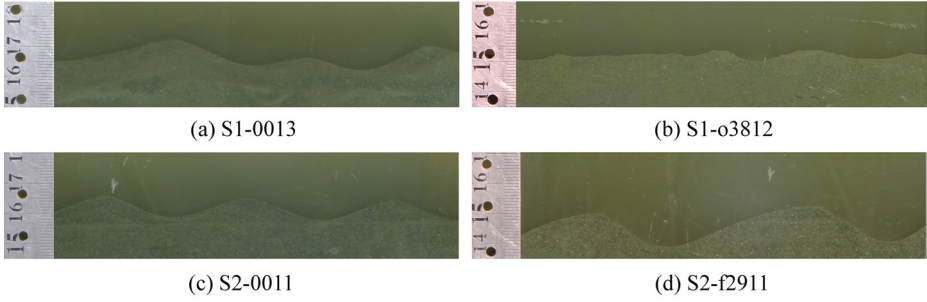


Figure 3.6: Photography of ripples under wave-only and wave-with-current conditions (selected experiments). The scale bar in the left of each figure has a minimum scale of mm and the number is in a scale of cm.

Table 3.4: Sediment composition of bed materials after the experiments (selected experiment groups).

Experiment number	Clay (%)	Silt (%)	Sand (%)	D50 (μm)
s1-0012	7.37	60.54	32.10	47.22
s1-o3112	5.19	59.47	35.35	50.34
s2-0011	1.05	24.30	74.65	88.21
s2-f3311	0.28	20.12	79.60	104.65

Note: After the experiments, several sediment samples were taken along the sediment bed. The results listed in the table are the averaged values over these samples.

grain size of the bed mixtures after the experiments changed less under wave-only conditions, whereas the finer fractions (i.e. clay and silt fractions) were reduced leading to an increased median grain size (coarser bed) when the currents were loaded. On the one hand, the finer grains of the bed are easier to be eroded and transported by currents than coarser ones; On the other hand, compared with natural circumstances, the sediment source in the flume experiment is limited to continuously supply the sufficient fine materials and to maintain the overall bed composition.

During the experiments with sediment S1 (i.e. silt-enriched mixtures), we found that the layer (sublayer) under the surface of the sediment bed (i.e. wave ripples) developed into a hard (high-strength) layer. During the experiments, the instantaneous properties (e.g. pore pressure, porosity, bulk density, etc.) of the sediment bed were not measured. Nevertheless, following previous studies, which focused on the response of the silty bed under waves (Foda and Tzang, 1994; Liu et al., 2013; Mutlu Sumer et al., 2006; Tzang, 1998; etc.), and considering the observed phenomena during our experiments, we suggest a hypothesized description to explain the whole processes of the silt-enriched bed morphology development. At the beginning of the experiment, the oscillatory wave motion helps to build up the excess pore pressure in the sediment bed. Over time, the excess

pore pressure reaches a maximum value resulting in the beginning of the bed liquefaction. The bed liquefaction initiates the sediment-water interface progressively expanding downward. Meanwhile, the pore water escapes from the bed, starting at the bottom of the sediment bed progressively moving upward. Thus, the two processes shape the bed into a two-layer system: the sublayer (bottom layer) in a densely packed state, and the surface layer in a liquefied state. Finally, the surface layer develops as a high concentration layer, and the sublayer is turned into a hard (high-strength) layer with a rippled surface. When the currents are superimposed to the waves, not only the high concentration layer, but also the topmost of the sublayer (i.e. ripples) are eroded and transported by the currents. The remaining part of the sublayer is left behind; the erosion of this hardened layer requires a higher critical erosion velocity. The experiments of Roberts et al. (1998) illustrate that the sediment with a median grain size smaller than 40 μm is no longer eroded as a single particle, but as chunks of sediments. Therefore, the shapes of bed forms are more irregular for sediment S1 under wave and current conditions. Besides, the processes also explain why the buildup of the equilibrium sediment concentration near the bottom layer requires more time (see Figure 3.4)

The development of a very fine sand-dominated bed (i.e. sediment S2), does not follow the same process as the sediment S1. With the onset of the currents, the growth of the ripples is similar to the sandy bed, documented in previous studies (e.g. Van Rijn, 1993). The different phenomena between these two bed materials imply that the high silt content of sediment S1 (~60%) is probably the reason causing the hard (high-strength) sublayer.

3.3.2. HIGH CONCENTRATION LAYER UNDER WAVES

DURING rough weather with waves, a near bottom layer with large sediment concentration can be formed over a silty tidal flat area (Li and Cao, 2009). In most experiments of sediment S1 and S2 under wave-only conditions, this distinguishable High Concentration Layer (HCL) was also observed (Figure 3.7). However, the HCL is not recognizable under the wave-current conditions. This is due to the presence of a current, which increases the vertical mixing process, and the sediment supply limited by the length of the sediment section.

During the measuring period, the concentration of the HCL appears to be stable according to the relatively stable OBS outputs. The value of ranges from 11 g/l to 50 g/l for the sediment S1 and ranges from 6 g/l to 22 g/l for the sediment S2 under waves (see Table 3.2 and Table 3.3). The results show that the concentration suspended from a fine

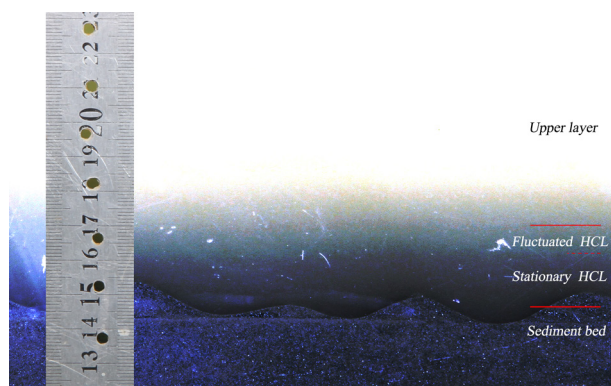


Figure 3.7: Photograph by long-time exposure of experiment s2-0010. The darker color represents a higher concentration. The upper layer is diluted to highlight the HCL, but it still has small concentrations.

sediment bed (i.e. sediment S1) is larger than that from a coarse bed (i.e. sediment S2).

Figure 3.8 shows the sediment composition at the lowest measuring point (approximately 1 cm above the bed) compared with the sediment composition of the bed material. The suspension inside the HCL is mainly composed by non-cohesive/coarser sediment, because cohesive fraction (i.e. clay fraction)/finer sediment can be washed out and suspended more easily. Furthermore, the suspension inside the HCL is totally different from the fluid mud observed in the cohesive muddy tidal flat area (Winterwerp and Van Kesteren, 2004).

It seems more realistic that the grain size is finer in suspension than in bed materials (e.g. Figure 3.8 for S2). However, for the sediment S1, the content of mud (i.e., silt and clay) is slightly smaller than that of bed material, while the sand content is larger. The increased coarse grains in the HCL of S1 can be explained by the vertical sorting process of sand and mud. The mud fraction tends to suspend into the entire water column, while the sand fraction is only active in the near bottom layer due to the larger settling velocity. This process increases the relative content of sand, resulting in coarse grains near bottom. A more extreme example for silt-dominated bed sediment can be found in the study of Lamb and Parsons (2005). In their experiments, the sand content of the original bed materials is only 20%, while it is increased to almost 80% in the near bed zone when HCL is formed.

3.3.3. VERTICAL PROFILE OF SUSPENDED SEDIMENT CONCENTRATION

THE measured sediment concentration is divided into a clay, a silt and a sand concentration, respectively, according to the percentage of each fraction measured by

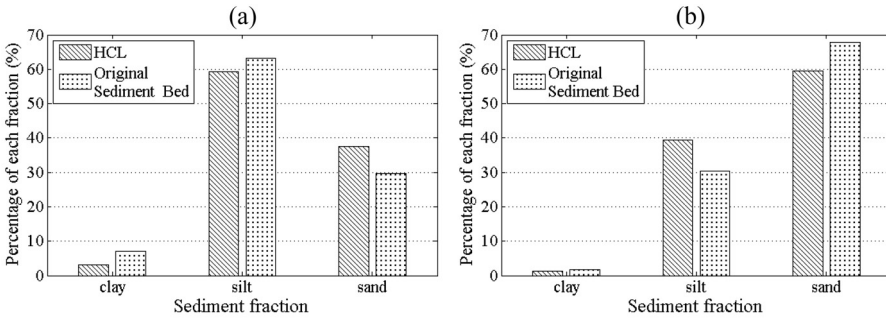


Figure 3.8: Comparison of sediment compositions between the lowest measuring point and the original bed materials for sediment S1 (a) and S2 (b) under wave-only conditions. The corresponding experiments are: s1-0011 and s2-0011.

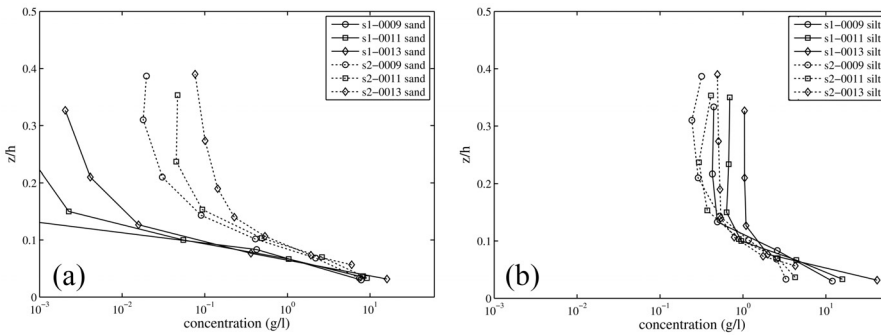


Figure 3.9: Vertical profiles of sand concentration (a) and silt concentration (b) under waves.

particle size analyzer. Herein, only the silt and sand concentration is discussed, as the percentage and concentration of clay in both sediments S1 and S2 are much smaller compared with the sand and silt fractions.

Figure 3.9 shows the results under wave-only conditions for sediments S1 and S2 respectively (selected experimental groups). In general, the total concentration of sediment S1 is larger than the concentration of sediment S2 under the same wave condition, implying that a finer sediment corresponds to a larger concentration. It is noted that the sand concentration in the upper layer of sediments S1 and S2 is small and does not contribute much to the total concentration. Therefore, in the upper layer, the total concentration is largely determined by the silt concentrations.

For the sand concentration, the increased wave height leads to higher concentrations in the upper layer of the depth. Furthermore, the increase of the available sand content (from ~30% in S1 to ~70% in S2) can enhance the increase of sand concentrations in the upper layer. In addition, the larger turbulence damping, caused by the higher silt

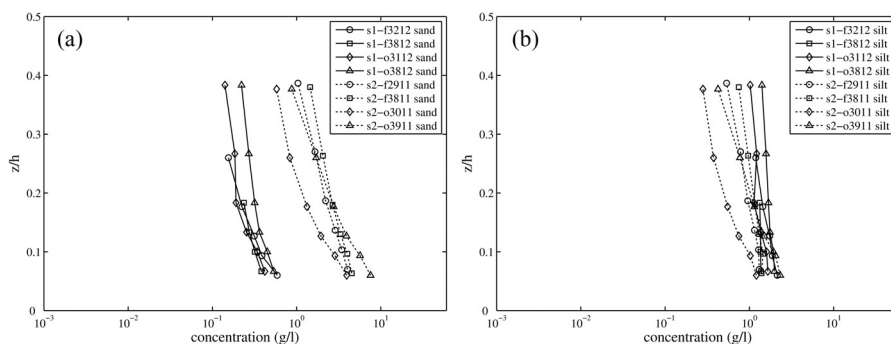


Figure 3.10: Vertical profiles of sand concentration (a) and silt concentration (b) under wave-with-current conditions.

concentration near bottom for sediment S1, may also restrict the increase of the sand concentration in the upper layer. Note that the increase of the concentrations in the upper layer is larger than in the near bed zone with the increase of wave height. The sand concentration decreases with a large gradient from bottom to upper layer over the entire water depth.

For the silt fraction, the concentration also increases with increased wave height. A relatively large gradient of the concentration profile is found only within the elevation of 0.1 times of the total water depth (i.e. the length scale of the HCL); in the upper layer the concentration is nearly constant. The silt concentration near the bottom of sediment S1 is much larger than sediment S2 under the same wave condition. This is due to the silt content of sediment S1, which is much higher than the silt content of sediment S2.

Figure 3.10 shows the influence of current velocity on the concentration profile of sand and silt fractions. A large current velocity can increase the concentration in the upper layer, whereas the concentration in the near bottom zone is somewhat smaller than under wave-only conditions. The stronger vertical mixing effect caused by the current restricts the development of a HCL. The direction of the current does not have a significant influence on the concentration profiles.

Another phenomenon to be noted is that the total concentration of S1 is smaller than that of S2, which seems different from the wave-only conditions. Furthermore, the silt concentration profile of sediment S1 is almost uniform over the water depth. It may be due to a dense packing state of the sublayer of sediment bed, which is caused by high silt contents. After the surface layer is washed out by currents, the sublayer is hardly erodible unless larger bed shear stresses are imposed. The sediment supply is thus limited by the hardened sublayer resulting in a vertically homogenous concentration profile.

Therefore, the total concentration of sediment S1 is relatively small. The effect of a hard (high-strength) sublayer on the concentrations is complicated and beyond the scope of the present study.

3.3.4. VERTICAL PROFILE OF SEDIMENT GRAIN SIZE

FIGURE 3.11 shows the measured vertical distribution of sediment grain size for six groups of experiments (i.e., s1-0012, s1-f3212, s1-o3812, s2-0011, s2-f2911, and s2-o3611). The median grain size of the corresponding original bed materials (i.e., S1 and S2, respectively) are indicated by the vertical lines in the figure. Vertical sorting of sediment in the near bed layer is obvious. The grain size of the suspended sediment, even located close to the bed (i.e. 1–3 cm), is different from that of the bed material for all groups of experiments. It confirms the statement of Sisternans et al. (2001) that the near bed vertical sorting of sediment was significant. This phenomenon of sediment S2 is more significant, in comparison with sediment S1.

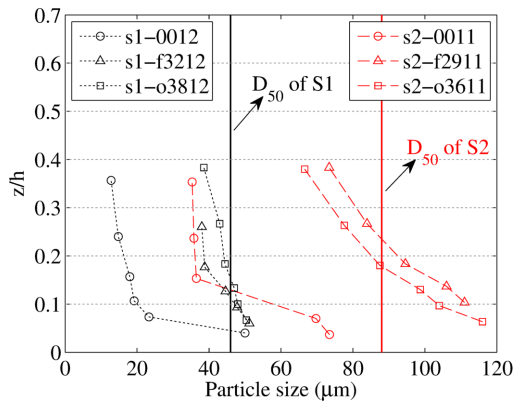


Figure 3.11: Measured vertical profiles of median sediment sizes for experiments s1-0012, s1-f3212, s1-o3812, s2-0011, s2-f2911 and s2-o3611, in comparison with the median grain size of the original bed sediment samples (S1 and S2, respectively).

According to the results of experiments, the grain size at the highest suction position (approximately 0.35h above the sediment bed) is greatly different than that at the lowest suction position (less than 0.1h above the sediment bed). On the one hand, under wave-only conditions, the grain size of suspensions has an abrupt decrease with the increase of elevation. This phenomenon is corresponding to the HCL under the wave-only conditions. The critical height for the abrupt grain size change is benefit to determine the height of the HCL. The results suggest that the thickness of HCL of sediment S2 is larger

than that of sediment S1, in accordance with the observed results (Yao et al. 2015).

On the other hand, the grain sizes near the bottom layer under wave-current conditions are coarser than the original bed material. It may be due to the strong bed shear stress under such conditions. The fine material can be transported to higher elevations and taken away by the flow, whereas the coarse material is trapped in the near bottom area. Simultaneously, bed materials become coarser than the initial bed materials. Besides, sediment supply for suspensions is always limited in flume experiments. All these factors result in coarser grain sizes at the lower elevations than the original bed material. These results indicate that the grain size of the suspension varies significantly from the bed material. Furthermore, the degree of coarsen of the suspended sediment of sediment S1 is much more slight than that of sediments S2. It may be due to “the hard (high-strength) layer”, which can prevent the further erosion of the bed material and eventually influence sediment suspension.

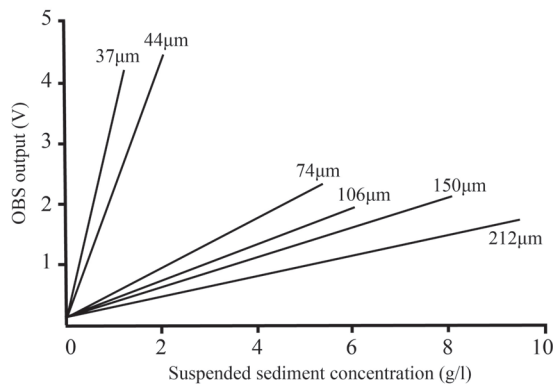
3.4. CONCLUSIONS

WE have carried out a series of laboratory experiments to investigate the sediment transport in a silt range. Two types of sand/silt mixtures collected from a silty tidal flat have been used as bed materials, under both wave-only and wave-with-current conditions, respectively. Under wave-only conditions, a recognizable HCL is produced with HCL-averaged concentrations ranging from 11 g/l to 50 g/l, and from 7 g/l to 22 g/l for sediments S1 and S2, respectively. Together with the HCL, wave ripples have been observed for both types of sediments. The different phenomena of wave ripples between these two bed materials are mainly due to high silt content of sediment S1 (~60%), which would probably results in the hard (high-strength) sublayer.

Furthermore, the sediment inside the HCL has a certain amount of sand content, which is different from the fluid mud in the cohesive muddy tidal flat area. The vertical concentration profiles of silt and sand have been presented and analyzed separately. The profile of the sand concentration is consistent with previous studies on sand, while the pattern of the silt concentration appears different. Inside the HCL, the silt concentration decreases upwards, following approximately the logarithmic form, but the concentration is homogenously distributed outside of the HCL. Under the wave-current conditions in the laboratory, due to the limited sediment supply, the bed material and the suspended sediments in the near bottom layer are both became coarser then the original bed samples. It confirms that the near bed vertical sorting of sediment is significant, especially for a graded sediment, e.g. silt-sand mixed bed.

4

CONVERSION OF ELECTRO-OPTICAL SIGNALS TO SEDIMENT CONCENTRATION IN A SILT-SAND SUSPENSION



OBS calibration results for different particle sizes (adopted from Conner and De Visser, 1992).

This Chapter is based on a journal paper submitted to *Coastal Engineering*.

Abstract: The Optical Backscatter Sensor (OBS) has been widely used to measure suspended sediment concentration in both field and laboratory conditions, even though it is very sensitive to many factors. The most significant factor suggested is the grain size. In order to enhance the quality of OBS data, an improved approach is proposed, based on the “mixture of linear component response” method (Green and Boon III, 1993) to account for the effect of grain size. In addition to an original sediment sample, which commonly serves as a single calibration material, an accompanying sediment sample is necessary to calibrate OBS sensors. A multi-fraction sediment model is used to predict the grain size distribution in suspension. Compared with existing methods, the improved approach does not require a sieving procedure nor the assumption that the sediment fractions of the calibrated sediment sample exhibit the same sensitivities as those of the suspended sediments. The applicability of our method has been verified by a series of laboratory experiments over silt-sand mixtures. The results show that this method successfully yields continuous concentration profiles, which agree well with the measurements using a suction method. The converted concentrations of the time-averaged OBS measurements by traditional method and by the improved method, respectively, are compared with the suction measurements. The results of linear regression analyses show that the coefficient of determination increases (e.g. from 0.55 to 0.92 for wave-current conditions) and the Root Mean Square Error decreases (e.g. from 0.97 to 0.39 for wave-current conditions). It demonstrates that improved method enhances the quality of OBS conversion. Furthermore, suggestions on selecting the accompanying sediment sample (i.e. on grain size and composition) are given.

Highlights:

- We propose an improved approach to convert the OBS signal to the suspended sediment concentration with higher reliability.
- This approach considers the effect of grain size on the performance of OBS.
- This approach can be applied for the mixed sediment, especially for the silt-sand mixtures.
- This approach has been successfully examined by flume experiments.

4.1. INTRODUCTION

THE Optical Backscatter Sensor (OBS) measurement technique was first introduced by Downing et al. (1981). It has been widely used to measure suspended sediment concentration (SSC) in marine and freshwater environments, with the advantages of low cost, durability and applicability for a broad concentration range (Downing, 2006; Greenwood and Jagger, 1995). It has rather successfully been used to monitor SSC when sediment concentration ranges and sediment size distributions do not change during the measurements (Downing, 2006). Compared with the traditional suction method (or pumping method), the advantages of OBS measurements are obvious. A high temporal and spatial resolution of SSC can be obtained through OBS measurements (Downing et al., 1981, Wren et al., 2000).

The response of OBS sensors can be influenced by several factors, such as sediment concentration magnitude (Kineke and Sternberg, 1992), bubbles (Smith et al., 2002), varying levels of darkness (Sutherland et al., 2000), chemical and biological fouling (Ahn et al., 1992; Schoellhamer, 1993) and particle size (Ludwig and Hanes, 1990; Conner and De Visser, 1992; Black and Rosenberg, 1994; Battisto et al., 1999; Sutherland et al., 2000). Greenwood and Jagger (1995) examined the sensitivity of optical sensors to grain size within the sand mode and found that the outputs of OBS were greatly affected, with an increase of 80% when the mean grain size decreased from 450 to 250 μm . Small particle sizes in particular have a more significant influence on the OBS response (Greenwood and Jagger, 1995; Van Rijn et al., 2000). Particle size has a dominant effect when the grain diameter is less than 100 μm (Conner and De Visser, 1992). For instance, output can change with 70% when particle size ranges from 20 μm to 50 μm (Wren et al., 2000). Thus, converting OBS output to sediment concentration should be done with caution, especially for non-homogeneous sediment environments with a silt-sand mixture.

A common calibration method in the laboratory is to prepare an appropriate number of samples of different concentrations. In-situ calibration, with periodically taken water-sediment samples in the vicinity of an OBS sensor for a range of conditions, is the most common method for field measurements. Usually, regression analysis will result in a calibration factor to convert OBS outputs to SSC. These two methods can give reasonable results when the particle size does not change much spatially and temporally. However, the accuracy of the converted concentration has been reported to be poor in many studies (e.g. Gibbs and Wolanski, 1992; Greenwood and Jagger, 1995; Battisto et al., 1999; Lunven and Gentien, 2000; Fugate and Friedrichs, 2002) due to the considerable effect of the sediment size.

The traditional method for converting OBS output to SSC by a calibration curve based

on the bed material only is not reliable for a non-homogenous suspension environment (e.g. a silt-sand mixture). Therefore, the main objective of this study is to appropriately modify the conversion method. First, existing methods for improving the reliability of the converted OBS concentration (OC) are reviewed. Next, an improved approach to convert OBS output to sediment concentration is proposed. Then, the effectiveness of our approach is examined by a series of laboratory experiments based on a silt-sand mixture. Finally, by taking reliable suction values as a reference, the improvement of the converted optical concentration is discussed.

4.2. APPROACHES FOR CONVERTING OBS MEASUREMENTS

4.2.1. EXISTING METHODS

IT is generally suggested that the sediment concentration is linearly related to the OBS net output O_{OBS}^* for low concentration ranges (Green et al., 2000, Downing, 2006), while non-linearly (e.g. quadratic) related to O_{OBS}^* for a relatively high concentration ranges (Downing, 2006, Kineke et al., 1992, Xu, 1997). Take the linear relationship as an example

$$O_{OBS}^* = S \cdot C \quad (4.1)$$

where, O_{OBS}^* is OBS net output (OBS total output - OBS electronic offset); C is the sediment concentration; S is the OBS sensitivity coefficient.

Since OBS can be significantly influenced by grain size, many previous studies focused on estimating the relationship between the sensitivity coefficient and the particle size (Baker and Lavelle, 1984; Ludwig and Hanes, 1990; Lynch et al., 1994; Campbell Scientific, 2008; Downing, 2008). To improve the OBS reliability, corrections on the sensitivity coefficient have been proposed according to the median grain size (Conner and De Visser, 1992; Downing, 2008). However, this method is highly empirical, due to controversial suggestions on the value of empirical coefficients (Conner and De Visser, 1992; Downing, 2008; Mie, 1908), which restricts its applicability. Besides, Black and Rosenberg (1994) proposed an alternative method through correcting sediment concentration directly with the consideration of grain size effect, feasible to be applied for a sandy beach. However, the errors are likely to be considerable in the marine environment, where the concentration of fine material is not locally determined and the relationship for the fine material (<63 μm) is unknown (Bunt et al., 1999).

Instead of considering the median grain size difference for correcting the OBS measurements, an alternative method is to derive the sensitivity coefficients for different

sediment fractions. It suggests that the total OBS output for mixtures composed of different fractions is the linear sum of the output for each fraction by assuming that fraction interaction (e.g. grain shielding and multiple scattering) does not significantly affect sensor response (Green and Boon III, 1993). The suggested procedures can be described as:

(1) Sieve the sediment sample to several fractions, e.g. silt, very fine sand, fine sand, coarse sand etc. Note that the limits for the distinguishing fractions are essentially arbitrary;

(2) Calibrate the OBS sensor separately for each fraction, and the relationship between OBS output and concentration can be deduced. Take a linear relationship as an example

$$O_{i,OBS}^* = S_i \cdot C_i \quad (4.2)$$

$i=1, 2, \dots, n$, with n is the number of fractions.

(3) Measure the sediment composition where OBS sensors are installed, i.e. the percentage of each fraction P_i , $i=1, 2, \dots, n$;

(4) Convert the measured OBS output into SSC:

$$C(z) = O_{OBS}^* / \sum_{i=1}^n S_i P_i \quad (4.3)$$

Green and Boon III (1993) suggested dividing the mixtures into two fractions (hereafter referred to as the two-fraction method), i.e. a silt fraction with a grain size less than $62 \mu\text{m}$, and a sand fraction with a grain size larger than $62 \mu\text{m}$ (Figure 4.1). The obtained calibration curves are named enveloping lines. Given the percentage of the silt and sand fraction (P_{silt} and P_{sand}) of a suspension, the total sensitivity S_t can be corrected by assuming a mixture of linear response:

$$S_t = S_{silt} P_{silt} + S_{sand} P_{sand} \quad (4.4)$$

The corrected sensitivity coefficient varies with the sediment composition, i.e. with the relative percentage of silt and sand fraction. Compared to the “median grain size” methods, the “mixture of linear component response” method is more reasonable and suitable for mixtures, as it considers the composition rather than only median grain size.

In reality, the sediment composition in suspensions changes spatially and temporally, so the sensitivity coefficients of the suspensions are different from those of the bed material. However, the “mixture of linear component response” method ignores the difference in fraction-composition between the calibrated and observed materials (e.g. bed

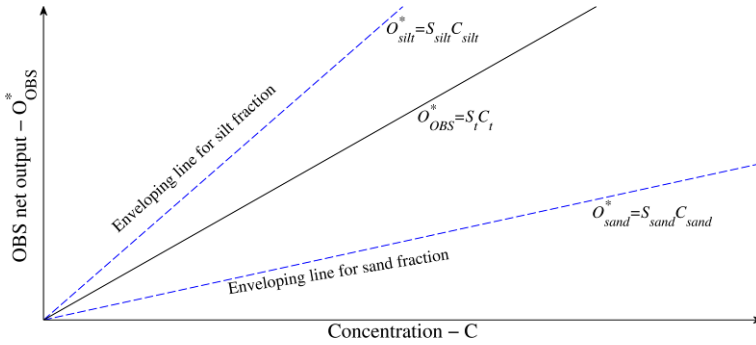


Figure 4.1: Definition of enveloping lines.

4

material and suspensions). Potential errors would be provoked when taking the calibration performance of the bed materials to convert the OBS measurements for suspensions in the whole water column.

Sediment composition, as a requirement for applying the “mixture of linear component response” method, is not possible to be measured simultaneously and continuously with the OBS sensor. Alternatively, Xu (1997) suggested estimating the sediment composition using a multi-fraction sediment model, in which the concentration of each sediment fraction in suspension (C_i) was calculated first, based on a reference concentration (C_{ai}). Subsequently, sediment composition of the suspension can be determined by the ratio between the concentration of each fraction and the total concentration. To calculate C_{ai} , Xu assumed that the sediment composition at the reference level equals that of the bed material. However, according to Sisternans et al. (2001) and Chapter 3 (Figure 3.11), the near bed vertical sorting of sediment was significant, especially for a graded sediment (e.g. silt-sand mixed bed). Therefore, we argue that the sediment composition at the reference level should be estimated.

4.2.2. IMPROVED APPROACH

IMPROVED CORRECTING METHOD

IT is possible that the disadvantage of the “mixture of linear component response” method can be surmounted by dividing bed materials into sufficient number of fractions and by calibrating each fraction separately. However, this solution would be extremely time-consuming when more OBS sensors are applied. Besides, it is difficult to sieve silt into sub-fractions. Hence, we propose an alternative solution to correct the sensitivity coefficient for each fraction, by considering other sediment samples with dif-

ferent sediment compositions. Corresponding to the two-fraction method, steps of the improved approach are listed as follows:

(1) Collect another sediment sample (accompanying sample, referred to as AS) in addition to the original sediment sample (referred to as OS). The grain size of AS is determined by the grain size difference between the sediment monitored by OBS and the original sediment for calibration (usually the local bed material in laboratory study). A requirement is that the grain size distributions of AS and OS should more or less overlapping. Then, measure the composition of these two sediments (i.e. P_{silt} and P_{sand} of AS and OS), respectively. Note that an equivalent number of sediment samples to size classes intended to be distinguished is the minimal requirement. (See section 4.5.3 for more details). Thus, with more accompanying samples (i.e. n , $n > 2$) the two-fraction method can be extended to n -fraction method, which may have a higher accuracy.

(2) Calibrate OBS sensors with the collected two sediment samples respectively, without sieving both of them into multi-fractions. Sensitivity coefficients of AS and OS ($S_{i,t}$) are obtained in this step; the subscript 'i' denotes the sediment samples used for calibration, and $i = OS, AS$.

(3) Calculate the sensitivity coefficients for the silt and sand fractions (i.e. S_{silt} and S_{sand}). The sensitivity coefficients for silt and sand fractions are deduced inversely, based on the calibrated sensitivities $S_{i,t}$, assuming that AS and OS have the same sensitivity for the same fraction. According to Eq. (4.4), if a linear relationship is obtained for the OBS calibration, the total sensitivity can be written as:

$$S_{AS,t} = S_{silt} \cdot P_{AS,silt} + S_{sand} \cdot P_{AS,sand} \quad (4.5)$$

$$S_{OS,t} = S_{silt} \cdot P_{OS,silt} + S_{sand} \cdot P_{OS,sand} \quad (4.6)$$

Subsequently, S_{silt} and S_{sand} can be deduced by solving Eq. (4.5) and Eq. (4.6).

(4) Predict the grain size distribution of suspensions at each elevation when measurements are not available. The grain size distribution is modelled by a multi-fraction sediment model (discussed in detail in the next section), which first have to be calibrated by several hydrodynamic conditions. Therefore, the corresponding measurements are needed. It is noted that the purpose of the model is to estimate the percentage of each fraction rather than the accurate concentration.

(5) Convert OBS output into concentration based on corrected sensitivity coefficients S_{silt} and S_{sand} together with the percentages of fractions (Eq. (4.1) and Eq.(4.4)).

MODELLING GRAIN SIZE DISTRIBUTION OF SUSPENDED SEDIMENT

A Multi-fraction sediment model (MFSM) is developed to predict the vertical distribution of different fractions by calculating the concentration of each sediment fraction, respectively. At a steady state, the 2D advection-diffusion equation for sediment transportation reads:

$$\frac{\partial}{\partial z} \left(\varepsilon_{s,i} \frac{\partial C_i}{\partial z} \right) + \omega_{s,i} \frac{\partial C_i}{\partial z} = u \frac{\partial C_i}{\partial x} \quad (4.7)$$

where, C_i is the suspended sediment concentration; $\omega_{s,i}$ is the settling velocity; $\varepsilon_{s,i}$ is the turbulent mixing coefficient; u is the horizontal current velocity in X-direction; the subscript i represents fraction i . The settling velocity $\omega_{s,i}$ and the turbulent mixing coefficient $\varepsilon_{s,i}$ are calculated based on Van Rijn's formulas (van Rijn, 1993, 2006). In case of high concentration, the considerations of hindered setting (on $\omega_{s,i}$) and stratification effect (on $\varepsilon_{s,i}$) are based on Van Rijn (2007b). Note that Eq. (4.7) neglects the horizontal diffusion term, which is much smaller than the horizontal advection term.

In this study, the reference concentration C_{ai} is used as the bed boundary condition to derive the sediment concentration of each fraction (C_i) at different elevations. C_{ai} is predicted, according to Van Rijn (2007b), with specific modifications for silt and fine sand range sediment:

$$C_{ai} = 0.015 P_{bed,i} f_{silt,i} \frac{D_i}{z_a} \frac{T_i^{1.5}}{D_{*,i}^{0.3}} \quad (4.8)$$

where, $D_{*,i}$, T_i , D_i are the dimensionless particle parameter, the dimensionless bed-shear stress parameter and the mean grain size (in units of m) of fraction i , respectively; $f_{silt,i}$ is the silt factor, and in this study, $f_{silt,i} = 3D_{sand}/D_i$ ($f_{silt,i}=1$ for $D_i > 3D_{sand} \approx 180 \mu m$); $P_{bed,i}$ is the percentage of fraction i in the bed material; z_a is the reference height (in unit of m), and $z_a = \max \{0.5k_{s,c,r}, 0.5k_{s,w,r}, 0.01\}$, $k_{s,c,r}$ and $k_{s,w,r}$ are current related and wave related bed form roughness, respectively. Furthermore, the calculation of C_{ai} considers the effect of cohesive materials on critical bed shear stress (Van Ledden, 2003; van Rijn, 2007a), and the interaction among different fractions (Egiazaroff, 1965; Kleinhans and Van Rijn, 2002).

Subsequently, Eq. (4.7) can be solved numerically for certain hydrodynamic conditions and bed materials. Thus, the percentage of fraction i ($i=1, 2, \dots, n$) at elevation is obtained as:

$$P_i(z) = C_i(z)/C_t(z) \quad (4.9)$$

where, $C_t(z)$ is the total sediment concentration at elevation z , and $C_t(z) = \sum_{i=1}^n C_i(z)$; $C_i(z)$ is the sediment concentration of fraction i at elevation z .

4.3. LABORATORY EXPERIMENT

4.3.1. EXPERIMENT DESCRIPTION

A series of flume experiments, which has been carried out in the hydraulic laboratory of Hohai University, China, are used to investigate the applicability of the improved approaches on OBS conversion for natural graded sediment under different hydrodynamic conditions (See Chapter 3 for more details). Here, we take five experiments, which use the sediment S2 as the original bed material (OS), as an example, i.e. s2-0009, s2-0011, s2-f2609, s2-f2911, s2-o3011, s2-o3611 (the experiment number is based on section 3.2).

Time-averaged and time-series sediment concentrations were measured simultaneously during each experiment by a transverse suction system and OBS sensors, respectively. Three OBS sensors (OBS 3+, for a more detailed reference of the description and parameter, see Campbell Scientific, 2008) were used for monitoring the SSC time-series at different elevations. Before each experiment, the initial OBS signal was recorded. This signal was larger than the electronic offset during calibration. The difference between the initial signal and the electronic offset is due to the background turbidity of the flume water and should be eliminated from the raw signal during conversion.

4.3.2. OBS CALIBRATION

IN addition to the bed sediment, another sediment sample, i.e. role of AS, was required in this study. The clay-silt-sand mixture, sediment S1, which was collected in the supra-tidal zone of the Tiaozini tidal flat (Figure 3.2a), is taken as the accompanying sediment (AS) for the original bed sediment S2 (OS). The grain size distributions of the two sediment samples are shown in Figure 3.2b.

Sediment samples of AS and OS were dried and used to prepare a series of water-sediment samples with different sediment concentrations, respectively. Each OBS sensor was calibrated with the water-sediment samples of OS and AS. Figure 4.2 shows the results of calibration, taking the OBS #1 sensor as an example. The different OBS responses for the same sediment concentrations of OS and AS imply that the effect of particle size on OBS output is significant, which is in agreement with previous studies. Be-

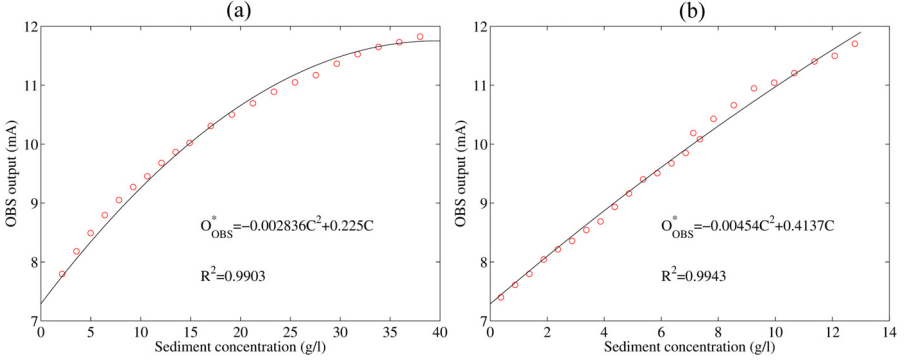


Figure 4.2: Calibration curves for sensor OBS#1 using (a): the grain size of the original sample (OS); and (b): the accompanying sample (AS). The red circles represent calibration results. Non-linear regression was used to fit relationships to the whole range of calibration results; the calibration equations and coefficients of determination (R^2) are also shown.

sides, the calibration curve of OS is non-linear for a relatively large concentration range. Therefore, non-linear fitting (i.e. quadratic) was applied, yielding a high coefficients of determination ($R^2 > 0.99$). Note that, it is possible to apply a higher order non-linear relationship to fit the calibration results. The order has no influence on the feasibility of the improved approach. If a quadratic relationship is applied to the calibration:

$$O_{OBS}^* = S_{t,1} \cdot C^2 + S_{t,2} \cdot C \quad (4.10)$$

the relationship between the sensitivity coefficients for mixtures ($S_{t,1}$, $S_{t,2}$) and for the silt and sand fractions are:

$$S_{t,1} = S_{silt,1} \cdot P_{silt}^2 + S_{sand,1} \cdot P_{sand}^2 \quad (4.11)$$

$$S_{t,2} = S_{silt,2} \cdot P_{silt} + S_{sand,2} \cdot P_{sand} \quad (4.12)$$

4.4. EXAMINATION OF THE IMPROVED APPROACH

4.4.1. VERIFICATION OF THE MODELLED GRAIN SIZE DISTRIBUTION

THE bed sediment was classified into 11 fractions (including 1 clay fraction, 4 sub-silt-fractions and 6 sub-sand-fractions) to calculate the grain size distribution of each experiment (Table 4.1). The computed results are compared with the measured grain size distributions by the suction system in Figure 4.3, taking three experiments (i.e. s2-0011, s2-f2911 and s2-o3611) as examples. Generally, the results indicate a good model

Table 4.1: Grain size fractions of the bed material used in the MFSM-model.

Fraction	1	2	3	4	5	6
Range (μm)	<8	8-16	16-31	31-48	48-62	62-80
Mean size (μm)	3.39	11.17	26.70	40.66	55.18	70.86
Percentage (%)	1.80	1.00	1.66	10.05	12.38	16.43
Fraction	7	8	9	10	11	
Range (μm)	80-98	98-125	125-180	180-250	>250	
Mean size (μm)	77.78	110.47	147.99	207.23	323.27	
Percentage (%)	14.43	15.70	16.86	6.98	2.71	

performance, especially for the wave-current combined conditions (Figure 4.3c-4.3f). As the percentages of silt and sand fractions (P_{silt} and P_{sand} , taking $62 \mu\text{m}$ as a criterion) are crucial for the improved approach, we further examine the model performance quantitatively using the absolute bias of P_{silt} ($|\text{measured}-\text{modelled}|$). Under wave-current combined conditions, the averaged bias (over all modelled elevations) for experiment s2-f2911 and s2-o3611 are 5.3% and 4.0%, respectively. For wave-only conditions (e.g. experiment s2-0011), the averaged bias over elevations less than 10 cm is 5.1%, whereas the bias increases to 9.6 % at the elevation of 10.5 cm (i.e. Figure 4.3b). There are two possible explanations for the higher bias. First, the measured ripple steepness for experiment s2-0011 is larger than 0.1. For practical purpose, we adopt a time-average modelling approach, which ignores the time-varying intra-wave processes (e.g. vortex formation and shedding during flow reversal over steep ripple; see Davis and Thorne, 2005). The ignorance may result in the deviations especially for pure wave conditions. Second, sediment samples collected at higher elevations mainly consist of fine materials. We observed that a part of sucked sediment sample was attached to the filter paper during filtering and drying processes. It is hard to separate this part of sediment sample from the filter paper, probably leading to an underestimation of the fine sediment content. Nevertheless, we examined that the error of the converted sediment concentration due to the bias of P_{silt} is less than 9% in this study. Therefore, the present modelling approach is considered to be reliable.

4.4.2. OBS OUTPUT CONVERSION

BASED on the calibrated OBS sensitivities of AS and OS, the sensitivity coefficients of the silt and sand fractions were calculated through Eq.(4.11) and Eq.(4.12). Subsequently, together with the simulated composition of suspensions, the measured OBS output was converted into sediment concentration by the improved approach (referred to as corrected OC). Besides, the concentration converted directly by the calibration

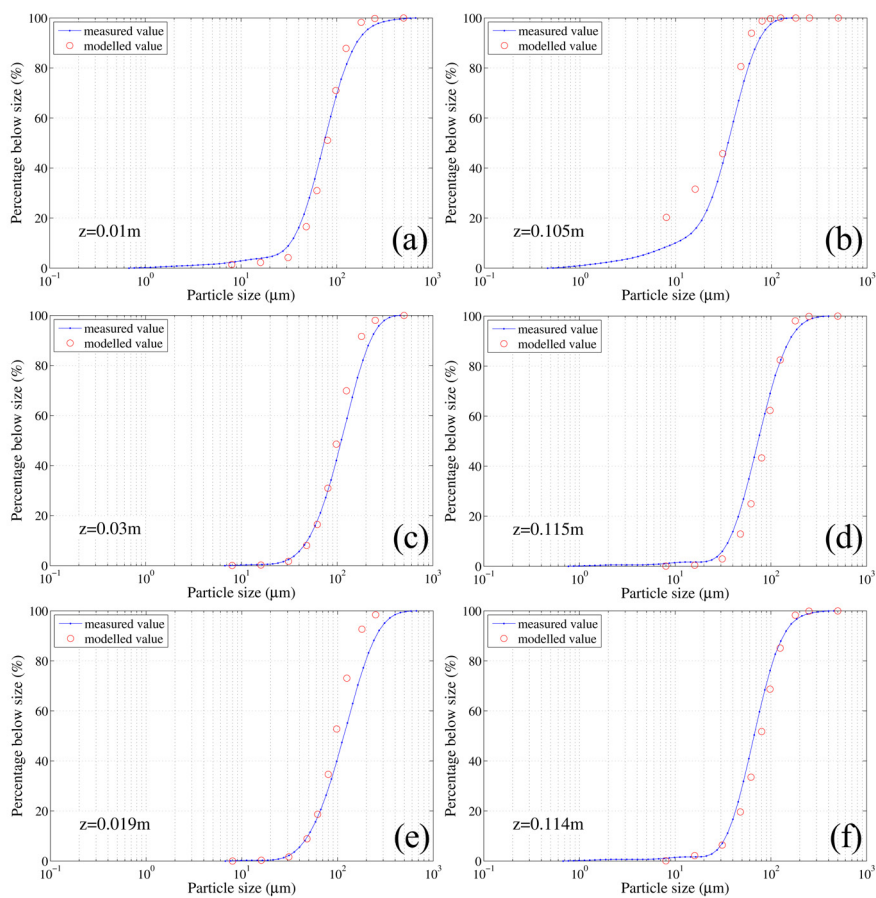


Figure 4.3: Comparison of the measured grain size distribution with the simulated cumulative frequency curve for experiment s2-0011 (a, b), experiment s2-f2911 (c, d) and experiment s2-o3611 (e, f). The "percentage below size (%)" is defined by volume. The results from two elevations for each experiment are used for illustration.

curve of OS (referred to as uncorrected OC) was calculated to illustrate the degree of modification by the improved approach.

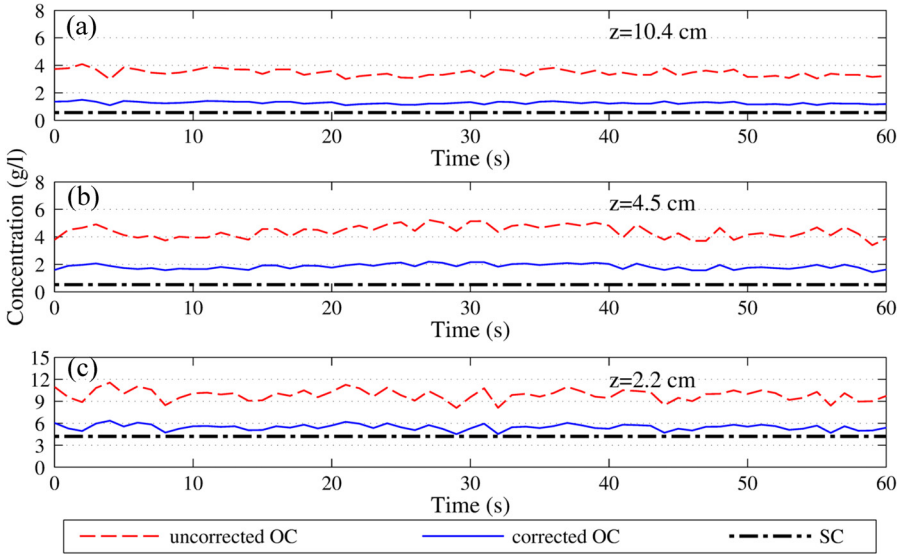


Figure 4.4: Time series (60 seconds) of sediment concentration measured at three elevations using sensor OBS#1 without correction and with the new procedure. The time-averaged suction measurement (SC) is shown as a reference. The original sample (OS) was used in experiment s2-0011. Three elevations are 10.4 cm (a), 4.5 cm (b) and 2.2 cm (c), respectively.

The discrepancy between converted concentration (referred to as OC) with/without correction by our approach varies with different sensors and experiments. We take the results of the OBS #1 sensor of the two experiments as examples in Figure 4.4 and Figure 4.5. The corrected OC are always smaller than uncorrected OC under wave-only conditions (Figure 4.4), whereas under wave-current conditions, the corrected OC are larger near the bottom and smaller in the upper layer (Figure 4.5). The overestimation/underestimation of uncorrected OC in comparison with the corrected OC is due to the particle size effect on the OBS response, which leads to a larger/smaller OBS output for the same concentration of finer/coarser sediment samples, respectively. Greenwood and Jagger (1995) also emphasized the occurrence of overestimation of concentration based on the calibration with bed sample, when grain size decreases with elevations. Moreover, the difference between the corrected OC and uncorrected OC under the wave-only condition (Figure 4.4) is larger than under the wave-current condition (Figure 4.5), because the composition of the suspension under the wave-current condition is much closer to that of the bed material in comparison with under the wave-only condition (Figure 3.11).

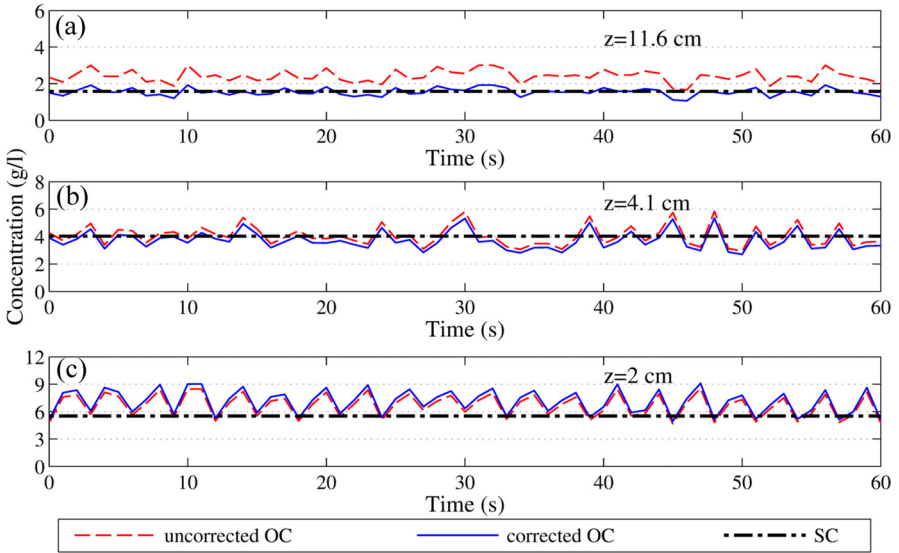


Figure 4.5: Time series (60 seconds) of sediment concentration measured at three elevations using sensor OBS#1 without correction and with the new procedure. The time-averaged suction measurement (SC) is shown as a reference. The original sample (OS) was used in experiment s2-f2911. Three elevations are 11.6 cm (a), 4.1 cm (b) and 2 cm (c), respectively.

As it is unable to obtain the absolute time-series concentration, the time-averaged sediment concentration measured by the suction system (referred to as SC) in this study is considered to be reliable because the intake sampling velocity (about 50 cm/s in this experiment) was larger than the ambient current (Van Rijn et al., 2000). Therefore, SC is used as a criterion to assess the quality of OC (Figure 4.4 and Figure 4.5). It shows that the uncorrected OC deviate substantially from the suction measurements. In general, the concentrations converted by the improved approach show a better agreement with SC than the uncorrected OC. It implies that the improved method indeed plays an effective role in improving the reliability of OBS measurements, except for the near bottom layer under wave-current conditions. We suggest that the unsatisfactory correction is due to that the median grain size of the corresponding suspension is larger than that of the original bed sediment.

4.4.3. COMPARISON BETWEEN THE OPTICAL AND SUCTION CONCENTRATIONS

IT is impossible to obtain the absolute measurements of sediment concentration for comparison with the concentrations measured with OBS, particularly when it is vary-

ing at a high frequency. Suction methods produce time-averaged concentration values and are not the best option for time-series comparison. Therefore, in this study, we only consider the averaged concentration over a significant time interval, rather than the time-varying concentration. For each experiment, the time-series (with 1 s interval) of the OBS measurements at 29 heights were averaged for each monitoring period of about 220 s. Subsequently, the time-averaged OBS measurements were converted to the corrected/uncorrected OC, respectively. The vertical distribution of the time-averaged corrected/uncorrected OC is then compared with the suction measurement to assess the improvement of data quality in detail.

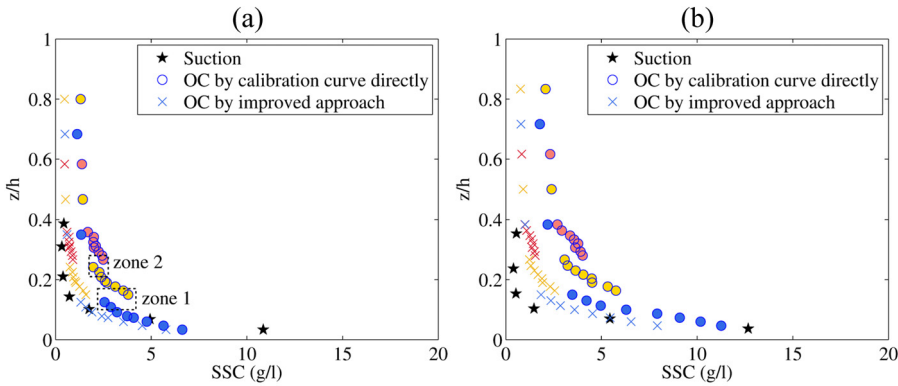


Figure 4.6: Plots of time-averaged suspended sediment concentration (SSC) with respect to the relative depth (z/h) under wave-only conditions: experiment s2-0009 (a) and s2-0011 (b). The comparisons shown are those determined by simple calibration, by the improved approach presented in this study and by using suction sampling at a number of elevations above the bed. Colors of the dots represent the measurements by different OBS sensors. Blue: sensor#1; Yellow: sensor#2; Red: sensor#3. To illustrate discontinuity of the profile, zone 1 and zone 2 in figure (a), marked by rectangular shapes, denote the region of interest (Same for the other experiments).

The comparisons between corrected/uncorrected OC and SC for wave-only conditions and wave-current combination conditions are shown in Figure 4.6 and Figure 4.7, respectively. The accuracy of OC has been greatly improved after correction, as it is closer to the suction value. Moreover, under wave-only conditions, the distribution of corrected OC has a similar 'L' pattern as the suction measurement. A high concentration layer is located 3-5 cm above the bed, which is consistent with the distribution of SC (Yao et al., 2015) and observed phenomena (Figure 3.7). Furthermore, the vertical distribution of sediment concentration measured by the suction technology is captured by the corrected OC with a satisfactory agreement, especially for the wave-current conditions.

Another remarkable improvement is that our approach improves the continuity of the vertical profile of OC (Figure 4.6 and Figure 4.7). The discontinuity in the profile of

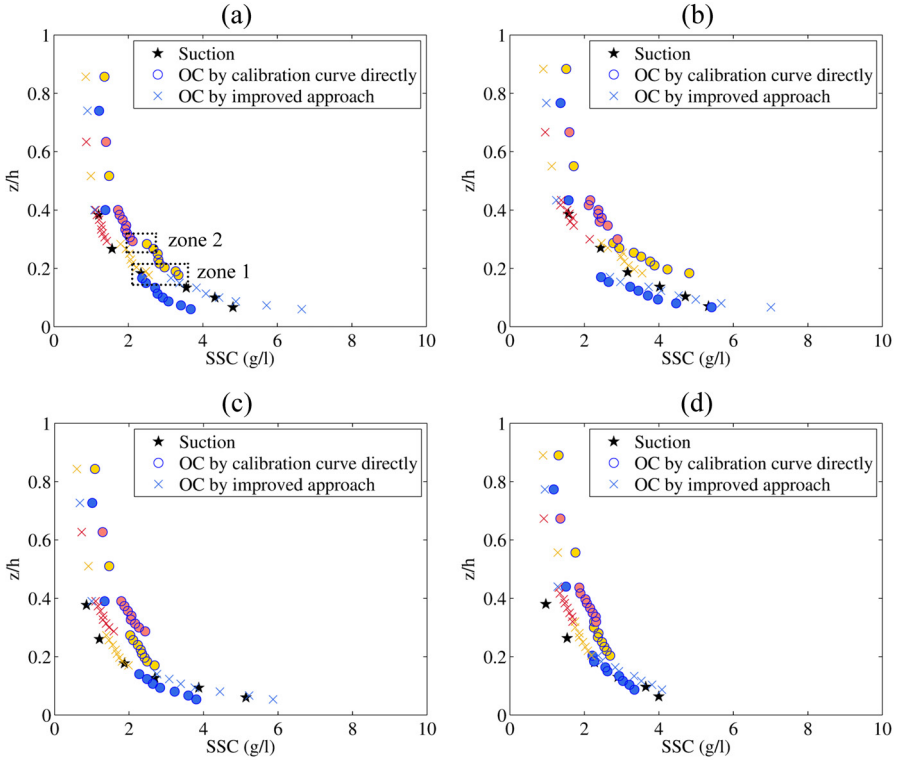


Figure 4.7: Plots of time-averaged suspended sediment concentration (SSC) with respect to the relative depth (z/h) under wave-current conditions: experiment s2-f2609 (a), s2-f2911 (b), s2-o3011 (c) and s2-o3611 (d). The comparisons shown are those determined by simple calibration, by the improved approach presented in this study and by using suction sampling at a number of elevations above the bed. Colors of the dots represent the measurements of different OBS sensors. Blue: sensor#1; Yellow: sensor#2; Red: sensor#3. To illustrate discontinuity in the profile, zone 1 and zone 2 in figure (a), marked by rectangular shapes, denote the region of interest (Same for the other experiments).

OC always occurs at the intermediate region of the two OBS sensors' measurements (e.g. zone 1 and zone 2 in Figure 4.6 and 4.7). The discontinuity may be due to the different responses of different sensors to the grain size effect. To illustrate the improvement clearly, the corresponding concentrations of two sensors at the intermediate region are extrapolated respectively. The discrepancy (Δ) between the extrapolated concentrations by the two sensors is used to illustrate the degree of the discontinuity. The discontinuity and the corresponding improvement for the experiments are shown in Table 6.2. The smaller the discrepancy, the better the continuity of the vertical profile appears. The improvement of discontinuity is more than 60% by the improved approach for both zones, except for zone 2 in experiment s2-o3611. However, that is because both corrected and uncorrected concentration profiles of s2-o3611 show a good degree of continuity. The

improvement of the two experiments is therefore limited.

Table 4.2: Discontinuity improvement of the vertical distribution profile of correct/uncorrected OC.

No.	zone 1			zone 2		
	Δ_{un}	Δ_{cr}	Improvement (%)	Δ_{un}	Δ_{cr}	Improvement (%)
s2-0009	1.73	0.58	66.29	0.80	0.27	66.82
s2-0011	2.74	1.01	63.19	1.04	0.36	65.57
s2-f2609	1.03	0.50	51.24	0.31	0.31	0
s2-f2911	2.74	1.08	60.53	0.22	0.19	15.08
s2-o3011	1.03	0.27	73.84	0.52	0.29	43.77
s2-o3611	0.47	0.19	59.59	0.06	0.06	0

Note: Δ denotes discrepancy between the extrapolated concentrations for the intermediate region by two adjacent sensors. Subscript 'un' and 'cr' denote the discrepancy for the uncorrected and corrected profile, respectively. Zone 1 and Zone 2 denote the intermediate regions between two adjacent sensors, shown in Figure 4.6 and Figure 4.7.

4.5. DISCUSSION

4.5.1. ADVANTAGE OF THE IMPROVED APPROACH IN A SILT-SAND SUSPENSION ENVIRONMENT

LUDWIG and Hanes (1990) suggested that the OBS device was not applicable for sand/mud mixtures. To overcome the restriction of OBS to non-homogeneous sediment, Green and Boon III (1993) and Conner and De Visser (1992) proposed a “multi-sensor approach”, that is to co-deploy another (type of) sensor together with the OBS devices (i.e. measure sediment concentration or measure the particle size) for the field study. With respect to the laboratory study, Green and Boon III (1993) recommended a two-fraction method, using a single set of calibrated sensitivity coefficients for suspensions at any elevation. However, the compositions of sub-fractions, i.e. both silt and sand fractions, vary for the suspensions, and these of suspensions are also different from the corresponding fractions of the calibrated sample. The larger the grain size difference, the farther removed the enveloping lines of suspensions are from those of the calibrated sediment. There are no simple remedies for this problem as it is not practical to calibrate the accurate sensitivities for all suspensions monitored by OBS. We aim to find a set of applicable sensitivity coefficients without complicated procedures, striking a balance between accuracy and efficiency. The chosen sensitivities should have reasonable accuracy when applying them to convert OBS measurements for both finer and coarser suspensions than the calibrated sediment samples.

Our work extends this two-fraction method by considering another accompanying

sediment sample (AS), which has relatively different composition from the original sediment sample (OS). According to our study, as AS is finer than the OS, the enveloping lines of AS are located somewhere above those of OS. The derived enveloping lines, according to our method, are located between those of AS and OS, which provides a better representation of the suspension. Moreover, one of the advantages of the improved method is that it does not require sieving the sediment into fractions for calibration. It does not only save time, but also appears practical, especially for silt-dominated sediment. It is hard to sieve silt into sub-fractions. Our approach can avoid such disadvantage and has been demonstrated to provide satisfactory results for both finer and coarser suspensions.

Additionally, the grain size distribution is predicted by a numerical model and, in our approach, it does not need to be measured by another device. When the OBS is deployed over a long-time and at several locations, it is not always possible to obtain enough data (e.g. sediment composition) to correct the OBS output. Our method provides an alternative solution for predicting sediment composition. Its ability on estimating the sediment composition has been validated in the laboratory situation.

4.5.2. THE ACCURACY OF THE IMPROVED APPROACH

IN order to quantitatively elaborate the accuracy of the improved method for the OBS conversion, linear regression analyses were conducted between the corrected OC and the SC. For comparison, we also analyzed the relationship between the SC and the uncorrected OC. The results are listed in Table 4.3.

Table 4.3: Goodness of fit between the corrected/uncorrected OC and the SC.

	Wave-only conditions		wave-current conditions	
	$R^2(-)$	RMSE (-)	$R^2(-)$	RMSE (-)
SC & uncorrected OC	0.724	1.284	0.557	0.966
SC & corrected OC	0.8652	0.897	0.926	0.394

For both the wave-only and wave-current combined conditions, the relationship between the OC and the SC is greatly improved by our approach. According to the regression coefficients, a close relationship between the corrected OC and the SC can be illustrated by the decreased Root Mean Squared Error (RMSE) as well as the increased coefficient of determination (R^2). R^2 is a better measure of the goodness of fit, because it gives the actual amount of variance exhibited by the linear equation. The improvement under wave-only conditions is relatively smaller than that under wave-current condi-

tions. Specifically, R^2 increases from 0.55 to 0.92 for the wave-current conditions, which illustrates a good agreement between the corrected OC and SC.

4.5.3. SUGGESTIONS ON THE SELECTION OF THE ACCOMPANYING SEDIMENT SAMPLE (AS)

COMMONLY, the bed material or the collected suspended sample is always taken as the original sediment (OS) for OBS calibration under both laboratory and field conditions (e.g. Ludwig et al., 1990, Lunven et al., 2000, Greenwood et al., 2001). In this study, we suggest that accompanying sediment is additionally required for improving the OBS conversion. There are several factors of influence for the determination of the grain size of AS, e.g. the median grain size of OS, the hydrodynamic conditions and the grain size of the suspensions at the interested elevations.

It is our experience that it is better to conduct preliminary tests (or experiments) first, and subsequently determine the grain size of AS based on the results (i.e. the grain size of the suspended sediment at elevations of interest). (1) If mostly interested in the coarser suspensions than the OS (e.g. lower suspensions of experiment s2-f2609 and s2-o3611 in Figure 3.11), the grain size of AS should be larger than that of OS to obtain a reliable conversion. The best choice is a grain size of AS similar to that of the coarsest suspensions. (2) If mainly focused on the finer suspension than the OS, AS should be smaller than OS. It is better that AS has a similar grain size as the finest suspended sediment. Otherwise the accuracy for converting the suspensions which are finer than AS is more or less restricted; (3) The most complicated case is that both coarser suspensions and finer suspensions are monitored by OBS and required conversion. A general rule is to collect two accompanying sediment samples, one coarser and one finer than the OS; the coarser/finer AS can help the conversion of coarser/finer suspensions, respectively. Alternatively, it is also possible to collect only one accompanying sediment sample for this case. We suggest choosing the finer AS rather than the coarser AS, with the consideration that most of the suspensions are finer sediment and that the OBS is more sensitive to the fine sediment. The grain size of the chosen AS is suggested to be similar or a bit coarser than the minimal grain size of the suspended sediment to guarantee a generally reliable conversion.

In addition to the determination of the grain size of AS, another requirement, when selecting AS, is that the grain size distributions of AS and OS should have overlaps. Thus, AS can be collected from the nearby location of OS, or can be suspensions pumped in the field or laboratory study, or, it can even be prepared artificially. Regarding the location

restriction, it is better, but not necessary, that AS and OS should have a similar environment. Similar environments may have implications for common mineralogy, shape and topology of the grains, which may all affect the OBS response. Nevertheless, the necessity of similar environments reduces if more fractions are divided into during OBS conversion (i.e. n -fraction method) for improving the accurateness of conversion.

4.6. CONCLUSION

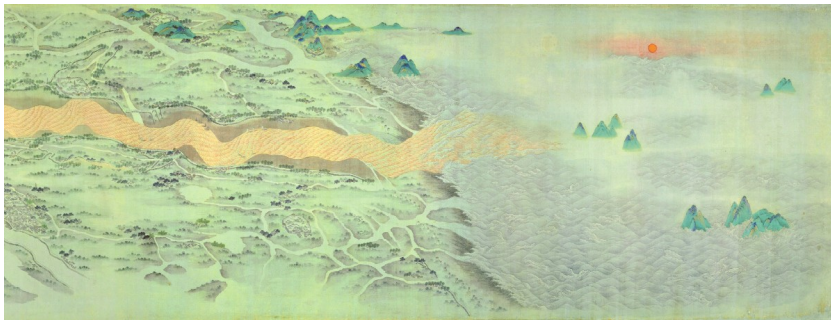
OBS sensors are widely used to monitor SSC in both field and laboratory conditions. However, the reliability of SSC derived from an OBS signal is not always high, because the OBS output is highly sensitive to particle size. In order to enhance the reliability of OC, specifically for silt-sand suspension regions as tidal flats, where the grain size varies temporally and spatially, an improved approach has been proposed based on the “mixture of linear component response” method.

The modified method extends an existing two-fraction method by considering one accompanying sediment sample (AS) besides the original bed sediment (OS) for OBS calibration. The enveloping curve for each fraction is deduced inversely, omitting time-consuming and sometimes impossible sieving processes (e.g. sub-silt fractions). Besides, a multi-fraction sediment model is recommended to predict the grain size distribution, when the corresponding grain size measurements are unavailable. Subsequently, OBS outputs at different elevations can be converted into concentrations, based on sets of enveloping lines and sediment composition in suspension. A series of laboratory experiments was carried out to investigate and validate this method. The results show that this method successfully yields continuous vertical concentration profiles from originally discontinuous OC profiles, which were converted without grain size correction. Furthermore, corrected OC, in our approach, agrees well with the concentration profile measured by the suction method. Compared with the uncorrected OC, the corrected OC shows a closer linear relationship with the SC, indicating an improved data quality.

Linear regression analyses (using coefficients RMSE and R^2) demonstrate the validity and accuracy of the method. The criteria on selecting AS are also discussed. The grain size of AS depends on the grain size of suspension and the grain size of OS. Thus, preliminary tests are suggested for the determination of the grain size of AS. Another requirement is that the grain size of AS and OS should have overlaps, while it is not necessary that OS and AS have a similar environment.

5

EXPLORATORY MORPHODYNAMIC HINDCAST OF THE EVOLUTION OF THE ABANDONED YELLOW RIVER DELTA, 1578-1855 AD



This figure is part of the “Yellow River Picture”. It was probably drawn in 1661-1680 AD. Available at: http://www.mygoods.com.tw/Search/search_info?id=13249&did=13167.

This chapter is based on the journal paper submitted to *Marine Geology*.

Abstract: The Abandoned Yellow River Delta (AYD), formed when the Yellow River was flowing into the southern Yellow Sea during 1128-1855 AD, is a representative example of the sensitivity of deltas to a modification of their environment. Reconstructing a reliable natural evolution of the AYD before 1855 AD based on a process-based morphological model can give insight into the morphodynamic evolution of such a large-scale fine-grained delta. Through an analysis of the temporal delta evolution and residual sediment transport, the evolution mechanisms of the AYD have been investigated. Uncertainties, which are inevitable due to lack of historical data, are assessed together with the corresponding influences on the evolution of the deltaic system by considering a series of scenarios. Based on an evaluation of the uncertainties and a comparison with historical maps, the simulated AYD is evaluated to be reliable. Subsequently, suggestions are proposed on the distribution of the AYD at the end of its progradation stage. This study is different from existing studies on the AYD, which are all based on geological approaches. It provides insight into the evolution of the AYD through an alternative way, viz. a process-based morphodynamic-modelling approach.

Highlights:

- Provide insight into the evolution of the Abandoned Yellow River Delta (AYD) through a process-based morphodynamic-modelling approach.
- Quantify the influence of uncertainty in model setting and initial state on the morphological evolution.
- The model improves the understanding of the mechanisms underlying the evolution of the AYD.
- The model provides relatively reliable suggestions on the spatial distribution of the AYD.

5.1. INTRODUCTION

A river delta can be formed when a river flows into a relatively larger water body (e.g. ocean, lake, and gulf). The morphology of a delta is a dynamic balance between the fluvial discharge, marine energy conditions, accommodation space and overall geological setting (Wright and Coleman, 1973; Giosan, 2007; Hanebuth et al., 2012) with contributions from sea-level rise and human activities (Edmonds and Slingerland, 2009). Deltas are fragile geomorphic landscapes, which can change dramatically with the slightest modifications of these conditions (Giosan, 2007). For example, the historical equilibrium of many deltas has been broken due to changes between sediment supply and sediment dispersal (e.g. Ebro Delta and Nile Delta, Jimenez et al., 1997; Syvitski and Saito, 2007; Frihy et al., 2008; Gelfenbaum et al., 2009). An extreme example is the Abandoned Yellow River (Huanghe) delta (AYD), which was formed during 1128 - 1855 AD (Xue, 1993) (Figure 5.1 and 5.2). It has undergone severe erosion since 1855 AD, when the Yellow River shifted its course away to the north and no more sediment was delivered to the AYD (Ren & Shi, 1986; Xue, 1993; Saito et al., 2000; Liu et al., 2013).

Under energetic hydrodynamics (e.g. tidal currents) and abundant fluvial sediment from the old Yellow River (OYR) during 1128-1855 AD, the hydrodynamics, morphology and shoreline in the western Southern Yellow Sea (SYS) were inevitably modified (Liu et al., 2013). For instance, the Jiangsu Coast (Figure 5.1), where the OYR discharged into the SYS, changed from a sandy beach to a silt-clayey coast (Liu et al., 2010; Xue et al., 2011). Besides, a considerable part of the well-known radial sand ridges in the SYS (Figure 5.1) was stated to be made of the sediment from the OYR (Ren and Shi, 1986). Considerable efforts have been devoted to investigate the erosion process and to forecast the fate of the abandoned delta (e.g. Zhang et al., 1998; Liu, 2011; Zhou et al., 2014). However, the morphodynamics during delta progradation period have drawn little attention (Liu et al., 2013; Xia et al., 2015).

Geleynse et al. (2011) stated that a good understanding of the present state of deltas is required to understand their future dynamics. Enriching our understanding of the evolution before abandonment, such as morphodynamic mechanisms, spatial distribution of sediment and the size of the deltaic system, is important to investigate the subsequent erosion processes. However, studies on the understanding of the sedimentary characteristics of the progradation of the AYD are qualified as superficial (Liu et al., 2013). Either the methodologies applied are limited to be geological and geophysical approaches, including sedimentological, mineralogical and geochemical methods (Yang et al. 2003), or the objective of the existing studies is focused on the speculation on the spatial distribution of the AYD (Liu et al. 2013). Unfortunately, the results of the spatial distribution of

the AYD are not consistent with each other, and even considered as controversial. This may be partly due to the inherent restriction of a geological approach, which commonly focuses on the sedimentary record rather than on the recovery of historical events including erosion. Therefore, an alternative approach is suggested to improve the understanding of the progradation process of the AYD.

This study aims to document the natural evolution of the progradation process of the AYD, with particular focus on the hindcast of the depositional process of sediment, taking into account uncertain conditions. Due to scarce existing data, we combined several available complementary sources of information in this study. (1) Historical records and maps during the delta progradation period are presented to offer a general impression on the progradation of the AYD and the evolution of the adjacent Jiangsu Coast. Prominent events of the OYR are reviewed and major evolution features of the AYD are deduced. Also, geological evidence for discriminating the delta range and estimating the delta size is reviewed. (2) An efficient way to investigate long-term morphodynamics is to apply a reduced complexity numerical model (Seybold et al., 2009; Geleynse et al., 2010). Thus, in order to interpret a morphological evolution process of the AYD during past centuries, we have constructed a process-based morphodynamic model. (3) As a delta is a dynamic large-scale terrestrial-oceanic system (Swenson, 2005), changes in any of the uncertainties in this system can alter the overall distribution of sediment and delta morphology (Gelfenbaum et al., 2009). Thus, uncertainty of the model parameter settings, due to scarce historical data, has a critical impact on hindcasting the evolution of the deltaic system. Therefore, a series of scenarios is designed with various settings of uncertain parameters to hindcast the consequent distribution of the AYD. (4) Model results are presented as maps. Subsequently, the reliability of model results and their uncertainties are assessed based on the comparison with historical maps and the results of geological studies.

5.2. STUDY AREA, DATA AND METHODS

5.2.1. GENERAL INFORMATION

THE Yellow Sea, located between the Chinese mainland and the Korean Peninsula, is divided into the Northern Yellow Sea sector (NYS) and the Southern Yellow Sea sector (SYS) according to the geographic position relative to the Shandong Peninsula (Figure 5.1) (Wang and Aubrey, 1987). The SYS, located between the Shandong Peninsula and the East China Sea, has an area of over 300,000 km² and an average depth of 45 m. Tide is a major force in this area, especially the semidiurnal tide (Liu et al., 2013). The tidal

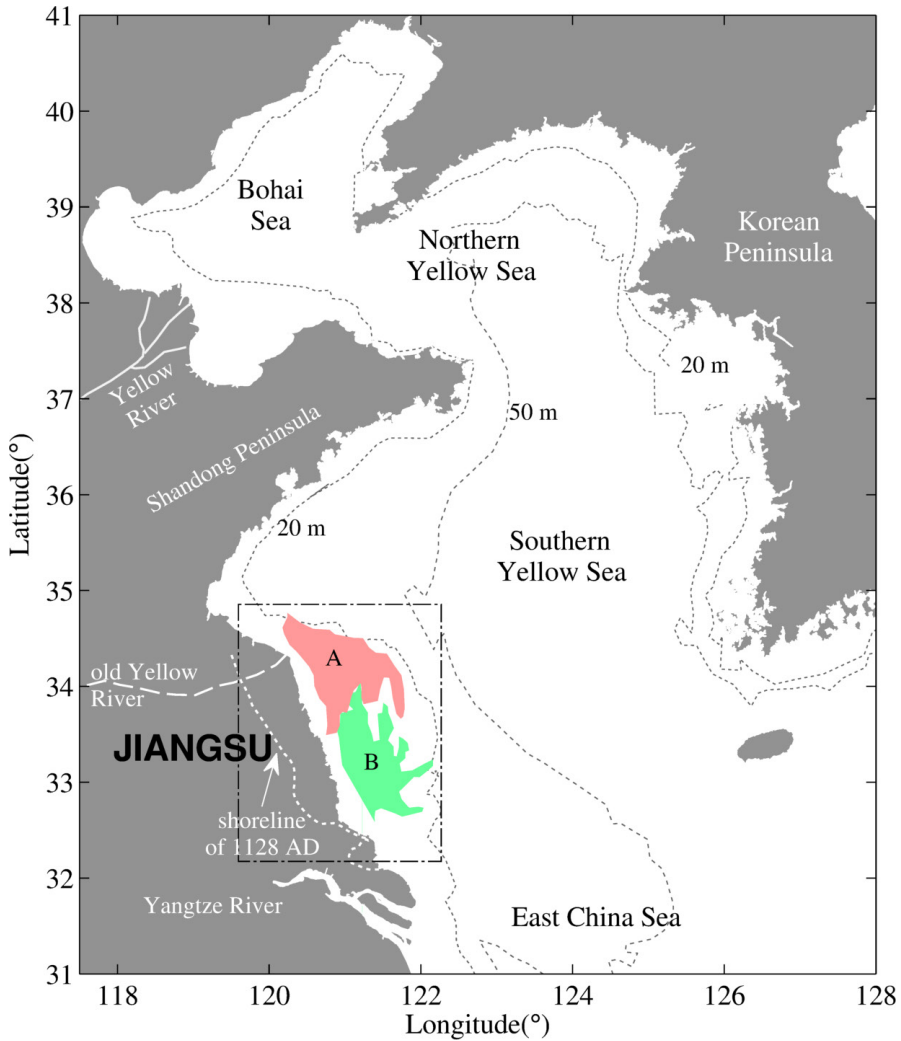


Figure 5.1: Map of the study area (inside the dotted rectangular), with 20 m and 50 m isobath in the Yellow Sea. The reference shoreline of the Jiangsu Coast in 1128 AD is modified after Yang et al. (2003) and Gao (2009). The location of the OYR is modified after Lim et al. (2007) and Liu et al. (2013). Colored region A and B represent the approximate location of the AYD and radial sand ridges field, respectively (modified after Park et al., 2000).

range of the M2 constituent is about 2 - 4 m along the Jiangsu Coast (Yang et al., 2003; Su et al., 2015). The western part of the SYS is dominated by a strong tidal current (i.e. the maximum velocity reaches 1.4 m/s; Teague et al., 1998), with convergent-divergent tidal currents in the radial sand ridge area and north-south rectilinear currents around the AYD (Zhu and Chang, 2000; Yang et al., 2003).

The Yellow River, which discharges into the Bohai Sea at present (Figure 5.1), is well-known for the large amount of silt it carries (Tregear, 1965; Van Maren et al., 2009). While it has a modest freshwater discharge (4.9×10^{10} m³/y), it carries the second largest sediment load in the world, estimated to be 1.2×10^9 t/y, reaching the ocean (according to data observed between 1950 – 1970; Milliman et al., 1987; Wang and Aubrey, 1987; Liu et al., 2013). Its course was alternated northward or southward frequently and unexpectedly in the historical time period described below (Figure 5.2). The last time it shifted southward and discharged into the SYS happened during 1128-1855 AD.

5

According to historical documents, four historical phases during the evolution of the AYD are distinguished: (1) 1128-1494 AD. In 1128 AD, an artificial distributary channel was excavated for a military strategic reason, and about 60%–80% of the total discharge of the OYR occupied the Huai River (Huaihe) channel into the SYS at the Jiangsu Coast (Zhang, 1984; Zhou et al., 2014). River-course shifts and crevasses frequently occurred during 1128–1494 AD, resulting in large deposits in the lower flood- and fluvial plain, rather than contributing to delta seaward progradation (Ye, 1986; Li, 1991; Liu et al., 2013; Zhou et al., 2014); (2) 1495-1577 AD. Since 1495 AD, the OYR discharges exclusively into the SYS owing to anthropogenic embankments (Ye, 1986; Milliman et al., 1987; Li, 1991; Liu et al., 2013); (3) 1578-1855 AD. Another remarkable anthropogenic influence on the evolution of the OYR and the AYD is a well-known river-training project based on the strategy: “restrict the current to attack the silt” (Ye, 1986; Li, 1991; Xue et al., 2011; Zhang et al., 2014; Chen et al., 2015). It started to impact the evolution of the AYD since 1578 AD and sediment began to deposit mostly at the river mouth. Its effect lasted for the following hundreds of years until 1855 AD; (4) 1855 AD. In 1855 AD, a significant breach changed the river course (Ye, 1986; Xue, 1993; Syvitski and Saito, 2007; Zhou et al., 2014). An abrupt stop of sediment supply to the delta has resulted in severe erosion of the delta morphology (Wang and Aubrey, 1987).

Generally, during the time period 1128-1855 AD, anthropogenic influences are implied to significantly impact the lower Yellow River (Chen et al., 2015). The sediment loads, the position of river mouth, the river management strategy as well as the river course shift were all affected by humans (Wang and Aubrey, 1987; Zhang et al., 2014). Eventually, the morphological evolution of the AYD was greatly influenced. Especially,

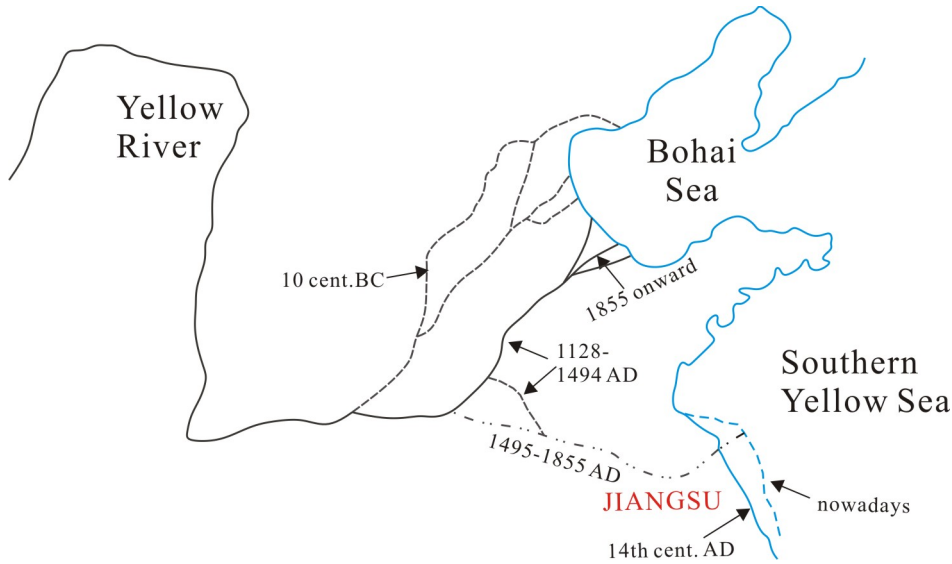


Figure 5.2: Shift of the course of the Yellow River (modified after Tregear, 1965; Wang and Aubrey, 1987 and Zhang et al., 1998).

since 1578 AD, the channel of the OYR was almost fixed and the deltaic progradation rate increased dramatically as a result of human embankments and channel training (Xue et al., 2011; Chen et al., 2015).

Historical maps offer a pictorial impression of the Jiangsu Coast and the AYD. In this study, several ancient maps are collected to interpret the progradation of the delta (See Appendix). Considering the purpose of the historical maps, i.e. primarily as a tool for government allocation of land, collecting taxes, defense and design of cities as well as management of farmland irrigation, and due to the restriction of measurement instruments in these early ages, most historical maps were not constructed with a recognizable coordinate system (e.g. longitude and latitude coordinate). In order to take advantage of historical maps for scientific research, efforts have been made to reference these maps to the longitude and latitude system (e.g. Zhang, 1984), and the adjusted shorelines have been shown in recent literature (e.g. Gao, 2009; Zhou et al., 2014). Adding coordinates to historical maps does benefit scientific study; however, it needs to be kept in mind that the geometrical accuracy of the results may not be as high as expected. Nevertheless, if taking the original historical maps as conceptual maps, the derived qualitative results are relatively credible. Two features of the Jiangsu Coast during 1578~1855 AD summarized through historical maps are remarkable: 1) A significant geometrical feature of the Jiangsu Coast was a previously dense channel network, and, subsequently, the region

with a dense channel network was reduced with time; 2) numerous shoals were generated along the Jiangsu Coast over time (See Appendix). Although the shoals were shown with different shapes, the existence and general location of the shoals were similar.

5.2.2. SPATIAL DISTRIBUTION OF THE AYD

A Deltaic system may be distinguished in the subaqueous delta and subaerial delta, which are defined traditionally according to the relative position to the mean sea level (Wright and Coleman, 1974). Simultaneously with the progradation of the subaerial delta, a huge subaqueous delta had been formed (Ren and Shi, 1986; Li et al., 2001; Yang et al., 2002; Liu et al., 2013). For instance, it is reported that the size of the modern Yellow River delta plain extended more than 5710 km² into the Bohai Sea within 150 years (Syvitski and Saito, 2007). However, the marine hydrodynamics and local bathymetries are different for the modern Yellow River delta and the AYD.

In the last decades, geographic features of the AYD were studied using geochronological data, as well as drilling, seismic, stratigraphic, sedimentological and geochemical surveys (e.g. Liu et al., 2012, 2013; Wang et al., 2012). The obtained understandings of the scope and size of the delta are controversial (Xia et al., 2015). There are dozens of viewpoints with respect to the spatial distribution of the subaerial delta and the subaqueous delta. The detailed controversial estimations of the subaerial delta in terms of alongshore length and size are shown in Table 5.1 and Figure 5.3a, and those of the subaqueous delta are shown in Table 5.2 and Figure 5.3b. Note, that the literature on the distribution of subaerial delta did not document the detailed distribution boundary, but only highlighted the northernmost and southernmost boundaries.

Figure 5.3 shows that, for both the subaerial and subaqueous delta, the uncertainty concerning the location of the northern boundary is relatively small. The major controversies concentrate on the determination of the southern and the eastern boundaries of the delta. Estimations for the southern boundary of the delta vary from 33°50'N (Sheyang Estuary) to 32°35'N (near Yangkou), with more than 144 km difference (Figure 5.3a, b). Besides, the estimated eastern boundary of the subaqueous delta ranges from 121°E to almost 123°E, with more than 180 km difference (Figure 5.3b). Uncertainty of the southern and eastern boundaries may be due to the limitation of sufficient surveys. The existing surveys mainly focused on the region near the river mouth, rather than covering the total estimated scope (e.g. Yuan and Chen, 1984; Liu et al., 2013). Moreover, the estimated shape of the subaqueous delta is quite different (Figure 5.3b), including a symmetric fan shape (e.g. ⑫), an asymmetric fan shape (e.g. ②), a lateral elongate

Table 5.1: Estimations of the size of subaerial delta of the AYD developed between 1128 – 1855 AD.

No.	Length (km)	Area (km ²)	Reference
i	260	7100	Cheng and Xue (1997); Xue et al. (2003); Huang et al. (2005); Liu et al. (2013)
ii	173	12760	Wang (1998)
iii	240	16000	Ye (1986); Gao et al. (1989); Li (1991)
iv	120	7160 ⁺ ; 4500	Zhang (1984); Ren et al. (1994) ⁺
v	218	7000	Yuan and Chen (1984)
vi	117	-	Wan (1989)
vii	100	7000	Chen et al. (1993)

The number of these viewpoints is according to the geographical position of the announced northern and southern boundaries (see Figure 5.3a).

asymmetric shape (e.g. ⑩) and a longitudinal elongate asymmetric shape (e.g. ⑨). Up to now, the accuracy and consistency of the scope and size of the AYD obtained by the geological approaches is considered as quite poor (Liu et al., 2013).

5.2.3. MORPHODYNAMIC MODELING

MODEL DESCRIPTION

A long-term process-based 2DH morphological model using Delft3D software is set up to simulate the dynamic progradation process of delta and to reconstruct the AYD. Different from the geological point of view, the interest of the process-based morphodynamics model is the coupling of physical processes including the hydrodynamics, the sediment transport and the bed morphology.

Delft3D solves the unsteady shallow-water equations in two/three dimensions. Sediment transport and morphological changes are computed simultaneously with the flow. It can simulate hydrodynamic and morphological changes at timescales from seconds to thousands of years by using a representative hydrodynamic setting and a morphological acceleration factor (De Vriend et al., 1993; Roelvink, 2006; Dastgheib et al., 2008). Validation of the basic sediment transport and morphology updating model were reported in Lesser et al. (2004) and Ranasinghe et al. (2011). Delft3D has been successfully applied in a range of fluvial and coastal environments to study the nearshore morphology, such as evolution of rivers and deltas (e.g. Edmonds and Slingerland, 2009; Caldwell and Edmonds, 2014). Besides, it has been applied to model high sediment concentrations in the modern Yellow River (van Maren et al., 2009). We implement this process-based model with reduced complexity, attempting to gain insight into the progradation of the AYD.

- (1) Hindcasting time frame

Table 5.2: Estimations of the size of subaqueous delta of the AYD developed between 1128 – 1855 AD.

No.	Eastern boundary or width (km)	Northern boundary	Southern boundary	Area (km ²)	Reference
①	122°50'E; 220 km 50 m isobath;	34°45'N	32°35'N	46000	Yuan and Chen (1984)
②	122°30'E; 30 (40) m isobath	34°50'N	33°05'N	26000 [#]	Xu (2005)
③	121°42'E; 160 km	34°45'N	32°42'N	22000 [#]	Liu et al. (2013)
④	96 km; 25 (40) m isobath	34°32'N	32°39'N	21000	Huang et al. (2005)
⑤	30 (40) m isobath	34°32'N	33°33'N	19000 [#]	Gao et al. (1989); Li (1991)
⑥	122°E; 20 (30) m isobath	34°32'N	33°50'N	-	Yu et al. (1986)
⑦	25 m isobath; 90~160 km	34°32'N	33°41'N	-	Xia et al. (2015)
⑧	25 m isobath	34°45'N	33°33'N	18000 [#]	Ren and Shi (1986); Ren et al. (1994)
⑨	20 m isobath	34°40'N	32°39'N	9000 [#]	Cheng and Xue (1997)
⑩	121°38'E; 120 km	34°32'N	33°50'N	7600	Yang (1985)
⑪	17 m isobath; 72 km	34°32'N	33°50'N	6000	Wan (1989)
⑫	15m isobath; 25~100 km	34°36'N	33°33'N	>6000 [#]	Ye (1986)

The isobath refers to the bathymetry at present. [#]: the area could not be obtained from the corresponding reference but estimated by Xia et al. (2015) by means of ArcGIS.

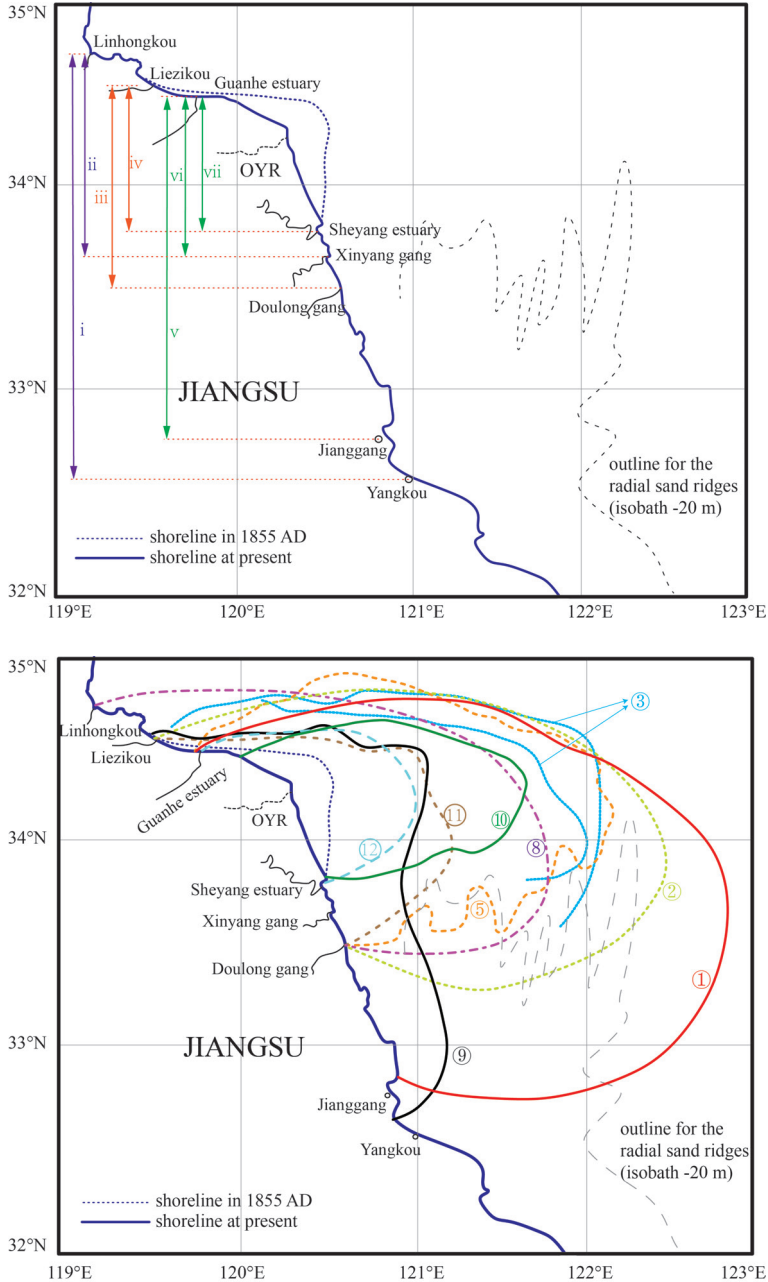


Figure 5.3: Overview of viewpoints on the spatial distribution of (upper) the subaerial delta and (lower) the subaqueous delta (modified after Liu et al., 2013 and Xia et al., 2015). The numbers in panels are consistent with those in Table 5.1 and Table 5.2, respectively.

Due to the significant anthropogenic influences on the OYR, the selection of the hindcasting time frame should be made with caution to match the distinct historical phases. For example, during the period before 1578 AD, the progradation rate of the delta is relatively small because of the frequently shifted river course (Li, 1991). The river course was less active after 1578 AD because of the river training project, resulting in a rapid progradation of the delta (Zhou et al., 2014). Therefore, the period between 1578 - 1855 AD is selected as the hindcasting period.

(2) Model domain and grids

The model domain covers the western part of the SYS, located between the Shandong Peninsula and the Yangtze River Estuary (Figure 5.4a). Note that, considering the geological estimation of the possible distribution of the AYD (Figure 5.3), a large-scale domain is required for simulating a large-scale delta. To be consistent with the simulating time frame, the reference Jiangsu shoreline of 1578 AD is taken as the western land boundary. The east and south boundaries are set as open boundaries (Figure 5.4a). To enhance the computational efficiency for a morphological simulation covering almost 300 years over a large-scale domain, and to highlight the simulation accuracy around the river mouth, the model is decomposed into three sub-domains (see 'Domain Decomposition Technique' in Deltares, 2012 for more detail) (Figure 5.4a). Domain decomposition is efficient to nest models with different scales of grid (Smith et al., 2004) and its feasibility for morphological simulation has been demonstrated by previous studies (e.g. Luijendijk et al., 2004; Yossef et al., 2008; Ruggiero et al., 2009; Nguyen et al., 2010). In each sub-domain, curvilinear grids are created under spherical coordinates (Figure 5.4b). The grid resolution varies from 279 m to 3190 m, with adequate spatial resolution in the vicinity of the river mouth.

(3) Initial bathymetry

Due to lack of historical data, the initial bathymetry for the model is constructed schematically based on the mean water depth at present in the SYS (~45 m), taking into account the estimated total sediment volume carried by the OYR into the SYS since 1578 AD (e.g. Li, 1991; Zhang et al., 2014) and the mean sea level rise (~2 mm/year; State Oceanic Administration, 2003). Furthermore, the nearshore bathymetries are optimized by analyzing several published sedimentary data (e.g. Ye, 1986; Li, 1991; Yang et al., 2002). The bathymetry around the radial sand ridges is determined with a consideration that the distributary channels of the ancient Yangtze (Changjiang) River underlay the southern part of sand ridges (Wang et al., 2012). The overall configuration of the initial bathymetry is shown in Figure 5.6a. The bed slope of the SYS near the river mouth is set as -0.175‰ (Figure 5.4c), according to a schematized 2D numerical model about

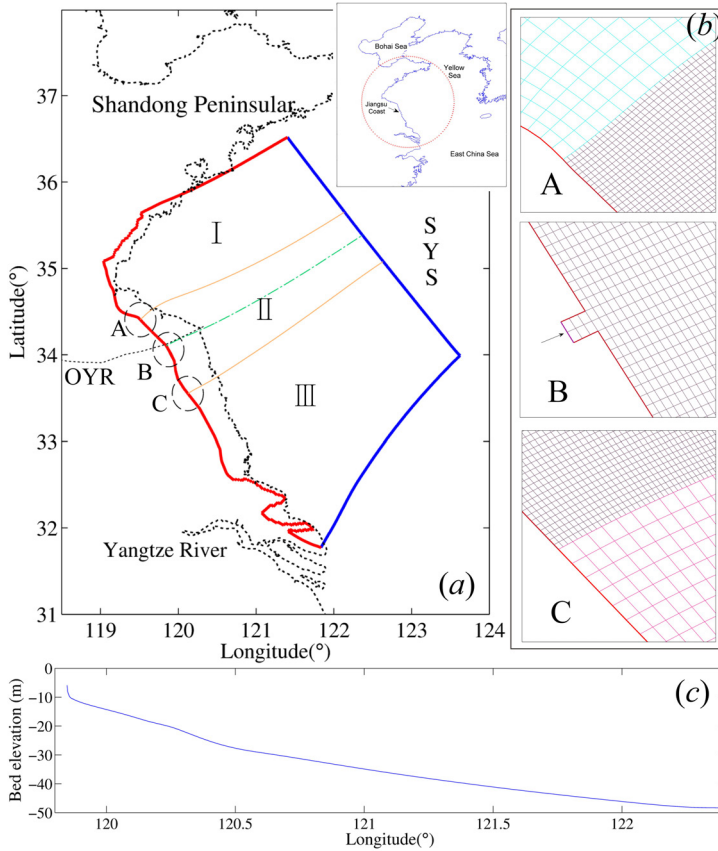


Figure 5.4: Domain and grid of the morphological model. (a) Configuration of land boundaries (red lines) and open boundaries (blue lines). The land boundary near the Jiangsu Coast is the reference shoreline of 1578 AD (modified after Gao, 2009). Black dotted lines denote the shoreline at present. Three sub-domains divided by the orange lines are named as I, II and III. (b) Enlarged grids of the adjacent sub-domains at regions A and C (different sub-domains use different colors), with enlarged figure for the river boundary (B). The grid of the sub-domain II has a relatively higher resolution ($\sim 279 \text{ m} \times 375 \text{ m}$). (c) Longitudinal profile of the initial bathymetry near the river mouth (green lines in panel (a)).

the Jiangsu coast (i.e. 0.16‰~0.46‰; Zhu and Chang, 2001). The hydraulic roughness is considered through a constant Manning coefficient with a value of 0.016, based on modelling experiences in the SYS (Su et al., 2015). The time step of the flow computation is 60 s for reasons of accuracy and stability.

(4) Hydrodynamics

Local hydrodynamics, such as tides, waves and alongshore currents are responsible for the delta morphology and nearshore bathymetry development (Orton and Reading, 1993; Liu et al., 2013). However, no measurements are available during the period of 1578 – 1855 AD (Syvitski and Saito, 2007). Tides are the most dominant factor for the study area among marine dynamics, particularly the M2 constituent (Zhu and Chang, 2000). Besides, the tidal force is demonstrated to be stable in the past thousands of years (Zhu, 1998; Uehara et al., 2002; Wang et al., 2012), compared with other uncertain hydrodynamic forces (e.g. wave and wind). Thus, tide is considered as the only hydrodynamic force in the model on which to concentrate to investigate the effect of other uncertain model settings (e.g. initial bathymetry, the amount of sediment supply) on the progradation of the AYD. The M2 tidal constituent, the primary tidal component in the SYS, is prescribed along the open boundaries. The phases and amplitudes of the M2 tide constituent are extracted from a well calibrated present-day tidal wave model, which covers the Bohai Sea, the Yellow Sea and the East China Sea (Su et al., 2015).

With respect to the river boundary, only the data of the modern Yellow River can provide some inspiration for the determination of river discharge of the OYR. The multi-year averaged discharge of the modern Yellow River is 1630 m³/s. Floods frequently occurred in the historical time period (Chen et al., 2015) and floods lead to high concentrated flow (Wang and Xu, 1999; Li et al., 2014). We admit that the process of river discharge is a non-linear process (e.g. flood). However, to enhance the computational efficiency of long-term morphological changes, we set the feeding river discharge of the OYR in the model a constant value and ignore the increased water and sediment discharge during floods. According to a series of preliminary calibrations (not shown here), we set the water discharge in the model as 2550 m³/s.

(5) Sediment transport

It was reported that almost 4/5 of the Jiangsu Coast was sandy before the OYR flowing into the SYS (Xue et al., 2011). Thus, the bottom sediment of the SYS is set as sand, with a uniform grain size of 200 μm ignoring spatial variation. The multi-year averaged median grain size of the modern Yellow River is 19 μm (Chinese Ministry of Water Resources, 2011). Gao et al. (1989) and Chen et al. (2015) recommended that the median grain size for historical periods was slightly smaller (~15 μm). Therefore, the size of the sediment

carried by the OYR is set as 15 μm in the model, with a settling velocity of 0.2 mm/s.

Non-cohesive sediment transport is calculated following Van Rijn (1993) formulations. Cohesive sediment transport is calculated following Partheniades-Krone formulations (Partheniades, 1965):

$$E = M \left(\frac{\tau_b - \tau_{cr,E}}{\tau_{cr,E}} \right), \quad \tau_b > \tau_{cr,E} \quad (5.1)$$

$$D = \omega_s c \left(\frac{\tau_{cr,D} - \tau_b}{\tau_{cr,D}} \right), \quad \tau_b < \tau_{cr,D} \quad (5.2)$$

in which, E and D are erosion/deposition fluxes ($\text{kg}/\text{m}^2\text{s}$); M is an erosion parameter ($\text{kg}/\text{m}^2\text{s}$); τ_b is the maximum bed shear stress (N/m^2); $\tau_{cr,E}$ and $\tau_{cr,D}$ are the critical erosion/deposition shear stress (N/m^2) (When $\tau_b < \tau_{cr,E}$, $E = 0$; when $\tau_b > \tau_{cr,D}$, $D = 0$); c is the sediment concentration (kg/m^3). Hindered settling effects are considered in the model with the Richardson-Zaki equations as $\omega_s = \omega_0(1 - \phi)^n$, in which ω_0 is the particle settling velocity in clear water and ω_s is the particle fall velocity under the volumetric sediment concentration ϕ . More details can be found in Delft3D manual and van Maren et al. (2009). The simulated sediment fluxes as well as the local bed morphology depend on the relationship between deposition (D) and erosion (E), which further depend on $\tau_{cr,E}$, $\tau_{cr,D}$, c and M . The existence $\tau_{cr,D}$ of is debated (Edmonds and Slingerland, 2009): sedimentation can occur simultaneously with erosion (Winterwerp, 2006), or not (Maa et al., 2008). Van Maren et al. (2009) argued that sedimentation never happens for hyperconcentrated flow (over 200 kg/m^3). Besides, he recommended that it is comparable to either use a smaller $\tau_{cr,D}$ or use a larger M . Thus, with a consideration of the depth-averaged sediment concentration of the OYR considered in the model (i.e. not the hyperconcentrated flow), we choose to tune parameter to make the simulations realistic. In this study, $\tau_{cr,E}$ and $\tau_{cr,D}$ are set to be 0.5 N/m^2 and 1000 N/m^2 , indicating sedimentation occurs constantly. The erosion parameter M is set as 0.01 $\text{kg}/\text{m}^2\text{s}$. Additional experiments (not shown here) demonstrated that, if smaller erosion parameters were applied to the model, severe sedimentation would occur along the river channel, resulting in a filled-up, and even, blocked channel. When larger erosion parameters were assigned, the progradation ratio of the AYD was decreased. And, eventually the simulations would not catch the protuberance feature near the river mouth, which is inconsistent with the records in the literature (e.g. Zhang, 1984; Ye, 1986; Liu et al., 2013).

The sediment supply at the upstream river boundary is determined according to the annual sediment load transported into the SYS by the OYR. It has been predicted by several previous studies, whereas the estimations varied greatly. For instance, the expected

annual sediment amount was 2×10^8 t/y by Zhang et al. (2014), $2.5\text{--}3.9 \times 10^8$ t/y by Li (1991), 5×10^8 t/y by Huang et al. (2005) and 6×10^8 t/y by Ren (2006). In this study, the sediment concentration is set as 3 kg/m^3 , yielding an annual averaged sediment load of 2.4×10^8 t/y. The sand fluxes are given by a Neumann boundary condition (i.e. zero concentration gradient) at the offshore inflow open boundaries. Thus, the bed level at the open boundaries is constant.

A spin-up period of 720 minutes without morphological updating allows the flow to stabilize. An acceleration factor of 108 is used, by which the morphological change in every time step is multiplied (Roelvink, 2006), aiming to accelerate the evolution appropriately and to make the long-term simulation more efficient (Dissanayake et al., 2009). Drying and flooding processes are defined by a threshold depth of 0.1 m in this study.

5

SPECIFICATION OF MODEL SCENARIOS

TO determine the reasonability of the uncertainties, a series of scenarios is designed. The simulation presented in section 5.2.3.1 is taken as a reference run. Various scenarios are designed based on the reference run, with a consideration of one uncertain parameter in each scenario while holding other parameters constant.

Bathymetric data, sediment discharge and river discharge were reported to determine the progradation ratio of a deltaic system (Wright and Coleman, 1973; Orton and Reading, 1993; Gelfenbaum et al., 2009; Kleinhans et al., 2010). Specifically, with respect to the modern Yellow River Delta, the ratio between sediment concentration (c) and water discharge (q) was proposed to be important (Li et al., 2001; Hu and Cao, 2003). However, these parameters of importance are all uncertain for simulating the progradation of the AYD. The uncertainty of the initial bathymetry is discussed through varying initial bed slopes, with $\pm 10\%$ deviations of the slope in the reference run (case BL and BH in Table 5.3). The possibility of other estimated volumes of sediment supply (mentioned in section 5.2.3.1) is applied to evaluate the influence of sediment availability (case SL and SH in Table 5.3). Through varying the water discharge and sediment concentration while keeping the total sediment supply the same, a relatively larger c/q (i.e. ~ 1.5 times larger) is applied to the case WS. The water discharge (q) in the case WS equals the multi-year averaged discharge of the modern Yellow River (i.e. $1630 \text{ m}^3/\text{s}$).

In the reference run, the temporally varying sediment discharge from the river is simplified into a constant during the 277 years simulation. It is worthwhile to assess whether a significant change of final morphologies can be caused by this simplification (case VV in Table 5.3). Besides, although tide conditions are not taken uncertain in this study, different distribution features of the modern Yellow River delta (local M2 tide amplitude is

Table 5.3: Applied sensitivity parameters for different scenarios.

Parameter	Reference	Scenarios	
Initial bed slope	0.175‰	0.157‰ (BL)	0.192‰ (BH)
Sediment availability	2.4×10^8 t/y	0.8×10^8 t/y (SL)	4×10^8 t/y (SH)
c/q ratio	3/2550	4.8/1600 (WS)	
Annual variation of sediment load	no	yes (VV) ⁺	
Tidal amplitude*	T	T×0.5 (WL)	T×2 (WH)

The names of scenarios are listed in parentheses, following the assigned value of uncertainties. ⁺In case VV, the sediment load changes temporally from 2 to 6 kg/m³ and the variation of sediment concentration is corresponding to the temporal variations of shoreline extension rates illustrated in Ye (1986) and Zhang et al. (2014). *“T” denotes the prescribed tidal amplitude in the reference run; the tidal amplitude prescribed along the open boundaries in case WL and WH is half and twice of that in the reference run, respectively.

0.2~0.4 m) and the AYD (local M2 tide amplitude is 0.6~1 m) inspired us to discuss the contribution of the tidal regime on the evolution of a fine-sediment delta (case WL and WH in Table 5.3).

5.3. MODEL RESULTS

5.3.1. MODEL RESULTS FOR THE AYD

HYDRODYNAMICS ALONG THE JIANGSU COAST

THE simulated co-tidal chart and tidal current ellipses corresponding to the initial bathymetry (reference run) are shown in Figure 5.5. In comparison with the Marine Atlas of the Bohai Sea, the Yellow Sea, and the East China Sea (Atlas of the Oceans Editorial Board, 1993), the tidal wave propagation of the M2 constituent is similar to the present situation, as Uehara et al. (2002) argued. For instance, an amphidromic point out of the OYR river mouth and a converged tidal wave near the radial sand ridges area are both well modelled (Figure 5.5a). The tidal ellipses of the Jiangsu Coast indicate two remarkable tidal current patterns: a rectilinear current along the northern Jiangsu Coast (especially near the OYR) and a radial current pattern surrounding the southern Jiangsu Coast (Figure 5.5b). Besides, the local tidal currents are relatively strong, exceeding 1 m/s for both remarkable patterns. Rotating tidal currents can be found at the northernmost and southernmost of the Jiangsu Coast. However, the direction of rotation is counter-clockwise in the northern part while clockwise in the southern part. The tidal current strength at these two parts also varies. The tidal current magnitude of the southern rotating current is much (about three times) larger than the northern one (Figure 5.5b).

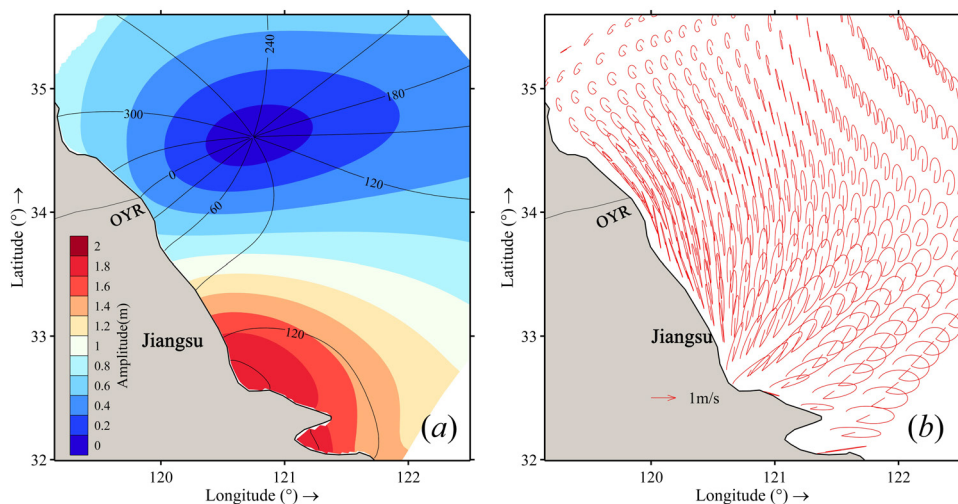


Figure 5.5: The simulated co-tidal chart (a) and tidal ellipses (b) of the M2 constituent near the Jiangsu Coast.

5

MORPHOLOGICAL EVOLUTION

COHESIVENESS of sediment is demonstrated to be a controller with respect to the pattern of deltas (Edmonds and Slingerland, 2009). Under river discharge only and without marine hydrodynamics, the delta changes from a fan-shape to a bird's-foot shape with the increase of cohesiveness (Edmonds and Slingerland, 2009). The local hydrodynamics, especially along the Jiangsu Coast, are recognized to be energetic (Figure 5.5). Thus, the evolution of AYD, formed by fine-grained sediment under energetic tidal currents, is suggested to be different from the results of Edmonds and Slingerland (2009). A recognized hypothesis on the evolution trend of the AYD has been proposed by Zhang (1984), who suggested that delta progradation was through the migration of nearshore shoals gradually towards the mainland. This hypothesis is hard to be validated through geological observations, whereas a process-based morphological model is capable to elaborately describe the temporal evolution process of the delta and to examine the hypothesis.

Figure 5.6 shows the simulated temporal morphological evolution of the AYD. A remarkable feature is the large area of sedimentation along the Jiangsu Coast, with a protuberance near the river mouth. To clearly describe the delta progradation process, the delta is divided into southern and northern sections, according to the geographic position relative to the extension direction of the river channel. After 50 years in the simulation, a fluvial delta has emerged around the river mouth (Figure 5.6b). It indicates that the delta is characterized by an asymmetric distribution in the north and south direc-

tion, with the southern delta much more developed. During the next 50 years, both the northern and southern deltas expand gradually towards the sea (Figure 5.6c). Along the Jiangsu Coast, the protuberance at the river mouth is extraordinarily obvious, which indicates a faster progradation rate near the river mouth than along the adjacent regions. Besides, several patterns of shoals occur near the river mouth. With continuous sediment input, the nearshore shoals, located both north and south of the delta, gradually grow and build up in the following 50 years (Figure 5.6d). Afterward, these developed shoals start to merge with the main delta, leading to the expansion of the subaerial delta (Figure 5.6e). At the same time, the tidal channels located inside the delta are eroding. In the following decades until 1855 AD (Figure 5.6f), offshore shoals outside the northern delta are under strong development and gradually build up outside the river mouth. Simultaneously, the southern part of the delta continues to migrate seaward, and large shoals are in development.

Through the analysis of the temporal evolution of the AYD, the progradation mechanisms for the northern delta and the southern delta are indicated to be different. For the southern delta, the growth is mainly through the merging of the nearshore shoals, as suggested by Zhang (1984). The shoals grow with continuous sediment supply, resulting in narrowing channels. Consequently, it exhibits the phenomena for the southern coastline to gradually prograde seaward. Simultaneously, new shoals are formed, and the fate of new shoals is similar as long as the sediment supply is continuous. However, the evolution of the northern delta is the result of the growth of several independent shoals, which grow separately and have no trend to merge together (Figure 5.6). The channels among the shoals separate the shoals into individual features. The empirical hypothesis suggested by Zhang (1984) captures the evolution mechanism of the southern delta, however, it is hard to comprehensively represent the formation mechanism of the northern delta.

TIDE RESIDUAL SEDIMENT TRANSPORT

DUE to the rapid progradation of the AYD, the overall sediment transport pattern may vary throughout the whole period of the morphological evolution. In this section, two time points during the evolution period are taken as an example to investigate the temporal changes of sediment transport. Figure 5.7 shows the tide residual sediment transport patterns after a 100 years and a 200 years simulation, respectively. After a 100 years simulation, large volumes of sediment are mainly concentrated outside the southern delta, with a relatively small portion outside the northern delta (Figure 5.7a). For the southern part, the main transport direction of residual sediment transport

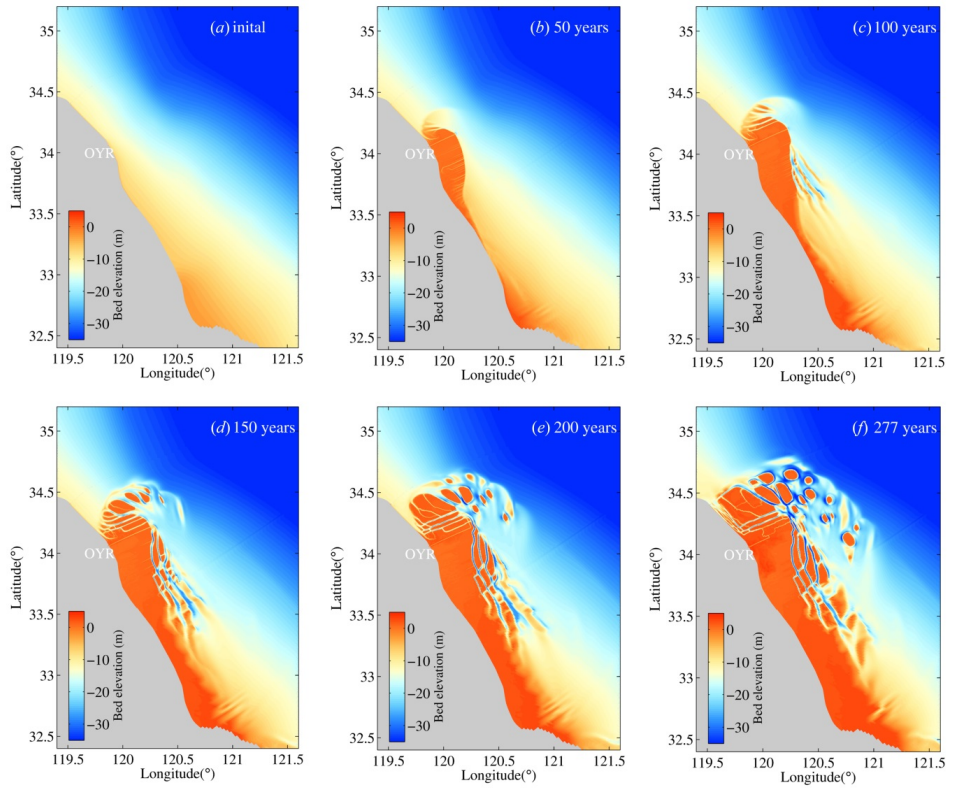


Figure 5.6: Temporal evolution of the AYD. (a) ~ (f) show the initial morphology (1578 AD) and the morphological evolution after 50y, 100y, 150y, 200y and 277y (1855 AD), respectively.

is southward along the shoreline. Specifically, a portion of residual sediment around the southernmost region of a newly generated subaerial delta is transported landward, resulting in significant sedimentation and rapid expansion of the southern delta. Different features are shown for the northern part, where the active sediment region is rather small compared to the southern part (Figure 5.7a). Besides, the tide residual sediment transport is first northward, along the shoreline, and then turns landward, forming a counter-clockwise circulation. The different features of sediment transport at the northern and southern parts can explain the different patterns of the northern and southern delta (Figure 5.6c). On the other hand, the residual sediment transport can get feedback from morphological changes (e.g. submerged shoals), which can be recognized by the complicated transport directions in the yellow rectangular region in Figure 5.7a.

The distribution patterns of the tide residual sediment transport in the southern and northern directions after a 200 years simulation do not show the asymmetric feature as 100 years earlier (Figure 5.7b). Both the magnitude and the distribution extension near the northern part have a significant increase. The extension of the northern part is mostly seaward, although the counter-clockwise sediment transport circulation still points towards land and prevents the sediment transporting northward. The counter-clockwise transport, on the other hand, favors the formation and growth of offshore shoals (Figure 5.6e, f). The sediment transport direction near the southern delta is not landward as 100 years earlier, but at a certain angle. Thus, instead of a rapid seaward expansion, the southern delta keeps progradation seaward and southward with a moderate speed.

The most active region for the tide residual sediment along the Jiangsu Coast is represented as an 'L' type pattern after a 100 years simulation (Figure 5.7a). That is to say, the width of distribution scope of tide residual sediment activity has a considerable increase at the southernmost region. However, an opposite pattern appears after a 200 years simulation (Figure 5.7b), which turns out to be a 'T' pattern. The widest region of high activity level changes to the northernmost region. This indicates that the shoals located at the northern part are at a rapidly growing stage. The conversion of the distribution pattern implies that the progradation emphasis of the deltaic system changes from significant expansion of the southern delta to development of shoals in the northern delta.

DISTRIBUTION OF SEDIMENTATION (OYR-DERIVED SEDIMENT)

IT is important to gain an understanding of the morphological influence extension of the OYR-derived sediment before the abruptly stop of sediment supply (i.e. before

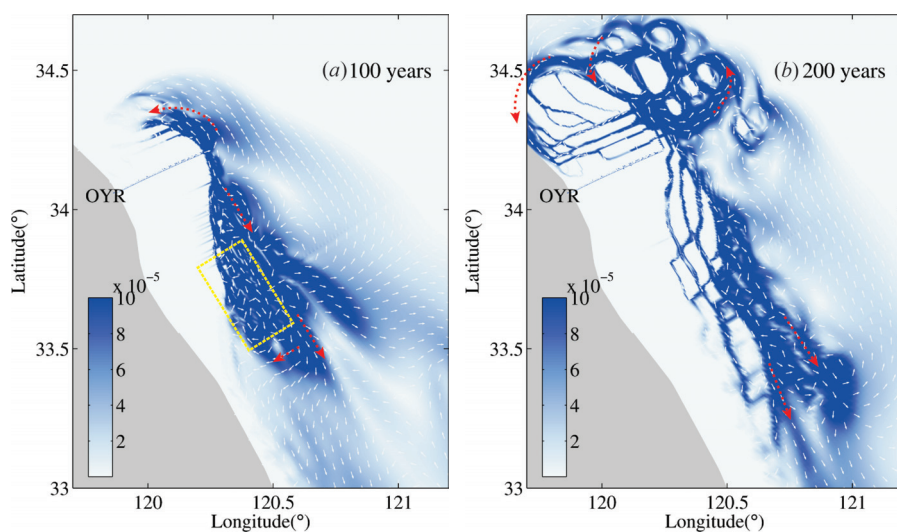


Figure 5.7: Tide residual sediment transport along the AYD after a 100 years (a) and a 200 years (b) simulation. The magnitude is in the unit of m^3/sm . The direction is shown by white arrows. The transport directions of large magnitude regions are highlighted by red arrows.

5

1855 AD), as the extension of sedimentation provides a crucial and fundamental information for the erosion stage of the AYD (after 1855 AD). However, field data obtained by geological methods, such as drill cores, are insufficient to give a comprehensive insight. Note that, due to the continuous severe erosion of the delta after 1855 AD, the distribution of sedimentation (especially derived by the OYR) has undergone significant changes. It is impossible for geological results to reconstruct the scene before erosion happened. Ren et al. (1994) estimated that the distributed area of the OYR-derived sediment ranged from Lianyungang in the north to nearly Yangkou in the south, larger than the scope of the subaqueous delta. However, there is no direct or proper evidence to support this statement.

Figure 5.8 shows the deposited thickness distribution of the OYR-derived sediment after the 277 years simulation (for 1855 AD). In this study, a deposition thickness larger than 10 cm is taken as a criterion to discriminate the influence scope of the sediment derived by the OYR (Figure 5.8). Similarly to the distribution of the delta, the distribution of sedimentation is characterized by asymmetry. Most of the sediment is deposited in zone I, accounting for ~63% of total sediment volume and the maximum deposition thickness exceeds 30 m. The averaged deposition thickness for zone II and III is about 1.4 m and 0.5 m, respectively. The sedimentation reaches as far as ~230 km south of the river mouth, and ~76 km north of the river mouth. The seaward boundary is mostly

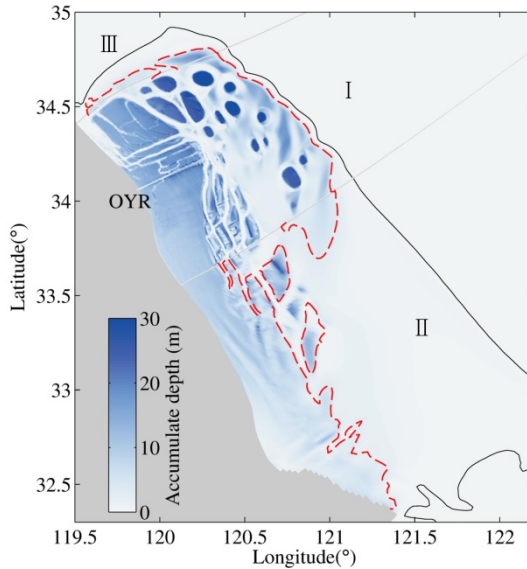


Figure 5.8: Map showing the simulated deposition distribution of OYR-derived sediment. Zone I, II and III are divided according to the relative position with the OYR (separated by lateral light gray lines). Black lines denote the range in which the sediment carried by the OYR can influence the local morphology according to the discriminate criterion of accumulate deposition thickness > 10 cm. The outline of accumulate deposition thickness > 3 m is represented by the red dotted lines.

parallel with the land boundary, ~63 km away from the river mouth.

The thickness of subaqueous part of the AYD was investigated to be less than 3 m (Li, 1991). An accumulated deposition depth of 3 m is also shown in Figure 5.8, denoting a ‘quasi-subaqueous’ delta. Through comparison between the boundaries of the 3 m-deposition region and the 10 cm-deposition region, considerable deviations occur at the southern SYS. This implies that the influence of OYR-derived sediment on the evolution of radial sand ridges field is not significant during the propagation of the AYD before 1855 AD. The main effort of the OYR-derived sediment focuses on the progradation of the deltaic system.

5.3.2. CONTRIBUTION OF UNCERTAINTY TO DELTA EVOLUTION

PATTERN OF DELTAIC SYSTEM

FIGURE 5.9 shows the sensitivity of uncertainties on the morphological evolution of the delta. The qualitative comparison of the AYD’s distribution pattern between the scenarios and the reference run (Figure 5.9a) is discussed in this section.

The effect of the bed slope of the initial bathymetry is assessed by case BL and BH (Figure 5.9b, c). Compared with the reference run, the relative location of the subaqueous delta to the subaerial delta is significantly changed. In the reference run, the subaqueous delta is distributed surrounding the subaerial delta. However, it changes to the northeast of the subaerial delta when the initial bathymetry becomes gentler. When the initial slope is steeper, the subaqueous delta is located in the deeper water off the east edge of the subaerial delta. Besides, the development and the location of shoals are greatly influenced by the initial bed slope, according to the comparisons of the deposition thickness of the sediment (Figure 5.10). The comparisons indicate that a gentler slope promotes the generation of more merged shoals nearshore. The response of the deltaic system may be due to the fact that a gentle topography is favorable to attract sediment deposition nearshore, while a steep slope tends to transport the sediment across-shelf. Thus, the evolution of the subaerial delta and the growth of shoals are accelerated by a gentle slope, while decelerated by a steep slope.

5

The effect of sediment supply on the evolution of the deltaic system can be revealed through a comparison between the reference run (Figure 5.9a) and the cases SL (Figure 5.9e) and SH (Figure 5.9f) for low and high supply, respectively. A significant influence is found on the evolution level of the subaerial delta and the subaqueous delta. An extremely wide deltaic system evolves in case SH, whereas the width is greatly decreased in case SL, although the northern and southern extension of the deltaic system is similar in these cases. The front of the southern subaerial delta is composed of a series of parallel nearshore shoals in case SL, while they are integrated as a part in case SH. It illustrates that an abundant sediment supply is beneficial for the rapid progradation of the delta, through acceleration of the merging of nearshore shoals with the mainland. The results show good agreement with the viewpoint that sediment supply can affect the progradation ratio and position of deltas (Zhang et al., 2014). Besides, the comparisons show that an abundant sediment supply also favors the growth of offshore shoals, as the amount of offshore shoals increases with the increase of sediment supply.

Once the amount of sediment, feeding the deltaic system, is kept constant, deviations, such as c/q ratio (Figure 5.9d) and temporal variation of sediment concentration c (Figure 5.9g), do not lead to obvious influences on the distribution and development of the deltaic system. Influences are limited to the evolution of offshore shoals. Thus, the importance of the variability of water discharge and temporally sediment concentration are relatively minor, in comparison with the effect of the total sediment availability.

With respect to the effect of tidal hydrodynamics, distinct variations of the pattern of the delta can be observed (Figure 5.9h, i). The shape of the simulated AYD in case WL

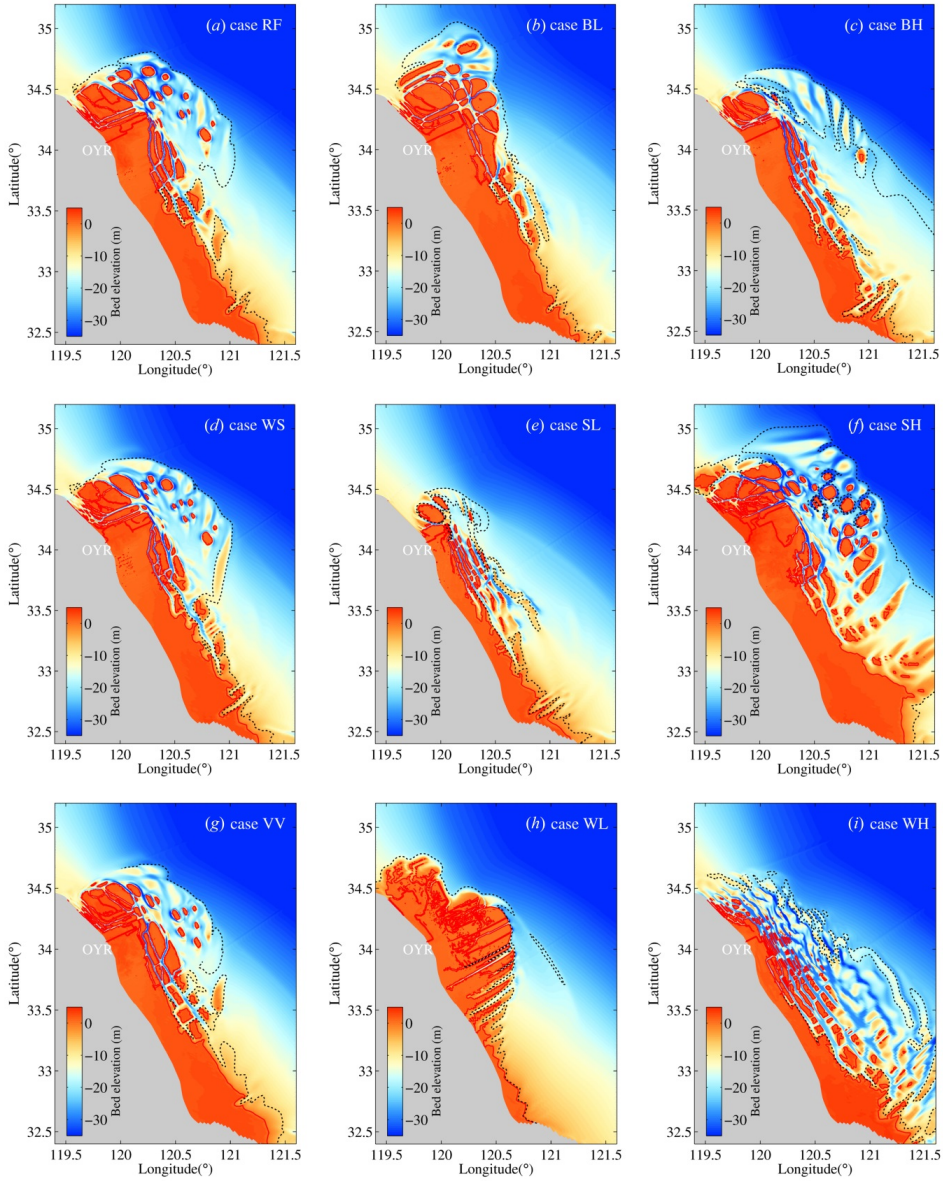


Figure 5.9: Sensitivity analysis results of the pattern of the delta under different scenarios after a 277 years simulation. Figure (a) ~ (i) represent the results of the reference run and other cases. The name of the scenario is listed. Subaerial and quasi-subaqueous portion is bounded by red lines and dotted black lines, respectively. The criterion for determine subaerial and subaqueous is by 0 m isobath and 3 m deposition thickness, respectively.

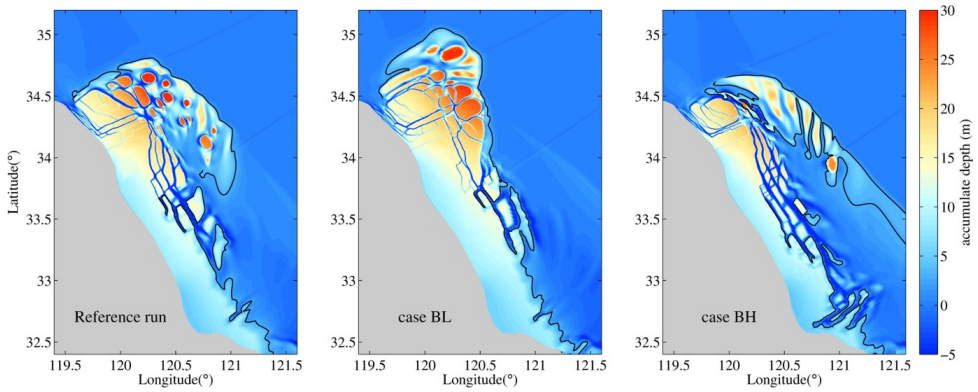


Figure 5.10: Sensitivity analysis results of the accumulated thickness of sediment under different scenarios after a 277 years simulation. The name of the scenario is listed. Quasi-subaqueous portion is bounded by black lines, representing 3 m deposition thickness.

5

is similar to that of the modern Yellow River delta (with two main branches and shown as a bird-foot shape). However, the deltaic system has an extremely elongate shape in case WH with a large number of parallel shoals. This may be due to a different sediment-carrying capacity associated with a different strength of hydrodynamics. If the tide is strengthened, the sediment derived by the OYR is transported by the alongshore tidal current (case WH), rather than deposited around the river mouth (case WL). Besides, the different shape of the deltaic system indicates that the dominant hydrodynamic forces are different in these cases, thus the relative strength ratio between the tidal regime and the fluvial is responsible for the classification of delta. Features of a fluvial-dominated delta and a tide-dominated delta are shown in case WL and WH, respectively. Thus, the special elongate-shape subaerial delta and the huge area of the subaqueous delta of the AYD are determined by the moderate energetic tidal regime.

SIZE OF DELTAIC SYSTEM

IN this section, quantitative analyses on the feedback of produced morphologies of delta by uncertain factors (e.g. sediment discharge) are carried out. Based on our study results (i.e. Figure 5.9), tide is the predominant factor governing the overall pattern of a fine sediment deltaic system. On the other hand, previous studies have stated that the tidal regime near the Jiangsu coast remains stable within thousands of years (e.g. Zhu, 1998; Wang et al., 2012), which means that the tidal forcing in the present morphological modelling is dependable. Thus, only the other six scenarios are compared with the reference run to evaluate the influence.

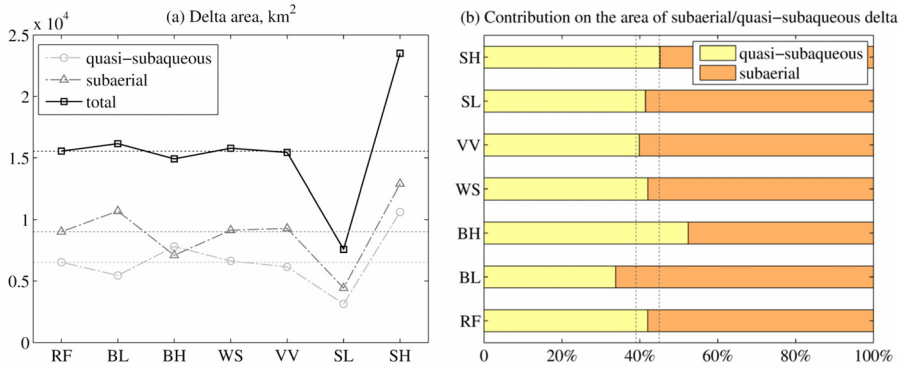


Figure 5.11: (a) Sensitivity analysis results of the area of total delta, subaerial delta and quasi-subaqueous delta after a 277 years simulation of different scenarios. The abbreviations for scenarios listed on the X-axis are similar as in Table 5.3. The dashed lines denote the estimated value of the reference run. (b) The comparison of sediment contribution to the subaerial and quasi-subaqueous delta. The ratios of subaerial and subaqueous delta account for the total delta are shown in different colors. The dashed lines denote deviations of $\pm 3\%$ from the result of the reference run.

The influence of the initial bed slope variability on the overall area of the delta is not obvious (Figure 5.11a, see case BL and BH), whereas it has a significant influence on the relative area ratio between the subaerial and subaqueous delta (Figure 5.11b, see case BL and BH). A relatively gentle slope is beneficial for the progradation of subaerial delta (Figure 5.9b). Thus, the relative area ratio of the subaerial delta increases in case BL. Conversely, a relatively steep slope is beneficial for cross shore sediment transport (Figure 5.9c). Consequently, the relative area ratio of the subaerial delta decreases in case BH. The results generally agree with the standpoint that the mode of accommodation for deposition has a considerable effect on the evolution of a delta (Orton and Reading, 1993), especially the size of the subaerial delta (Kim et al., 2009). Besides, we highlight that mode of accommodation is a critical parameter in determining the relative development of the subaerial or subaqueous portion of a deltaic system, whereas its effect on the size of subaerial delta is secondary compared to the effect of sediment availability.

The changes of the area of the delta in cases SL and SH are considerable in comparison with other considered uncertainties (Figure 5.11a). It indicates that, sediment availability is a key factor governing the size of deltas. However, the relative area ratio of the subaerial and subaqueous portions in the deltaic system in case SL and SH is similar to that in the reference run, with a deviation less than 3% (Figure 5.11b). Thus, we suggest that the status of the relative ratio between the subaerial and subaqueous portions is mainly governed by the marine hydrodynamic conditions and the duration of hydrodynamic action. The influence of the c/q ratio (case WS) on the delta size (on both the

total absolute area and the relative ratio between the subaerial and subaqueous deltas) can be ignored according to our results (Figure 5.11). Another minimal effect on the size of the deltaic system is illustrated to be the temporal variation of sediment concentration (Figure 5.11, see case VV).

In conclusion, the bed slope of the initial bathymetry influences the possible sedimentation areas, and eventually determines the relative distribution and size of the subaerial and the subaqueous delta. The availability of sediment supplied to the delta plays a key role in determining the progradation rate and the size of the whole deltaic system, while it contributes little to the ratio of the subaerial or subaqueous areas. Once the overall amount of sediment supply is constant, variations such as the c/q ratio and the temporal variation of sediment concentration have little influence on the final evolution of AYD. Local marine hydrodynamics play a remarkable role in determining the shape and classification of a deltaic system.

5.4. DISCUSSION

5.4.1. RELIABILITY OF THE REFERENCE RUN

CHEN et al. (2015) suggest that an exploratory modeling cannot be fully verified. However, historical records and maps can offer a reference to explore the degree in which simulations match the historical evolutions. In this study, the simulated 0 m isobath is defined as the shoreline. The simulated shoreline for 1855 AD is quantitatively compared with the reference shorelines collected from the literature (e.g. Zhang, 1984; Gao, 2009). The comparison is shown in Figure 5.12. Despite a series of uncertainties and simplifications of the model parameters, the general shape of the shoreline simulated by the reference run is comparable to the historical data.

In spite of a good agreement between overall shorelines, the protruding pattern of the shoreline for 1855 AD near the river mouth is not well mimicked by the reference run (Figure 5.12). However, the simulated protuberance has a quite good agreement with the shoreline in the 1890s. We suggest that there are mainly two reasons leading to the deviation between simulations and the reference shoreline of 1855 AD. On the one hand, it may be due to the schematizations of model for uncertainty, e.g. the neglect of wave influence and the local detailed geological features around the river mouth. On the other hand, the reference shoreline of 1855 AD may not be as accurate as expected. The historical maps shown in Figure 5.13 were painted by a traditional Chinese cartography

method (Ji li hua fang)¹, which are suggested to be more reliable than the maps shown in the Appendix. It is noteworthy that the curvilinear shoreline near Yangkou is well exhibited in both historical maps (Figure 5.13). However, no protruding feature near the river mouth is exhibited in these two historical maps. Therefore, we suggest that the modelled result with a moderate protuberance around the river mouth might be more reliable.

A feature highlighted in the historical drawings is the dense channel network (Figure 5.13 and Appendix). In comparison with the historical maps, the subaerial delta (bed elevation > 0 m) is also simulated to be a complicated system composed by merged shoals and tidal channels (Figure 5.12). Thus, this feature is well reproduced by the model. Note that, the simulated delta more southern than 33.3°N lacks this feature. It is mainly due to the grid resolution, which is relatively high near the river mouth, while it is low at the farther regions.

Another feature shown in historical maps is the existence of a number of shoals. In the historical map “Qing Empire’s complete map of all under heaven” (Figure 5.13b), a series of shoals is highlighted along the Jiangsu Coast, located between 33°N and 34°N. In our model, the same region outside the mainland comprises of both subaerial and subaqueous portions (Figure 5.6f). Thus, this morphological feature exhibited in the historical maps is also well captured, no matter whether the shoals in the historical map are subaerial or subaqueous shoals. With respect to the pictorial historical maps (See Appendix), although the shape of shoals is drawn to be different, three regions featured with shoals can be summarized as (1) northeast of the OYR’s river mouth, (2) central of the Jiangsu Coast and (3) the southernmost region of the Jiangsu Coast. The model simulations generally reproduce the distribution of the shoals (Figure 5.6f), except for the southernmost region. These not well-modelled shoals may be due to an inappropriate setting of the sediment input through the southern open boundary, which, in reality, may have been discharged by the Yangtze River. In addition, the southernmost shoals are near the boundary of our model, which is out of the scope of our interest.

In conclusion, the simulated AYD in the reference run is comparable with the historical maps, despite uncertainties and schematization in the model. Therefore, the evolution process and the dynamic mechanism of delta, simulated by the reference run, are expected to be reliable.

It is suggested that a process-based morphological model is valuable if the model parameters are in a reasonable range (Van der Wegen et al., 2011). In order to assess the

¹Ji li hua fang: use a series of squares as grids, ignoring the curvature of the earth surface. The scale of the map is according to the length of the square. For example, the scale of figure 5.13b is that each square denotes 50 km×50 km.

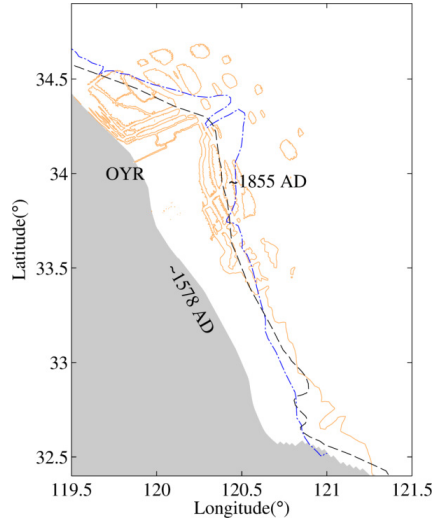


Figure 5.12: Simulated shoreline for 1855 AD in comparison with the reference shorelines. In this study, shoreline is distinguished as 0 m isobath (orange lines). Blue and black lines are reference shorelines for 1855 AD (modified after Zhou et al., 2014) and in the 1890s (modified after Zhang, 1984; Gao, 2009), respectively.

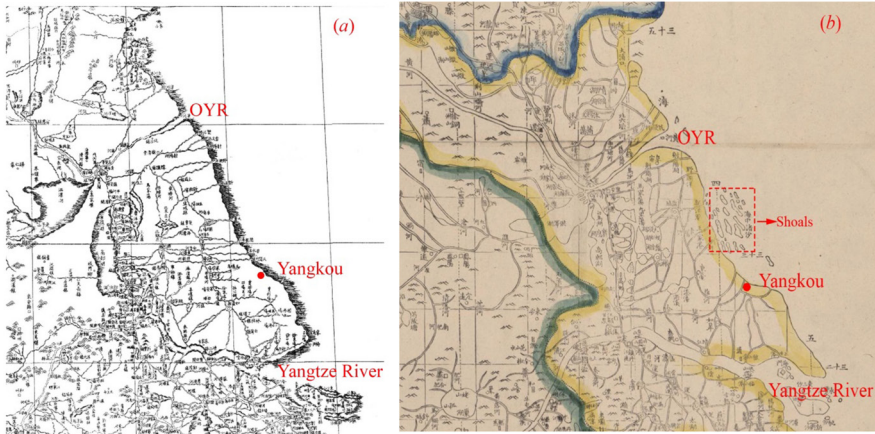


Figure 5.13: (a) Part of the historical map of “Huang yu quan tu”, drawn between 1721-1722 AD. It is the first Chinese national map painted with longitudinal and latitudinal grids, with a scale of 1:400,000. The digital version is available at <http://www.loc.gov/item/2002626779/>. (b) Part of a historical map “Qing Empire’s complete map of all under heaven”, drawn between 1832-1842 AD. The digital version is available at: <http://www.loc.gov/item/gm71005054/>. The shoals drawn in the map were highlighted. Important geographic positions are indicated by: the OYR, Yangkou and the Yangtze River, to distinguish the boundary of the Jiangsu Coast.

reasonability of uncertainty, the results of the scenarios are compared with the historical maps and the results of the existing geological surveys. As the simulated shoreline of the reference run has been verified having a good accordance with the historical maps (Figure 5.12), the large variation of the simulated subaerial delta in the case SL/SH is not realistic. Consequently, the amount of sediment supply in the reference run is considered more reasonable. Furthermore, the detailed OYR-derived sediment and water discharge are hard to be determined, as the influence of c/q ratio and temporal variation of sediment concentration on the morphological evolution of the AYD is small. Nevertheless, we suggest that it is possible to use a representative sediment concentration, similar to the representative tide, to reduce the computational effort of a long-term morphological model to a reasonable level. Besides, a moderate modification of c/q ratio in view of the lack of data is acceptable for generating reliable long-term morphology changes. On the other hand, we have demonstrated that the amount of sediment supply has little influence on the relative ratio of the area between the subaerial and the subaqueous delta in a deltaic system. Thus, the area of the subaqueous delta simulated by the reference run is considered as reliable, based on the reliable simulation of the subaerial delta, when other uncertainties do not change. As to the geological position of the subaqueous delta, the results of the reference run, rather than the case BL and BH (i.e. the effect of the initial bed slope), are in accordance with the geological surveys (Figure 5.3b). Therefore, the setting of the slope of initial bathymetry in the reference run is also suggested appropriate. In summary, we suggest that the settings of the reference run are representative in reproducing the historical maps.

5.4.2. SUGGESTION ON THE SPATIAL DISTRIBUTION OF THE AYD

As mentioned in section 5.2.2, there are many controversial viewpoints on the delta distribution, indicating limited hindcast understanding of the AYD. According to the reference run, the area of subaerial delta, formed between 1578-1855 AD, is simulated as $0.90 \times 10^4 \text{ km}^2$. The area formed between 1128-1578 AD is calculated as $0.74 \times 10^4 \text{ km}^2$, based on the reference shoreline of 1127 AD and 1578 AD (Gao, 2009). Thus, the total subaerial delta of the AYD until 1855 AD is estimated to be $1.64 \times 10^4 \text{ km}^2$. The area of subaqueous delta formed between 1578-1855 AD in the model is $0.65 \times 10^4 \text{ km}^2$. Thus, we suggest the total area of the AYD should be about $2.29 \times 10^4 \text{ km}^2$. The results have a good agreement with the estimations by Hu, Saito and Kempe (1998), which announced that the OYR formed an area of $2.70 \times 10^4 \text{ km}^2$ during the 700 year period.

The simulated distribution of the subaerial delta is shown in Figure 5.14. The north-

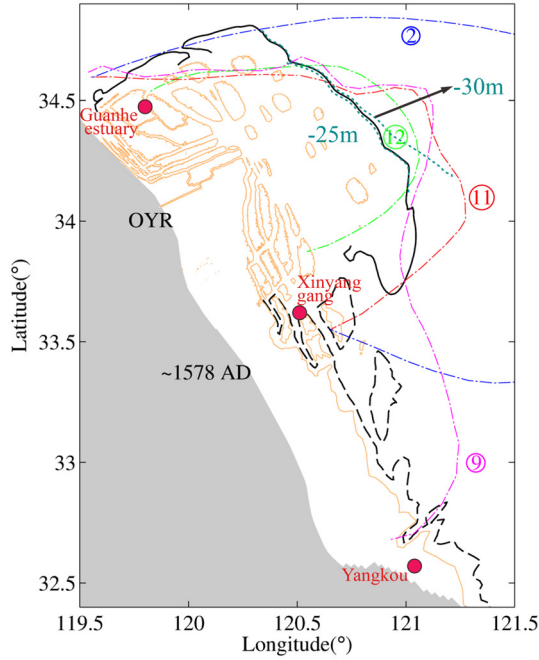


Figure 5.14: Simulated subaerial delta (bed elevation > 0 m, bounded by orange lines) and contour lines of 3 m accumulated deposition (bounded by black lines). Several previous estimations for the scope of subaqueous delta are collected and showed with color dotted lines. The numbers of the estimations are consistent with Table 5.2. Two contour lines representing 25 m and 30 m isobath (according to the simulated results for 1855 AD), respectively, are shown in dashed dark green lines. Several important geographic sites are pointed out, such as Guanhe estuary, Xinyang gang and Yangkou, according to their nowadays location.

ern boundary of subaerial delta extends to approximately 34.55°N, near the Guanhe estuary. The southern boundary reaches to the present location of the radial sand ridge field, near Yangkou. According to the location of southern and northern boundaries, the simulated results have a reasonable agreement with viewpoint V in Table 5.1 and Figure 5.3a. Furthermore, the seaward extension of subaerial delta is simulated to be 43 km between 1578-1855 AD. As data on the seaward extension of river mouth is scarce, geological field investigations are suggested in future research to validate the simulation.

The distribution of quasi-subaqueous delta, shown in Figure 5.14, has a similar “northern wide, southern thin” shape to the viewpoint ⑨ in Table 5.2 and Figure 5.4. However, after comparison with the boundary of the subaerial delta, the “thin” southern quasi-subaqueous delta is more like submerged shoals or the face of the subaerial delta. Thus, we consider that the subaqueous delta was distributed between 33.7° N and 34.8° N. In general, although the distribution asymmetry of the subaerial delta is significant, the dis-

tribution of the subaqueous delta is shown as completely symmetrical. The simulated northern boundary had a good agreement with most of the previous viewpoints (Table 5.2). The simulated southern boundary is near the Xinyang Gang (see the location in Figure 5.14), which is in accordance with estimate ⑦ (Table 5.2). Furthermore, the seaward boundary of the subaqueous delta is simulated to be located between the 25 m and 30 m isobath (according to the simulated results for 1855 AD), approximately 86–110 km width (Figure 5.14). Assuming the seaward extension during 1128–1578 AD does not exceed the extension during 1578–1855 AD, the total progradation distance has a reasonable agreement with estimates ⑦ and ⑫ (Table 5.2). Thus, the geologically based viewpoint ⑦ in Table 5.2 is generally indicated to have a satisfactory agreement with the simulations for the subaqueous delta of the AYD. It should be highlighted that, besides evaluating and validating the previous geological estimations, our results provide more detailed geometric features for the distribution of the AYD.

5.4.3. LIMITATION OF THIS STUDY

THE model has ignored waves and short term events (e.g. storms and floods). The wave climate, which consists mostly of locally wind-generated waves (Huang et al., 2005), may have some impact on the evolution of shallow water regions and shaping the shoreline. However, Zhang et al. (1998) state that waves only influence local-scale morphologies, rather than the overall-scale, and that the effect of waves is secondary in comparison with the effect of the tide regarding the morphological evolutions of the Jiangsu Coast. Figure 5.15 shows an examination of the hydrodynamic conditions for relevant coastal environments. It shows that, once we only consider the tidal range of the M2 tide, the AYD is demonstrated as a tide-dominated system. If the contribution of other tidal components on the tidal range would be induced, the dots representing the AYD would be located above our estimated location. Therefore, the AYD is considered as a tide-dominated system during its evolution stage, at least since 1578 AD. Although we assume wave, storm and flood play a weak role during the evolution of the AYD, it is worthwhile to explore the influence of waves, storms and floods on the shape and evolution of AYD in the future.

The influence of the simplifications of other parameters on the evolution of the AYD is not assessed in this study, such as sea level rise and sediment properties of the OYR. Although the cohesiveness of sediment is suggested to be an important factor for delta evolution (Edmonds and Slingerland, 2009), we assume that it was stable during the past centuries (coming from Loess Plateau) and may not be essential enough to influence

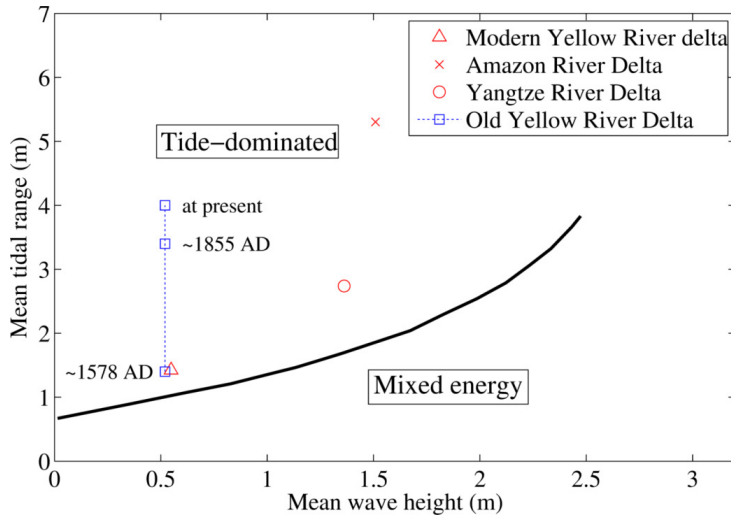


Figure 5.15: General relationships between wave height and tidal range for clay-silt sediment for determine the tide-dominated delta (Modified after Davis and Hayes, 1984; Orton and Reading, 1993). The dots for the AYD is based on the simulated M2 tide amplitude in this study and the measured multi-year averaged wave parameters in Lianyungang during 1961-1968 (Qiu, 2005).

the delta progradation of the AYD. These limitations could be remedied in the future. Nevertheless, the present study proves that the numerical modeling has the ability to reproduce the historical morphological changes on a large scale.

5.5. CONCLUSION

THE evolution of a deltaic system is sensitive to the modification of environmental parameters, such as fluvial discharge, mode of accommodation, sediment supply etc. The AYD, formed by the OYR during 1128-1855 AD, is now undergoing a severe erosion process due to the abrupt stop of sediment supply. Geological approaches are insufficient to provide a comprehensive understanding of the progradation process of the AYD, such as the distribution of the deltaic system and the deposition of sediment derived by the OYR. To investigate the morphodynamic evolution of such a fine grain sized delta and to provide reliable fundamental data for analyzing the following erosion process, a process-based morphological model was applied to reproduce a reliable natural progradation of the AYD. Due to scarcity of historical data, several alternative sources, such as historical records, maps and geological survey estimations were combined in this study.

The simulation results show that the progradation mechanism of the AYD varies spa-

tially and temporally. For the northern and southern part of the delta, the progradation modes are different. The progradation of the southern delta is by means of the growth of shoals and subsequent merging with the mainland, whereas the shoals in the northern part gradually become isolated and are independent from the progradation of the northern delta. Based on the analysis of the tide residual sediment transport, the progradation emphasis of the deltaic system converts from the rapid expansion of the southern delta to the development of shoals in the northern part during a period of a 100 to a 200 years simulation. The distribution of the subaerial delta and the deposition of the sediment derived by the OYR show a significant asymmetrical feature. However, the subaqueous delta is suggested to have a relative symmetric distribution pattern.

Uncertainties are inevitable in the model settings due to the lack of historical data. Scenarios were designed and carried out to investigate the influence of uncertainties on the development and the distribution of the delta, including the effect on the contribution of subaerial and subaqueous delta. The tidal regime is suggested to be the key factor in determining the type and principle evolution trend of the delta. Sediment supply is dominant with respect to the progradation rate and the size of delta, while the relative area ratio between subaerial and subaqueous delta is independent of sediment availability. In contrast, the slope of accommodation has a considerable effect on determining the distribution location of the deltaic system and the relative ratio between the subaerial and the subaqueous delta, while its effect on the overall area of the delta is secondary compared to the sediment availability. The effects of c/q ratio and temporal variation of sediment concentration are demonstrated to be minor with respect to the final evolution of the deltaic system.

Detailed comparisons between the simulation results and the historical data reveal that the reference run in the present study has the ability to reconstruct the AYD with a satisfactory reliability. The analysis of contributions of uncertainty on the morphological evolution of a delta suggests that the settings of uncertainty parameters in the reference run are acceptable. Subsequently, suggestions on the size of AYD (till 1855 AD) were provided.

In contrast with geological findings, the simulation results provide comprehensive fundamental information (e.g. reliable bathymetry data) for analyzing the subsequent severe erosion of the AYD, which lasts since 1855 AD. Future work, apart from assessing the sensitivity of the results response to the unconsidered uncertainty, will be aimed at the erosion stage of the AYD, to investigate the contribution of the AYD's erosion on the evolution of the radial sand ridges.

Appendix:

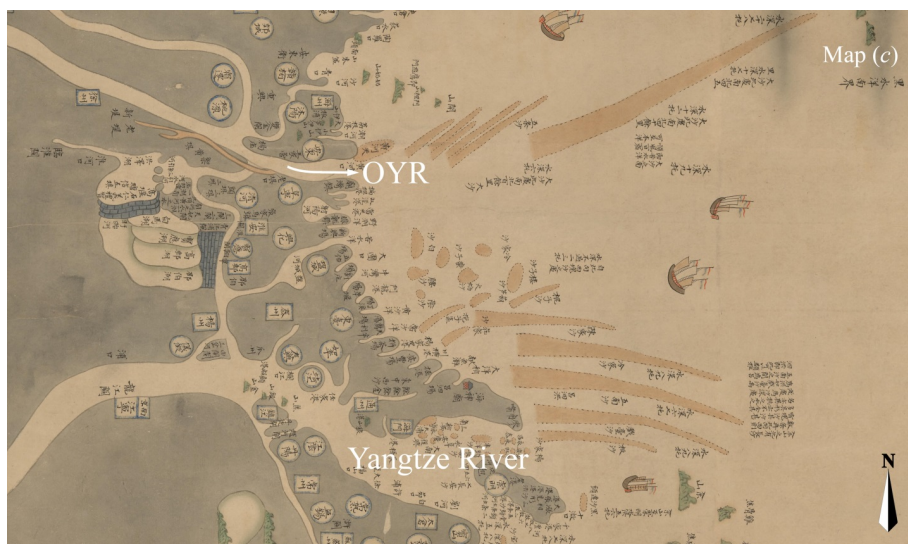
The main aim of historical maps and the restriction of historical measuring instruments is for land allocation. Therefore, most ancient maps only show a conceptual distribution of mainland (and a few of them includes nearshore ridges). These maps neither indicate longitude or latitude nor a scale. Here, we list three historical maps. To easily discriminate the Jiangsu Coast (located between the OYR and the Yangtze River) and the OYR, the position of the OYR and the Yangtze River is especially highlighted.



Map A: This map is part of the “Provincial atlas of the great Qing Dynasty”. It was drawn during 1754-1760 AD. The OYR was painted with a darker Yellow color, to discriminate the OYR from the tidal channels. With respect to the areas shown with white color bounded by black lines, we assume that it represented the subaerial region. The red circulars and quadrilaterals are named after local administrations. There are three blocks in the maps emphasized as shoals. Source: Library of Congress. Digital version is available at: <http://www.loc.gov/item/2002626726/>.



Map B: This map is part of the “Hai jiang yang jie xing shi tu”, which was drawn up with the aim of giving an overview on the coastline, islands and ridges. Note that the orientation of this map is different from other maps. It was drawn between 1787-1801 AD. The shoreline of the Jiangsu Coast was treated as a straight line in this map. Different colors are assigned to represent the mainland, ridges and water. The most significant features of this map are the shoals, inside the shaded regions. A series of shoals located northeast of the OYR is perpendicular to the shoreline. Shoals off the central Jiangsu Coast are parallel to the shoreline. There are also several sporadic ridges located off the southern Jiangsu Coast. Source: Library of Congress. Digital version is available at: <http://www.loc.gov/item/gm71005021/>.



5

Map C: This map is part of the “Jiang hai quan tu”, drawn between 1812-1843 AD. This map was drawn as a guideline for navigation, to avoid emerged ridges, so the coast line and the major rivers of estuaries, islands and ridges along the Jiangsu Coast were labeled. The shoreline of the Jiangsu Coast was drawn as arcuate pattern. The shoals were painted with khaki color and bounded by dotted lines. The land was painted with gray colors. Source: Library of Congress. A digital version is available at: <http://www.loc.gov/item/gm71005059/>. Note that the scale and direction of the shoals drawn in this map are significantly different from that in the Map B.

6

EXPLORATORY MORPHODYNAMIC MODELLING ON THE EVOLUTION OF THE JIANGSU COAST SINCE 1855



The Old Yellow River estuary at present. Source: <http://www.tupian.baik.com>.

This chapter is based on the journal paper submitted to *Marine Geology*.

Abstract: In this study, we aim to investigate the overall morphological evolution of the Jiangsu coast after 1855, when the Yellow River shifted northward. We focus on the fine sediment transport between two large-scale geomorphological units, i.e. the Abandoned Yellow River Delta (AYD) and the Radial Sand Ridges (RSRs). An existing morphodynamic model, which was established for reproducing the development of the AYD before 1855, is modified and extended. In addition to the tidal forcing, waves and human interventions (i.e. revetments) are considered in the model. The model results have been compared with the existing data. Both the evolution trend of the Jiangsu coast, which is “erosion in the north and sedimentation in the south”, and the spatial distribution of the offshore shoals show good agreement. The simulated fine sediment deposition extensions in different periods are consistent with the geological measurements. The results reveal that the old Yellow River derived sediment not only contributes to the sedimentation in the RSRs, but can also be transported to the adjacent zones, especially further south/southeast. Moreover, the spatial distribution of fine sediment deposits varies in the RSRs. The different sedimentary environments in the Dongsha and Tiaozini ridges result in significant grain size differences in these two neighboring ridges. A sensitivity analysis indicates that tide plays a key role in dominating the long-term morphological evolution of the Jiangsu coast and the total erosion from the AYD. On smaller scales, the effect of revetments on the evolution of the nearshore zone as well as the effect of wind waves on the erosion of offshore shoals is relatively important. The effect of a gradual bottom sediment coarsening process along the Jiangsu coast is identified. Due to the coarsening process, there is less fine sediment deposition in the northern offshore zone of the RSRs, while there is more in the seaward part of the central RSRs (i.e. the Tiaozini ridge).

Highlights:

- Provide insight into the evolution of the Jiangsu coast through a process-based morphodynamic modelling approach.
- While a sediment source for the whole RSRs, the old Yellow River derived sediment can also be transported to the adjacent regions, especially the south/southeast regions.
- Tide is a crucial factor in determining large-scale morphological evolution of the Jiangsu coast.
- Coarsening bottom sediment can eventually change the sedimentary environment of the RSRs.

6.1. INTRODUCTION

THE geomorphology of a river-dominated delta is strongly determined by the river induced sediment input (Gelfenbaum et al., 2009). If a river goes through changes upstream, e.g. switching courses, the previously formed delta lobes may be abandoned. An example is the Abandoned Yellow River Delta (AYD) in the Southern Yellow Sea (SYS), China. It was formed and developed during 1128-1855 AD (Figure 6.1), when the Old Yellow River (OYR) reached the Jiangsu coast and discharged into the SYS. Since 1855 AD the Yellow River shifted its course to the Bohai Sea (Ren and Shi, 1986; Xue, 1993; Saito et al., 2000; Liu et al., 2013). Subsequently, both the subaerial and subaqueous parts of the AYD experienced severe morphological changes (mainly erosion), due to the cutoff of the sediment supply and local energetic hydrodynamic conditions (Saito and Yang, 1995; Zhou et al., 2014). In addition to several geological studies on the development of the AYD before 1855 AD (e.g. Liu et al., 2013), a morphodynamic modelling approach has been applied to explore the formation and evolution of the AYD as well as the relevant influence of the OYR-derived sediment on the morphological evolution of the Jiangsu coast during 1128-1855 AD (see Chapter 5, and hereafter referred to as: “the companion study”).

In this study, we focus on updating our understanding of the morphodynamic changes along the Jiangsu coast after 1855, when no more sediment was provided by the OYR. Many existing studies have investigated the morphological and hydrodynamic changes during this period, especially concentrating on the erosion of the AYD, e.g. the cross-shore profile changes (Zhang et al., 1998), estimating the overall volume of the erosion (Saito and Yang, 1995), the transport direction of eroded sediment (Ren and Shi, 1986; Saito and Yang, 1995; Shi et al., 2012; Zhou et al., 2014) and the feedback of erosion to the tidal dynamics (Chen et al., 2009). Most of the studies are based on shoreline comparisons in different periods (e.g. Chen et al., 2009; Zhou et al., 2014). However, the reliability of the shorelines collected from historical maps is doubtful (see the companion study). Furthermore, such methods do not provide details of the process dynamics.

Besides the AYD, another large-scale geomorphological unit in the SYS, is a series of distinct sand ridges (Liu and Xia, 1985), named the Radial Sand Ridges (RSRs; Figure 6.1). The RSRs cover an area of 22,470 km² (200 km in the north-south direction and 90 km in the east-west direction), with water depths ranging from 0 to 25 m (Wang et al., 1999; Li et al., 2001). Most of the ridges are submerged, accounting for 86% of the RSRs area (Wang, 2002). The Tiaozini ridge and the Dongsha ridge are the two largest ridges in the RSRs (Figure 6.1). Previous research has revealed that the tidal currents play a dominant role in the formation and development of the RSRs, while the contributions of

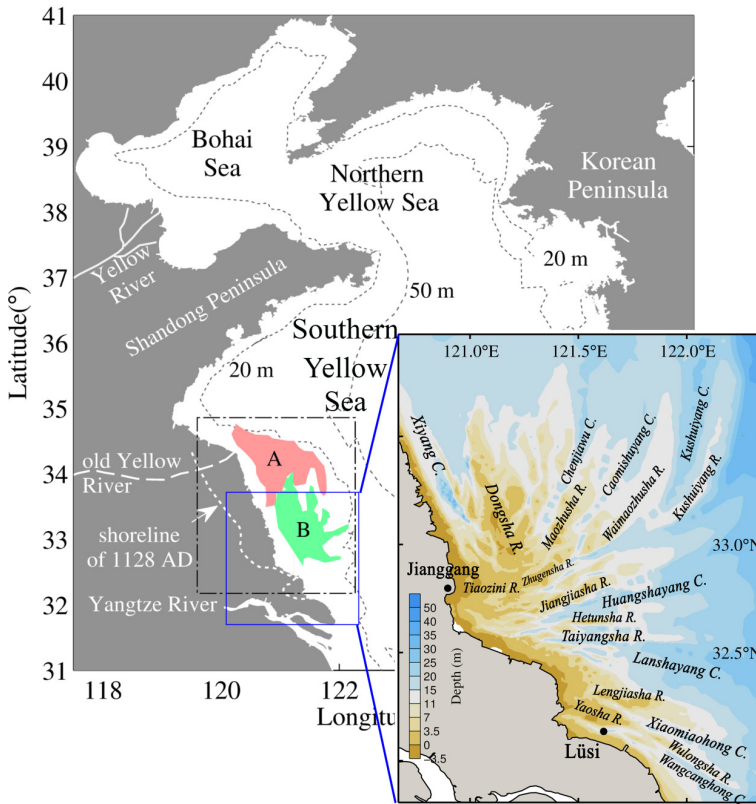


Figure 6.1: Maps of the study area, with 20m and 50m isobaths. The reference shoreline of the Jiangsu Coast in 1128 AD is modified after Gao (2009) and Yang et al. (2003). The location of the OYR is modified after Lim et al. (2007) and Liu et al. (2013). Colored regions A and B represent the approximate location of the AYD and radial sand ridges field, respectively (modified after Park et al., 2000). The detailed diagram for the RSRs is enlarged and marked with the name of local ridges (abbr. R.) and channels (abbr. C.).

storms/waves are secondary (Zhang et al., 1999). It is generally accepted and understood that the formation period of the RSRs took place several thousand years ago (Wang et al., 2012; Zhang, 1991). However, the relevant sediment sources of the RSRs are debatable according to various published existing results (Chen et al., 2013), even though these results are based on geological (e.g. Li et al., 2001; Yang et al., 2002; Wen et al., 2011; Wang et al., 2012) and geochemical (e.g. Yang et al., 2002; Wang et al., 2015) measurements. Doubts are mainly concentrated on the OYR and the Paleo-Yangtze River, both of which had discharged into the SYS, but during different periods (Liu et al., 1989; Yin et al., 2008). Specifically, with respect to the role of the OYR, there is a wide range of viewpoints: (1) it provides a majority of the sediment for the whole RSRs (Ren and Shi, 1986; Zhang, 1991); (2) it is a sediment source for the northern RSRs (Cai and Ma, 1992; Wang and

Zhang, 1998; Li et al., 2001); (3) it is source of the fine sediment (e.g. clay) for the northern RSRs (Y. Wang et al., 2012); (4) it is not a sediment source, whereas the Paleo-Yangtze River-derived sediment during BP 60,000-10,000 (Li et al., 2001; Y. Wang et al., 2012) is the single material basis for the RSRs (Yang, 1985; Fu and Zhu, 1986). These conflictive viewpoints may be due to the inherent restriction of geological approaches (e.g. localized measurements), which lack of a large-scale dynamic point of view associated with sediment transport and morphological changes. The existing knowledge on the RSRs is far from enough for understanding its formation and evolution for both hindcast and forecast purposes.

In the years since 1855, the total amount of eroded sediment from the AYD was roughly estimated as 5×10^8 t/y (Hu et al., 1998). It is unknown whether such amounts of sediment benefit the development of the RSRs. Furthermore, the bed sediment types throughout the RSRs vary greatly (i.e. from fine silt to fine sand, Li et al., 2001; Zhang, 2012). For example, the averaged grain sizes of the two largest ridges, i.e. the Tiaozini ridge and the Dongsha ridge, have a significant difference: the Dongsha ridge is rich in sand, whereas silt is abundant in the Tiaozini ridge. Note that, the geographical positions of these two ridges are close (Figure 6.1). The processes and mechanisms behind the complicated sediment distribution patterns deserve more attention.

Since 1855, the dominant coastal processes changed significantly due to the abrupt stop of the water/sediment discharges of the OYR. For example, compared with the fluvial and tidal processes, the wave effect was relatively weak during the period of 1128~1855. However, since 1855, wind waves have been more significant in the erosion of the AYD as well as the sediment transport in the RSRs and tidal flats (Zhang et al., 1999; Wang et al., 2014). It is uncertain whether the wave effect is as important as the previous studies estimated and how it affects the long-term morphological changes of the Jiangsu coast. Furthermore, to prevent a retreat of the shoreline, since the 1930s sea dikes have been built near the river mouth of the OYR (Liu et al., 2013). At present, most of the Jiangsu coastline is sheltered by artificial sea dikes (Ma et al., 2014; Syvitski, 2015). Due to this human intervention, landward retreat of the shoreline has significantly been reduced. However, the erosion of the shore-face and offshore seabed has become more acute (Cai et al., 2009). The importance of human activity on the large-scale and long-term morphological evolution of the Jiangsu coast (including both the AYD and the RSRs) requires further attentions.

In this study, we aim to understand the morphodynamic processes of the Jiangsu coast since 1855, especially focusing on the role of the OYR-derived sediment for the evolution of the RSRs. First, our process-based morphodynamic model (i.e. the companion

study) is modified for application to the period after 1855. The model takes tide, wave and human interferences (i.e. sea dikes) into account, aiming to provide reliable predictions on the long-term morphological evolution of the Jiangsu coast. Subsequently, qualitative validations of the model results (i.e. shoreline evolution, distribution of off-shore shoals, deposition of the fine sediment in the RSRs) are carried out. Based on the analysis of the fine sediment deposition and sediment budget in the RSRs, the contribution of the sediment, eroded from the AYD, to the development of the RSRs is investigated. Furthermore, the relative importance of tide, wave and human activities on the large-scale and long-term morphological evolution of the Jiangsu coast is evaluated. Finally, since the availability of fine sediment along the Jiangsu coast is nowadays considerably reduced (Chen et al., 2014; Zhang et al., 2014), the effect of coarse bottom sediment on the fine sediment distribution in the RSRs is further investigated.

6.2. DATA AND METHODS

6.2.1. DATA ON MORPHOLOGICAL CHANGES OF THE JIANGSU COAST

TO reveal the general trend of shoreline evolution, shorelines of the Jiangsu coast at different periods are collected and shown in Figure 6.2. The shorelines are collected from both the earlier literature (i.e. the “after-correction” historical shorelines; e.g. Zhou et al., 2014, for the period before the 1970s) and the existing marine charts (for the period after the 1970s). However, we note that the original shorelines shown in historical maps are poorly quantified due to technical restrictions at that time (e.g. before the 1970s). For example, the marine chart of 1934, shown in Figure 6.3a, reveals a relatively high resolution of offshore bathymetry, whereas it fails to illustrate a reliable Jiangsu shoreline and near-shore bathymetry. Moreover, errors are inevitable during artificial registration of historical maps with the present coordinate systems (e.g. longitude and latitude system). The announced “after-correction” historical shorelines in different references contradict each other. For example, the shorelines in the 1890s (collected from Gao, 2009) and in 1900 (collected from Zhou et al., 2014) vary substantially (Figure 6.2). It is therefore questionable to use these maps for quantitative analysis of the morphological changes.

On the other hand, it is still possible to obtain a general qualitative evolution trend of the Jiangsu coast based on these historical shorelines. According to the direction of shoreline changes (i.e. erosion and sedimentation features), the entire Jiangsu coast can be divided into three segments. Continuous shoreline retreat (i.e. net erosion part) occurs in the northern Jiangsu, bounded by the Guanhe estuary and the Sheyang estuary (Figure 6.2). The shoreline progradation zone (i.e. net sedimentation part) is in the

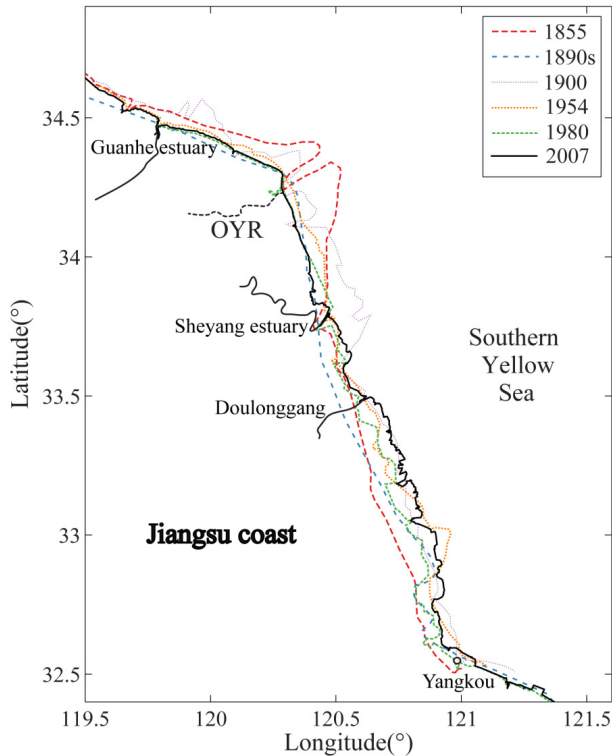


Figure 6.2: Evolution of the shoreline of the Jiangsu coast during 1855–2007 based on historical maps. The shorelines in 1855 and in 1900 are collected from Zhou et al. (2014); the shoreline in the 1890s is based on Gao (2009); the shorelines in 1954 and in 1980 are based on marine charts L500 (available from the University of Texas Libraries: <http://www.lib.utexas.edu/maps/ams/china/> and G-10D (available from the University of Texas Libraries: <http://www.lib.utexas.edu/maps/tpc/Europe-asia-africa-index.html>); the shoreline in 2007 is based on recent field measurements and remote sensing (Zhang, 2012).

southern Jiangsu, bounded by the Doulonggang and Yangkou (Figure 6.2). In the area between the aforementioned two zones, little shoreline changes are identified. This area can be treated as a transition zone. Similar division criteria can be found in many existing studies (e.g. Zhang et al., 2002; Liu et al., 2011; Gu et al., 2012; Zhang et al., 2014).

Another important geological feature to illustrate the morphological changes along the Jiangsu coast is the spatial distribution of offshore shoals. Bathymetric data for the nearshore zone of the Jiangsu coast until the 1980s is scarce (Wang et al., 2014). Although it is possible to obtain the overall distribution of shoals before the 1980s through historical maps, the distributions are mainly “empirical-based” results without support of measured data. Figure 6.3 presents two collected maps as examples to show the distribution of offshore shoals in the past. In general, the distribution of shoals in these

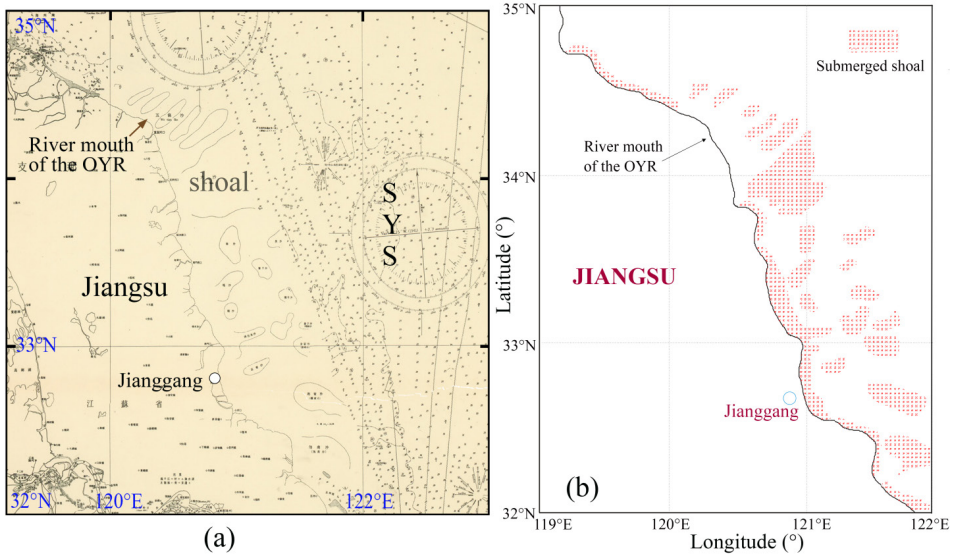


Figure 6.3: (a) Part of Japan marine chart in 1934, focusing on the Jiangsu coast (available at Tohoku University library <http://chiri.es.tohoku.ac.jp/~gaihozu/index.php?lang=en-US>). Note that, dense data are available for the offshore zone while there are no data for the near-shore zone. Specifically, the shoreline of the Jiangsu coast is displayed as a dotted line; (b) the “empirical” distribution of submerged shoals along the Jiangsu coast in the 1950s (modified after Geng et al., 1983).

two maps display a similar qualitative pattern. The distribution of offshore shoals can be artificially divided into two parts, according to the geographical location and the pattern of shoals. First, off the OYR estuary (geographical location not exceeding 121°E), the submerged shoals are distributed in a rhythmic pattern. Second, off the central and southern Jiangsu coast, the offshore shoals are mainly in a random pattern. Compared with the distribution pattern of the offshore shoals before 1855 (see Appendix of Chapter 5), a remarkable change is found in the vicinity of the OYR estuary. These shoals near the OYR estuary gradually became submerged with a southward movement after 1855. Note that, all the shoals were changed due to being submerged at least in the 1950s according to the “empirical-based” map (Figure 6.3b). Moreover, the historical maps reveal that the distributions of the offshore shoals off the central and southern Jiangsu coast appear different from the present day radial pattern ridges. The discrepancies may be due to the lack of comprehensive investigations of the geomorphological features of the RSRs until the 1980s/1990s (Wang et al., 2012).

6.2.2. DATA ON THE FINE SEDIMENT DISTRIBUTION IN THE RSRs

WITH respect to systematical investigations in the RSRs, there are mainly three large-scale field surveys, starting from the early 1980s (Wang et al., 2014; Zhang, 2012). These surveys reveal that the main sediment type over the ridges is fine sand. The contents of silt and clayey silt increase on the tidal flats and in the tidal channels. Moreover, a general evolution trend of the sediment size in the RSRs is that deposition gradually becomes finer nearshore and coarser offshore, although the bottom sediment of the whole Jiangsu coast has a pronounced coarsening trend (Zhang, 2012).

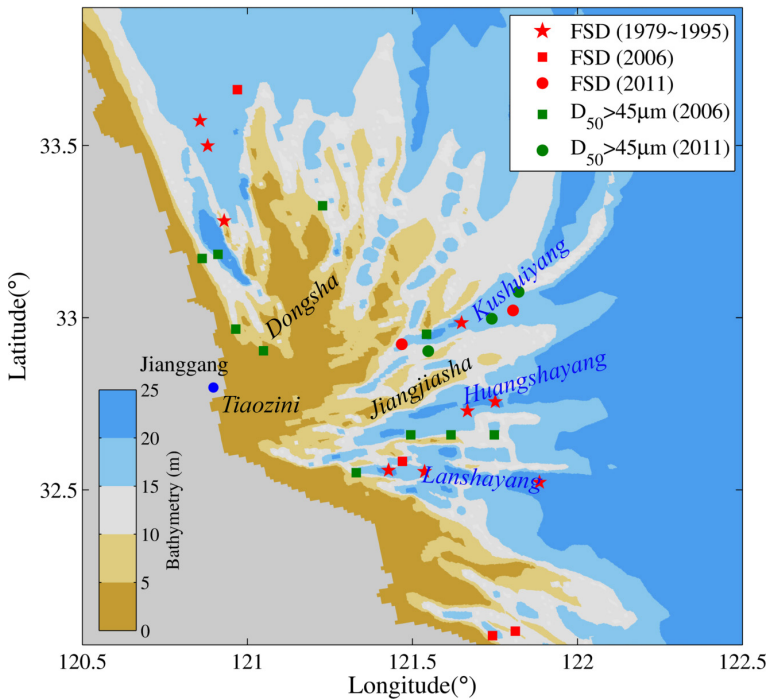


Figure 6.4: The distribution of different sediment sizes in the topmost bottom sediment layer (thickness less than 10 cm). Different grain sizes are represented by different symbols: the sediment with median grain size between 15 and 45 μm , namely “FSD”, is shown by red symbols; the sediment with median grain size larger than 45 μm , is shown by green symbols. These data are collected from surveys in 1979-1995 (represented by stars; Wang, 2002), in 2006 (represented by squares; Zhang, 2012), in 2011 (represented by circles; Tang, 2014; Wang et al., 2014). The background bathymetric data is based on the official marine charts published by the Navigation Guarantee Department of the Chinese Navy Headquarters (1979) and recent field measurements (Zhang, 2012).

Investigations of the grain sizes (i.e. through bed material sampling, seismic profiling and drilling approaches) provide an overview of the diverse sediment types throughout the RSRs. The deeper layer of the cores is mainly composed of fine sand, which is sug-

gested to have originated from the Paleo-Yangtze River (e.g. late Pleistocene, Wang et al., 2012). Grain sizes of the superficial layer vary greatly, and both silt and sand fractions have been observed. The grain size of suspended sediment of the Yellow River is reported as 15~45 μm (Wang, 2002). The sediment with grain sizes ranging from 15 μm to 45 μm in the superficial bed layer (i.e. 10 cm thickness) is defined in this study as “Fine-Silt-Dominated sediment” (FSD). We assume that the distributions of FSD are the potential deposition zones of the OYR-derived sediment.

We collected bed material measurements in the recent 30 years (during 1979~2011) from both large-scale survey reports (e.g. Wang, 2002; Zhang, 2012) and from recent small-scale measurements (e.g. Tang, 2014; Wang et al., 2014). Specifically, the survey during 1979~1995 (Wang, 2002) covered the whole RSR field (32.0~33.6°N; 120.2~121.9°E). Another large-scale survey was carried out in 2006 (Zhang, 2012), with a total of 14 bed sampling stations in the RSRs. A recent local-scale survey, focusing on the Kushuiyang channel, was carried out in 2011 by Nanjing University (e.g. Tang, 2014; Wang et al., 2014). Besides the observed FSD stations in these surveys, in recent surveys (i.e. the surveys in 2006 and 2011) other stations with a relatively coarser sediment size (i.e. $D_{50} > 45 \mu\text{m}$) were also collected. The collected distributions of FSD and relatively coarser sediment are shown in Figure 6.4. It reveals a complicated environment of the RSRs with spatially-varying sediment sizes. For example, in the Kushuiyang channel, the grain size can vary from 30 μm to 150 μm within a distance of 7 km.

6.2.3. MORPHODYNAMIC MODELLING

MODEL DESCRIPTION

THE existing morphodynamic model for the Jiangsu coast (see the companion study; Chapter 5) is modified and extended to investigate the morphodynamic changes after 1855 by setting the water and sediment discharge of the OYR to zero. The model is constructed based on Delft3D software (Deltares, 2012). The basic model configurations are kept more or less the same as those of the companion study, e.g. the model domain (Figure 6.5a), the open boundaries (M2 tidal constituent), sediment fractions (15 μm and 200 μm). The parameters for basic model setting and sediment transport are adopted from the companion study as well and are listed in Table 6.1. These settings have already been validated as being reasonable by the companion study.

The initial bathymetry and sediment bed composition of this study are generated based on the results of the companion study, shown in Figure 6.6. In particular, according to historical shorelines (e.g. Gao, 2009; Zhou et al., 2014), the originally generated bathymetric data is slightly modified by correcting the nearshore bathymetry in

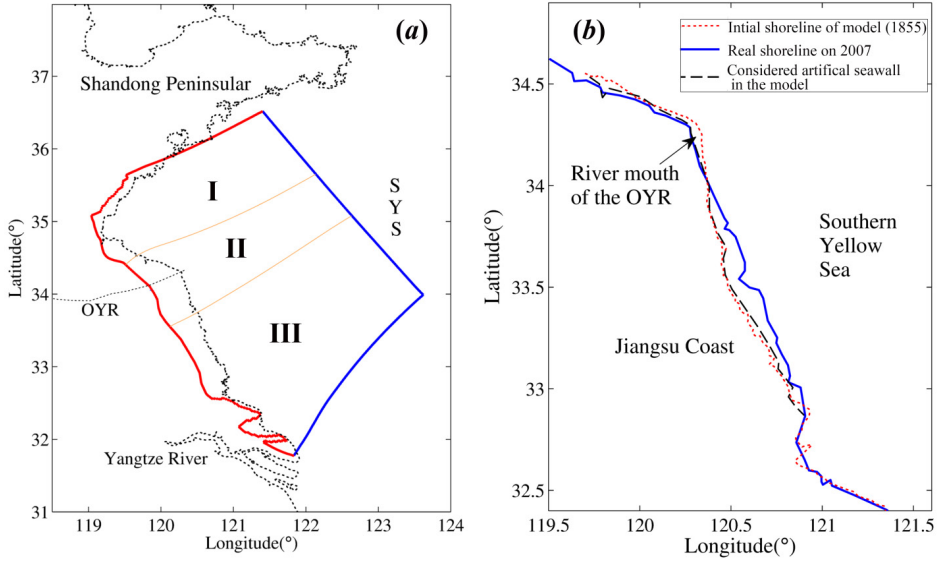


Figure 6.5: (a) Configuration of land boundaries (red lines) and open boundaries (blue lines). The land boundary near the Jiangsu Coast is the reference shoreline of 1578 AD (modified after Gao, 2009). Black dotted lines indicate the shoreline at present. Three sub-domains (i.e. I, II and III) are divided by the orange lines; (b) position of the considered "artificial sea dikes" in the model, in comparison with the initial shoreline (1855) in the model and the real shoreline at present (2007).

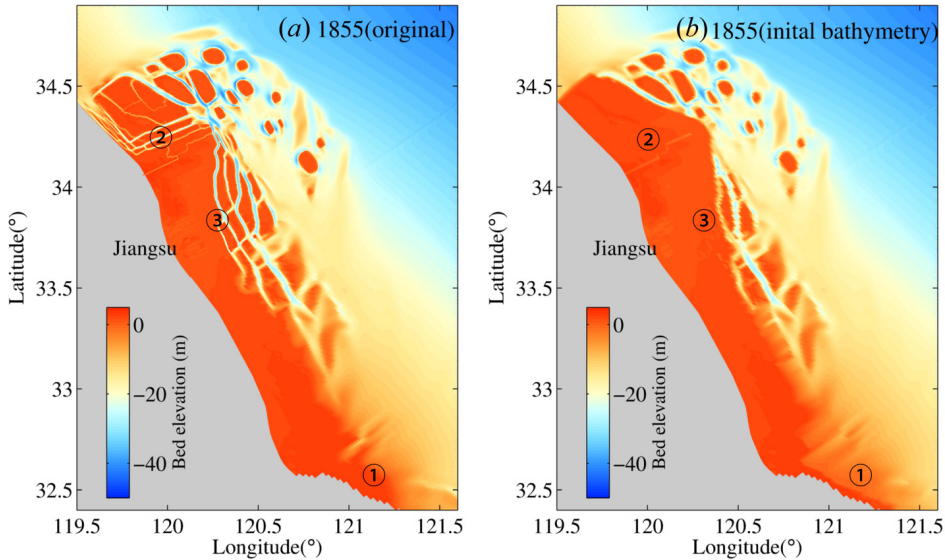


Figure 6.6: (a) Bathymetry in 1855 generated by the companion study (i.e. Chapter 5); (b) modified initial bathymetry applied in the present study. Note that, slight modifications are made in three regions (i.e. ①, ②, ③) according to historical maps.

Table 6.1: Overview of parameter settings in the model.

Parameter	Value
Time frame	1855~2055
Erosion parameter	0.01 kg/m ² s
Manning coefficient	0.016
Mor-factor	108
Critical shear stress for deposition	1000 N/m ²
Critical shear stress for erosion	0.5 N/m ²

the southern Jiangsu coast (region ① in Figure 6.6) and by filling several small interior tidal channels (region ②, ③ in Figure 6.6). The sediment bed compositions are adjusted correspondingly.

It has been suggested that waves play a relatively important role in the erosion of the AYD (Liu, 2011; Zhang et al., 2015). Therefore, it is necessary to include the wave effect in this study. For a small-scale region (e.g. lagoon, estuary), it may be feasible to consider the wave effect on a long-term morphological change by applying several sets of carefully selected representative waves (e.g. Dissanayake and Wurpts, 2013). However, wind and wave climates in a large-scale region, such as the inner shelf along the Jiangsu coast, are highly variable, both spatially (Qiu, 2005) and temporally (due to the monsoon effect, Wang et al., 2014). Furthermore, there are only two nearshore wave stations along the Jiangsu coast (i.e. Lianyungang station and Lvsi station), which are insufficient to represent the wind/wave climate of the whole domain. Taking a multi-year averaged wave climate as an example, the wave statics of these two stations are shown in Figure 6.7. For the Lianyungang station (34.8°N, 119.4°E), located in the northern Jiangsu coast, the wave is predominant in NE direction with a 25% occurrence. At the Lvsi station (32.3°N, 122.0°E) the wave climate is completely different: waves are only recognizable in one half of the year. The predominant direction is N and NE, with only a 6% occurrence. It is thus difficult to apply the “representative wind/wave” method for the whole inner shelf along the Jiangsu coast.

The primary interest of the present study is to understand the erosion process of the AYD and the influence of eroded sediment on the RSR after 1855. Therefore, in this study we consider the wave effect in a schematic manner, i.e. a simplified wind climate in the northern model domain (i.e. more north than 33.8°N). Since the waves along the Jiangsu coast mainly consist of wind waves (Huang et al., 2005), the wind considered in the model is set according to the observation in Lianyungang (Huang et al., 2005; Qiu, 2005) and China Marine Environment Report (<http://www.nmdis.gov.cn/gongbao/nrhuanjing/nr1998/>), with a NE direction and a speed of 4.5~5 m/s. Due to the restric-

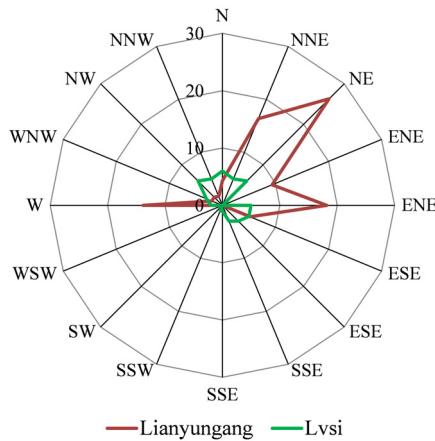


Figure 6.7: Frequency distribution of wave directions at two stations of the Jiangsu coast: Lianyungang (red line) and Lvsi (green line); modified after Zhang (2013). Different circles denote different levels of concurrency frequency.

tion of computational efficiency, we assume that the speed of the wind/wave from other directions with a total 75% occurrence is zero. The simplified wind forcing is applied to produce waves by the SWAN model. Default settings of the parameters in SWAN are used. The corresponding modelled averaged wave height for the Lianyungang is 0.3~0.5 m, similar to the measured one (i.e. 0.39 m; Qiu, 2005).

The tidal flow and waves are coupled online to calculate the sediment transport and the morphological changes. The current-wave interactions are taken into account by this online coupling approach (for more detail see Deltares, 2012). The model is run with and without (NE) wind waves, respectively. The final morphodynamic results (e.g. bed level changes) are derived by averaging the results of these two runs with a weighting factor (i.e. the occurrence of the simplified wind field).

Although the Jiangsu coast revetments are most common human interferences to protect against erosion, especially for the AYD region. In this study, revetments are represented by setting a series of non-erodible cells (viz. artificial sea dikes) along the Jiangsu coast. The positions of these non-erodible cells are defined according to both the initial shoreline in 1855 and the shoreline at present (see dashed lines in Figure 6.5b). The inclusion of these sea dikes in the model can prevent the landward retreat of shoreline, while it has little effect on potential shoreline progradation.

SPECIFICATION OF MODEL SCENARIOS

DIFFERENT scenarios are designed to investigate the relative effect of tide, wave and human activities (i.e. sea dikes) on the morphological evolution of the Jiangsu

coast. The simulation, considering all these three aspects (i.e. tide, wave and human activity) together, is taken as the reference run (RF). In each other scenario, we change one aspect of these influence factors and keep other aspects unchanged (see Table 6.2).

Table 6.2: Overview of the designed scenarios.

Parameters	Cases				
	Case TI	Case TW	Case TH	Case RF	Case BS
Tide	✓	✓	✓	✓	✓
Wave	×	✓	×	✓	✓
Human activity	×	×	✓	✓	✓
Bed coarsening	×	×	×	×	✓

Note: the time frame for the case BS is between 2007~2055. The initial condition (e.g. bathymetric data) of case BS is based on the results of case RF.

A recent field survey showed that the sand content near the river mouth of the OYR has increased, while the content of clay shows an opposite trend (Chen et al., 2014; Wen et al., 2014). It indicates that the continuous erosion of fine sediment in the AYD results in a gradually coarsening sediment bed. Besides, the survey on the RSRs also shows a similar coarsening sediment bed trend (Zhang, 2012). Moreover, the coarsening bottom sediment phenomena were observed in our previous flume experiments (under wave-current combination; Chapter 3) over a silt-dominated sediment bed, which was collected from the tidal flats of the Jiangsu coast (i.e. the Tiaozini ridge). Insufficient sediment supply and a self-packing effect of bottom sediment are considered as possible reasons for the coarsened bed in the flume experiments. From a long-term viewpoint, the availability of fine sediment along the Jiangsu coast is limited due to an absence of sediment sources and to continuous erosion. Thus, the Jiangsu coast, which is now abundant with silty sediment, is expected to experience the same coarsening process. Here we assume that the size of the fine sediment increases from 15 to 38 μm (i.e. case BS in Table 6.2), after a certain simulation time period (i.e. since 2007), in order to qualitatively analyze the influence of coarsening sediment bed on the morphological evolution. The other parameters and considered influencing factors in case BS remain the same as the RF case.

6.3. MODEL RESULTS

6.3.1. MORPHOLOGICAL EVOLUTION ALONG THE JIANGSU COAST

THE simulated morphologies in 1955 and 2007 (i.e. case RF) along the Jiangsu coast are shown in Figure 6.8. In 1955, the simulated shoreline near the OYR estuary has

retreated to the location of sea dikes (i.e. the un-erodible cells; Figure 6.8a). This region suffers severe erosion in comparison with the other parts of the Jiangsu coast. In contrast, pronounced shoreline progradation is found in the southern Jiangsu coast. In the area between the aforementioned two segments, namely zone B (see Figure 6.8a), the shoreline shows less variation over time. The simulated results of 2007 exhibit similar evolutionary features (Figure 6.8b). Specifically, compared with the results in 1955, the northern part of the zone B suffered erosion in 2007. In general, the simulated shoreline changes of the Jiangsu coast depict an overall trend of “erosion in the north and sedimentation in the south”, which is in a good qualitative agreement with the historical records (Figure 6.2).

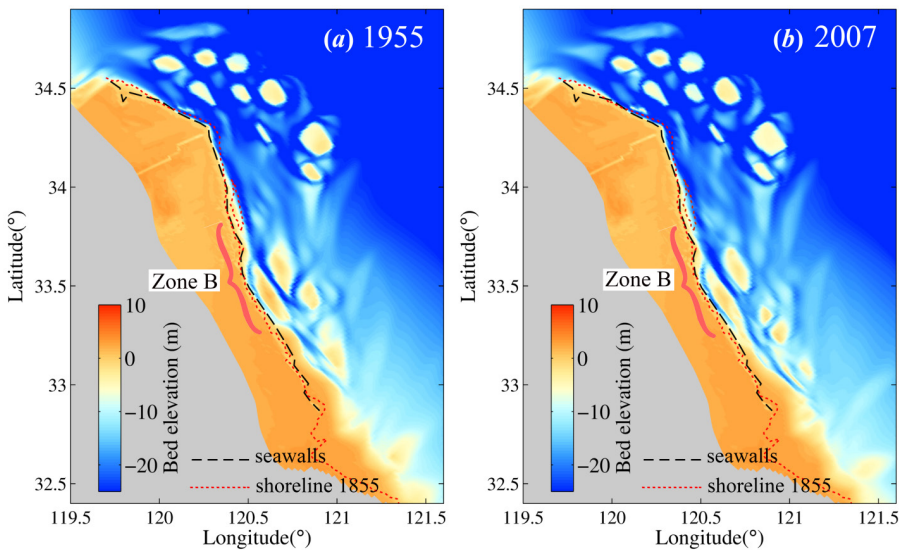


Figure 6.8: Simulated morphologies near the Jiangsu coast by the reference run for 1955 (a) and 2007 (b), respectively. The black dash line denotes the “artificial sea dikes” considered in the model. The red dotted line denotes the initial shoreline of the model (i.e. in 1855).

With respect to the morphological changes offshore (i.e. the distribution of the offshore shoals), the model results show that the initial subaerial shoals are all submerged in 1955 (Figure 6.8a). Compared with the initial condition (Figure 6.6b), the shoals around the river mouth of the OYR move seaward (i.e. eastward), but do not exceed the longitude of 121°E. This pattern is in a reasonable agreement with the existing understanding (i.e. Figure 6.3). Off the central and southern Jiangsu coast, the existence of a series of sporadic offshore shoals is reproduced by the simulations, although the detailed shape of these shoals is different from the existing maps (i.e. Figure 6.3). The simulated morpho-

logical evolution agrees qualitatively well with the historical maps. The simulated morphologies in 2007 (Figure 6.8b) are more or less similar to those in 1955. Compared with the measured bathymetric data at present (Figure 6.1), a remarkable difference is that the model does not reproduce the morphological component of the RSRs (i.e. complicated arrangement of ridges and channels). This may be attributed to the schematization of the initial bathymetry. Because the bathymetry in the RSRs has not been measured until the 1980s (Wang et al., 2014), the initial bathymetry of the RSRs (i.e. in 1578 AD) in our models was assumed as linearized bottom slopes without any features of ridges and channels (see the companion study). Existing studies have suggested that the RSRs are probably formed in the late Pleistocene (Wang et al., 2012). In other words, the RSRs may require thousands of years to develop such morphological features, which is beyond the simulation time span of our models (i.e. hundreds years).

6.3.2. DISTRIBUTION OF SEDIMENTATION (THE OYR-DERIVED SEDIMENT)

DUE to our primary focus, we mainly compare the fine sediment (15 μm) deposition in the RSRs in this study. Note that, the only source of the fine sediment in this model is the OYR during 1578~1855 AD (see the companion study; Chapter 5 for more information). Therefore, the 15- μm -fraction is referred to as the OYR-derived sediment.

Figure 6.9 shows the accumulated thickness of the OYR-derived sediment in the RSRs during 1855~2007. Fine sediments are not uniformly distributed in the RSRs. From landward to seaward, the fine sediment in the nearshore and further offshore zone keeps accumulating especially the Tiaozini ridge is simulated with fine sediment deposition of more than 3 m since 1855. But the intermediate zone (e.g. the Dongsha ridge, located nearby the Tiaozini ridge) between the aforementioned two zones is undergoing erosion. The continued sorting in this zone results in a coarser bottom sediment feature. In reality, the Dongsha ridge is mainly composed by fine sand within a 20 m sediment thickness (Wang et al., 2015), whereas the Tiaozini ridge has abundant silt contents with particle size ranging 15~62 μm (Chen et al., 2012). The significant grain size change of these two adjacent regions is thus well reproduced by our model. Furthermore, Jiang et al. (2012) have investigated the sedimentation rates for depositions in the Dongsha ridge and the Tiaozini ridge through the ^{210}Pb technique. The sedimentation rate of the Dongsha ridge could not be obtained, due to the substantial erosion. Conversely, the sedimentation rate of the Tiaozini ridge is extraordinary. Thus, the simulated results are in agreement with recent geological measurements.

The sediment sorting in the intermediate zone may be due to the decrease of sed-

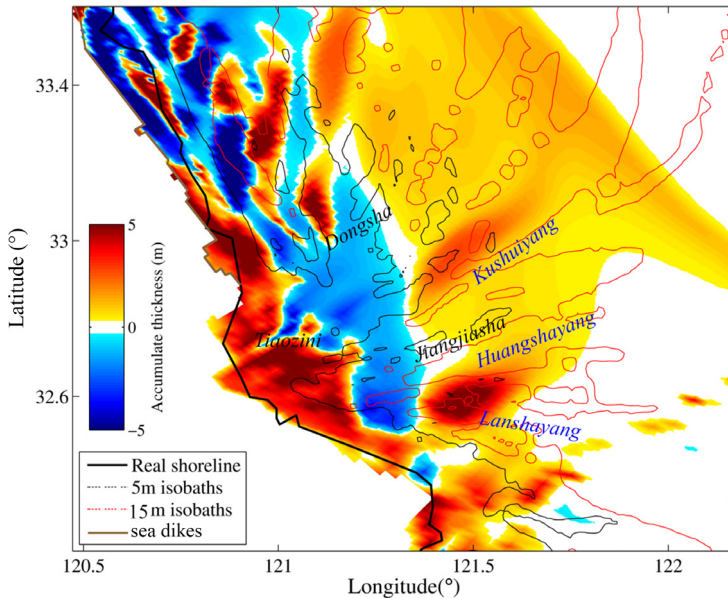


Figure 6.9: Accumulated thickness of fine sediment during 1855-2007 (according to case RF). The source of the isobaths and shoreline refer to Figure 6.4. The sea dikes considered in the model are also shown.

iment input to the RSRs after 1855, since the tidal regimes have been relatively stable (Uehara et al., 2002; Zhu and Chen, 2005). Before 1855, the erosion of fine sediment may also have been evident, but it could be re-filled by the external sediment supply from the OYR. However, after 1855, the external sediment supply was extremely reduced (also refer to section 6.4.1) and the erosion of fine sediment in the intermediate zone is particularly obvious. Consequently, the significant difference of the grain sizes between the Tiaozini and Dongsha ridges is evident. Moreover, the findings indicate that the position with the sorting effect is independent of the complicated ridge-channel topography, which is not presented in the model.

We further compare the model results with the existing field surveys on bed materials. In line with the companion study, the deposition thickness of fine sediment, larger than 10 cm, is taken as a criterion to discriminate the spatial distribution of fine sediment deposits. The collected distributions of FSD (see section 6.2.2) and relative coarser sediment ($D_{50} > 45 \mu\text{m}$) are used to validate the simulated deposition ranges of fine sediment. Since fine sediment deposition may change over time, the model results at four time points (i.e. 1979, 1995, 2006 and 2020, with ~14 years intervals) are presented and compared with the measurements. The comparisons between simulations and the measurements during time-span of 1979-1995 and 2006-2020 are shown in Figure 6.10 and

Figure 6.11, respectively. Note that, the background bathymetry is the measured bathymetric data in 2007, rather than that in the model. Showing a present bathymetry map aims to conveniently mark locations by the name of ridges and channels.

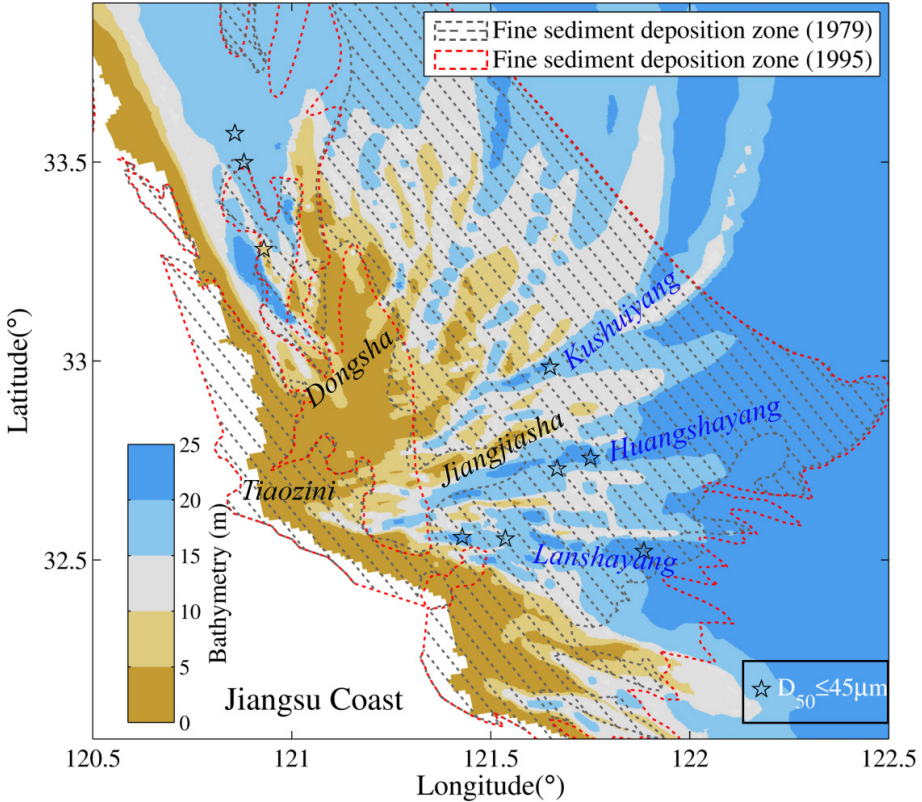


Figure 6.10: Simulated sedimentation range of fine sediment ($D_{50}=15\ \mu\text{m}$) in the RSRs in 1979 and 1995, respectively. The sedimentation range is determined by criterion that the accumulated deposition thickness is larger than 10 cm since 1855. The stars represent the observed distribution of FSD ($D_{50}<45\ \mu\text{m}$) in the survey during 1979–1995. The sources of the FSD observations and the background bathymetry refer to Section 6.2.2 and Figure 6.4.

Figure 6.10 shows that the simulated spatial distributions of the fine sediment deposits in 1979 and 1995 are similar in the whole RSRs, except the Jiangjiasha ridge and the southern area. The results show that nearly all these “FSD” points are located within the calculated fine sediment deposition range with only one exception (i.e. the northernmost FSD” point; see Figure 6.10). Even this northernmost “FSD” point is close to our artificially defined boundary of the deposition zone (i.e. >10 cm deposition thickness). The overall agreement between simulations and the field measurements during 1979–1995 is considered satisfactory.

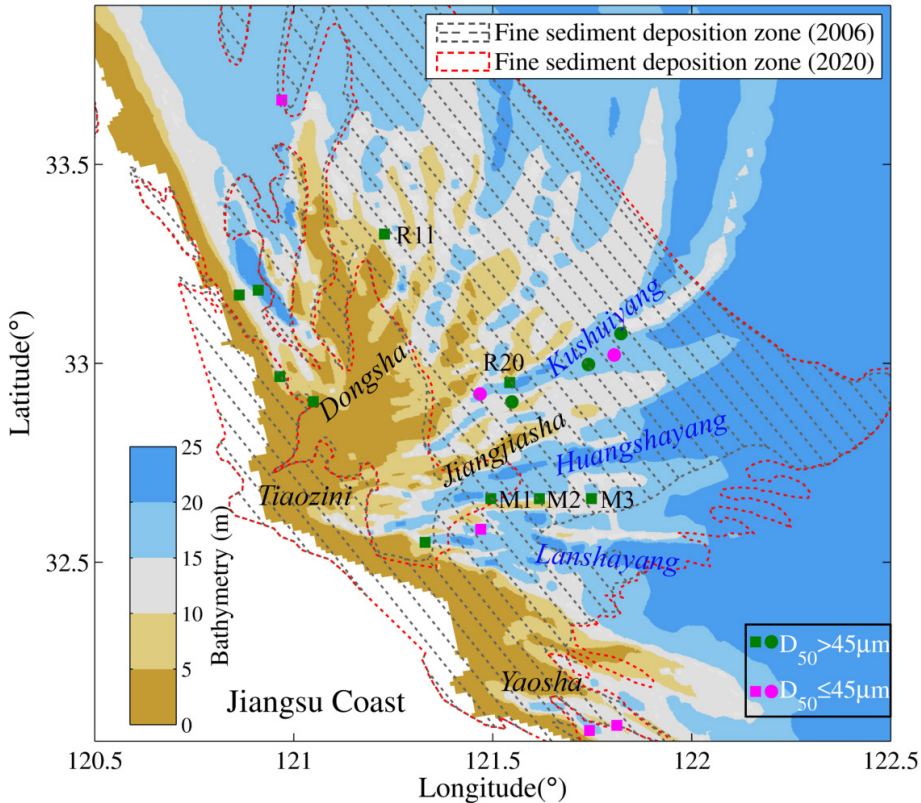


Figure 6.11: Simulated sedimentation range of fine sediment ($D_{50}=15\ \mu\text{m}$) in the RSRs in 2006 and 2020, respectively. The sedimentation range is determined by the criterion that the accumulated deposition thickness is larger than 10 cm since 1855. The green and red dots represent the observed distributions of the relatively coarser sediment and FSD (taking $45\ \mu\text{m}$ as a criterion), respectively. The sources of the observations and the background bathymetry refer to Section 6.2.2 and Figure 6.4.

Figure 6.11 shows the simulated spatial distributions of fine sediment deposition in 2006 and 2020, which depict similar patterns compared with those in 1979 and 1995 (see Figure 6.10). For example, there is still little fine sediment deposition in the Dongsha ridge. The measurements of two categories: grain size $> 45\ \mu\text{m}$ and grain size $\leq 45\ \mu\text{m}$ (i.e. “FSD” point) of the field surveys in 2006 and 2011 are compared with the simulations. The results show that all “FSD” points are located inside the simulated fine sediment deposition range, indicating a good agreement. For the points with grain size $> 45\ \mu\text{m}$, the near shore points are perfectly out of the simulated zone of the fine sediment, whereas the offshore points have a relatively poor agreement. Specifically, (1) at point R11, the measured grain size is $53\ \mu\text{m}$, which is a little larger than our pre-defined criterion (i.e., $45\ \mu\text{m}$) of the “FSD”. Besides, it locates near the boundary of the simulated

fine sediment deposition range. Thus, the simulated results can be considered as acceptable. (2) The points in the Kushuiyang channel, as aforementioned in section 6.2.2, display a fairly complicated distribution of fine and coarse sediment. It may be due to the complex bathymetry and the local flow structures, leading to a complex distribution of the fine sediments. Reproducing the variations of grain sizes requires a morphological model with multiple sediment fractions based on a high-resolution bathymetry, which is beyond the ability and focus of the present study. (3) Points M1, M2 and M3 located on the Hetunsha ridge, are located between the zones with periodical changes of fine sediment depositions, i.e. the vicinity areas of the Jiangjiasha ridge and the Lanshayang channel, according to the results from 1979 to 2020 (Figure 6.10, 6.11). The missing geomorphological feature near these three points may be part of the reason. Nevertheless, the deviation is acceptable given our rather schematized morphological model.

In summary, the agreements between the simulations and the existing observed data (both the FSD and the relative coarser sediment) demonstrate that the model performance on the overall spatial distribution of fine sediment deposition is very reasonable.

6

6.3.3. PRELIMINARY RESULTS ON THE CONTRIBUTION OF TIDE, WAVE AND HUMAN ACTIVITIES ON THE MORPHOLOGICAL EVOLUTION OF THE JIANGSU COAST

IN this section, the relative importance of different factors (i.e. tide, wave and human activities) on the morphological evolution of the Jiangsu coast (including the AYD and RSR) is analyzed in terms of the general morphological evolution pattern and the erosion/deposition volume of fine sediment.

Figure 6.12 shows the simulated morphologies along the Jiangsu coast in 2007, for different scenarios. In general, the simulated shorelines and the distribution pattern of the offshore shoals in all three scenarios (i.e. case TH, TW and TI) are similar to that in case RF. All simulated shorelines show a trend of “erosion in the north and sedimentation in the south”, which is in accordance with the historical change (Figure 6.2). Since the factors of influence change in these cases, except the tidal forcing, the results indicate the predominant role of the tide on the morphological evolution of the Jiangsu coast, whereas the effect of wave and artificial structures is of minor importance on the large-scale evolution trend.

The Jiangsu coast can be divided into three zones according to the corresponding morphological features. Figure 6.13a shows the positions of these three zones, namely zone I (representing the subaerial delta of AYD), zone II (representing the subaqueous delta of AYD), and the RSR zone. Note that, the RSR zone only contains the northern

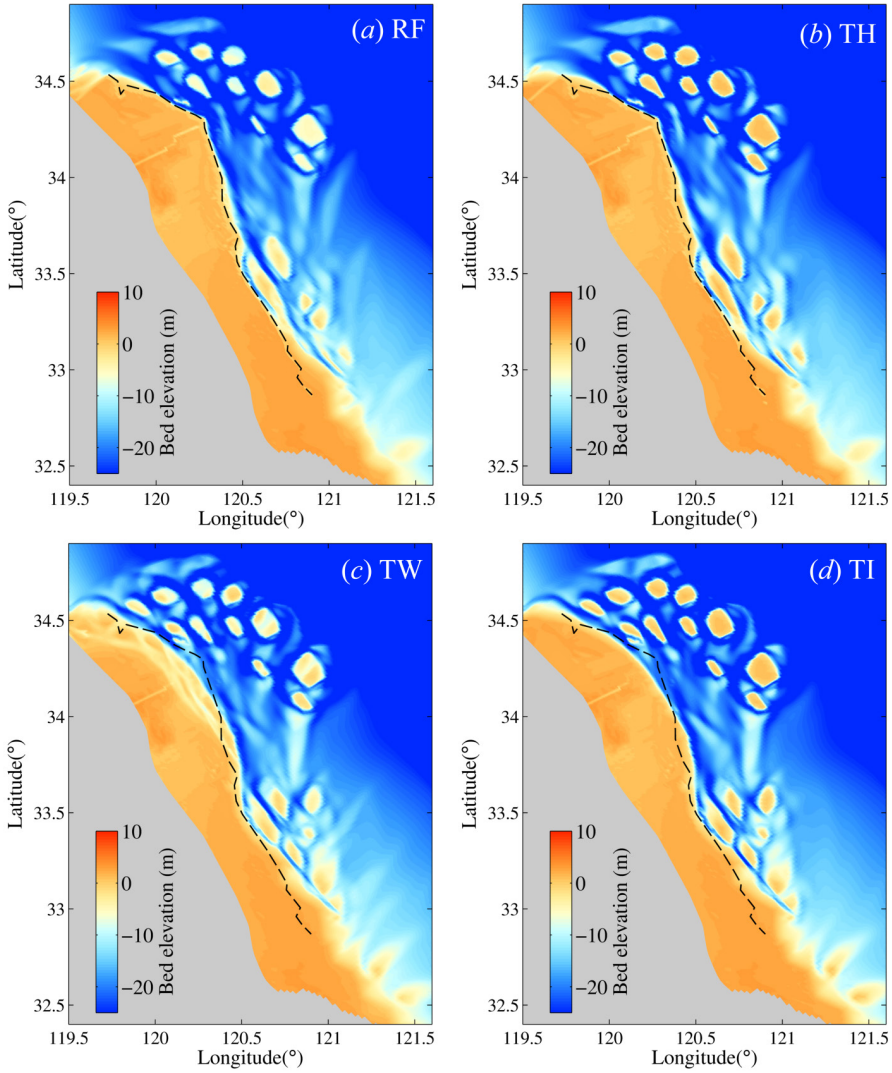


Figure 6.12: Simulated bathymetries along the Jiangsu coast in different scenarios: (a) - (d) represent the results for 2007 of case RF, case TH, case TW and case TI, respectively. Details about the model setting of these scenarios refer to Table 6.2.

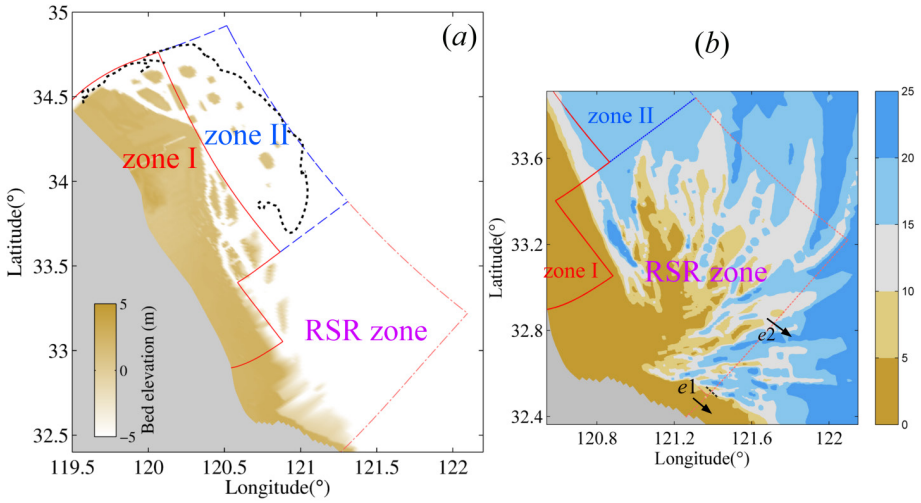


Figure 6.13: (a) Littoral zones along the Jiangsu coast: zone I (representing the subaerial AYD), zone II (representing the subaqueous AYD) and RSR zone (representing a major part of the RSRs). The black dotted lines denote the range of subaqueous delta in 1855, according to the results of the companion study. (b) Comparison between the range of the RSR zone and the present bathymetry in the RSRs. The southern boundary of the RSR zone is divided into two transects: e1 and e2, according to local bathymetric feature.

and central part of the actual RSRs. Figure 6.13b shows the comparison between the RSR zone and the “actual” RSRs.

The net annual-averaged sediment budget (this study only refers to the fine sediment, i.e. originally discharged by the OYR) of each zone is calculated based on the sediment transport across the boundary of each zone. The unbalanced sediment input (*Input*) and sediment output (*Output*) of each zone results in sediment volume changes:

$$\Delta V = Input - Output \quad (6.1)$$

where, ΔV is the net sediment volume change (i.e. erosion or sedimentation). The calculated results (not shown here) show that net negative sediment budget (i.e. erosion) appears in zone I and zone II, whereas net positive sediment budget (i.e. sedimentation) occurs in the RSR zone. Therefore, the total sediment budget of zone I and zone II is defined as the total volume of eroded sediment, which may play a role as a sediment source for the adjacent regions. Figure 6.14 shows the erosion/deposition volume of the fine sediment in different zones. The total amounts of eroded sediment in different cases are shown in Figure 6.14a. There is no obvious difference of the erosion volume between these cases. Especially, the simulated result of case TI (consider tide only) is more or less

the same as that of case RF. This again confirms the dominant role of tide on the erosion of the AYD.

Besides similar features between these cases, different erosion patterns can be identified in the vicinity of OYR estuary between the different cases (Figure 6.12). A highlighted feature is that the offshore shoals have changed from subaerial to subaqueous when imposing wind waves (Figure 6.12). Additionally, the relative contribution of the subaerial delta (zone I) and the subaqueous delta (zone II) exhibits significant deviations in different cases (Figure 6.14b). Similarly, the contribution of these eroded sediments to the RSR zone is also different (Figure 6.14c). For instance, in the presence of waves, erosion from the subaerial delta and sedimentation in the RSR zone (case TW vs. case TI) are enhanced, however, the effect of waves can be ignored when sea dikes are considered (case RF vs. case TH). The previous understanding of the importance of the wind wave effect for the erosion of the AYD seems insufficient. Although sea dikes can greatly reduce the erosion from the subaerial delta (case TI vs. case TH; case TW vs. case RF), the volume of erosion in the subaqueous delta increases (Figure 6.14).

In summary, both the quantitative and the qualitative analyses on the morphological changes of the Jiangsu coast demonstrate that tide is the most dominant factor for the large-scale evolution of the Jiangsu coast. It determines the evolutionary trend of the shoreline, the distribution of offshore shoals, as well as the total eroded volume of the AYD. Two other factors, i.e. wave action and human activities, also give rise to more or less morphological changes. The effect of sea dikes is relatively important in the nearshore zone, such as leading to less erosion from the subaerial delta and less sedimentation in the RSRs. Waves exert an opposite effect; however, its effect is ignorable in the case with sea dikes. Nevertheless, the effect of waves on the erosion of offshore shoals (i.e. turning subaerial shoals to submerged) is remarkable.

6.3.4. TRANSPORT OF THE OYR-DERIVED SEDIMENT AFTER 1855

ACCORDING to our results in section 6.3.3, the deposition in the RSR zone occupies ~19% of the total volume of eroded sediment (Figure 6.14). The transport directions of the other ~81% of sediment deserve special attention, since such large amounts of fine sediment may give rise to significant morphological changes (e.g. mud patches; Lee and Chough, 1989; Lim et al., 2007).

Based on the annual-averaged sediment transport of case RF, the overall sediment transport pathways of each transect are calculated and presented in Figure 6.15a. With respect to the volume changes in each sub-zone, when net erosion is evident (e.g. zone II), Eq. (6.1) changes to:

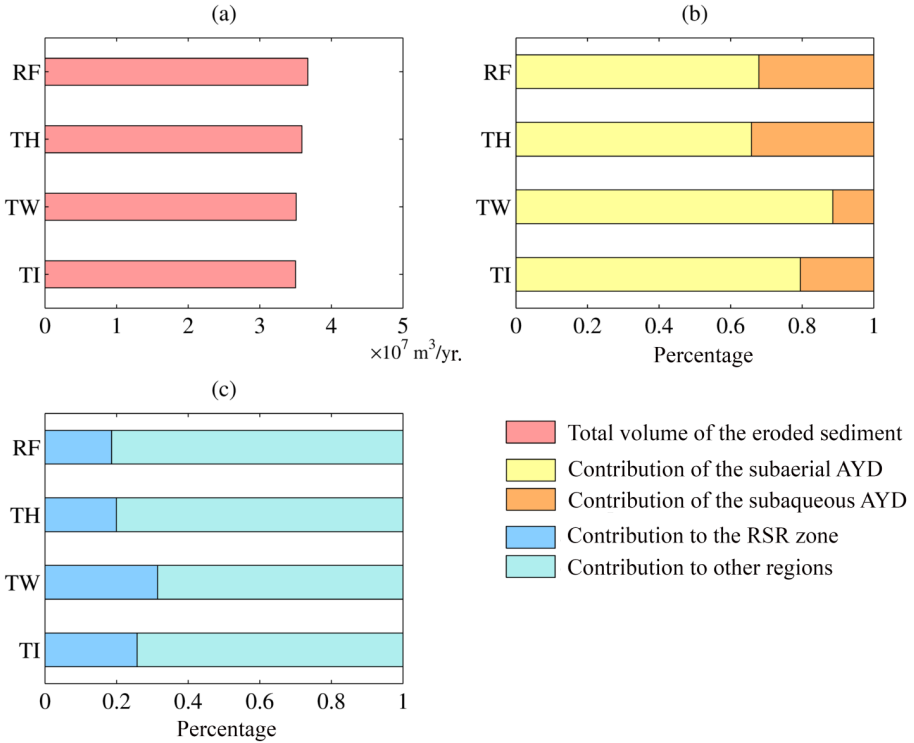


Figure 6.14: Erosion and deposition volume of fine sediment along the Jiangsu coast in different scenarios, taken in a 152 year simulation, since 1855 as an example. (a) Total volume of annual sediment budget provided by the AYD in difference cases; (b) relative contribution of the subaerial and subaqueous portion of the AYD to the eroded sediment in difference cases; (c) relative contribution of the eroded sediment from the AYD to the RSRs and other regions in difference cases.

$$Input + Erosion = Output \quad (6.2)$$

When net sedimentation is evident (e.g. RSR zone), Eq. (6.1) becomes:

$$Input = Output + Sedimentation \quad (6.3)$$

Subsequently, the relative contribution of each term (i.e. Input, Erosion, Output and Sedimentation) in terms of percentage can be calculated for each sub-zone through Eq. (6.2) or Eq. (6.3). In the present study, we mainly focus on the RSR zone and zone II. The results of these zones are shown in Figure 6.15b and 6.15c, respectively.

With respect to the RSR zone (Figure 6.15b), where sedimentation is evident, the sediment gain is the only input from zone I through transects c1, d1 and e3. The sediment

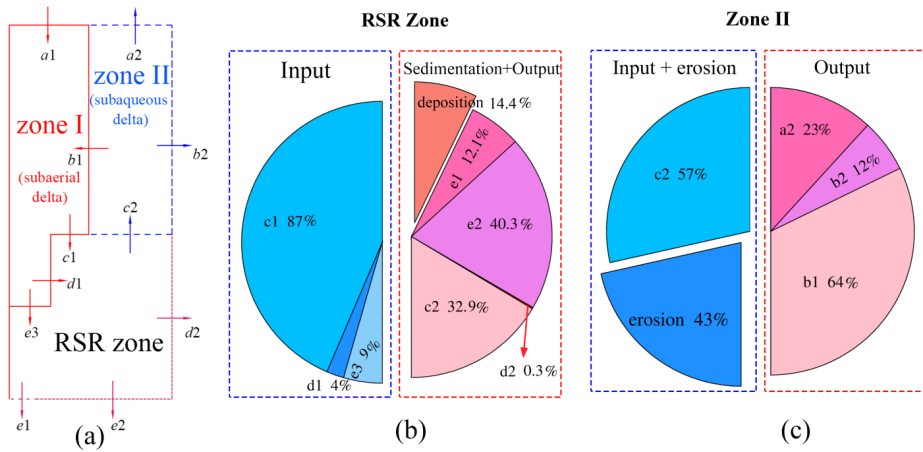


Figure 6.15: (a) Schematic diagram showing the sub-zone distribution with annual-averaged sediment transport direction per transect during 1855–2007. Relative importance of sediment input and output for the RSR zone and zone II are shown in (b) and (c), respectively. The geophysical location of these two sub-zones and corresponding transects refer to Figure 6.12. In figure (b) and (c), sediment input/erosion is shown by blue tint (left half of the pie chart); sediment output/sedimentation is shown by red tint (right half of the pie chart). The percentage of each transect is calculated according to the averaged sediment transport of case RF within 152 years (i.e. 1855–2007).

is mainly transported along-shore in the RSR zone, while the amount of sediment transport seaward (through transect d2) is ignorable. Half of the input sediment is transported to the further southern regions (through transects e1 and e2). Specifically, more than 1/5 of these sediments may be of benefit for the development of tidal flats and ridges in the southern part of the RSRs (through transect e1, see Figure 6.13b). Consequently, the south/southeast regions are expected to have a large quantity of the OYR-derived sediment. This understanding is in accordance with observed geological evidence (e.g. Alexander et al., 1991; Kim et al., 2013), for example the existence of the OYR-derived sediment in the modern Yangtze River delta (Liu et al., 2010).

Regarding zone II, the single external sediment source is provided by the RSR zone (through transect c2), while local bottom erosion serves as the internal sediment source (Figure 6.15c). Different from the RSR zone, more than 80% of the output sediment transports in the cross-shore direction. In particular, the landward transport (through transect b1) is dominant compared with the seaward and northward transport. Moreover, an anti-clockwise sediment transport circulation can be identified among these three zones (i.e. $c2 \rightarrow b1 \rightarrow c1, d1, e3 \rightarrow c2$ in Figure 6.15a). Besides, for the northernmost boundary of zone I and zone II, the magnitude of net sediment input (through transect a1) accounts for ~87% of the net sediment output (through transect a2). Thus, there is a small amount of sediment transporting towards northern regions (i.e. the Haizhou Bay). Geological

studies have provided evidence for the northward sediment transport pathway along the northern coast (i.e. through analyzing the measured grain-size trend; Zhang and Feng, 2011).

6.4. DISCUSSION

6.4.1. THE CONTRIBUTION OF THE OYR-DERIVED SEDIMENT TO THE RSRs

THE contribution of the OYR to the fine sediment contents in the RSRs can be divided into two stages, caused by the abrupt cutoff of the OYR in 1855. In its first stage (i.e. during 1128~1855), the OYR-derived sediment not only deposited near the river mouth, but also contributed to the deposition in the RSRs (see the companion study; Chapter 5). The net sediment deposition in the RSR zone (see Figure 6.13 for location) is calculated as $\sim 1.7 \times 10^7 \text{ m}^3/\text{y}$ during that period. In the second stage (i.e. after 1855), the overall sedimentation pattern is reversed. The AYD suffered severe erosion and started to serve as the sediment source for the surrounding area. Meanwhile, the fine sediment keeps depositing in the RSR zone, approximately $6.8 \times 10^6 \text{ m}^3/\text{y}$, which is only half of that in the previous stage. Nevertheless, the results indicate that the RSRs are still fed by the OYR-derived sediment, even in the case that the OYR has shifted away.

Based on the analysis of spatial distribution of fine sediment in the RSRs (see section 6.3.2), the influence zone of the OYR-derived sediment is not only in the northern RSRs, but also covering most of the southern RSRs, especially the tidal flats and the ridges (Figure 6.9). Thus, according to the simulation results in these two stages, we conclude that: (1) the OYR is one of the sediment sources of the RSRs; (2) since the sediment derived by the OYR is mainly silt (15~45 μm , Wang, 2002), the sediment feeding the RSRs is mainly fine sediment; (3) the deposition range of the OYR-derived sediment on the RSRs is not restricted only to the northern RSRs, nor restricted to the period of 1128~1855.

According to the present study and the companion study (Chapter 5), the total amount of sediment feeding the RSR zone (see Figure 6.13 for location) by the OYR-derived sediment is $\sim 5.7 \times 10^9 \text{ m}^3$ during 1578~2007. Note that, this value may be underestimated for the whole RSRs, as the southern part of the RSRs does not include the pre-defined RSR zone in this study. The annual-averaged sediment discharge of the modern Yangtze River is $1.8 \times 10^8 \text{ m}^3/\text{y}$ (Saito et al., 2001). Thus, the amount of OYR-derived fine sediment deposition in the RSRs (i.e. $\sim 5.7 \times 10^9 \text{ m}^3$ during ~430 years) is equivalent to the accumulated sediment discharge of the Yangtze River in ~32 years. It is reported that the paleo-Yangtze River has directly discharged into the central Jiangsu coast during the late Pleistocene (Wang et al., 2012), and the river mouth has gradually shifted southward

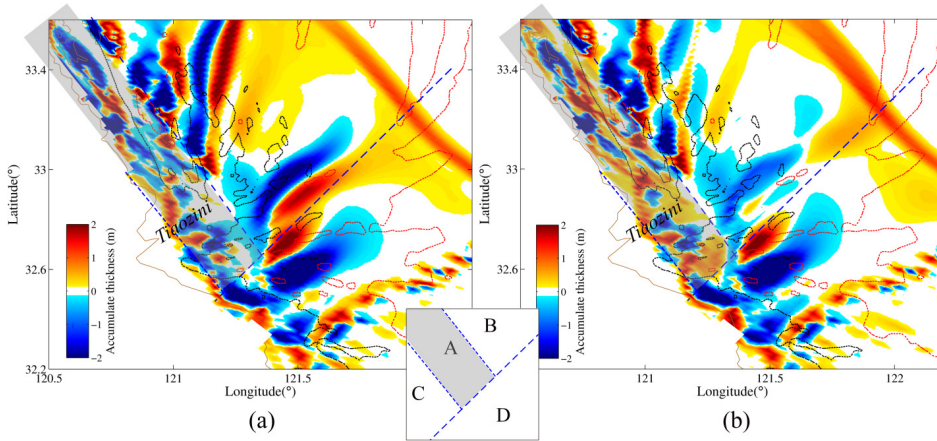


Figure 6.16: Accumulated thickness of fine sediment in the RSRs during ~50 years: (a) case RF; (b) case BS. The brown line denotes the shoreline in 1855 in the model. Black and red dotted lines denote the 5 m and 15 m isobaths. The source for the bathymetric data and shoreline can refer to Figure 6.4. Four sub-zones (i.e. A, B C and D) are divided by blue dashed lines. The number and position of these zones are displayed in the conceptual sketch.

in the past thousands of years. Thus, the OYR-derived volume of fine sediment is not substantial regarding the overall sediment contents in the RSRs. Nevertheless, the OYR-derived sediment can influence the surface sediment feature of the RSRs, which is in a silt-sand dominated range (Liu et al., 1989).

6.4.2. FATE OR FORTUNE: WITH A CONSIDERATION OF COARSENESED SEDIMENT BED

GRADUALLY coarsening bottom sediment in the RSRs and around the AYD has been reported in several recent studies (Zhang, 2012; Chen et al., 2014). As the AYD is a major sediment source for the RSRs nowadays, the coarsened bottom sediment may exert impact on the evolution of fine sediment deposition in the RSRs. The influence is explored through comparing the results of case RF and case BS within a 50 years simulation, i.e. without/with a consideration of coarsened sediment bed (Table 6.2). Figure 6.16a and 6.16b show the simulated accumulated thickness of fine sediment in case RF and case BS, respectively. To illustrate the spatial varying influences in the RSRs, four sub-zones are divided and numbered.

The results depict that the sub-zone C and the sub-zone D, i.e. the nearshore region of the RSRs and the southern RSRs, are less influenced. However, the changes of the other two sub-zones are extraordinary obvious. The sub-zone A contains part of the tidal flats zone along the central Jiangsu coast and the intermediate zone of the RSRs

(see section 6.2.2). Compared with the results of case RE, more fine sediment deposition can be identified in case BS. On the other hand, the results reveal that, the sub-zone B, i.e. the northern offshore zone of the RSRs, has less deposition of fine sediment in case BS than in case RE. Besides, when coarsened bottom sediment is considered, the severe sedimentation/erosion with “band” patterns is significantly reduced in terms of both intensity and spatial range. Thus, the seaward part of the Tiaozini ridge and the northern offshore zone of the RSRs are sensitive to the coarsened bottom sediment.

6.4.3. LIMITATIONS AND SUGGESTIONS FOR THE FURTHER RESEARCH

THE short-time scale forcing, i.e. due to storms / typhoons, is not included in the present study. On the one hand, it is difficult to consider it in a long-term morphodynamic model; on the other hand, a storm may significantly alter the morphologies (Liu et al., 1989; Yin et al., 2008). However, it is unknown whether and how the morphology can be recovered by tidal regimes after a storm. Future studies on the morphological changes by a storm on a long-term scale are required.

The wave effect is considered in this study, but in a highly schematic manner. The sensitivity analyses indicate that the wave effect is of minor importance on the large-scale morphological changes of the Jiangsu coast. However, it is still necessary to verify the wave effect more comprehensively. Therefore, long-term measurements on the wind/wave climate are required. Furthermore, due to the temporal and spatial variation of the wind wave climate, measurements should be carried out on a sufficient number of stations around the whole Jiangsu coast.

According to our simulations, the RSRs cannot be formed based on a linearized initial bathymetry on a time scale of hundreds of years with a sediment supply from the OYR. Moreover, the existence of Paleo-Yangtze River-derived fine sand in the RSRs has been demonstrated by geological studies (e.g. Wang et al., 2012; Gao and Collins, 2014). A recent morphodynamic study also indicated that, it takes thousands of years for the development of such radial-shape ridges from an initial linearized initial bathymetry, assuming infinite bottom sediment availability (Tao et al., 2015 submitted to Journal of Geophysical Research; personal communication). Therefore, before the OYR discharged into SYS, several preliminary submerged ridges might already have existed in the area of the RSRs. These preliminary ridges are probably developed by a long-term interaction between local tidal regimes and previously existing sediment, e.g. derived by the Paleo-Yangtze River. With a huge external sediment supply by the OYR, the morphological evolution in the RSRs may have been significantly accelerated, which was beneficial for the growth of the submerged ridges to subaerial ridges. To assess the reliability of this

hypothesis, an important aspect is to validate the existence of the “significant evolution stage” of the RSRs under the effect of the OYR. In a future study, we suggest to use a series of schematized radial-shaped ridges as the initial bathymetry in the RSR zone instead of the linearized bathymetry. This would enhance the understanding of the morphological evolution of the RSRs.

6.5. CONCLUSION

CURRENT understanding of the Jiangsu coast evolution is mainly based on the historical records, marine charts and geological measurements. In this study, our earlier process-based morphodynamic model (see the companion study; Chapter 5) has been modified and extended to investigate the morphodynamic changes along the Jiangsu coast after 1855, when the OYR shifted away. In addition to the tidal forcing, waves and human interventions (i.e. sea dikes) are considered in the model. The overall evolutionary trend of the shoreline, which is “erosion in the north and sedimentation in the south”, and the spatial distribution of the offshore shoals, are well reproduced by the model. Furthermore, the distribution pattern of the fine sediments has a reasonable agreement with bed sample surveys conducted in different periods.

Subsequently, the relative importance of tide, wave and artificial sea dikes on the morphological evolution of the Jiangsu coast is investigated, through a qualitative analysis of the evolution pattern and a quantitative comparison of the erosion/deposition volume of the fine sediment. Tide is demonstrated as the most dominant factor, which determines the overall evolution trend of the shoreline, the distribution of the offshore shoals and the total erosion volume in the AYD. The effect of sea dikes is relatively important in protecting the subaerial delta in the nearshore zone. Wave exerts an opposite effect; however, its effect is ignorable compared to that of the sea dikes. Nevertheless, the effect of waves on the erosion of offshore shoals (i.e. turning subaerial shoals to submerged) is remarkable.

Our results show that the OYR-derived sediment is one of the fine sediment sources for the RSRs. The OYR-derived sediment covers not only most regions in the RSRs, but also reaches the further northern and southern zones of the Jiangsu coast. Also, the period of influence is not restricted to 1128~1855. Furthermore, the amount of the OYR-derived sediment deposition in the RSRs is fairly small compared with the total sediment volume in the RSRs. Combining our results with existing geological evidence, we conclude that there could have been a series of preliminary ridges before the OYR discharged into the SYS in 1128. The OYR-derived sediment has probably accelerated the growth of these ridges. Future studies are required to assess the reliability of this hypoth-

esis.

The spatial distribution pattern of fine sediment indicates a spatially varied sedimentary environment throughout the RSRs. It is consistent with the grain size differences between the Tiaozini ridge and the Dongsha ridge. Additionally, the spatial deposition pattern of fine sediment can be significantly influenced by the gradually bottom sediment coarsening process along the Jiangsu coast. It would lead to less fine sediment depositions in the northern offshore zone of the RSRs, while more fine sediment depositions in the seaward part of the central RSRs (i.e. the Tiaozini ridge).

7

CONCLUSIONS AND FUTURE WORK

To strive, to seek, to find, and not to yield.

Alfred, Lord Tennyson (1809 ~ 1892)

7.1. SYNTHESIS AND CONCLUSIONS

THE present study focuses on increasing understanding of the hydrodynamic and morphodynamic processes along the Jiangsu coast, with an emphasis on analyzing mechanisms controlling the long-term evolution of the Jiangsu coast. Through successive steps of analyzing the existing data (i.e. geological evidences and historical maps), establishing numerical models and conducting flume experiments, the objectives which have been reached are listed as follows.

7.1.1. HYDRODYNAMIC ASPECT (TIDAL WAVE SYSTEMS)

TIDE, especially the M2 tide, is the most crucial driving force for the Jiangsu coast. The formation mechanism of the local tidal wave system is always hypothesized relating to the geographic position of the Shandong Peninsula. Little effort has been made to verify this hypothesis. As a distinct tidal current pattern, the radial tidal current pattern off the Jiangsu coast also experiences a similar hypothesis: related to the geographic position of the Shandong Peninsula and local morphological feature (i.e. radial-shaped morphology). Further discussions on the tidal wave systems and tidal current off the Jiangsu coast have been carried out in Chapter 2, mainly focusing on the role the Shandong Peninsula and local bathymetry. Based on this chapter,

I: The rotating tidal wave system in the southern Yellow Sea is found to be formed mainly by the interaction between the north rotating tidal wave system in the northern Yellow Sea and the incoming tidal wave from the East China Sea. The Shandong Peninsula only plays a role on enhancing the local rotating tidal wave system in the southern Yellow Sea by generating locally reflected tidal waves, which changes the position of the amphidromic point eastward (Chapter 2);

II: We have verified the existence of radial tidal current around the radial sand ridges is independent with local morphologies and the geographic position of the Shandong Peninsula (Chapter 2);

7.1.2. IMPROVE THE OBS UTILIZATION IN A SILT-SAND ENVIRONMENT

SUSPENDED sediment concentration (SSC) is an important parameter for both field measurements and laboratory experiments. Two commonly used approaches for measuring SSC is suction approach and OBS instrument. Suction can catch a time-averaged SSC, however, it fails to capture the temporal variation of SSC. OBS can provide temporal information on SSC, but its ability for mixed suspensions has been demonstrated as poor. The sediments along the Jiangsu coast are mainly silt-dominated clay-silt-sand mixtures. Thus, how to enhance the accuracy of the converted OBS measure-

ments is crucial for the present and future studies. In Chapter 4, an improved approach has been proposed, which takes the grain size effect on the OBS response into account. Additionally, the ability of this approach has been evaluated through a series of laboratory experiments based on the collected field sediments of the Jiangsu coast (Chapter 3). Based on these two chapters,

III: A high sediment concentration layer (HCL) near the bottom is a feature of silty sediment under relatively large wave conditions. Through comparing the experimental results on two sediment samples with different silt content, we found that the magnitude of sediment concentration in the HCL, pattern of rippled bed greatly relate to the silt content. Smaller silt content leads to relatively small SSC in the HCL and more regular ripples under wave-current conditions (Chapter 3);

IV: An improved approach for converting OBS signal to sediment concentration for graded sediment with fine materials (i.e. silt-sand mixtures) has been proposed, taking the grain size effect on the OBS output into account. The modified approach can omit time-consuming and sometimes impossible sieving processes (e.g. for sub-silt fractions) in comparison with previous method (i.e. the “mixture of linear component response” method). The ability of this approach on enhancing the reliability of the OBS measurements over silt-sand suspension has been validated by our flume experiments (Chapter 4);

7.1.3. LONG-TERM SIMULATION OF THE MORPHODYNAMIC EVOLUTION OF THE JIANGSU COAST, WITH AN EMPHASIS ON REPRODUCING THE EVOLUTION OF THE AYD

THE derived sediment by the Yellow River during 1128~1855 not only results in a creation of a deltaic system (i.e. AYD) but also transforms the Jiangsu coast from sandy (before 1128) to silty (at present). Up to the present time, the AYD has experienced formation, progradation and erosion within a time-span of 700 years, corresponding to the shift of river course. Investigation of the evolution of the AYD may enhance our understanding of the evolution of a delta with fine sediment, especially in case that the dynamic equilibrium of many deltas has been interfered due to constructions in the upstream, such as damming the river leading to less sediment supply. However, the present understandings of these evolution stages are far from enough and even conflict with each other. For instance, previous studies (mostly using the geological methods) have failed to achieve an agreement on the relationship between the two large-scale geomorphological units along the Jiangsu coast (i.e. the AYD and the RSRs). The dramatic sediment erosion and deposition may decrease the accuracy of previous studies, because

they ignore the reworking of sediment by hydrodynamic processes (Rao et al., 2014; Barnard et al., 2013). Thus, in this study, we apply a process-based morphodynamic modelling approach to reproduce the evolution of the Jiangsu coast. The evolution of the AYD is simulated and analyzed in Chapter 5 (formation and progradation stage) and Chapter 6 (erosion stage). Based on these two chapters,

V: A process-based morphodynamic model has been established to simulate the progradation of the AYD (1578~1855). In spite of the simplifications on model setting, detailed comparisons between the simulations and the historical data reveal that the model can satisfactorily reproduce the progradation stage of the AYD (Chapter 5);

VI: Uncertainties in the morphodynamic model settings are inevitable due to the lack of historical data. Through series of scenarios, the influence of uncertainties on the development and the distribution of the delta have been investigated. The tide is the key factor in determining the shape of the AYD. Sediment supply is dominant with respect to the progradation rate and the size of delta, while the relative area ratio between subaerial and subaqueous delta is independent of sediment availability. In contrast, the bottom slope of the accommodation zone has a considerable effect on determining the distribution location of the deltaic system and the relative ratio between the subaerial and the subaqueous delta, but its effect on the overall area of the delta is secondary. The effects of c/q ratio (i.e. the ratio between river sediment concentration and water discharge) and temporal variation of sediment concentration are demonstrated to be minor (Chapter 5);

VII: The process-based morphodynamic model has been extended to investigate the morphodynamic changes along the Jiangsu coast after 1855 (the erosion stage), when the OYR shifted away. At this stage, the fluvial influence is absent, whereas wind waves and human interventions (i.e. sea dikes) are considered in addition to the tidal forcing. Relative importance of tide, wave and artificial sea dikes on the morphological evolution of the Jiangsu coast after 1855 has been investigated. Tide is demonstrated as the most dominant factor, which determines the overall evolution trend of shoreline, distribution of the offshore shoals and the total erosion volume in the AYD. The effect of sea dikes is relatively important on protecting the subaerial delta in the nearshore zone. Wave exerts an opposite effect; however, its effect is ignorable in case of implementation of sea dikes. Nevertheless, the effect of wave on the erosion of offshore shoals (i.e. turning subaerial shoals to submerged) is remarkable (Chapter 6);

VIII: The OYR-derived sediment has been demonstrated to be one of the fine sediment sources for the RSRs. The OYR-derived sediment not only covers most regions of the RSRs but also reaches further northern and southern zones of the Jiangsu coast. Be-

sides, the influencing period is not restricted in the period of 1128–1855. Furthermore, the spatial distribution pattern of fine sediment indicates a spatially varying sedimentary environment throughout the RSRs. Additionally, the spatial deposition pattern of fine sediment can be significantly influenced by the coarsening process of bottom sediment along the Jiangsu coast (Chapter 6).

7.2. FUTURE WORK AND RECOMMENDATIONS

ALTHOUGH the present work enhances the understanding of the local tidal wave system, converting OBS signal for fine mixed sediment and long-term evolution of the Jiangsu coast, future work is required to further update our knowledge:

(1) Although the radial tidal current has been demonstrated to be independent with the local bathymetry, local radial morphological feature may be related to the local hydrodynamic features (such as suitable water depth and tidal current velocity), sediment availability (the amount of sediment) and the evolution length of time (~thousands of years). Determining the influence of these parameters is critical for investigating the long-term evolution of the RSRs and is favorable for examining the reliability of various conflicting geological conclusions.

(2) Besides waves, the silt-dominated sediment is also sensitive to the strong wind conditions, especially in shallow coastal waters. It is difficult to carry out field measurements during rough weather. Thus, future studies should pay more attention to the influence of wind through flume experiments.

(3) We suggest further verifying the capability of the proposed approach on converting OBS signal for fine mixed sediment, such as more detailed discussions on the sensitivity of the criterion on selecting the accompanying sediment.

(4) Due to the restriction of computational efficiency, wind wave forcing has not been imposed in the long-term morphological model for simulating the progradation of the AYD. Although the delta during that period (i.e. 1128–1855) is classified to be a tide-fluvial co-dominated system, it is worthwhile to evaluate the contribution of wind waves on the overall progradation trend of the AYD, especially the distribution and the shape of the offshore shoals.

(5) Although we have considered the wind wave effect during the erosion stage of the AYD (i.e. since 1855), it is only considered in a schematic manner due to both the computational efficiency and the complexities of wind wave climate around the Jiangsu coast. To achieve more accurate estimation of wind wave effects on the erosion of the Jiangsu coast, a more complex model with a consideration of the spatial and temporal variation of the wind wave climate would need to be conducted in the future.

(6) Associated our results with the existing geological evidence, we assume that there would be a series of preliminary ridges at the present location of the RSRs before the OYR discharged into the southern Yellow Sea in 1128. The functionality of the OYR-derived sediment is probably to accelerate the growth of these ridges. Future studies are required to assess the reliability of this hypothesis.

(7) Although several geochemical and geological studies have been applied to investigate the role of the modern Yangtze River, these studies are failed to reach an agreement with respect to its contribution to the RSRs. It is preferable to discuss the role of the modern Yangtze River through a morphodynamic modelling approach.

REFERENCES

- Ahn, Y., Bricaud, A., Morel, A., 1992. Light backscattering efficiency and related properties of some phytoplankters. *Deep Sea Res.* 39, 1835–1855.
- Alexander, C.R., DeMaster, D.J., Nittrouer, C.A., 1991. Sediment accumulation in a modern epicontinental shelf setting: the Yellow Sea. *Mar. Geol.* 98, 51–72.
- An, H.S., 1977. A numerical experiment of the M2 tide in the Yellow Sea, *J. Oceanogr.* 33 (2), 103–110.
- Atlas of the Oceans Editorial Board, 1993. *Marine Atlas of the Bohai Sea, Yellow Sea and East China Sea (Hydrological)*. The Ocean Press, Beijing.
- Baker, E.T., Lavelle, J.W., 1984. The effect of particle size on the light attenuation coefficient of natural suspensions. *J. Geophys. Res. Ocean.* 89, 8197–8203.
- Bao, X.W., Gao, G.P., Yan, J., 2001. Three dimensional simulation of tide and tidal current characteristics in the East China Sea, *Acta Oceanol Sin* 24 (2), 135–149.
- Bartzke, G., Bryan, K.R., Pilditch, C.A., Huhn, K., 2013. On the Stabilizing Influence of Silt on Sand Beds. *J Sediment Res* 83, 691–703.
- Battisto, G.M., Friedrichs, C.T., Miller, H.C., Resio, D.T., 1999. Response of OBS to mixed grain size suspensions during Sandy Duck'97. *Coastal Sediments Conference 99*, ADCE, New York. 297-312.
- Berne, S., Vagner, P., Guichard, F., Lericolais, G., 2002. Pleistocene forced regressions and tidal sand ridges in the East China Sea. *Mar. Geol.* 188, 293–315.
- Black, K.P., Rosenberg, M.A., 1994. Suspended sand measurements in a turbulent environment: field comparison of optical and pump sampling techniques. *Coast. Eng.* 24, 137–150.
- Bunt, J.A.C., Larcombe, P., Jago, C.F., 1999. Quantifying the response of optical backscatter devices and transmissometers to variations in suspended particulate matter. *Cont. Shelf Res.* 19, 1199–1220.
- Cai, F., Su, X., Liu, J., Li, B., Lei, G., 2009. Coastal erosion in China under the condition of global climate change and measures for its prevention. *Prog. Nat. Sci.* 19, 415–426.
- Cai, M.L., Ma, Z.Q., 1992. On the feasibility of port building in the areas of Jiangsu residual shoal using the tidal-channels-a case study of Huangsayang. *Coast. Eng.* 11, 34–42 (In Chinese with English abstract).
- Caldwell, R., Edmonds, D., 2014. The effects of sediment properties on deltaic processes and morphologies: A numerical modeling study. *J. Geophys. Res. Surf.* 119, 961–982.
- Campbell Scientific, 2008. Operator's manual: OBS 3+ suspended solids and turbidity Monitor.

- Cao Z.D, Yang S.S., and Yang H., 2003. Definition of Silt-sandy Beach and Its Characteristics of Sediment Movement. *Port Waterw. Eng.* 5, 1–4. (In Chinese with English abstract)
- Carter, R.W.G., Woodroffe, C.D., 1997. *Coastal Evolution: Late Quaternary Shoreline Morphodynamics*, Cambridge University Press.
- Chen, C., Wang, Y.G., Huang, H.M., Yuan, C.G., 2013. Advancement in impacts of tidal dynamics on radial sand ridges. *Port Waterw. Eng.* 8, 17–24 (In Chinese with English abstract).
- Chen, H.Q., Peng, J., Chen, S.L., Liu, F.C., 2014. Spatial variability characteristics of sediment grain size in sea area of the abandon Yellow River Delta, north of Jiangsu Province. *J. Appl. Oceanogr.* 33, 574–580 (In Chinese with English abstract).
- Chen, J., Wei, X.Q., Zhou, Y., 2012. Morphodynamics responses of the Erfenshui water-dividing beach ridge of the Tiaozini tidal sandbank, Jiangsu coast, China, *6th International Conference on Asian and Pacific Coasts (APAC)*, 175–182.
- Chen, K.F., 2008. *Research of land and ocean interactions progress of the coastal zone in Jiangsu Province since the Yellow River flows northward*, Ph.D. thesis, Nanjing Hydraulic Research Institute, China.
- Chen, K.F., Wang, Y.H., Lu, P.D., Zheng, J.H., 2009. Effects of coastline changes on tide system of Yellow Sea off Jiangsu coast, China. *China Ocean Eng.* 23, 741–750.
- Chen, X.X., Miao, J.Y., Song, Y.Q., 1993. A preliminary study of Huaihe River delta. *Mar. Sci.* 4, 10–13 (In Chinese with English abstract).
- Chen, Y., Overeem, I., Kettner, A.J., Gao, S., Syvitski, J.P.M., 2015. Modeling Flood Dynamics along the Super-elevated Channel Belt of the Yellow River over the Last 3000 years. *J. Geophys. Res. Earth Surf.* 120, 1321-1351.
- Cheng, D.Z., 2009. *Numerical Simulation of the Tides and Currents in the East China Sea*, M.Sc. thesis, Third Institute of Oceanography state Oceanic Administration, China.
- Cheng, G.D., Xue, C.T., 1997. *Sedimentary Geology of the Yellow River Delta*. Geological Publishing House, Beijing (In Chinese).
- Chinese Ministry of Water Resources, 2011. *Chinese river sediment bulletin*. Beijing (In Chinese).
- Choi, B., 1980. *A tidal model of the Yellow Sea and the Eastern China Sea*, Korea Ocean Research and Development Institute.
- Conner, C.S., De Visser, A.M., 1992. A laboratory investigation of particle size effects on an optical backscatterance sensor. *Mar. Geol.* 108, 151–159.
- Dastgheib, A., Roelvink, J.A., Wang, Z.B., 2008. Long-term process-based morphological modeling of the Marsdiep Tidal Basin. *Mar. Geol.* 256, 90–100.
- Davis, R.A., Hayes, M.O., 1984. What is a wave-dominated coast? *Mar. Geol.* 60, 313–329.
- Deltares, 2012. *Delft3D-FLOW user manual*.
- De Vriend, H., Capobianco, M., Chesher, T., de Swart, H.E., Latteux, B., Stive, M.J.F., 1993. Approaches to long-term modelling of coastal morphology: a review. *Coast. Eng.* 21, 225–269.
- Dietrich, G., 1963. *General Oceanography*, Wiley, New York.
- Dissanayake, D.M.P.K., Roelvink, J.A., van der Wegen, M., 2009. Modelled channel patterns in a schematized tidal inlet. *Coast. Eng.* 56, 1069–1083.

- Dissanayake, P., Wurpts, A., 2013. Modelling an anthropogenic effect of a tidal basin evolution applying tidal and wave boundary forcings: Ley Bay, East Frisian Wadden Sea. *Coast. Eng.* 82, 9–24.
- Downing, J., 2006. Twenty-five years with OBS sensors: The good, the bad, and the ugly. *Cont. Shelf Res.* 26, 2299–2318.
- Downing, J., 2008. *Effects of Sediment Size on OBS Measurements*.
- Downing, J.P., Sternberg, R.W., Lister, C.R.B., 1981. New instrumentation for the investigation of sediment suspension processes in the shallow marine environment. *Mar. Geol.* 42, 19–34.
- Dronkers, J., 2005. *Dynamics of Coastal Systems*. World Scientific, Singapore.
- Dyer, K.R., Huntley, D.A., 1999. The origin, classification and modelling of sand banks and ridges, *Cont Shelf Res.* 19, 1285–1330.
- Edmonds, D.A., Slingerland, R.L., 2009. Significant effect of sediment cohesion on delta morphology. *Nat. Geosci.* 3, 105–109.
- Egiazaroff, I.V., 1965. Calculation of Nonuniform Sediment Concentrations. *J. Hydraul. Div.* 91, 225–247.
- Elias, E.P.L., van der Spek, A.J.E., 2006. Long-term morphodynamic evolution of Texel Inlet and its ebb-tidal delta (The Netherlands). *Mar. Geol.* 225, 5–21.
- Fang, G.H., 1986. Tide and tidal current charts for the marginal seas adjacent to China, *Chin. J. Oceanol. Limnol.* 4 (1), 1–16.
- Foda, M.A., Tzang, S.Y., 1994. Resonant fluidization of silty soil by water waves. *J. Geophys. Res.* 99, 20463–20475.
- Frihy, O.E., Shereet, S.M., El Banna, M.M., 2008. Pattern of Beach Erosion and Scour Depth along the Rosetta Promontory and their Effect on the Existing Protection Works, Nile Delta, Egypt. *J. Coast. Res.* 24, 857–866.
- Fu, M.Z., Zhu, D.K., 1986. The sediment sources of the offshore submarine sand ridge field of the coast of Jiangsu Province. *J. Nanjing Univ. (Natural Sci.)* 22, 536–544 (In Chinese with English abstract).
- Fugate, D.C., Friedrichs, C.T., 2002. Determining concentration and fall velocity of estuarine particle populations using ADV, OBS and LISST. *Cont. Shelf Res.* 22, 1867–1886.
- Galloway, W.D., 1975. *Process Framework for describing the morphologic and stratigraphic evolution of deltaic depositional systems, Deltas, Models for Exploration*. Houston Geological Society, Houston, TX, 86–98.
- Gao, S., 2009. Modeling the preservation potential of tidal flat sedimentary records, Jiangsu coast, eastern China. *Cont. Shelf Res.* 29, 1927–1936.
- Gao, S., Collins, M.B., 2014. Holocene sedimentary systems on continental shelves. *Mar. Geol.* 352, 268–294.
- Gao, S.M., Li, Y.F., An, F.T., 1989. *The Formation and Sedimentary Environments of the Yellow River Delta*. Science Press, Beijing (In Chinese).

- Geleynse, N., Storms, J.E.A., Stive, M.J.F., Jagers, H.R.A., Walstra, D.J.R., 2010. Modeling of a mixed-load fluvio-deltaic system. *Geophys. Res. Lett.* 37.
- Geleynse, N., Storms, J.E.A., Walstra, D.J.R., Jagers, H.R.A., Wang, Z.B., Stive, M.J.F., 2011. Controls on river delta formation; insights from numerical modelling. *Earth Planet. Sci. Lett.* 302, 217–226.
- Gelfenbaum, G., Stevens, A., Elias, E., Warrick, J., 2009. Modeling Sediment Transport and Delta Morphology on the Dammed Elwha River, *6th Proceedings of Coastal Dynamics*. 1–15.
- Geng, X.S., Wan, Y.S., Li, S.W., Zhang, Q.N., Xu, X.S., 1983. Preliminary study on the evolution and dynamic pattern of northern Jiangsu coast. *Acta Oceanol. Sin.* 5, 62–70 (In Chinese with English abstract).
- Gibbs, R., Wolanski, E., 1992. The effect of flocs on optical backscattering measurements of suspended material concentration. *Mar. Geol.* 107, 289–291.
- Giosan, L., 2007. Morphodynamic feedbacks on deltaic coasts: Lessons from the wave-dominated Danube delta, *6th Proceedings of Coastal Sediments*. 1–14.
- Green, M.O., Bell, R.G., Dolphin, T.J., Swales, A., 2000. Silt and sand transport in a deep tidal channel of a large estuary (Manukau Harbour, New Zealand). *Mar. Geol.* 163, 217–240.
- Green, M.O., Boon III, J.D., 1993. The measurement of constituent concentrations in nonhomogeneous sediment suspensions using optical backscatter sensors. *Mar. Geol.* 110, 73–81.
- Greenwood, B., Jagger, K., 1995. Sensitivity of optical sensors to grain-size variation in the sand mode: Implications for transport measurements. Canadian Coastal Conference, *Canadian Coastal Science and Engineering Association*, Dartmouth. 383–398.
- Greenwood, B., Xu, Z.M., 2001. Size fractionation by suspension transport: a large scale flume experiment with shoaling waves. *Mar. Geol.* 176(1): 157–174.
- Gu, D.Q., Fu, J., Yan, W.W., Cong, B.L., 2012. Evaluation of coastal wetlands degradation in Yancheng city and zonal diagnosis. *Wetl. Sci.* 10, 1–7 (In Chinese with English abstract).
- Guo, X.Y., Yanagi, T., 1998. Three-dimensional structure of tidal current in the East China Sea and the Yellow Sea, *J. Oceanogr.* 54 (6), 651–668.
- Hanebuth, T.J.J., Proske, U., Saito, Y., Nguyen, V.L., Ta, T.K.O., 2012. Early growth stage of a large delta — Transformation from estuarine-platform to deltaic-progradational conditions (the northeastern Mekong River Delta, Vietnam). *Sediment. Geol.* 261–262, 108–119.
- Hu, C.H., Cao, W.H., 2003. Variation, regulation and control of flow and sediment in the Yellow River Estuary: I. Mechanism of flow-sediment transport and evolution. *J. Sediment Res.* 5, 1–8 (In Chinese with English abstract).
- Hu, D., Saito, Y. and Kempe, S., 1998. Sediment and nutrient transport to the coastal zone. *Asian change in the context of global climate change: impact of natural and anthropogenic changes in Asia on global biogeochemical cycles* 3, 245–270.
- Huang, H.J., Li, F., Pang, J.Z., 2005. *Study on the Land-Ocean Interaction between the Yellow River Delta and the Bohai and the Yellow Seas*. Science Press, Beijing.
- Huang, Y.C., Wang, W.Q., 1987 Study on the dynamic mechanism of the radial sand ridges off northern Jiangsu coast, *Acta Oceanol Sin* 9 (2), 209–215 (In Chinese with English abstract).

- Hydrographer of the Navy, 1979. *Admiralty Tide Table*, Vol.3. Pacific Ocean and Adjacent Areas, Hydrographer of the Navy, Taunton, U.K.
- Intergovernmental Oceanographic Commission, International Hydrographic Organization, and British Oceanographic Data Centre, 2003. *Centenary Edition of the GEBCO Digital Atlas*.
- Jacobs, W., Le Hir, P., Van Kesteren, W., Cann, P., 2011. Erosion threshold of sand–mud mixtures. *Cont. Shelf Res.*, *Proceedings of the 9th International Conference on Nearshore and Estuarine Cohesive Sediment Transport Processes* 31, S14–S25.
- Jimenez, J., Sanchez-Arcilla, A., Valdemoro, H., 1997. Processes reshaping the Ebro delta. *Mar. Geol.* 144, 59–79.
- Kang, Y.Q., 1984. An analytic model of tidal waves in the Yellow Sea, *J Mar Res.* 42(3), 473-485.
- Kang, S.K., Lee, S.R., Yum, K.D., 1991. Tidal computation of the East China Sea, the Yellow Sea and the East Sea, *Oceanography of Asian Marginal Seas*, ed. Takano, K. (Elsevier Oceanography Series 54), 25-48.
- Kang, S.K., Lee, S.R., Lie, H.J., 1998. Fine grid tidal modeling of the Yellow and East China Seas, *Cont. Shelf Res.* 18 (7), 739-772.
- Kang, S.K., Jung, K.T., Kim, E.J., So, J.K., Park, J.J., 2013. Tidal regime change due to the large scale of reclamation in the west coast of the Korean Peninsula in the Yellow and East China Sea, *J. Coast. Res.* 65, 254-259.
- Kidder, T.R., Zhuang, Y., 2015. Anthropocene archaeology of the Yellow River, China, 5000-2000 BP. *Holocene* 25, 1627–1639.
- Kim, W., Dai, A., Muto, T., Parker, G., 2009. Delta progradation driven by an advancing sediment source: Coupled theory and experiment describing the evolution of elongated deltas. *Water Resour. Res.* 45, w06428.
- Kim, W., Doh, S.J., Yu, Y., Lee, Y. II, 2013. Magnetic evaluation of sediment provenance in the northern East China Sea using fuzzy c-means cluster analysis. *Mar. Geol.* 337, 9–19.
- Kineke, G.C., Sternberg, R.W., 1992. Measurements of high concentration suspended sediments using the optical backscatterance sensor. *Mar. Geol.* 108, 253–258.
- Kleinhans, M.G., Van Rijn, L.C., 2002. Stochastic Prediction of Sediment Transport in Sand-Gravel Bed Rivers. *J. Hydraul. Eng.* 128, 412–425.
- Kleinhans, M.G., Weerts, H.J.T., Cohen, K.M., 2010. Avulsion in action: Reconstruction and modelling sedimentation pace and upstream flood water levels following a Medieval tidal-river diversion catastrophe (Biesbosch, The Netherlands, 1421–1750AD). *Geomorphology* 118, 65–79.
- Kuang, C., Mao, X., Liu, P., Deng, L., Gu, J., Ma, Z., Du, D., Yang, J., Liu, F., Song, H., 2015. Influence of Wind Force on a Silt-Muddy Coast: Huanghua Harbor Coast, China. *J. Waterway, Port, Coastal, Ocean Eng.* 144,05015001.
- Lamb, M.P., Parsons, J.D., 2005. High-density suspensions formed under waves. *J. Sediment. Res.* 75, 386–397.
- Lambe, T.W., Whitman, R.V., 1979. *Soil mechanics, SI version*. Wiley.
- Larsen, L.H., Cannon, G.A., Choi, B.H., 1985. East China Sea tide currents, *Cont. Shelf Res.* 4, 77-103.

- Lee, J.C., Jung, K.T., 1999. Application of eddy viscosity closure models for the M2 tide and tidal current in the Yellow Sea and the East China Sea, *Cont. Shelf Res.* 19, 445-475.
- Lee, H., Chough, S., 1989. Sediment distribution, dispersal and budget in the Yellow Sea. *Mar. Geol.* 87, 195-205.
- Lee, S., Lie, H.J., Cho, C.H., Kang, S.K., Teague, W.J., Chang, K., Song, K.M., Oh, K.H., 2011. Vertical structure of the M2 tidal current in the Yellow Sea, *Ocean Sci. J.* 46(2), 73-84.
- Lesser, G.R., Roelvink, J.A., van Kester, J.A.T.M., Stelling, G.S., 2004. Development and validation of a three-dimensional morphological model. *Coast. Eng.* 51, 883-915.
- Li, C.X., Zhang, J.Q., Fan, D.D., Deng, B., 2001. Holocene regression and the tidal radial sand ridge system formation in the Jiangsu coastal zone, East China. *Mar. Geol.* 173, 97-120.
- Li, F., Li, Y.Z., Zhang, X.R., 2001. Impact of variation of water and sediment fluxes on sustainable use of marine environment and resources in the Huanghe river estuary and adjacent sea III. Impact of long-term stabilization of the lower course of the Huanghe river on the construction of coas. *Stud. Mar. Sin.* 42, 68-82 (In Chinese with English abstract).
- Li, L., 2003. *Numerical simulation with finite elements method in the Bohai Sea, the Yellow Sea and the East China Sea*, Ph.D. thesis, Ocean University of China, China.
- Li M.G., Cao Z.D., 2009. Review on the study of sediment problems on the silt-sandy coast. *J Sediment Res*, 2, 72-80. (In Chinese with English abstract)
- Li, M.Z., King, E.L., 2007. Multibeam bathymetric investigations of the morphology of sand ridges and associated bedforms and their relation to storm processes, Sable Island Bank, Scotian Shelf. *Mar. Geol.* 243, 200-228.
- Li, W., van Maren, D.S., Wang, Z.B., de Vriend, H.J., Wu, B.S., 2014. Peak discharge increase in hyperconcentrated floods. *Adv. Water Resour.* 67, 65-77.
- Li, Y.F., 1991. The development of the abandoned Yellow River Delta. *Geogr. Res.* 10, 29-39 (In Chinese with English abstract).
- Lie, H.J., 1999. On the Huanghai (Yellow) Sea circulation: a review by current measurements, *Acta Oceanol Sin* 18:355-373.
- Lim, D.I., Choi, J.Y., Jung, H.S., Rho, K.C., Ahn, K.S., 2007. Recent sediment accumulation and origin of shelf mud deposits in the Yellow and East China Seas. *Prog. Oceanogr.* 73, 145-159.
- Lin, H., Lv, G.N., Song, Z.Y., 2000. *Tide wave system in East China Sea and simulation of coastal process*, The Science Press, Beijing (In Chinese with English abstract).
- Liu, J., Kong, X., Saito, Y., Liu, J.P., Yang, Z., Wen, C., 2013. Subaqueous deltaic formation of the Old Yellow River (AD 1128-1855) on the western South Yellow Sea. *Mar. Geol.* 344, 19-33.
- Liu, J., Saito, Y., Kong, X., Wang, H., Xiang, L., Wen, C., Nakashima, R., 2010. Sedimentary record of environmental evolution off the Yangtze River estuary, East China Sea, during the last ~13,000 years, with special reference to the influence of the Yellow River on the Yangtze River delta during the last 600 years. *Quat. Sci. Rev.* 29, 2424-2438.
- Liu, T., Shi, X., Li, C., Yang, G., 2012. The reverse sediment transport trend between abandoned Huanghe River (Yellow River) Delta and radial sand ridges along Jiangsu coastline of China—an evidence from grain size analysis. *Acta Oceanol. Sin.* 31, 83-91.

- Liu, X., 2011. The coastal erosion of the abandoned Yellow River Delta in northern Jiangsu province, China: Based on analysis of remote sensing images, *19th International Conference on Geoinformatics*. 1–5.
- Liu, X.L., Jia, Y.G., Zheng, J.W., Hou, W., Zhang, L., Zhang, L.P., Shan, H.X., 2013. Experimental evidence of wave-induced inhomogeneity in the strength of silty seabed sediments: Yellow River Delta, China. *Ocean Eng* 59, 120–128.
- Liu, X.J., Gao, S., Wang, Y.P., 2010. Modeling channel scour associated with shore-attached tidal ridges: a case study from Rudong coast, Jiangsu Province. *Mar. Sci. Bull.* 29, 3–8 (In Chinese with English abstract).
- Liu, X.J., Gao, S., Wang, Y.P., 2011. Modeling profile shape evolution for accreting tidal flats composed of mud and sand: A case study of the central Jiangsu coast, China. *Cont. Shelf Res.* 31, 1750–1760.
- Liu, Z.X., Huang, Y.C., Zhang Q.N., 1989. Tidal Current Ridges in the Southwestern Yellow Sea. *J. Sediment. Res.* Vol. 59, 432–437.
- Liu, Z.X., Xia, D.X., 1985. A preliminary study of tidal current ridges. *Chinese J. Oceanol. Limnol.* 3, 118–133 (In Chinese with English abstract).
- Liu, Z.X., Xia, D.X., Wang, K.Y., 1998. Tidal depositional systems and patterns of China's continental shelf. *Oceanol. Limnol. Sin.* 29, 141–147 (In Chinese with English abstract).
- Ludwig, K.A., Hanes, D.M., 1990. A laboratory evaluation of optical backscatterance suspended solids sensors exposed to sand-mud mixtures. *Mar. Geol.* 94, 173–179.
- Luijendijk, A.P., Bos, K.J., Venuti, A., Serafini, E., Passacantando, D., Brotto, M.T., 2004. Numerical and physical modelling of scour development at the Malamocco inlet, *Proceedings of 2nd International Conference on Scour and Erosion*. Singapore, 1–8.
- Lunven, M., Gentien, P., 2000. Suspended sediments in a macrotidal estuary: comparison and use of different sensors. *Oceanol. Acta* 23, 245–260.
- Lynch, J.F., Irish, J.D., Sherwood, C.R., Agrawal, Y.C., 1994. Determining suspended sediment particle size information from acoustical and optical backscatter measurements. *Cont. Shelf Res.* 14, 1139–1165.
- Ma, Z.J., Melville, D.S., Liu, J.G., Chen, Y., Ren, W.W., Zhang, Z.W., Piersma, T., Li, B., 2014. Rethinking China's new great wall. *Science*. 346, 912–914.
- Maa, J.P., Kwon, J., Hwang, K., Ha, H., 2008. Critical Bed-Shear Stress for Cohesive Sediment Deposition. *J. Hydraul. Eng.* 134, 1767–1771.
- Maa, J.P., Xu, J.P., Victor, M., 1992. Notes on the performance of an optical backscatter sensor for cohesive sediments. *Mar. Geol.* 104(1), 215–218.
- Mie, G., 1908. Beitrage zur Optik truber medien. *Ann. Phys.* 377.
- Milliman, J., Qin, Y.S., Ren, M.E., Saito, Y., 1987. Man's influence on the erosion and transport of sediment by Asian rivers: the Yellow River (Huanghe) example. *J. Geol.* 95, 751–762.
- Mitchener, H., Torfs, H., 1996. Erosion of mud/sand mixtures. *Coast. Eng.* 29, 1–25.
- Mutlu Sumer, B., Hatipoglu, F., Fredsøe, J., Kaan Sumer, S., 2006. The sequence of sediment behaviour during wave-induced liquefaction. *Sedimentology* 53, 611–629.

- National marine data and information service, ed., 2005. *Tide table 2006*, Shandong Cartographic Publishing House, Jinan.
- Nguyen, D., Etri, T., Runte, K.H., Mayerle, R., 2010. Morphodynamic modeling of the medium-term migration of a tidal channel using process-based model, *Proceedings of 32nd Conference on Coastal Engineering*. Shanghai, 1–13.
- Nielsen, P., 1992. *Coastal bottom boundary layers and sediment transport*. World Scientific.
- Ogura, S., 1933. *The tides in the seas adjacent to Japan*, Hydrographic Department.
- Off, T., 1963. Rhythmic linear sand bodies caused by tidal currents, *Am. Assoc. Pet. Geol. Bull.* 47 (2), 324–341.
- Orton, G., Reading, H., 1993. Variability of deltaic processes in terms of sediment supply, with particular emphasis on grain size. *Sedimentology* 40, 475–512.
- Park, S., Lee, H., Han, H., Lee, G., Kim, D., Yoo, D., 2000. Evolution of late Quaternary mud deposits and recent sediment budget in the southeastern Yellow Sea. *Mar. Geol.* 170, 271–288.
- Partheniades, E., 1965. Erosion and Deposition of Cohesive Soils. *J. Hydraul. Div.* 91, 105–139.
- Qiu, J.F., 2005. *The study of wave and wind fields of Jiangsu Coastline*. Msc thesis. Hohai University.
- Ranasinghe, R., Swinkels, C., Luijendijk, A., Roelvink, A.D., Bosboom, J., Stive, M.J.F., Walstra, D.J., 2011. Morphodynamic upscaling with the MOREFAC approach: Dependencies and sensitivities. *Coast. Eng.* 58, 806–811.
- Rao, W.B., Mao, C.P., Wang, Y.G., Su, J.B., Balsam, W., Ji, J.F., 2015. Geochemical constraints on the provenance of surface sediments of radial sand ridges off the Jiangsu coastal zone, East China. *Mar. Geol.* 359, 35–49.
- Ren, M.E., 2006. Sediment discharge of the Yellow River, China: past, present and future-A Synthesis. *Adv. earth Sci.* 21, 551–563 (In Chinese with English abstract).
- Ren, M.E., Shi, Y., 1986. Sediment discharge of the Yellow River (China) and its effect on the sedimentation of the Bohai and the Yellow Sea. *Cont. Shelf Res.* 6, 785–810.
- Ren, M.E., Xu, T.G., Zhu, J.W., Chen, B.B. et al. ed., 1986. *The comprehensive investigative report on the resources of the coastal zone and tidal flats of Jiangsu Province*, China Ocean Press, Beijing.
- Ren, M.E., Zeng, Z.X., Cui, G.H., 1994. *China's Three Biggest Deltas*. Higher Education Press, Beijing.
- Roberts, J., Jepsen, R., Gotthard, D., Lick, W., 1998. Effects of Particle Size and Bulk Density on Erosion of Quartz Particles. *J. Hydraul. Eng.* 124, 1261–1267.
- Roelvink, J.A., 2006. Coastal morphodynamic evolution techniques. *Coast. Eng.* 53, 277–287.
- Ruggiero, P., Walstra, D.J.R., Gelfenbaum, G., van Ormondt, M., 2009. Seasonal-scale nearshore morphological evolution: Field observations and numerical modeling. *Coast. Eng.* 56, 1153–1172.
- Saito, Y., Wei, H., Zhou, Y., Nishimura, A., 2000. Delta progradation and chenier formation in the Huanghe (Yellow River) delta, China. *J. Asian Earth* 18, 489–497.
- Saito, Y., Yang, Z.S., 1995. Historical change of the Huanghe (Yellow River) and its impact on the sediment budget of the East China Sea, *Proceedings of International Symposium on Global Flues of Carbon and Its Related Substances in the Coastal Sea-Ocean-Atmosphere System*. 7–12.

- Saito, Y., Yang, Z., Hori, K., 2001. The Huanghe (Yellow River) and Changjiang (Yangtze River) deltas: a review on their characteristics, evolution and sediment discharge during the Holocene. *Geomorphology* 41, 219–231.
- Sanay, R., Voulgaris, G., Warner, J.C., 2007. Tidal asymmetry and residual circulation over linear sandbanks and their implication on sediment transport: A process-oriented numerical study, *J. Geophys. Res. Oceans*. 112, 1-15.
- Schoellhamer, D.H., 1993. Biological interference of optical backscatterance sensors in Tampa Bay, Florida. *Mar. Geol.* 110, 303–313.
- Schwiderski, E., 1980. On charting global ocean tides, *Rev. Geophys.* 18, 243-268.
- Seybold, H.J., Molnar, P., Singer, H.M., Andrade, J.S., Herrmann, H.J., Kinzelbach, W., 2009. Simulation of birdfoot delta formation with application to the Mississippi Delta. *J. Geophys. Res.* 114, F03012.
- Shen, Y.J., Huang, D.Y., Qian, C.C., 1993. Preliminary research on the formation of semi-diurnal tidal system in the Yellow Sea, *Acta Oceanol Sin* 15, 16-24 (In Chinese with English abstract).
- Shi, X.F., Liu, Y.G., Chen, Z.H., Wei, J.W., Ge, S.L., 2012. Origin, transport processes and distribution pattern of modern sediments in the Yellow Sea. *Sediments Morphol. Sediment. Process. Cont. Shelves Adv. Technol. Res. Appl. Spec. Publ.* 44 IAS 44, 321–350.
- Sistermanns, P.G.J., van de Graaff, J., van Rijn, L.C., 2001. Vertical Sorting of Graded Sediment by Waves and Currents. *Coastal Engineering Conference 2000*, ASCE. Vol. 3, 2780-2793.
- Slaa, S.T., He, Q., van Maren, D.S., Winterwerp, J.C., 2013. Sedimentation processes in silt-rich sediment systems. *Ocean Dyn.* 63, 399–421.
- Slaa, S.T., van Maren, D.S., He, Q., Winterwerp, J., 2015. Hindered Settling of Silt. *J. Hydraul. Eng.* 04015020.
- Smith, B., Bjorstad, P., Gropp, W., 2004. *Domain Decomposition: Parallel Multilevel Methods for Elliptic Partial Differential Equations*. Cambridge University Press.
- Smith, G., Moocke, G., van Ballegooyen, R., Soltau, C., 2002. Consequences of sediment discharge from dune mining at Elizabeth Bay, Namibia. *J. Coast. Res.* 185, 776–791.
- Song, D.H., Wang, X.H., Zhu, X.M., Bao, X.W., 2013. Modeling studies of the far-field effects of tidal flat reclamation on tidal dynamics in the East China Seas, *Estuar Coast Shelf S* 133, 147-160.
- Soulsby, R., 1997. *Dynamics of Marine Sands: A Manual for Practical Applications*. Thomas Telford.
- State Oceanic Administration, 2003. *Chinese sea level rise bulletin*, 2003. Beijing (In Chinese).
- Su, M., Stive, M.J.F., Zhang, C.K., Yao, P., Chen, Y.P., Wang, Z.B., 2013a. The tidal wave system in the Chinese marginal seas, *Proc. 7th Int. Conf. on Coastal Dynamic*, Arcachon, 1559-1570.
- Su, M., Wang, Z.B., Zhang, C.K., Yao, P., Stive, M.J.F., 2013b. Further research on the tidal wave system in the southern Yellow Sea, *Proc. 35th IAHR World Congress*, Chengdu.
- Su, M., Yao, P., Wang, Z.B., Zhang, C.K., Stive, M.J.F., 2015. Tidal wave propagation in the Yellow Sea. *Coast. Eng. J.* 57, 1550008.
- Sutherland, T.F., Lane, P.M., Amos, C.L., Downing, J., 2000. The calibration of optical backscatter sensors for suspended sediment of varying darkness levels. *Mar. Geol.* 162, 587–597.

- Swenson, J.B., 2005. Fluvial and marine controls on combined subaerial and subaqueous delta progradation: Morphodynamic modeling of compound-cliniform development. *J. Geophys. Res.* 110, F02013.
- Syvitski, J.P.M., Saito, Y., 2007. Morphodynamics of deltas under the influence of humans. *Glob. Planet. Change* 57, 261–282.
- Syvitski, J.P.M., 2015. Challenges in Deltas under Pressure, *Proceedings of the 36th IAHR Congress*. Den Haag, the Netherlands.
- Tang, W., 2014. *Study on the sedimentary facies and environment evolution of DT05 core in Kushuiyang Jiangsu offshore, Southern Yellow Sea*. Master thesis. Nanjing University.
- Tao, J.F., Zhang, C.K., Yang, T., 2011a. Numerical simulation of tides and sediment transport on reclamation of Jiangsu coast mud flat, *Proc. 15th China Ocean Engineering Conf*, Taiyuan, 973–977 (In Chinese with English abstract).
- Tao, J.F., Zhang, C.K., Yao, J., 2011b. Effect of large-scale reclamation of tidal flats on tides and tidal currents in offshore areas of Jiangsu Province, *J. Hohai Univ. (Natural Sciences)* 39 (2), 225–230 (In Chinese with English abstract).
- Teague, W.J., Perkins, H.T., Hallock, Z.R., Jacobs, G.A., 1998. Current and tide observations in the southern Yellow Sea. *J. Geophys. Res.* 103, 27,783–27,793.
- Tregear, T., 1965. *A geography of China*. University of London Press LTD.
- Tzang, S.Y., 1998. Unfluidized soil responses of a silty seabed to monochromatic waves. *Coast Eng* 35, 283–301.
- Uehara, K., Saito, Y., Hori, K., 2002. Paleotidal regime in the Changjiang (Yangtze) Estuary, the East China Sea, and the Yellow Sea at 6 ka and 10 ka estimated from a numerical model. *Mar. Geol.* 183, 179–192.
- Van de Meene, J.W.H., Van Rijn, L.C., 2000. The shoreface-connected ridges along the central Dutch coast - Part 1: Field observations. *Cont. Shelf Res.* 20, 2295–2323.
- Van der Wegen, M., Jaffe, B.E., Roelvink, J.A., 2011. Process-based, morphodynamic hindcast of decadal deposition patterns in San Pablo Bay, California, 1856–1887. *J. Geophys. Res.* 116, F02008.
- Van Ledden, M., 2003. *Sand-mud segregation in estuaries and tidal basins*. Delft university of technology, Delft.
- Van Ledden, M., van Kesteren, W.G.M., Winterwerp, J.C., 2004. A conceptual framework for the erosion behaviour of sand–mud mixtures. *Cont. Shelf Res.* 24, 1–11.
- van Maren, D.S., 2004. *Morphodynamics of a cyclic prograding delta: the Red River, Vietnam*. Utrecht University.
- Van Maren, D.S., 2007. Grain size and sediment concentration effects on channel patterns of silt-laden rivers. *Sediment. Geol.*, 202, 297–316.
- Van Maren, D.S., Winterwerp, J.C., Wang, Z.Y., Pu, Q., 2009. Suspended sediment dynamics and morphodynamics in the Yellow River, China. *Sedimentology* 56, 785–806.
- Van Maren, D.S., Winterwerp, J.C., Wu, B.S., Zhou, J.J., 2009. Modelling hyperconcentrated flow in

- the Yellow River. *Earth Surf. Process. Landforms* 34, 596–612.
- Van Rijn, L.C., 1993. *Principles of Sediment Transport in Rivers, Estuaries and Coastal Seas, Aqua publications*. Aqua publications, Amsterdam.
- Van Rijn, L.C., 2006. *Principles of sediment transport in rivers, estuaries and coastal seas Part 2 Supplement (update)*. Amsterdam Aqua Publications Utrecht Univ., Department of Physical Geography, Amsterdam; Utrecht.
- Van Rijn, L.C., 2007a. Unified view of sediment transport by currents and waves. I: Initiation of motion, bed roughness, and bed-load transport. *J. Hydraul. Eng.* 133, 649–667.
- Van Rijn, L.C., 2007b. Unified view of sediment transport by currents and waves. II: Suspended transport. *J. Hydraul. Eng.* 133, 668–689.
- Van Rijn, L.C., 2007c. Unified view of sediment transport by currents and waves. III: Graded beds. *J. Hydraul. Eng.* 133, 761–775.
- Van Rijn, L.C., Grasmeyer, B.T., Ruessink, B.G., 2000. *Measurement errors of instruments for velocity, wave height, sand concentration and bed levels in field conditions*, Delft Hydraulics Report. Delft, the Netherlands.
- Vorosmarty, C.J., Fekete, B.M., Tucker, B.A., 1998. *Global River Discharge, 1807-1991, V.1.1 (RivDIS)*. Data set, <http://www.daac.ornl.gov>.
- Wan, Y.S., 1989. Development and decline of ancient Huanghe River estuary delta in Northern Jiangsu. *Oceanol. Limnol. Sin.* 20, 66–74 (In Chinese with English abstract).
- Wan, Z.W., Qiao, E.L., Yuan, Y.L., 1998. Three-dimensional numerical modelling of tidal waves in the Bohai, Yellow and East China Seas, *Chin. J. Oceanol. Limnol* 29 (6), 611-616 (In Chinese with English abstract).
- Wang, G., Xu, M., 1999. Analysis of peculiarities of 92.8 flood event in the lower Yellow River. *Int. J. Sediment Res.* 14, 205–213.
- Wang, K., Fang, G., Fang, S., 1999. A 3D numerical simulation of M2 tidal and tidal currents in the Bohai Sea, Yellow Sea and the East China Sea, *Acta Oceanol. Sin.* 21, 1-13.
- Wang, K.C., 1998. Study on the evolution of the tail reaches of the Abandoned Yellow River during the Ming-Qing dynasty and its patterns, in: Liu, H.Y. (Ed.), *The Investigation of the Abandoned Yellow River Course during the Ming-Qing Dynasty*. Hohai University Press, Nanjing, 252–2 (In Chinese).
- Wang, L., Hu, S., Yu, G., Ma, M., Liao, M., 2015. Paleoenvironmental reconstruction of the radial sand ridge field in the South Yellow Sea (east China) since 45ka using the sediment magnetic properties and granulometry. *J. Appl. Geophys.* 122, 1–10.
- Wang, P.X., Li, Q.Y., Li, C.F., 2014. Paleooceanography and Sea-Level Changes, in: Wang, P.X., Li, Q.Y., Li, C.F. (Eds.), *Geology of the China Seas*. Elsevier, 469–570.
- Wang, X., Ke, X., 1997. Grain-size characteristics of the extant tidal flat sediments along the Jiangsu coast, China. *Sediment. Geol.* 112, 105–122.
- Wang, Y., 2002. *Radiating sand ridge field of the South Yellow Sea*. China Environmental Science Press, Beijing.
- Wang, Y., Aubrey, D., 1987. The characteristics of the China coastline. *Cont. Shelf Res.* 7, 329–349.

- Wang, Y., Zhang, Y.Z., Zou, X.Q., Zhu, D.K., Piper, D., 2012. The sand ridge field of the South Yellow Sea: Origin by river–sea interaction. *Mar. Geol.* 291–294, 132–146.
- Wang, Y., Zhu, D.K., Wu, X.G., 2002. Tidal flats and associated muddy coast of China, in: Terry Healy, Y.W. and J.-A.H. (Ed.), *Proceedings in Marine Science, Muddy Coasts of the World: Processes, Deposits and Function*. Elsevier, 319–345.
- Wang, Y., Zhu, D.K., You, K.Y., Pan, S.M., Zhu, X.D., 1999. Evolution of radiative sand ridge field of the South Yellow Sea and its sedimentary characteristics. *Sci. China (Series D)* 42, 97–112.
- Wang, Y., Zhu, D.K., Zou, L.F., Wang, X.Y., Jiang, S.L., Li, H.Y., Shi, B.W., Zhang, Y.Z., 1998. Evolution of radiative sand ridges field of the South Yellow Sea and its sedimentary characteristics. *Sci. China (Series D)* 28, 385–393 (In Chinese with English abstract).
- Wang, Y.H., Yin, Y., Xia, F., Zou, X.Q., 2014. Characteristics of sedimentary strata and environmental changes of Kushuiyang tidal channel in the radial tidal ridge field, southern Yellow Sea. *J. Nanjing Univ. (Natural Sci.)* 50, 564–575 (In Chinese with English abstract).
- Wang, Y.P., Gao, S., Jia, J., Thompson, C.E.L., Gao, J., Yang, Y., 2012. Sediment transport over an accretional intertidal flat with influences of reclamation, Jiangsu coast, China. *Mar. Geol.* 291–294, 147–161.
- Wang, Y.P., Zhang, R.S., 1998. Geomorphology responses on dynamics pattern of Jiangsu offshore sandbanks eastern China. *Mar. Sci.* 3, 43–47 (In Chinese with English abstract).
- Wang, Z.B., Louters, T., de Vriend, H.J., 1995. Morphodynamic modelling for a tidal inlet in the Wadden Sea. *Mar. Geol.* 126, 289–300.
- Wen, C., Liu, J., Wang, H., Xu, G., Qiu, J., Zhang, J., 2014. Sedimentary characteristics of relict deposits on the western South Yellow Sea. *J. Ocean Univ. China* 13, 205–214.
- Wen, C., Liu, J., Zhang, J.Q., Qiu, J.D., Diao, S.B., Yue, B.J., Sun, L.S., Kong, X.H., 2011. Sedimentary characteristics and evolutionary history of the distal part of the tidal sand ridges in the south Yellow Sea, off the Jiangsu coast. *Mar. Geol. Quat. Geol.* 31, 1–9 (In Chinese with English abstract).
- Winterwerp, J.C., 2006. Stratification effects by fine suspended sediment at low, medium, and very high concentrations. *J. Geophys. Res.* 111, C05012.
- Winterwerp, J.C., Van Kesteren, W.G., 2004. *Introduction to the physics of cohesive sediment in the marine environment*. Elsevier.
- Wren, D.G., Barkdoll, B.D., Kuhnle, R. A., Derrow, R.W., 2000. Field techniques for suspended-sediment measurement. *J. Hydraul. Eng.* 126(2), 97–104.
- Wright, L.D., Coleman, J.M., 1973. Variations in morphology of major river deltas as functions of ocean wave and river discharge regimes. *Am. Assoc. Pet. Geol. Bull.* 57, 370–398.
- Wright, L.D., Coleman, J.M., 1974. Mississippi River Mouth Processes: Effluent Dynamics and Morphologic Development. *J. Geol.* 82, 751–778.
- Wright, L.D., Thom, B.G., 1977. Coastal depositional landforms: a morphodynamic approach. *Prog. Phys. Geogr.* 1, 412–459.
- Xia, F., Zhang, Y.Z., Wang, R.F., Liu, J.P., Zhang, Z.K., Peng, X.Q., 2015. Review for the studies on sedimentation range of the Abandoned Yellow River subaqueous delta, North Jiangsu plain

- coast. *Acta Geogr. Sin.* 70, 29–48 (In Chinese with English abstract).
- Xing, F., Wang, Y.P., Wang, H.V., 2012. Tidal hydrodynamics and fine-grained sediment transport on the radial sand ridge system in the southern Yellow Sea, *Mar. Geol.* 291–294, 192–210.
- Xu, F., Tao, J., Zhou, Z., Cocco, G., Zhang, C., 2016. Mechanisms underlying the regional morphological differences between the northern and southern radial sand ridges along the Jiangsu Coast, China. *Mar. Geol.* 371, 1–17.
- Xu, J.P., 1997. Converting near-bottom OBS measurements into suspended sediment concentrations. *Geo-Marine Lett.* 17, 154–161.
- Xu, M., Lu, P.D., 2005. *Sediment movement and coastal evolution under the interaction between wave and current*, Nanjing Normal University Press, Nanjing (In Chinese).
- Xue, C.T., 1993. Historical changes in the Yellow River delta, China. *Mar. Geol.* 113, 321–329.
- Xue, C.T., Zhou, Y., Wang, G., 2003. Reviews of the Yellow River Delta Superlobes Since 700 BC. *Mar. Geol. Quat. Geol.* 23, 23–29 (In Chinese with English abstract).
- Xue, C.T., Liu, J., Kong, X.H., 2011. Channel shifting of lower Yellow River in 1128–1855AD and its influence to the sedimentation in Bohai, Yellow and East China Seas. *Mar. Geol. Quat. Geol.* 31, 25–36 (In Chinese with English abstract).
- Yao, P., Su, M., Wang, Z.B., van Rijn, L.C., Zhang, C.K., Chen, Y.P., Stive, M.J.F., 2015. Experiment inspired numerical modeling of sediment concentration over sand–silt mixtures. *Coast Eng.* 105, 75–89.
- Yang, C.S., 1985. On the origin of Jianggang radial sand ridges in Yellow Sea. *Mar. Geol. Quat. Geol.* 3, 35–44 (In Chinese with English abstract).
- Yang, H., Hou Q.Z., 2004. Study on Siltation in the Outer Channel of Huanghua Harbor. *J Waterway and Harbour*, 25(3), 59–63. (In Chinese with English abstract)
- Yang, S.Y., Jung, H.S., Lim, D. II, Li, C.X., 2003. A review on the provenance discrimination of sediments in the Yellow Sea. *Earth-Science Rev.* 63, 93–120.
- Yang, S.Y., Li, C.X., Jung, H.S., Lee, H.J., 2002. Discrimination of geochemical compositions between the Changjiang and the Huanghe sediments and its application for the identification of sediment source in the Jiangsu coastal plain, China. *Mar. Geol.* 186, 229–241.
- Yang, Z.G., 1985. Sedimentology and environment in South Huanghai Sea shelf since Late Pleistocene. *Mar. Geol. Quat. Geol.* 5, 1–19 (In Chinese with English abstract).
- Ye, A.L., Chen, Z.Y., 1987. Effect of bottom topography on tidal amphidromic system in semi-enclosed rectangular waters, *J. Ocean Univ. Qingdao* 17 (2), 1–7 (In Chinese with English abstract).
- Ye, Q.C., 1986. On the development of the abandoned Yellow River delta in northern Jiangsu Province. *Acta Geogr. Sin.* 41, 112–122 (In Chinese with English abstract).
- Ye, Q.H., 2012. *An approach towards generic coastal geomorphological modelling with applications*, Ph.D. thesis, Delft University of Technology, The Netherlands.
- Yin, Y., Zou, X., Zhu, D., Huang, J., 2008. Sedimentary facies of the central part of radial tidal sand ridge system of the eastern China coast. *Front. Earth Sci. China* 2, 408–417.

- Yossef, M.F.M., Jagers, H.R., Vuren, S.V., Sieben, A., 2008. Innovative techniques in modelling large-scale river morphology, *Proceeding of International Conference on Fluvial Hydraulics*. Cesme, Izmir, Turkey, 1065–1074.
- Yu, Y.F., Guo, M.K., Liu, L., 2006. Numerical research on the changes of tidal waves due to mean-sea-level rise in the Bohai Sea, the Huanghai Sea and the East China Sea I: Numerical modeling of current tidal waves in the areas, *J. Ocean Univ.* 36 (6), 859–867 (In Chinese with English abstract).
- Yu, Z.Y., Chen, D.C., Jin, L., 1986. The formation and erosion-reworking of the Abandoned Yellow River subaqueous delta, North Jiangsu. *Acta Oceanol. Sin.* 8, 197–206 (In Chinese).
- Yuan, Y.R., Chen, Q., 1984. Sediments and sedimentary facies of the Abandoned Yellow River underwater delta in the South Yellow Sea. *Mar. Geol. Quat. Geol.* 4, 34–43 (In Chinese with English abstract).
- Zhang, C.K., 2012. *General report on the Jiangsu marine Survey and assessment*. Science Press, Beijing.
- Zhang, C.K., 2013. *Basic Situation of Marine Environmental Resources in Jiangsu Province*. China Ocean Press, Beijing.
- Zhang, C.K., Chen, J., Lin, K., Ding, X.R., Yuan, R.H., Kang, Y.Y., 2011. Spatial layout of reclamation of coastal tidal flats in Jiangsu Province, *J. Hohai Univ. (Natural Sciences)* 39, 206–212 (In Chinese with English abstract).
- Zhang, C.K., Chen, J., 2012. Master plan of tidal flat reclamation along jiangsu coastal zone, *Proc. 6th Int. Conf. on Asian and Pacific Coasts (APAC)*. 139–146.
- Zhang, C.K., Yang, Y.Z., Tao, J.F., Chen, Y.P., Yao, P., Su, M., 2013. Suspended sediment fluxes in the radial sand ridge field of South Yellow Sea, *J. Coast. Res.* 65, 624–629.
- Zhang, C.Y., Feng, X.L., 2011. Natural and human-induced effects on grain size of surface sediments along the Lianyungang muddy coast, China. *Chinese J. Oceanol. Limnol.* 29, 387–397.
- Zhang, C.K., Zhang, D.S., Zhang, J., Wang, Z., 1999. Tidal current-induced formation-storm-induced change-tidal current-induced recovery - Interpretation of depositional dynamics of formation and evolution of radial sand ridges on the Yellow Sea seafloor. *Sci. China Ser. D Earth Sci.* 42, 1–12.
- Zhang, D.S., Zhang, J.L., 1996. M2 tidal wave in the Yellow Sea radiate shoal region, *J. Hohai Univ.* 24 (5), 35–40 (In Chinese with English abstract).
- Zhang, D.S., Zhang, J.L., Zhang, C.K., Wang, Z., 1998. Tidal current formation - storm history - tidal current reform: explanation the dynamic mechanism of radiating sand ridges of the Yellow Sea, *Sci China Ser D*, 28 (005), 394–402 (In Chinese).
- Zhang, G.W., 1991. Formation and evolution of sand ridges in the south Huanghai Sea shelf. *Mar. Geol. Quat. Geol.* 11, 25–35 (In Chinese with English abstract).
- Zhang, L., Chen, S.L., Liu, X.X., 2014. Evolution of the abandoned Huanghe (Yellow) River delta in north Jiangsu province in 800 years. *Oceanol. Limnol. Sin.* 45, 626–636 (In Chinese with English abstract).

- Zhang, L., Chen, S.L., Pan, S.Q., Yi, L., Jiang, C., 2014. Sediment variability and transport in the littoral area of the abandoned Yellow River Delta, northern Jiangsu. *J. Geogr. Sci.* 24, 717–730.
- Zhang, L., Chen, S., Yi, L., 2015. The Sediment Source and Transport Trends around the Abandoned Yellow River Delta, China. *Mar. Georesources Geotechnol.* 1–10.
- Zhang, R.S., 1984. Land-forming history of the Huanghe River delta and coastal plain of North Jiangsu. *Acta Geogr. Sin.* 39, 173–184 (In Chinese with English abstract).
- Zhang, R.S., Lu, L.Y., Wang, Y., 2002. The mechanism and trend of coastal erosion of Jiangsu Province in China. *Geogr. Res.* 21, 469–478 (In Chinese with English abstract).
- Zhang, W.S., 2005. *Numerical Modeling of Tides Wave in Margin Seas Near China*, Ph.D. thesis, Hohai University, China.
- Zhang, Y., Swift, D.J.P., Yu, Z., Jin, L., 1998. Modeling of coastal profile evolution on the abandoned delta of the Huanghe River. *Mar. Geol.* 145, 133–148.
- Zhao, B.R., Fang, G.H., Cao, D.M., 1994. The numerical simulation on the tide and tidal current of the Bohai Sea, the Yellow Sea and the East China Sea, *Acta Oceanol Sin* 16 (5), 1-10 (In Chinese).
- Zhao C.J., 2003. *Study on Power Sand Movement Laws in Coastal Dynamic Condition*. Tianjin: Tianjin University. (In Chinese with English abstract)
- Zhou, L.Y., Liu, J., Saito, Y., Zhang, Z., Chu, H., Hu, G., 2014. Coastal erosion as a major sediment supplier to continental shelves: example from the abandoned Old Huanghe (Yellow River) delta. *Cont. Shelf Res.* 82, 43–59.
- Zhu, X.M., 2009. *Numerical simulations and studies on the tides and tidal currents in the marginal seas adjacent to China*, MSc thesis, Ocean University of China, China (In Chinese with English abstract).
- Zhu, X.M., Bao, X.W., Song, D.H., Qiao, L.L., Huang, B.G., Shi, X.G., 2012a. Numerical study on the tides and tidal currents in Bohai Sea, Yellow Sea and East China Sea, *Oceanol Limnol Sin* 43(6), 1103-1113 (In Chinese with English abstract).
- Zhu, X.M., Liu, G.M., 2012b. Numerical study on the tidal currents, tidal energy fluxes and dissipation in the China seas, *Oceanol Limnol Sin* 43(3), 669-677 (In Chinese with English abstract).
- Zhu, Y.R., 1998. Numerical Simulation of Paleo-tidal current field in the subei littoral Plain area and its verification. *Mar. Sci. Bull.* 17, 1–7 (In Chinese with English abstract).
- Zhu, Y.R., Chang, R.F., 2000. Preliminary study of the dynamic origin of the distribution pattern of bottom sediments on the continental shelves of the Bohai Sea, Yellow Sea and East China Sea. *Estuar. Coast. Shelf Sci.* 51, 663–680.
- Zhu, Y.R., Chang, R.F., 2001a. On the relationships between the radial tidal current field and the radial sand ridges in the southern Yellow Sea: a numerical simulation. *Geo-Mar. Lett.* 21 (2), 59–65.
- Zhu, Y.R., Chang, R.F., 2001b. Sediment dynamics study on the origin of the radial sand ridges in the southern Yellow Sea, *Stud Mar Sin.* 43, 38-50 (In Chinese with English abstract).
- Zhu, Y.R., Chen, Q.Q., 2005. On the origin of the radial sand ridges in the southern Yellow Sea: Results from the modeling of the paleoradial tidal current fields off the paleo-Yangtze River

Estuary and northern Jiangsu coast. *J. Coast. Res.* 21, 1245–1256.

ACKNOWLEDGEMENTS

THE PhD “journey” is a long and unforgettable period. At this moment, I would like to express my heartfelt thanks to all the people who have helped me during this journey.

First and foremost, I would like to give my thanks to my promotors, Prof. Marcel Stive and Prof. Zheng Bing Wang. I feel lucky to have the opportunity to pursue my PhD study in the TU Delft. During the study in Delft, they are always ready to give me their expert guidance. And, they are always standing with me, when I face some difficulty issues. Prof. Marcel Stive is busy but he still paid lots of attention to my research work, helped me with my spoken and written English. In the meeting with him, he can always give many thoughtful suggestions and encourage me a lot. Prof. Wang is a very kindhearted professor as well. He greatly helped me with my written English and the knowledge on various academic aspects. The most important thing I learned from him is a rigorous attitude towards the academic questions. “Modelling is just an approach, and the most crucial issue is to gain a deep insight into the reason which leads to the simulated phenomenon”. Besides, it is a nice memory to spend several traditional Chinese festivals with both of you and your families. I am grateful that I belong to such a large and happy family.

Next, special thanks are given to Prof. Changkuan Zhang and Prof. Yongping Chen. I acknowledge them for providing data of the Jiangsu coast, welcoming me as a family when I arrived in Nanjing, and supporting the flume experiments in China. As experts on the Jiangsu coast, they provided many constructive suggestions on my research.

I also appreciate the help from Jianfeng Tao. His plenty of experience on modeling the Jiangsu coast inspired me in the morphodynamic modelling of the Jiangsu coast. Thanks are also given to Qinghua Ye for the technical help on debug and tuning Delft3D. I would like to thank Mariette van Tilburg for checking the English writing of several manuscripts and I really learn lots from the revision and suggestions. Besides, thanks Mariette also for translating the abstract and propositions of this thesis into Dutch. I also thank Cees Timmers for the funding for the laboratory experiments in 2013. Many thanks are given to all of the committee members for examining my thesis.

I want to thank my dearest friends in Delft and in China: Xiuhan Chen, Zhan Hu,

Xuexue Chen, Tianwen and Shouqian.

My colleagues and friends in Delft are also should be addressed thanks. Special thanks are given to my officemate: Wei Li, Phan Manh Hung, Hualong, Runxiang and Gensheng. Especially, I thank Wei for her kind help with life tips and academic attitude in my PhD life. Besides, our “Chinese team” works very well in the past years. An incomplete list of them is Lixia, Peng Dai, Sien, Rong, Yang, Chunyan, and Wenhao. I am not good at talking but listening to yours during lunch is the most relax time of a day. Thanks goes to Bram van Prooijen, Sierd de Vries, Matthieu de Schipper, Saulo Meirelles, João Mil-Homens, Truong Hong Son, Phan Khanh Linh, Trang Minh Duong, Qin Zhu for discussing on scientific and non-scientific topics.

我很感激父母无条件的支持和无微不至的关怀。孔子说：父母在，不远游，游必有方。作为独女，我常后悔放下你们来这么远的地方读这么久的书，让你们在需要我和想念我的时候只能通过短信或视频联系我。希望未来我们一起开心快乐的生活。另外，我也真诚的感恩亲戚和兄弟姐妹们在我出国这几年对我父母的照顾。

I would like to give my thanks and adore to my partner Peng Yao. You are the partner of my life and my research. I cherish both happy and sad memory with you. I always believe we are a group of “1+1>2”.

Finally, I acknowledge the sponsorships from the “China Scholar Council (CSC)”, “Het Lamminga Fonds”, and the jointly financial support by the Hohai University and the Delft University of Technology. Thanks for helping me with collecting historical maps by anonymous persons: 오길순 and “oldmap macau”.

Min Su

March 2016

CURRICULUM VITAE

Min SU

Min Su was born on 4th of November 1986 in Heze, Shandong Province of China.

She studied the Water Resources and Hydropower Engineering at Shandong Agriculture University from 2004 to 2008. She graduated with an honor of “the outstanding graduate of the Shandong Province”. In September 2008, she started the Master study in Hohai University, as the 1st place during the entrance examination. In the next three years, she participated in several large-scale and small-scale physical experiments.

In June of 2011, she obtained master degree of Harbor, Coastal and Nearshore Engineering. At the same year, she pursued her PhD study in Coastal Engineering at Delft University of Technology following the guidance of Prof. Marcel Stive and Prof. Zheng Bing Wang. She mainly focused on the evolution of the Jiangsu coast, through analyzing both the hydrodynamic and morphodynamic aspects. After her PhD, she plans to go on work as a researcher on the coastal zones, estuarine and deltaic zones.



LIST OF PUBLICATIONS

JOURNAL PUBLICATIONS

5. **M. Su**, P. Yao*, M.J.F. Stive, C.K. Zhang, Z.B. Wang, 2015. Conversion of electro-optical signals to sediment concentration in a silt-sand suspension environment. *Coastal Engineering*. [under review].
4. P. Yao, **M. Su***, M.J.F. Stive, C.K. Zhang, Z.B. Wang, 2015. Tidal current system in the South Yellow Sea. *Continental Shelf Research*. [under review].
3. P. Yao, **M. Su***, Z.B. Wang, L.C. van Rijn, C.K. Zhang, Y.P. Chen, M.J.F. Stive, 2015. Experiment inspired numerical modeling of sediment concentration over sand-silt mixtures. *Coastal Engineering*. doi:10.1016/j.coastaleng.2015.07.008.
2. **M. Su**, P. Yao*, Z.B. Wang, C.K. Zhang, M.J.F. Stive, 2015. Tidal Wave Propagation in the Yellow Sea. *Coastal Engineering Journal*. doi:10.1142/S0578563415500084.
1. C.K. Zhang, Y.Z. Yang, J.F. Tao, Y.P. Chen, P. Yao, **M. Su**, 2013. Suspended sediment fluxes in the radial sand ridge field of South Yellow Sea. *Journal of Coastal Research*. doi:10.2112/SI65-106.

SUBMITTED AND PREPARED

1. **M. Su**, P. Yao*, Z.B. Wang, C.K. Zhang, M.J.F. Stive, 2015. Exploratory morphodynamic hind-cast of the evolution of the Abandoned Yellow River delta, 1578-1855 AD. *Marine Geology*. [submitted].
2. **M. Su**, P. Yao*, Z.B. Wang, C.K. Zhang, M.J.F. Stive, 2015. Exploratory morphodynamic modelling on the evolution of the Jiangsu coast since 1855. *Marine Geology*. [submitted].
3. P. Yao, **M. Su***, Z.B. Wang, C.K. Zhang, M.J.F. Stive, 2015. Sediment transport modeling in a silt-sand mixed environment - A cast study of the Jiangsu coast. *Journal of Geophysical Research*. [submitted].
4. P. Yao, **M. Su***, Z.B. Wang, C.K. Zhang, M.J.F. Stive, 2015. Tide-induced sediment transport along the Jiangsu coast: spatial and temporal variability. [draft].

CONFERENCE PAPERS

6. **M. Su**, P. Yao, Z.B. Wang, C.K. Zhang, Y.P. Chen, M.J.F. Stive, 2015. Laboratory Studies on the Response of Fine Sediment to Wind. The 36th IAHR World Congress, Den Haag.
5. P. Yao, **M. Su**, Z.B. Wang, C.K. Zhang, Y.P. Chen, M.J.F. Stive, 2015. High concentration layer over silt-sand mixtures under waves. The 36th IAHR World Congress, Den Haag.
4. **M. Su**, Z.B. Wang, C.K. Zhang, P. Yao, M.J.F. Stive, 2013. Further Research on the Tidal Wave System in the Southern Yellow Sea. The 35th IAHR Congress, Chengdu.
3. P. Yao, M.J.F. Stive, C.K. Zhang, **M. Su**, Z.B. Wang, 2013. On the Formation of Radial Tidal Current off the Central Jiangsu Coast. The 35th IAHR Congress, Chengdu.
2. **M. Su**, M.J.F. Stive, C.K. Zhang, P. Yao, Y.P. Chen, Z.B. Wang, 2013. The tidal wave system in the Chinese marginal seas. The 7th International Conference on Coastal Dynamics, Arcachon.
1. P. Yao, Z.B. Wang, C.K. Zhang, **M. Su**, Y.P. Chen, M.J.F. Stive, 2013. The genesis of the radial tidal current off the Central Jiangsu Coast. The 7th International Conference on Coastal Dynamics, Arcachon.